Fluid structure interaction for fluid flow normal to deformable porous media

Sabine Muntz

Vom Fachbereich Mathematik der Technischen Universität
Kaiserslautern zur Verleihung des akademischen Grades

Doktor der Naturwissenschaften
(Doctor rerum naturalium, Dr. rer. nat.)

genehmigte Dissertation.

Gutachter:
Prof. Dr. habil. Oleg Iliev
Prof. D.Sc. Svetozar Margenov

Datum der Disputation: 02.12.2008

D 386

Acknowledgements

> *Many of the things you can count, don't count.*
> *Many of the things you can't count, really count.*
> *Albert Einstein*

At this point I would like to thank all people who contributed to my work in uncountable ways.

First of all, I thank Prof. Dr. habil. Oleg Iliev and Priv.-Doz. Dr. Heiko Andrä of the Fraunhofer ITWM[1] for supervising my PhD thesis.
I thank Oleg Iliev for introducing me to the interesting field of my research. I am very grateful for all fruitful discussions and useful advice that helped me gain deeper understanding of the topic and led me to new ideas. Many thanks to Heiko Andrä for productive conversations, for his help with various problems and especially for the enrichment of my research by his point of view as an expert in mechanical engineering.

I owe a lot of gratitude to Dr. Anna Naumovich and Dr. Dariusz Niedziela. Many scientific discussions and helpful advice, regarding the software, helped to accelerate my work.

Furthermore, I thank all my colleagues of the department "Flow and Material Simulation" of the Fraunhofer ITWM. I appreciated the friendly atmosphere very much.

For the financial support of this work I thank the Fraunhofer Gesellschaft.

Moreover, I would like to express my deepest gratitude to Prof. Quentin Fisher[2], Prof. Rob Knipe[3] and Dr. Simon Harris[3] for introducing me to another interesting application of my PhD research topic while I was doing a research fellowship at RDR[3] and the Centre for Computational Fluid Dynamics[4] in Leeds. Many thanks also to Dr. Lionel Elliot[5], Prof. Derek Ingham[5] and Jayne Harnett[3] for taking so good care of me.
This fellowship has been funded by the Marie Curie programme of the European Union.

Last but not least, I would like to thank my family and my friends Martina, Katrin and Emanuel for their understanding, neverending motivation and for always believing in me. I am very grateful to my boyfriend Peter for his love, encouragement and endless patience with me, especially during the last months of my PhD.

---

[1] Fraunhofer Institut für Techno- und Wirtschaftsmathematik, Kaiserslautern, Germany

[2] School of Earth and Environment, University of Leeds, UK

[3] Rock Deformation Research Ltd., Leeds, UK

[4] Faculty of Engineering, University of Leeds, UK

[5] Department of Applied Mathematics, University of Leeds, UK

Table of Contents

Introduction and outline

The interaction of fluid with deformable porous media can be found in many industrial and environmental applications, for example in filtration processes, oil production, geomechanics, flooding simulation, waste water treatment, breakwater design or production of food and beverages. We are mainly interested in applications in filtration. Filtration processes are mostly characterised by the performance and the life time of the filter medium. During the filtration process, the properties of the filter medium change: efficiency, pressure drop, permeability, porosity, mass flux, stresses and so on. These modifications might lead for example to a clogging of the filter or even to a destruction. Especially for ceramic filters it happens very often that they break when the stresses are too high. Of course, this has to be avoided and therefore, it is desirable to predict the filtration process by simulations, such that the interactions of the fluid flow and the solid skeleton are taken into account.

The simulation of the interaction of fluid flow with deformable porous media is a challenging task. There are different physical phenomena that have to be combined: complicated problems like fluid-structure interaction, flow in deformable porous media and coupling of free fluid and porous media flow are only subtasks for the complete problem. During the last years, efficient solvers for the subtasks, mentioned above, have been developed in the department ”Flow and Material Simulation” of the Fraunhofer ITWM[6]. Readers, interested in fluid-structure interaction, we refer to [1], [24], [34] and [44]. Algorithms for the coupling of free flow with rigid porous media and applications in oil filtration are described in [32], [33], [40] and [68]. A description of a flow solver for various applications, e.g. non-Newtonian fluids, granular flows, can be found in [47], [69] and [70]. We refer to [21], [46], [45] and [65] for reports on an efficient algorithm for flows in deformable porous media.

Domain decomposition (DD) methods are well-established tools for the numerical solution of such problems. The main idea is the division of the problem domain $\Omega \subset \mathbb{R}^3$ into finitely many smaller subdomains $\Omega_1, ..., \Omega_n$, $\Omega_i \subset \Omega$, $i = 1, ..., n \in \mathbb{N}$, where the subproblems can be solved independently and to relate the subdomains to each other through appropriate transmission conditions on the interfaces. The division of Ω into subdomains follows several aspects: First of all, it makes sense to delimit regions with different physical properties. They are described by different differential operators and thus, it is often computationally more efficient to apply various solvers and meshes, according to the numerical method and the features of the differential operator in the subdomains. Furthermore, it might also make sense to divide the subdomains into smaller subdo-

---

[6] Fraunhofer Institut für Techno- und Wirtschaftsmathematik, Kaiserslautern, Germany (www.itwm.fhg.de)

mains, for example, when singularities occur in the solution of the respective partial differential equation (PDE). In parallel computing, DD implies the distribution of the separate subdomains to different processors. DD methods can also be used as preconditioners: large systems of equations are subdivided into smaller ones. The subproblems are connected by appropriate transmission conditions across the interfaces, where the interface is defined as the common boundary of the adjacent subdomains.
The crucial point in DD methods is the coupling of different physical phenomena and/or meshes across the interfaces. The transmission conditions have to be formulated so that they ensure a proper exchange of information across the interface. Theory and applications of DD methods can be found in [37], [39] and [62].

DD methods are also applied in the simulation of filtration processes. The fluid flow in the fluid regions is usually modelled by the Navier-Stokes equations. In the porous medium people apply various physical laws. Very often, the interaction between the fluid and the solid structure inside the porous medium is neglected. It means, that the porous medium is considered to be rigid and one computes the fluid flow through the porous medium, depending only on the porosity and the permeability of the porous medium and the fluid properties. The elastic properties of the solid skeleton are not taken into account. The fluid flow in the porous domain is modelled by Darcy's law or the Brinkman equations. More details and applications of this approach in filtration can be found in [32], [33] and [40].

In this approach the elastic properties of the solid skeleton are not taken into account. Thus, on the one hand one cannot compute the effect of the fluid flow on the solid skeleton of the porous medium (fluid-to-solid coupling) and on the other hand, one does not care for the effects that the deformed porous medium might have on the fluid flow through it (solid-to-fluid coupling). This two-way coupling is very important. From the fluid-to-solid coupling we obtain the stresses in the solid skeleton. The solid-to-fluid coupling is essential, especially when dealing with slightly compressible or incompressible fluids. Then, changes in the stress field might have a significant influence on the pore pressure. The Biot poroelasticity system (see section 1.3.6) is a quasi-static system of equations that takes into account the interaction between the fluid flow and the solid skeleton inside the porous medium. In 1941, Maurice Biot was the first one who formulated the general three-dimensional theory of poroelasticity, see [8]. Applications can be found in various fields of science and engineering. For example in consolidation theory [5], [31], [42], [64] or filtration [2]. Multilayered media also often appear in such applications and have been studied in [46].

One of the crucial points in DD methods is the proper exchange of information across the interfaces, especially when different physical phenomena and/or grids have to be coupled. On the one hand, the coupling has to be physical and on the other hand, we have to ensure the well-posedness of the problems in the separate subdomains. Several types of coupling have been studied. For example, the coupling of two immiscible fluids (see e.g. [14], [27]) or the coupling of a fluid with a solid body (see e.g. [34], [44]). The coupling of the Biot equations for multilayered porous media is described in [46].

In the coupling of free fluid flow with porous media one has to distinguish between rigid and deformable porous media. In both categories, it plays a crucial role whether the fluid flows tangentially or perpendicularly to the porous medium. The general case, i.e. when the fluid flow is angular to the porous medium, is unclear how to handle. The coupling of fluid flow and rigid porous media is modelled by the Navier-Stokes equations in the free fluid regions and by Darcy's law or the Brinkman equations in the porous medium (see e.g. [30], [32], [40]). Here the transmission conditions differ, depending whether the fluid flow is parallel or nearly normal to the porous medium. In both cases the continuity of the mass flux across the interface is required. The description of interface conditions for all different cases of rigid porous media will be taken on in section 2.2. For detailed studies see e.g. [7], [40], [53].

To our knowledge, the coupling of free fluid flow and deformable porous media has only been studied for fluid flow parallel to the porous medium (see [59], [60]). The fact that the fluid flow is tangential to the porous medium plays an essential role in the formulation of the transmission conditions. Ralph Showalter [59] models the coupling of free fluid flow and poroelastic porous media by the coupling of the Stokes equations and the Biot poroelasticity equations. For flow tangential to the porous medium he requires the conservation of mass across the interface. Furthermore, he assumes that the stress difference between the fluid domain and the porous domain causes the Darcy flow across the interface. Moreover, he fulfils the conservation of momentum and he applies the Beavers-Joseph-Saffman condition which states that the common tangential stress is proportional to a slip rate. These conditions are written down in section 2.2, or see [59].

In this thesis we derive the transmission conditions for the coupling of fluid flow with poroelastic porous media, where the fluid flow is normal to the porous medium. For this purpose we consider a domain $\Omega \subset \mathbb{R}^3$ which consists of a fluid domain Ω_f and a porous domain Ω_p so that $\Omega = \Omega_f \cup \Omega_p$ and $\Omega_f \cap \Omega_p = \emptyset$, see figure 0.1. The boundary of the fluid domain is denoted

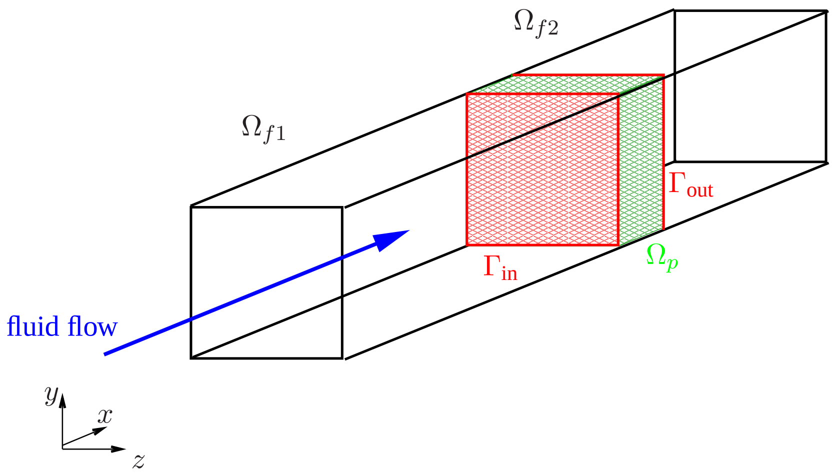

Figure 0.1: The model geometry for fluid flow normal to a porous medium. Ω_p: porous medium, Ω_{f1} and Ω_{f2}: disjoint fluid domains so that $\Omega_f = \Omega_{f1} \cup \Omega_{f2}$, $\Gamma := \Gamma_{\text{in}} \cup \Gamma_{\text{out}}$: interface between fluid domain and porous medium.

by $\partial\Omega_f$, the boundary of the porous domain by $\partial\Omega_p$. The interface Γ between $\partial\Omega_f$ and $\partial\Omega_p$ is defined as the intersection of the respective boundaries. Γ is split into the inflow interface $\Gamma_{\text{in}} = \partial\Omega_{f1} \cap \partial\Omega_p$ and the outflow interface $\Gamma_{\text{out}} = \Omega_p \cap \partial\Omega_{f2}$, where Ω_{f1} and Ω_{f2} are disjoint fluid domains such that $\Omega_f = \Omega_{f1} \cup \Omega_{f2}$. This distinction is needed for the derivation of the transmission conditions (see chapter 2). A 2d sketch of our model domain is shown in figure 2.1. For a more detailed description of the domain, we refer to section 2.1.

In this thesis a laminar incompressible Newtonian fluid is considered. It is modelled by the Stokes equations

$$\left.\begin{aligned} \varrho\frac{\partial \mathbf{v}}{\partial t} - \eta\Delta\mathbf{v} + \nabla p_f = \mathbf{f}_f \\ \nabla\cdot\mathbf{v} = 0 \end{aligned}\right. \qquad \text{in}\, \Omega_f\,,$$

where $\mathbf{v}$ denotes the velocity, p_f the pressure, ϱ the density and η the dynamic viscosity of the fluid. t is the variable for the time and $\mathbf{f}_f$ denotes external forces. The first equation is the momentum equation and the second one is the continuity equation. In order to have a well-posed problem, the Stokes equations are complemented with suitable boundary conditions (see section 1.1). For details and applications of the Stokes equations we refer to [18], [27], [63] or other books on fluid dynamics.

The fluid flow through the deformable porous medium is modelled by the quasi-static Biot poroelasticity equations

$$\left.\begin{aligned} -\nabla\cdot\sigma_p + \alpha\nabla p_p = \mathbf{0} \\ \frac{\partial}{\partial t}(\phi\beta p_p + \alpha\nabla\cdot\mathbf{u}) + \nabla\cdot\mathbf{q} = f_p \end{aligned}\right. \qquad \text{in}\, \Omega_p\,,$$

where $\mathbf{u}$ denotes the vector of displacements, σ_p the effective stress tensor, p_p the effective fluid pressure and $\mathbf{q}$ the fluid flux, which is defined by Darcy's law

$$\mathbf{q} = -\frac{k}{\eta}\nabla p_p\,.$$

ϕ stands for the porosity, η for the dynamic viscosity of the fluid, k for the permeability of the porous medium. f_p is a source term, which describes for example an extraction or injection process. β denotes the compressibility of the fluid and α is the so-called Biot-Willis constant, which accounts for the compressibility of the grains. A review of suitable boundary conditions and the boundary conditions we use is given in sections 1.3.6 and 2.1. For more details on the boundary conditions of the Biot system we refer to [56] - [58].

The transmission conditions for our purpose are derived from a microscopic consideration of the interface (see figure 2.2 on page 21). We formulate the mass conservation equation

$$\mathbf{v} = (1-\phi)\alpha\frac{\partial\mathbf{u}}{\partial t} + \mathbf{q} \qquad \text{on}\,\Gamma\,,$$

the continuity of tractions equation

$$\sigma_f\cdot\mathbf{n} = (1-\phi)\,\sigma_s\cdot\mathbf{n} + \phi\,\sigma_f^p\cdot\mathbf{n} \qquad \text{on}\,\Gamma\,,$$

and a pressure jump condition for the inflow interface

$$p_p = p_f + \frac{\varrho}{2} v_x^2 \left(1 - \frac{1}{\phi^2 C_{\text{c}}^2}\right) \qquad \text{on } \Gamma_{\text{in}} \, ,$$

as well as for the outflow interface

$$p_f = p_p + C_{\text{e}} \frac{\varrho}{2} {v_{fx}^p}^2 \left(1 - \phi^2\right) \qquad \text{on } \Gamma_{\text{out}} \, ,$$

respectively. The variables have the same meaning as in the Stokes equations and the Biot poroelasticity system. In the continuity of tractions equation, σ_f denotes the stress tensor of the fluid in Ω_f, σ_s is the stress tensor of the solid skeleton in the porous medium and σ_f^p stands for the stress tensor of the fluid in Ω_p. In the pressure jump conditions, C_{c} denotes the contraction number of a flow channel with a discontinuous constriction and C_{e} denotes the efficiency number of a step diffuser (with discontinuous expansion of the channel). The derivation of the transmission conditions in one and three dimensions is explained in section 2.2.

The analytical solution of such a big system is difficult or even impossible. Even the subproblems (i.e. Biot and Stokes equations) can only be solved analytically in special cases. Therefore, numerical methods have to be used for the solution of such problems.

There exist various methods for the numerical solution of the Navier-Stokes equations. The finite element method as well as the finite difference method are used. But very often one obtains a highly oscillatory pressure field. Therefore, the use of staggered grid was introduced. This is realised for example in the MAC method, which was one of the earliest and most widely used methods. Another group of methods that are often used are projection type methods. They are characterised by the use of a pressure-correction equation to enforce mass conservation. The SIMPLE algorithm is one of these methods. It is based on the idea of operator splitting. The momentum equation and the continuity equation are solved consecutively in order to decouple the computation of the pressure and the velocity. More details about all methods mentioned above can be found for example, in [18], [20] or [27]. The SIMPLE method will be used in our algorithm.

For the numerical solution of the Biot poroelasticity equations it has been found that the finite element or finite difference solutions on collocated grids often show an oscillatory non-physical behaviour. In order to overcome such instabilities, the use of staggered grids has been proposed and analytically investigated in [22], [23]. Based on these investigations, Dr. Anna Naumovich has developed an efficient multigrid solver for multilayered porous media (see [46]). This solver is used in the solution of our coupled problem.

We solve the coupled Biot-Stokes system by a DD approach using the SIMPLE-algorithm on a cell-centred grid for the Stokes equations and a multigrid solver on a staggered grid for the Biot equations.

Outline of the thesis

This thesis is structured in the following way:
Chapter 1 is devoted to notation and fundamental equations in fluid dynamics, linear elasticity and porous media. The goal of this chapter is to summarise all equations and concepts which are needed throughout this thesis. In the end, we give an example which clearly shows that for the processes we study, the Biot poroelasticity equations cannot be replaced by the elasticity equations.

In chapter 2 we first introduce the model geometry we are working on, including a detailed description of the interface between fluid region and porous domain on the microscopic level. Then, existing transmission conditions for the coupling of various equations are presented (e.g. fluid-fluid coupling, solid-fluid coupling, coupling of fluid and porous media for tangential fluid flow). Afterwards, the transmission conditions for coupling Stokes equations and the Biot poroelasticity equations for normal flow in one and three dimensions are derived. At the end, the continuous coupled formulation in 3d is given. The coupled formulation in 1d is treated in chapter 3. There, we also consider the extreme cases (fluid-fluid and fluid-solid) and finally, we give some numerical results.

Chapters 4 and 5 deal with the discretisation of the coupled Biot-Stokes system in three dimensions. In chapter 4 node-based matching grids are used for the discretisation of both, the fluid domain and the porous domain. In chapter 5 a cell-centred grid is used for the fluid domain and a staggered grid is used in the porous domain. These meshes are non-matching. In both chapters we give the discretisation of the Biot equations, the Stokes equations and the transmission conditions on the respective grids. Then, these equations are written in operator form and thus, the discrete coupled formulation is derived.

In chapter 6 the iterative solution procedure for the coupled Biot-Stokes system on non-matching meshes is explained. We describe the structure as well as details of the algorithm and present the software packages that are used. Finally, we show numerical results for steady state examples, for depth filtration and cake filtration examples. A summary concludes this thesis.

Chapter 1

Governing equations

This chapter is devoted to some basic laws in fluid flow, linear elasticity and porous media. The appropriate notation will be introduced and thus, it will provide a basis for the following chapters of the thesis.

First, we introduce the Navier-Stokes equations and the Stokes equations and give a definition for the stress tensor of incompressible Newtonian fluids. Then, we summarise the most important things about linear elasticity. The last part of this chapter is devoted to laws in porous media. We state Darcy's law and the Brinkman equations, which describe the fluid flow through a rigid porous medium. The Kozeny-Carman equation is derived next. It is a well-known relation between permeability and porosity in porous media. Since we are concerned with deformable porous media, we review the concept of effective stress, developed by Terzaghi, and explain the computation of effective elastic moduli in porous media. These two concepts enter the Biot poroelasticity equations, which model fluid flow through poroelastic media.

The correlation of the following equations will become clear in the subsequent chapters. This chapter introduces the fundamental equations that are needed in this thesis. Thus, we will hark back to the various laws at the corresponding places, where they are needed in the derivation of the coupled Biot-Stokes system.

1.1 Equations in free fluid flow

In general, fluid flow of Newtonian fluids with constant density in a pure fluid region $\Omega_f \subset \mathbb{R}^3$ is described by the Navier-Stokes equations

$$\left.\begin{aligned} \varrho\frac{\partial \mathbf{v}}{\partial t} - \eta\Delta\mathbf{v} + (\varrho\mathbf{v}, \nabla)\,\mathbf{v} + \nabla p_f &= \mathbf{f}_f \\ \nabla \cdot \mathbf{v} &= 0 \end{aligned}\right. \qquad \text{in } \Omega_f\,, \tag{1.1.1}$$

where $\mathbf{v}$ and p_f denote the velocity and the pressure of the fluid, respectively. ϱ stands for the density of the fluid, η is the dynamic viscosity and $\mathbf{f}_f$ is an additional force. The first equation of (1.1.1) is a momentum equation, the second one is the continuity equation. The term $\eta\Delta\mathbf{v}$ is the so-called diffusion or dissipation term and $(\varrho\mathbf{v}, \nabla)\,\mathbf{v}$ the convection term. The Navier-Stokes equations are used for a wide range of fluids like water or oil. Readers, interested in the Navier-Stokes equations, we refer to e.g. [9], [11], [18], [27], [63].

For small Reynolds number, i.e. for slow flow, large viscosity or small bodies, the convection term becomes negligible. The resulting equations are the Stokes equations:

$$\left.\begin{aligned} \varrho\frac{\partial \mathbf{v}}{\partial t} - \eta\Delta\mathbf{v} + \nabla p_f = \mathbf{f}_f \\ \nabla\cdot\mathbf{v} = 0 \end{aligned}\right. \quad \text{in}\,\Omega_f\,, \tag{1.1.2}$$

where the variables have the same meanings as explained for the Navier-Stokes equations. The first equation in (1.1.2) is the momentum equation and the second one is the continuity equation.
The Stokes equations have to be provided with suitable boundary conditions. Let the boundary of the domain $\partial\Omega_f$ consist of three disjoint parts: the inflow $\partial\Omega_{f,\text{in}}$, the outflow $\partial\Omega_{f,\text{out}}$ and a part $\partial\Omega_{f,\text{fixed}}$ where the fluid can neither enter nor leave the domain Ω_f, such that $\partial\Omega_f = \partial\Omega_{f,\text{in}} \cup \partial\Omega_{f,\text{out}} \cup \partial\Omega_{f,\text{fixed}}$ and the intersection of these three parts is the empty set. We use the following boundary conditions

$$\mathbf{v} = \mathbf{v}_0 \qquad \text{on } \partial\Omega_{f,\text{in}}\,, \tag{1.1.3a}$$

$$p_f = p_{f,0} \qquad \text{on } \partial\Omega_{f,\text{out}}\,, \tag{1.1.3b}$$

$$\mathbf{v} = 0 \qquad \text{on } \partial\Omega_{f,\text{fixed}}\,. \tag{1.1.3c}$$

The third condition (1.1.3c) is the so-called no-slip boundary condition. With these boundary conditions, the Stokes equations are a well-posed problem.
More details about the Stokes equations can be found, for example, in [11], [17] - [20] or other books on fluid dynamics.

The stress tensor σ_f for incompressible Newtonian fluids can be written as

$$\sigma_f = \eta(\nabla\mathbf{v} + (\nabla\mathbf{v})^T) - p_f\mathbf{I}\,, \tag{1.1.4}$$

where p_f is the fluid pressure and $\mathbf{I}$ is the unit matrix. The term $\eta(\nabla\mathbf{v} + (\nabla\mathbf{v})^T)$ in this equation is the viscous stress tensor. For some special cases (e.g. fluid without friction), the viscous stresses are neglected and thus, the stress tensor is simply

$$\sigma_f = -p_f\mathbf{I}\,. \tag{1.1.5}$$

This definition can be found, for example, in [4], [18], [27], [63].

1.2 Linear elasticity

The linear elasticity theory describes the behaviour of linear elastic materials. The term ”linear” refers to the fact that the theory is restricted to infinitesimal deformations. This is sufficient for many engineering problems. For the classical theory of linear elasticity, we refer to [6], [12], [25], [26], [66] or [67].
The traction vector in a point P is defined as

$$\mathbf{t} = \lim_{\Delta A\to 0}\frac{\Delta\mathbf{F}}{\Delta A} = \frac{d\mathbf{F}}{dA}\,,$$

where $\Delta\mathbf{F}$ is the force that acts on an area ΔA. The traction vector depends on the orientation of the cutting plane through point P.

The stress tensor σ is a second order tensor that describes the mechanical stresses in a point P of a solid body:

$$\sigma = \begin{pmatrix} \sigma_{xx} & \sigma_{xy} & \sigma_{xz} \\ \sigma_{xy} & \sigma_{yy} & \sigma_{yz} \\ \sigma_{xz} & \sigma_{yz} & \sigma_{zz} \end{pmatrix} .$$

Due to the balance of momentum, σ is a symmetric tensor. The diagonal elements are called normal stresses, the off-diagonal ones shear stresses. The traction vector in a point P is related to the stress tensor in the following way

$$\mathbf{t} = \sigma \cdot \mathbf{n} ,$$

where $\mathbf{n}$ is the outward pointing normal vector to the cutting area through the point P.

The kinematics of a deformable solid body is described by the terms of strain and displacement. Let Ω be a body in its initial undeformed state. Then, a point P can be identified by a position vector $\mathbf{X}$. By deformation, the body Ω passes into the deformed body Ω'. Thus, the point P is moved to a new position P'. Its new position is characterised by the spatial coordinates of the vector $\mathbf{x}$. Thus, the displacement $\mathbf{u}$ can be written as

$$\mathbf{u} = \mathbf{x} - \mathbf{X} .$$

In continuum mechanics, there are two different perspectives for the description of state and movement: The Eulerian or spatial description is related to a fixed coordinate system, i.e. the observer has a fixed position and sees e.g. how particles P pass by. He observes a fixed control volume and notices how states in this control volume change. Thereby it is unimportant which particle stays where at a certain point of time. This perspective enables us to describe large deformations and movements. Here, one would describe the state and deformation of a particle as

$$\mathbf{X} = \mathbf{X}(\mathbf{x}) , \qquad \mathbf{u} = \mathbf{u}(\mathbf{x}) .$$

The Eulerian description is especially used in fluid dynamics.

The Lagrangian or material description is related to a local coordinate system, which moves with the corresponding particle. Thus, the observer notices changes in the state. So, a particle's place and displacement would be described by

$$\mathbf{x} = \mathbf{x}(\mathbf{X}) , \qquad \mathbf{u} = \mathbf{u}(\mathbf{X}) ,$$

respectively. The Lagrangian perspective is typically used in solid mechanics for small as well as for finite deformations. Actually, for small deformations, the Eulerian and the Lagrangian description are conform.

Strains are functions of the displacements. Assuming small deformations, the components of the linearised strain tensor are the derivatives of the displacements:

$$\begin{aligned}
\varepsilon &= \frac{1}{2}(\nabla\mathbf{u} + (\nabla\mathbf{u})^T) \qquad (1.2.1)\\
&= \frac{1}{2}\left(\begin{pmatrix} u_{x,x} & u_{x,y} & u_{x,z} \\ u_{y,x} & u_{y,y} & u_{y,z} \\ u_{z,x} & u_{z,y} & u_{z,z} \end{pmatrix} + \begin{pmatrix} u_{x,x} & u_{y,x} & u_{z,x} \\ u_{x,y} & u_{y,y} & u_{z,y} \\ u_{x,z} & u_{y,z} & u_{z,z} \end{pmatrix}\right).
\end{aligned}$$

The subscripts $\cdot_{,x}$, $\cdot_{,y}$ and $\cdot_{,z}$ denote the derivatives with respect to x, y and z, respectively. Note that ε is symmetric.

The behaviour of a linear elastic material is characterised by Hooke's law. This is a linear relation between stresses and strains

$$\sigma_{ij} = \mathrm{E}_{ijkl}\varepsilon_{\mathbf{kl}}\,.$$

In general, E_{ijkl} is a 4th order tensor. It is called the elasticity tensor and has $3^4 = 81$ components. For symmetry reasons, the number of components of E_{ijkl} can be reduced to 21 independent elasticity constants, i.e. a general anisotropic material has 21 independent elastic constants.
For the special case of isotropic material, it can be shown that the elasticity tensor depends only on two independent elastic constants λ and μ

$$\sigma_{ij} = 2\mu\varepsilon_{\mathbf{ij}} + \lambda\varepsilon_{\mathbf{kk}}\delta_{\mathbf{ij}}\,,$$

where

$$\delta_{ij} = \begin{cases} 1 & \text{if}\, i = j \\ 0 & \text{if}\, i \neq j \end{cases}$$

is the Kronecker-Delta. The constants λ and μ are called the Lamé coefficients, named after Gabriel Lamé (1795-1870). In matrix notation, Hooke's law can be written as

$$\begin{aligned}
\sigma &= 2\mu\varepsilon + \lambda\nabla\cdot\mathbf{u}\,\mathbf{I} \qquad (1.2.2)\\
&= \begin{pmatrix} 2\mu u_{x,x} + \lambda\sum\limits_{i=x,y,z} u_{i,i} & \mu(u_{x,y}+u_{y,x}) & \mu(u_{x,z}+u_{z,x}) \\ \mu(u_{y,x}+u_{x,y}) & 2\mu u_{y,y} + \lambda\sum\limits_{i=x,y,z} u_{i,i} & \mu(u_{y,z}+u_{z,y}) \\ \mu(u_{z,x}+u_{x,z}) & \mu(u_{z,y}+u_{y,z}) & 2\mu u_{z,z} + \lambda\sum\limits_{i=x,y,z} u_{i,i} \end{pmatrix}.
\end{aligned}$$

The Lamé coefficients λ and μ can also be expressed by other elasticity constants. Relations which we will use in the following are

$$\lambda = \frac{\nu_s \mathrm{E}}{(1+\nu_s)(1-2\nu_s)} \quad \text{and} \quad \mu = \frac{\mathrm{E}}{2(1+\nu_s)}\,, \qquad (1.2.3)$$

where E is Young's modulus, or E-modulus and ν_s is Poisson's ratio, describing the transverse contraction of a material if a traction is applied. The E-modulus has the unit Pascal [Pa $= \frac{\mathrm{N}}{\mathrm{m}^2}$], Poisson's ratio is a dimensionless number.

1.3 Equations in porous media

A porous medium consists of a solid skeleton and an interconnected void space. In this thesis, such a porous domain is denoted by Ω_p. The solid skeleton of Ω_p can either be considered to be rigid or deformable. In the first case, the laws of Darcy (equation (1.3.2)) and Brinkman (equations (1.3.7a) and (1.3.7b)) are applied. For poroelastic media, the interaction between the solid and the fluid flow are taken into account, i.e. a change in the applied stress causes a change in fluid pressure or fluid mass (solid-to-fluid coupling) and a fluid pressure change implies a volume change of the porous medium (fluid-to-solid coupling). These effects are accounted for in the Biot poroelasticity equations (equations (1.3.16)).

On a microscopic level, quantities like velocity or pressure are irregular. Therefore, one uses volume-averaged values on the macroscopic level. These macroscopic quantities are obtained by averaging the appropriate quantity ς, e.g. velocity $\mathbf{v}_f^p$ or pressure p_p, over a representative elementary volume (REV) containing many pores (cf. [4], [40])

$$\overline{\varsigma} = \frac{1}{V_p} \int_{V_p} \varsigma \, dV \,, \tag{1.3.1}$$

where V_p denotes the volume of the domain occupied by the porous medium Ω_p.

In this section we first present Darcy's law. Then, we derive the Kozeny-Carman equation, a well-known relation between permeability and porosity in porous media. Afterwards, we present Brinkman equations, which are used for modelling fluid flow through rigid porous media. Since this is not sufficient for our purposes, we introduce the concept of effective stress which was originally developed by Terzaghi and show the computation of effective elastic moduli. These two concepts are necessary for the Biot poroelasticity equations, which describe fluid flow through poroelastic media, presented at the end of this section.

For the general theory of porous media, we refer the interested reader to [3] - [5], [10], [42], [64], just to name a few.

1.3.1 Darcy's law

In 1856 the French engineer Henry Darcy performed many experiments, where he investigated the amount of water flowing downwards through a vertical homogeneous column of sand. Thus, he found a proportionality relation between the flow rate $\mathbf{q}$ of the water and the applied pressure difference ∇p_p:

$$\mathbf{q} = -\frac{\mathbf{K}}{\eta} \nabla p_p \,,$$

where η denotes the dynamic viscosity of the fluid and $\mathbf{K}$ is the permeability tensor, which is in general of 2nd order. In case of isotropic media, the permeability is a scalar, denoted by k in this thesis. Darcy's law then reads as

$$\mathbf{q} = -\frac{k}{\eta} \nabla p_p \,. \tag{1.3.2}$$

Indeed, the flux, the permeability and the pressure are volume-averaged quantities and should be denoted with an overbar $\overline{\mathbf{q}} = -\frac{\overline{k}}{\eta} \nabla \overline{p_p}$, but for the sake of simplicity we will skip it in the following. Note that η is the absolute viscosity of the fluid.

Many experiments have been conducted to verify Darcy's law, but there are also many theoretical studies which approve the equation. One well-known verification is the derivation from Stokes equations by homogenisation (see e.g. [30], [43], [55]). Other derivations can be found in [5], [13], [48], [64]. In general, one can read about Darcy's law in almost all books on porous media. Applications are given in [13].

Note that $\mathbf{q}$ denotes the relative velocity of the fluid through the porous medium. Sometimes, it is called seepage velocity or filter velocity. To get the physical velocity $\mathbf{v}_f^p$ of the fluid, one needs to divide $\mathbf{q}$ by the porosity ϕ:

$$\mathbf{q} = \phi\, \mathbf{v}_f^p \,. \tag{1.3.3}$$

This relation is the so-called "Dupuit-Forchheimer assumption" (cf. [16], [27]).

1.3.2 The Kozeny-Carman equation

The Kozeny-Carman equation is the most widely accepted relationship between permeability and pore properties of a porous medium. Its derivation is based on the concepts of porosity, specific surface area, hydraulic radius and tortuosity. A detailed derivation can be found for example in [3], [5], [16], [27] or [36].

The basis of the Kozeny-Carman theory is a semiheuristic model of flow through solid matrices based on the concept of hydraulic radius. The hydraulic diameter is defined as

$$d_h = \frac{4 \cdot \text{void volume}}{\text{surface area}} = \frac{4\phi}{A(1-\phi)}\,,$$

where A is the volumetric or specific surface area based on the solid volume $\frac{A_{fs}}{V_s}$ (A_{fs}: interfacial area between fluid and solid phases, V_s: solid volume). ϕ denotes the porosity and thus, $1-\phi$ is the solid volume fraction.

The tortuosity is defined as the length of the path that a fluid particle travels from one point to another (L_e) divided by the length of a straight line connecting these two points (L). Including the tortuosity $\theta = \frac{L_e}{L}$, we get a modified pressure drop $\nabla p_{\text{mod}} = \frac{1}{\theta}\nabla p_p$, which can be justified by the additional travel length of the fluid particle.

It is assumed that the pore velocity $\mathbf{v}_f^p$ in the flow channels can be determined by an equation of Hagen-Poiseuille type. Adding the tortuosity and a shape factor s to this equation, we get for the pore velocity

$$\mathbf{v}_f^p = -\frac{d_h^2}{16 s\eta\theta}\nabla p_p\,,$$

where d_h is the diameter of the capillary tubes through the porous medium and η is the dynamic viscosity. $s = 2$ for circular capillaries and $2.0 - 2.5$ for rectangular, elliptical and annular shapes. With tortuosity Darcy's law reads

$$\mathbf{q} = \mathbf{v}_f^p \frac{\phi}{\theta} = -\frac{k}{\eta}\nabla p_p\,.$$

All together, this can be summarised to

$$k = \frac{\phi d_h^2}{16 s\theta^2} = \frac{\phi d_h^2}{16 s_k} = \frac{\phi^3}{s_k(1-\phi)^2 A^2}$$

where $s_k = s\theta^2$ is the so-called Kozeny constant. Introducing a mean particle diameter $d = \frac{6}{A}$, we obtain

$$k = \frac{\phi^3}{36 s_k (1-\phi)^2} d^2 \,. \tag{1.3.4}$$

Approximating θ by $\sqrt{2}$ and s by 2.5, the Kozeny constant becomes $s_k = 5$ for packed beds. With this, equation (1.3.4) becomes the Kozeny-Carman equation

$$k = \frac{\phi^3}{180(1-\phi)^2} d^2 \,, \tag{1.3.5}$$

or, shorter,

$$k = C_{\mathrm{KC}} \frac{\phi^3}{(1-\phi)^2} \,. \tag{1.3.6}$$

This model predicts the permeability of packed beds reasonably well but its application is limited. In [52] it is shown that $k = \frac{\phi^{5.5}}{5.6} d^2$ gives a better agreement with experimental data, where the porosity ranges from 0.35 to 0.67.

1.3.3 The Navier-Stokes-Brinkman system

Darcy's law is used for materials with low porosity and, since the no-slip boundary condition cannot be applied, for infinite domains. For highly porous media ($\phi > 90\ \%$) or in order to impose a no-slip condition along the boundary, one uses Brinkman's equation, an extension of Darcy's law:

$$\nabla \cdot (\overline{\eta} \nabla \mathbf{q}) - \eta \mathbf{K}^{-1} \mathbf{q} = \mathbf{f}_B + \nabla p_p \,. \tag{1.3.7a}$$

The variables have the same meaning as in the section on Darcy's law (section 1.3.1). Fluid flux, permeability and pressure are again volume-averaged quantities. Here, $\overline{\eta}$ is an effective viscosity, which can be different from η. Using η in both terms of Brinkman's equations, does not deliver good results. For low porosities, the term $\eta \mathbf{K}^{-1}$ dominates and thus, one gets approximately the same results as for the Darcy equation. For incompressible fluids, Brinkman's equation has to be complemented by the continuity equation

$$\nabla \cdot \mathbf{q} = 0 \tag{1.3.7b}$$

and appropriate boundary conditions. For a more detailed description of Brinkman's equation, please see [4], [30], [36], [48].

Brinkman's equation is often used to model fluid flow through porous media, especially because the equation is of the same type as the Navier-Stokes or Stokes equations, which describes the behaviour in the surrounding fluid domain. The two systems of equations, Brinkman's equation ((1.3.7a) and (1.3.7b)) and Navier-Stokes equations (1.1.1), are then written as the coupled Navier-Stokes-Brinkman system:

$$\begin{aligned} \underbrace{\overbrace{-\breve{\eta}\Delta\breve{\mathbf{v}}}^{(B1)} + (\varrho\breve{\mathbf{v}}, \nabla)\breve{\mathbf{v}}}_{(N1)} + \overbrace{\eta\breve{\mathbf{K}}^{-1}\mathbf{q} + \underbrace{\nabla p}_{(N2)}}^{(B2)} &= \overbrace{\underbrace{\breve{\mathbf{f}}}_{(N3)}}^{(B3)} \\ \nabla \cdot \breve{\mathbf{v}} &= 0 \end{aligned}$$

where the quantities with the $\breve{\cdot}$ -sign are defined as follows:

$$\breve{\eta} = \begin{cases} \eta & \text{in } \Omega_f \\ \overline{\eta} & \text{in } \Omega_p \end{cases} , \quad \breve{\mathbf{f}} = \begin{cases} \mathbf{f}_f & \text{in } \Omega_f \\ \mathbf{f}_B & \text{in } \Omega_p \end{cases} ,$$

$$\breve{\mathbf{K}}^{-1} = \begin{cases} 0 & \text{in } \Omega_f \\ \mathbf{K}^{-1} & \text{in } \Omega_p \end{cases} , \quad \breve{\mathbf{v}} = \begin{cases} \mathbf{v} & \text{in } \Omega_f \\ \mathbf{q} & \text{in } \Omega_p \end{cases} .$$

The terms $(N1)$, $(N2)$ and $(N3)$ together are the Navier-Stokes equations. $(B2)$ and $(B3)$ are Darcy's equation, and in combination with $(B1)$ this is Brinkman's equation.

More details on the Navier-Stokes-Brinkman system, coupling conditions, solution and applications can be found in [32] and [40]. In these works, the interaction between the fluid flow and the elastic behaviour of the solid skeleton of the porous medium is not taken into account. For certain applications it is very important to know what the stresses or deformations in the filter are. This drawback will be overcome by coupling the Stokes equations and the Biot poroelasticity equations. Such a system for fluid flow normal to porous media is derived in this thesis.

1.3.4 Total stress in porous media and the concept of effective stress by Terzaghi

In porous media we have two types of stresses: the total stress and the effective stress. The total stress is the sum of all stresses acting in the porous medium, whereas the effective stress is the stress that produces the strain in the solid matrix of a porous medium. When dealing with fluid flow through deformable porous media, the knowledge of this strain is indispensable. The concept of effective stress was introduced by Terzaghi in 1925. Good descriptions of this concept can be found, for example, in [3] - [5], [42] or [64].

For the description of total stress and effective stress in a porous medium, we recall the notation (1.3.1) for a volume averaged value of a quantity ς (e.g. pressure or stress) over a volume V_p. The total volume V_p of the porous medium can be split into the solid volume V_s and the fluid volume V_f^p. The volume average of a quantity ς over V_s or V_f^p, respectively, is denoted by

$$\overline{\varsigma}^s = \frac{1}{V_s} \int_{V_s} \varsigma \, dV \,, \qquad \text{or} \qquad \overline{\varsigma}^{fp} = \frac{1}{V_f^p} \int_{V_f^p} \varsigma \, dV \,.$$

The total stress $\overline{\sigma_{\text{tot}}}$ in a porous medium is then defined as

$$\overline{\sigma_{\text{tot}}} = \overline{\sigma_s} + \overline{\sigma_f^p} \,, \tag{1.3.8}$$

where $\overline{\sigma_s}$ denotes the solid stress and $\overline{\sigma_f^p}$ is the fluid stress. It is derived by summation of the averaged momentum balance equations for the fluid and solid phase in the porous medium (cf. [4], p. 150 et seqq.). Using definition (1.1.5) for the stress in fluid, the total stress can be expressed as

$$\overline{\sigma_{\text{tot}}} = \overline{\sigma_s} - \overline{p_p}\mathbf{I} \,,$$

or, incorporating the porosity,

$$\overline{\sigma_{\text{tot}}} = (1-\phi)\overline{\sigma_s}^s - \phi\overline{p_p}^{fp}\mathbf{I} \,. \tag{1.3.9}$$

This is the total stress, but which stress causes strain in the porous medium? We know that the total force acting on the solid matrix is composed of the forces from solid-solid contact and the forces from the fluid-solid contact. This has been first studied by Terzaghi. Terzaghi considers a porous medium to be a granular material and assumes that the grains are (almost) completely surrounded by an ambient fluid. In case the shear stress in the fluid is neglected, the pressure of the fluid produces a stress in the solid material, which is of the same size as the pressure itself. But this induced stress does not contribute to the deformation of the solid material.

But Terzaghi observed that the deformation of the solid matrix is larger than what can be caused by compression only. So, it must come from a rearrangement of the grains and from the transmission of forces at the contact points of the grains. The fluid pressure does not influence these contact forces. Therefore, the stress which induces the strain in the solid material is obtained by subtraction of the fluid pressure from the stress in the solid. Reformulation of equation (1.3.9) gives

$$\overline{\sigma_{\text{tot}}} = (1-\phi)(\overline{\sigma_s}^s + \overline{p_p}^{fp}\mathbf{I}) - (1-\phi)\overline{p_p}^{fp}\mathbf{I} - \phi\overline{p_p}^{fp}\mathbf{I}\,.$$

The last two terms sum up to $-\overline{p_p}^{fp}\mathbf{I}$. Thus, the effective stress is defined by

$$\overline{\sigma_p} = (1-\phi)(\overline{\sigma_s}^s + \overline{p_p}^{fp}\mathbf{I})\,. \tag{1.3.10}$$

From this equation it is visible that the effective stress consists of one part from the average stress within the solid material and one part from the averaged pressure in the fluid part of the porous medium.

In case, the viscous stress cannot be neglected, equation (1.3.9) becomes

$$\overline{\sigma_{\text{tot}}} = (1-\phi)\overline{\sigma_s}^s + \phi\overline{\sigma_f^p}^{fp}\,.$$

With this, the effective stress tensor can be written as

$$\overline{\sigma_p} = (1-\phi)(\overline{\sigma_s}^s - \overline{\sigma_f^p}^{fp})\,. \tag{1.3.11}$$

1.3.5 The computation of effective elastic moduli

The mechanical and acoustic properties of porous media are described by means of effective parameters, which depend on the material parameters of the solid skeleton and its porosity. For their determination, there are empirical equations as well as analytical ones. Theoretical models are often very complex.

In [51] several methods for the determination of such effective parameters are discussed. The authors check the applicability of some theoretical models and compare the results with data of numerical experiments.

For our purposes we use the Composite Sphere Method, which was originally introduced by Z. Hashin (see [28] and [29]). It shows good accuracy for all Poisson's ratios ν_s (error $\approx 5\ \%$), except when ν_s is around 0.3 and the porosity $\phi \approx 0.4$. Then the error can be $\approx 10\ \%$. The model can also be used to estimate the effective moduli of cellular materials.

In the following, $\overline{\mathcal{M}}$ stands for an effective elastic modulus of the porous medium, whereas $\mathcal{M}$

denotes the same property of the solid material (with zero porosity). Then, the effective elastic modulus of a porous material is defined by

$$\overline{\mathcal{M}} = \frac{(1-\phi)^2}{1+\kappa_{\mathcal{M}}\phi}\,\mathcal{M}\,, \tag{1.3.12}$$

where $\mathcal{M}$ can be replaced by the bulk modulus K, the shear modulus G or Young's modulus E. $\kappa_{\mathcal{M}}$ is a constant. Depending on the choice of the modulus, it has to be replaced by a corresponding expression. For Young's modulus E, $\kappa_{\mathcal{M}} = \kappa_{\mathrm{E}} = 2 - 3\nu_s$ and thus, equation (1.3.12) reads as

$$\overline{\mathrm{E}} = \frac{(1-\phi)^2}{1+(2-3\nu_s)\phi}\,\mathrm{E}\,. \tag{1.3.13}$$

For Poisson's ratio the following relation was found:

$$\overline{\nu_s} = \frac{1}{4}\,\frac{4\nu_s + 3\phi - 7\nu_s\phi}{1+(2-3\nu_s)\phi}\,. \tag{1.3.14}$$

It is remarkable that this value approaches 0.25 with increasing porosity, irrespective of the material's Poisson's ratio. For a derivation of these formulae, please read [50].

Using equations (1.2.3), we can compute the effective Lamé coefficients valid in the porous medium

$$\overline{\lambda} = \frac{\overline{\nu_s}\,\overline{\mathrm{E}}}{(1+\overline{\nu_s})(1-2\overline{\nu_s})} \quad \text{and} \quad \overline{\mu} = \frac{\overline{\mathrm{E}}}{2(1+\overline{\nu_s})}\,. \tag{1.3.15}$$

1.3.6 The Biot poroelasticity equations

In 1941, the Belgian-American Physicist Maurice Anthony Biot formulated the general three-dimensional theory of poroelasticity, see [8]. The Biot poroelasticity equations describe the consolidation of a linear elastic porous medium in a bounded domain $\Omega_p \subset \mathbb{R}^3$ with boundary $\partial\Omega_p$ and look as follows:

$$\left.\begin{aligned} -\nabla\cdot\overline{\sigma_p} + \alpha\nabla\overline{p_p} &= \mathbf{0} \\ \frac{\partial}{\partial t}(\phi\beta\overline{p_p} + \alpha\nabla\cdot\overline{\mathbf{u}}) + \nabla\cdot\mathbf{q} &= f_p(\mathbf{x},\mathbf{t}) \end{aligned}\right\} \quad \text{in}\,\Omega_p\,. \tag{1.3.16}$$

α is the so-called Biot-Willis constant, which accounts for the compressibility of the solid grains. ϕ stands for the porosity and β for the compressibility of the fluid. $f_p(\mathbf{x},\mathbf{t})$ is a source term, describing, for example, an injection or extraction process. $\overline{\sigma_p}$ denotes the effective stress tensor, defined in equation (1.3.10). According to equations (1.2.1) and (1.2.2), $\overline{\sigma_p}$ can also be written as

$$\overline{\sigma_p} = \overline{\mu}(\nabla\overline{\mathbf{u}} + (\nabla\overline{\mathbf{u}})^T) + \overline{\lambda}\nabla\cdot\overline{\mathbf{u}}\mathbf{I}\,.$$

$\overline{\mathbf{u}}$ denotes the volume average over the displacements in the porous domain Ω_p. $\mathbf{q}$ is the fluid flux, defined by Darcy's law

$$\mathbf{q} = -\frac{k}{\eta}\nabla p_p\,.$$

The first equation of the Biot system is the equilibrium equation for the momentum, the second one is the diffusion equation for the Darcy flow. The coupling terms $\alpha\nabla\overline{p_p}$ in the first equation and the term $\alpha\nabla \cdot \overline{\mathbf{u}}$ in the second equation are a result of the interaction of the fluid with the solid skeleton in the porous medium. $\alpha\nabla\overline{p_p}$ arises from the additional stress in the medium caused by the fluid pressure. $\alpha\nabla \cdot \overline{\mathbf{u}}$ stands for the additional fluid content due to local volume change.

The Biot model has to be complemented with suitable initial and boundary conditions for the elastic part as well as for the fluid part of the system. For the elastic part one can prescribe the displacements. Most commonly used is $\overline{\mathbf{u}} = \mathbf{0}$, which describes a clamped boundary. Also a traction $\overline{\sigma_p} \cdot \mathbf{n} = \mathbf{g}$ can be prescribed. For the fluid part of the system, we can apply a pressure $\overline{p_p} = p_0$ ($p_0 = 0$ corresponds to a drained boundary) or a flow condition $\mathbf{q} \cdot \mathbf{n} = q_0$ ($q_0 = 0$ characterises an impermeable wall). Please note that implying only Neumann boundary conditions (traction and fluid flux) leads to an ill-posed problem.
At time $t = 0$ one should prescribe the variation of fluid content, i.e. a value for $\phi\beta\overline{p_p} + \alpha\nabla \cdot \overline{\mathbf{u}}$.
For detailed studies on the Biot poroelasticity equations, we refer to [3], [5], [10], [46], [64]. A detailed discussion on the boundary conditions can be found in [56] - [58].

Note: In this chapter we have introduced the volume-averaged values, which we denoted by an overbar sign $\overline{(.)}$. For the sake of simplicity we will skip the overbar in the remainder of the thesis. From this chapter, it should have become clear that the volume-averaged values are needed for quantities in the porous medium.

1.4 Poroelasticity versus elasticity

The solution of the linear elasticity equations is well known and thus, one might try to replace the poroelasticity equations by the linear elasticity equations for certain applications.
Here, we conduct an experiment that shows that the poroelasticity equations cannot simply be replaced by the linear elasticity equations. Let us consider a porous medium that is fixed on the outer boundaries (left and right side in figure 1.1) and has no fluid flux through these walls. On the top (inflow) and bottom (outflow) wall, we apply a pressure and a traction condition.
Figure 1.2(a) shows the displacements computed by the linear elasticity equations. Of course, here, only the traction condition is taken into account. The deformations are largest on top of the porous medium where the load is applied. Towards the outflow of the porous medium, the displacements become smaller and smaller. Solving the Biot poroelasticity equations, the displacements are more or less uniform throughout the porous medium (see figure 1.2(b)). This shows the effect that the pore pressure exerts on the skeleton. By these two figures, it should become clear that the latter effect is not negligible.

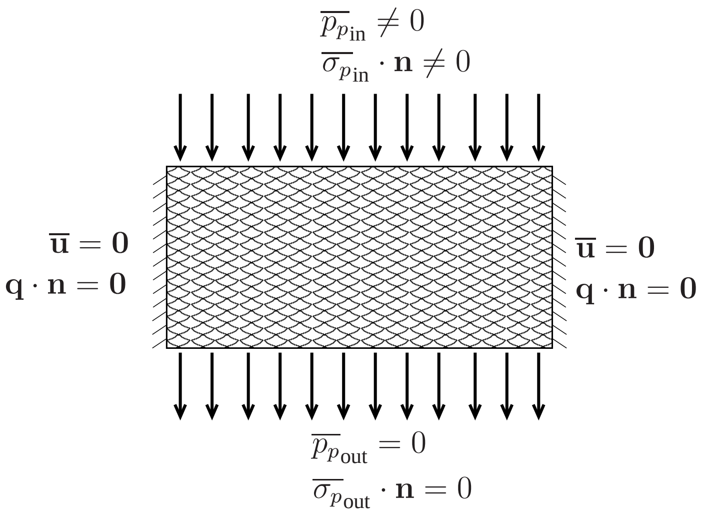

Figure 1.1: Porous medium clamped at the outer boundaries, loaded by a pressure and traction on the upper and lower faces (inflow and outflow, respectively).

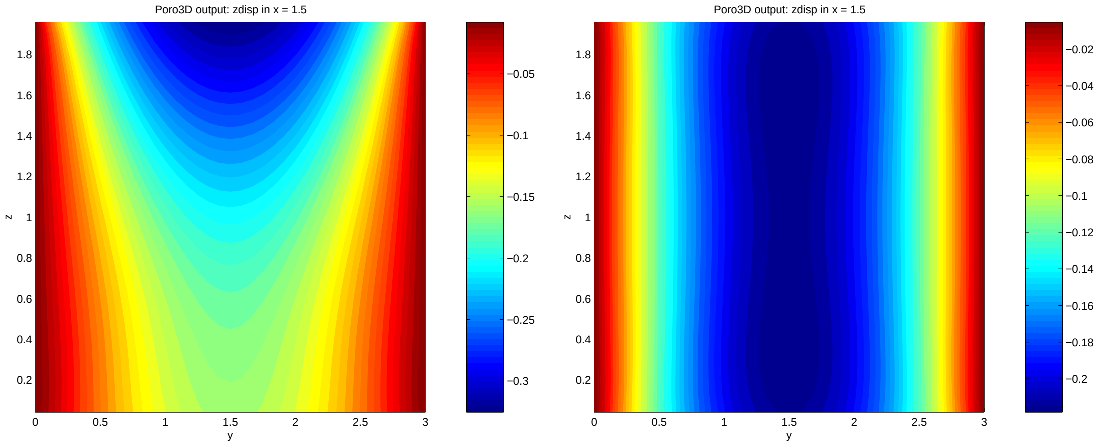

(a) (b)

Figure 1.2: Deformations in flow direction, computed by the linear elasticity equations (a) and computed by the Biot poroelasticity equations (b).

Chapter 2

The transmission conditions

In this chapter we derive the transmission conditions for coupling the Stokes equations and the Biot poroelasticity equations for fluid flow normal to porous media.
In literature, transmission conditions for fluid flow tangential to porous media can be found (see e.g. [7], [40], [59]), but for filtration processes it is important to have the coupling conditions for normal flow in order to be able to compute, for example, the resulting stresses. As far as we know, the transmission conditions for the coupling of the Stokes equations and the Biot poroelasticity equations for fluid flow normal to porous media have not been formulated before.
In this chapter we first present the model geometry we are working on, including a detailed description of the interface between the porous domain and the fluid domain. Then, we derive the transmission conditions in three and one dimensions and finally, we state the continuous coupled formulation in 3d.

2.1 The model geometry for fluid flow normal to porous media

Here, we describe the geometry which we consider to model fluid flow normal to a porous medium. Let $\Omega \subset \mathbb{R}^3$ be the entire domain, consisting of a fluid part Ω_f and a porous medium Ω_p, such that $\Omega = \Omega_f \cup \Omega_p$. Such a domain is depicted in figure 0.1. Here, the fluid domain consists of two disjoint parts, Ω_{f1} and Ω_{f2}, such that $\Omega_f = \Omega_{f1} \cup \Omega_{f2}$. The boundary of Ω is denoted by $\partial\Omega$. We use a domain decomposition approach to model the interaction between fluid and porous medium. We consider laminar incompressible flow, and thus, we use the Stokes equations in Ω_f, mentioned in section 1.1. The boundary of the fluid subdomains Ω_{f1} and Ω_{f2} is composed of three disjoint parts: a fixed boundary part $\partial\Omega_{f1,\text{fixed}}$ and $\partial\Omega_{f2,\text{fixed}}$, respectively, an inflow boundary part $\partial\Omega_{f1,\text{in}}$ and $\partial\Omega_{f2,\text{in}}$, respectively, and an outflow boundary part $\partial\Omega_{f1,\text{out}}$ and $\partial\Omega_{f2,\text{out}}$, respectively. Together, we get $\partial\Omega_{f1} = \partial\Omega_{f1,\text{fixed}} \cup \partial\Omega_{f1,\text{in}} \cup \partial\Omega_{f1,\text{out}}$ and $\partial\Omega_{f2} = \partial\Omega_{f2,\text{fixed}} \cup \partial\Omega_{f2,\text{in}} \cup \partial\Omega_{f2,\text{out}}$. The boundary of Ω_f is denoted by $\partial\Omega_f$. How it is composed, will be explained below after the description of the interface.
In the porous domain we solve the Biot poroelasticity equations (1.3.16). The porous medium is fixed along the impermeable channel walls. This part of the boundary is denoted by $\partial\Omega_{p,\text{fixed}}$. The inflow boundary of Ω_p is called $\partial\Omega_{p,\text{in}}$ and the outflow boundary $\partial\Omega_{p,\text{out}}$. It holds $\partial\Omega_p = \partial\Omega_{p,\text{in}} \cup \partial\Omega_{p,\text{out}} \cup \partial\Omega_{p,\text{fixed}}$, with $\partial\Omega_{p,\text{in}} \cap \partial\Omega_{p,\text{out}} = \emptyset$, $\partial\Omega_{p,\text{in}} \cap \partial\Omega_{p,\text{fixed}} = \emptyset$ and $\partial\Omega_{p,\text{fixed}} \cap \partial\Omega_{p,\text{out}} = \emptyset$.

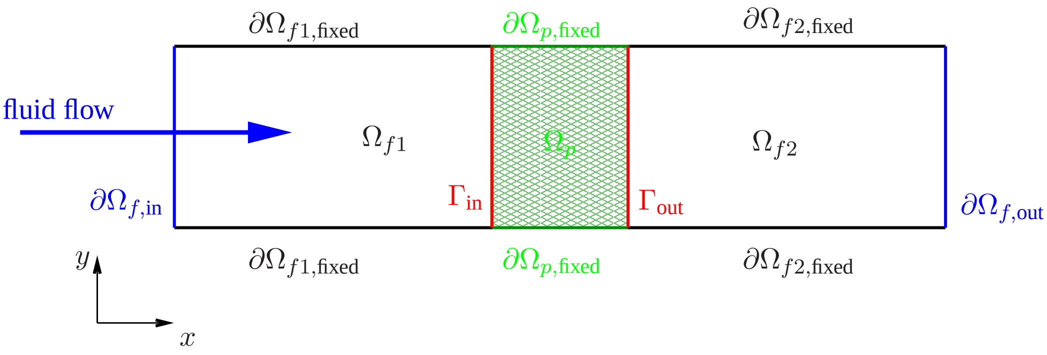

Figure 2.1: 2d sketch of the model geometry with notations for the domains and respective boundaries. Ω_p: porous domain, $\partial\Omega_{p,\text{fixed}}$: boundary parts of Ω_p, where the porous medium is fixed, Ω_{f1} and Ω_{f2}: fluid domains, $\partial\Omega_{f1,\text{fixed}}$ and $\partial\Omega_{f2,\text{fixed}}$: boundary parts of Ω_{f1} and Ω_{f2}, where no-slip boundary conditions are applied, $\partial\Omega_{f,\text{in}}$, $\partial\Omega_{f,\text{out}}$: inflow/outflow boundary of $\Omega_f = \Omega_{f1} \cup \Omega_{f2}$, Γ_{in}, Γ_{out}: inflow/outflow interface between Ω_p and Ω_f.

$\partial\Omega_{p,\text{fixed}}$ is fixed and impermeable. Therefore, we prescribe the following boundary conditions:

$$\mathbf{u} = \mathbf{0}\,, \;\; \mathbf{q}\cdot\mathbf{n} = 0 \qquad \text{on } \partial\Omega_{p,\text{fixed}}\,,$$

where $\mathbf{u}$ is the vector of displacements, $\mathbf{q}$ the fluid flux and $\mathbf{n}$ a normal vector pointing outwards from the porous medium. The boundary conditions on $\partial\Omega_{p,\text{in}}$ and $\partial\Omega_{p,\text{out}}$ are replaced by the transmission conditions.

The interface Γ between two domains is defined as the intersection of the boundaries of the respective domains. Thus, in our model geometry we have $\Gamma_{\text{in}} := \partial\Omega_{f1} \cap \partial\Omega_p$ and $\Gamma_{\text{out}} := \partial\Omega_p \cap \partial\Omega_{f2}$. Γ_{in} corresponds to $\partial\Omega_{f1,\text{out}} = \partial\Omega_{p,\text{in}}$ and Γ_{out} corresponds to $\partial\Omega_{p,\text{out}} = \partial\Omega_{f2,\text{in}}$. We distinguish between the inflow interface Γ_{in} and the outflow interface Γ_{out}. This is necessary later on for the formulation of the transmission conditions. But in the following we also often talk about ”the interface”. Then, we mean $\Gamma := \Gamma_{\text{in}} \cup \Gamma_{\text{out}}$. In case we distinguish between the two, it will be mentioned explicitly.
With these definitions, we can explain the boundary of Ω_f. It consists of four disjoint parts, namely the fixed boundary part $\partial\Omega_{f,\text{fixed}} := \partial\Omega_{f1,\text{fixed}} \cup \partial\Omega_{f2,\text{fixed}}$ with $\partial\Omega_{f1,\text{fixed}} \cap \partial\Omega_{f2,\text{fixed}} = \emptyset$, the inflow boundary part $\partial\Omega_{f,\text{in}} := \partial\Omega_{f1,\text{in}}$, the outflow boundary part $\partial\Omega_{f,\text{out}} := \partial\Omega_{f2,\text{out}}$ and the interface $\Gamma = \Gamma_{\text{in}} \cup \Gamma_{\text{out}}$ with $\Gamma_{\text{in}} = \partial\Omega_{f1,\text{out}}$ and $\Gamma_{\text{out}} = \partial\Omega_{f2,\text{in}}$. Thus, we have $\partial\Omega_f = \partial\Omega_{f,\text{fixed}} \cup \partial\Omega_{f,\text{in}} \cup \partial\Omega_{f,\text{out}} \cup \Gamma$, where all parts are disjoint. On $\partial\Omega_{f,\text{in}}$ we prescribe a Dirichlet velocity boundary condition (cf. equation (1.1.3a)), on $\partial\Omega_{f,\text{out}}$ we prescribe a Dirichlet pressure boundary condition (see equation (1.1.3b)) and on $\partial\Omega_{f,\text{fixed}}$ we prescribe the no-slip boundary condition (1.1.3c). The transmission conditions replace the boundary conditions on $\partial\Omega_{f1,\text{out}}$ and $\partial\Omega_{f2,\text{in}}$. Therefore, they are not given here.
A 2d sketch of the model geometry with appropriate boundary notations is shown in figure 2.1.

For the formulation of the transmission conditions we consider the interface on a microscopic

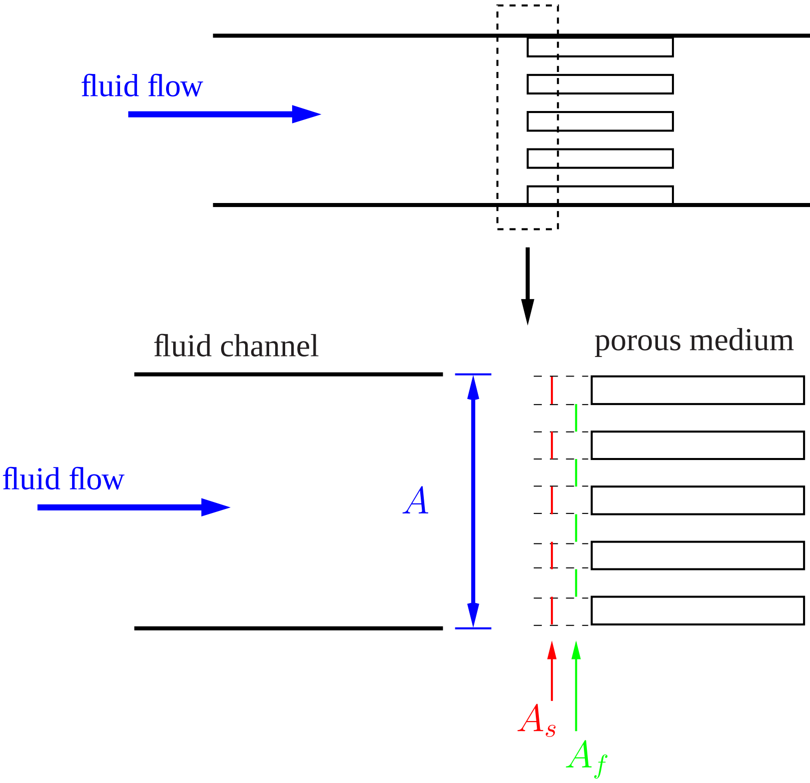

Figure 2.2: The inflow interface seen from the fluid side has area A, and from the porous side it has area $A_f + A_s$.

level. Let the total area of the interface be A. On the porous side of the interface we can distinguish between the fluid part of the interface A_f and the solid part A_s, which together sum up to $A = A_f + A_s$. The solid part A_s is the area where we have solid skeleton along the interface and the fluid part A_f is the sum of all pores exposed towards the adjacent fluid channel, as illustrated in figure 2.2. In this figure, the porous medium is indicated by the beams which picture the solid skeleton parts. In between there are the flow channels through the porous medium. With these notation, the porosity ϕ can be expressed as

$$\phi = \frac{A_f}{A} . \tag{2.1.1}$$

Consequently,

$$\frac{A_s}{A} = (1 - \phi) . \tag{2.1.2}$$

2.2 Derivation of the transmission conditions

The transmission conditions (sometimes also called interface conditions) are equations at the interface Γ between two or more neighbouring domains, reflecting the physical phenomena across the interface. The governing equations in the different domains do not necessarily need to be different. One also needs interface conditions when a domain is decomposed for parallel computation, for example. Then, the transmission conditions guarantee that the solutions along the interfaces are conform.

An example for the coupling of two equal physical phenomena is the coupling of the Navier-Stokes equations for two immiscible fluids with flat interfaces. There, the conservation of mass and the continuity of tractions is required across the interface (see e.g. [14] or [27]):

$$[\mathbf{v}]_{|\Gamma} = 0 \qquad \text{and} \qquad [\sigma \cdot \mathbf{n}]_{|\Gamma} = 0\,,$$

where the symbol $[.]_{|\Gamma}$ denotes the jump across the interface Γ. In 1d, these are two coupling conditions, in 3d six conditions.

Another application can be found in the treatment of multilayered porous media. There, the Biot poroelasticity equations need to be coupled across the interface. For the fluid part, the continuity of the pressure and the normal component of the fluid flux needs to be fulfilled. For the elasticity part one needs to guarantee the continuity of the displacements and the continuity of the tractions (see [45], [46]):

$$[p]_{|\Gamma} = 0\,, \qquad [\mathbf{q} \cdot \mathbf{n}]_{|\Gamma} = 0\,, \qquad [\mathbf{u}]_{|\Gamma} = 0 \quad \text{and} \quad [\sigma_p \cdot \mathbf{n}]_{|\Gamma} = 0\,.$$

In 1d these are four conditions, in 3d eight conditions.

Concluding from these two examples, one can see that the number of interface conditions corresponds to the total number of boundary conditions needed for the equations in the respective subdomains. When the physical phenomena in the subdomains differ, the situation is more involved, especially, when the equations in the subdomains are not of the same type.

From [34] one can find that for the coupling of the Stokes equations and the Lamé equations in 3d one also needs six coupling conditions. Namely the continuity of the velocity and the continuity of tractions in all three coordinate directions. This is for the general case. For stationary problems the fluid velocity is required to be 0 at the interface Γ.

For the coupling of free fluid flow and porous media, there are several approaches. Most common in literature is the use of the Navier-Stokes-Brinkman system ([32], [40]). The Brinkman extension of Darcy's law entails that it is of the same type of equation as the Navier-Stokes equations, which is not the case for Darcy's law itself. Therefore, the coupling of Navier-Stokes equations and Darcy law is more difficult (see [35], [41], [40] and references therein).

When coupling the Navier-Stokes equations with Darcy's law or Brinkman's equation, one distinguishes between two cases: fluid flow parallel to the porous medium and nearly normal flow. In the first case, the velocity in the fluid region is much larger than in the porous region, but the pressure gradients are of the same order. In the nearly normal flow case, the velocities are of the same order, but the pressure gradient in the porous medium is much larger than in the fluid region. In both cases one requires the continuity of the mass flux across the interface. Coupling Navier-Stokes equations with Darcy's law for parallel flow, one also has to fulfil continuity of pressure. Furthermore, G. S. Beavers and D. D. Joseph [7] found that there appears a slip velocity on the interface. This so-called Beavers-Joseph condition states that the tangential velocities in fluid and porous region depend on the permeability and a material parameter characterising the structure of the porous medium in the boundary region. A further extension to this condition has been found by P. G. Saffman [53].

Coupling Navier-Stokes equations and Darcy's law in the nearly normal flow case, additionally to the mass flux continuity, the tangential velocity components from the ”fluid side” of the interface are required to be 0. For details on the pressure condition we refer to [40] and references therein.

For the coupling of Navier-Stokes equations with the Brinkman equations, there are the same distinctions between parallel and nearly normal flow. In both cases, the continuity of the velocity has to be fulfilled. Regarding the other conditions, there were many experiments conducted and different interface conditions have been proposed. For normal flows one requires the continuity of the normal component of the stress tensor, whereas J. A. Ochoa-Tapia and S. Whitaker proposed a stress jump condition (see [49]) for parallel flows. For a more detailed discussion on this, see also [36].

The coupling of the Navier-Stokes equations with both, the Darcy law, and the Brinkman equations does not take into account the interaction between the fluid and the solid structure of the porous medium. This drawback is overcome by using the Biot equations in the porous domain. Showalter has studied the coupling of Stokes equations and Biot system for poroelastic porous media [59] as well as for viscous-plastic porous media [60]. His investigations are restricted to fluid flow parallel to the porous medium.
For fluid flow tangential to poroelastic media he found the following coupling conditions: First, he requires the conservation of mass across the interface Γ

$$(\alpha \mathbf{v}_f^p + \mathbf{q}) \cdot \mathbf{n} = \mathbf{v} \cdot \mathbf{n}\,. \tag{2.2.1a}$$

Further, he assumes that [59] ”*the Darcy flow across Γ is driven by the difference between the total normal stress of the fluid and the pressure internal to the porous medium*”

$$\sigma_f^{\mathrm{n}} - p_f + p_p = a\mathbf{q} \cdot \mathbf{n}\,, \tag{2.2.1b}$$

where $a \geq 0$ is the so-called fluid entry resistance of the porous medium. The conservation of momentum is split into its normal part

$$\sigma_p^{\mathrm{n}} - \alpha p_p = \alpha(\sigma_f^{\mathrm{n}} - p_f) \tag{2.2.1c}$$

and its tangential part

$$\sigma_f^{\mathrm{t}} = \sigma_p^{\mathrm{t}}\,, \tag{2.2.1d}$$

where σ_f^{t} is expressed by the Beavers-Joseph-Saffman condition, which states that the tangential stress in the fluid is proportional to the slip rate

$$\sigma_f^{\mathrm{t}} = \gamma\sqrt{\mathcal{Q}}(\mathbf{v}^{\mathrm{t}} - \mathbf{v}_f^{p\,\mathrm{t}})\,. \tag{2.2.1e}$$

Here, γ denotes the slip rate coefficient and $\mathcal{Q}$ the flow resistance tensor. The tangential part of a vector $\mathbf{w} = (w_x, w_y, w_z)^T$ is defined as $\mathbf{w}^{\mathrm{t}} = \mathbf{w} - (\mathbf{w} \cdot \mathbf{n})\mathbf{n}$ and the tangential part of a tensor $\mathbf{M}^{\mathrm{t}} = \mathbf{M}(\mathbf{n}) - \mathbf{M}(\mathbf{n})\mathbf{n}$ with

$$\mathbf{M}(\mathbf{n}) = \begin{pmatrix} \sum_i m_{ix} n_i \\ \sum_i m_{iy} n_i \\ \sum_i m_{iz} n_i \end{pmatrix}, \quad i = x, y, z\,,$$

where

$$\mathbf{M} = \begin{pmatrix} m_{xx} & m_{xy} & m_{xz} \\ m_{yx} & m_{yy} & m_{yz} \\ m_{zx} & m_{zy} & m_{zz} \end{pmatrix} \in \mathbb{R}^{3\times 3}\,.$$

Equations (2.2.1a) - (2.2.1e) are the transmission conditions for the coupling of the Stokes equations and the Biot poroelasticity equations for fluid flow tangential to the porous medium. In his paper [59] Showalter shows that they are sufficient to couple these two systems.
In the following we will derive similar conditions for fluid flow normal to the porous medium. We also require the conservation of mass and the continuity of tractions, but then we need a further condition on the pressure across the interface.

For the derivation of the transmission conditions for fluid flow normal to porous media, we consider the interface on a microscopic level, as displayed in figure 2.2. As we could see from the examples above, the number of transmission conditions must correspond to the sum of boundary conditions needed for both adjacent domains. In the 3d case, we have four boundary conditions for the Biot poroelasticity equations and maximum three boundary conditions for the Stokes equations (Dirichlet velocity boundary condition at the inflow of the fluid domain). Thus, we need seven transmission conditions in 3d. In the 1d case we have two boundary conditions for Biot and one boundary condition for the Stokes equations. So, three transmission conditions are needed.
As in the examples mentioned above, we require the conservation of mass and the continuity of tractions. Then, one condition is missing. We formulate a condition for the pressure. On the macroscopic scale, the interface between two domains can essentially be seen as a very thin layer. Across this layer, the pressure can differ substantially due to the pressure differential across the solid skeleton. But on the microscopic scale, the pressure has to be continuous [48]. We derive such a condition.

In our channel geometry there are two interfaces: the inflow interface Γ_{in}, where the fluid flows from the fluid region Ω_f into the porous region Ω_p and the outflow interface Γ_{out}, where the fluid leaves the porous medium and flows into Ω_f. The conservation of mass condition and the continuity of traction equation are identical, no matter which interface is considered. Therefore, talking about ”the interface” means $\Gamma = \Gamma_{\text{in}} \cup \Gamma_{\text{out}}$. For the pressure jump condition we distinguish between the two.
Note that three-dimensional vectors are denoted by bold letters ($\mathbf{v}$, $\mathbf{u}$, $\mathbf{q}$, ...), whereas one-dimensional values are written as lower case letters (v, u, q, ...).

2.2.1 The transmission conditions in three dimensions

We first derive the transmission conditions for the three-dimensional case. The transmission conditions in one dimension are deduced in the next section. We have chosen this order, because the transmission conditions are all derived from three-dimensional equations and we think that it is easier to understand in that way.

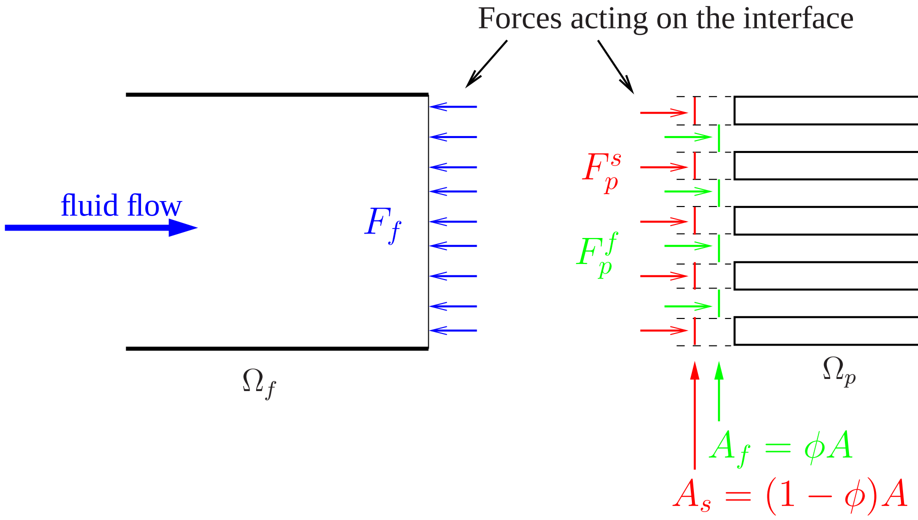

Figure 2.3: Forces acting on the inflow interface. The forces acting on the fluid area A split into forces acting on the solid skeleton A_s and the fluid channels A_f of the porous medium.

Conservation of mass

In order to have a physical coupling, we need to guarantee the conservation of mass across the interface. We equate the mass which ”enters” the interface from the left hand side with the mass which ”leaves” it on the right hand side

$$\int_A \varrho \mathbf{v}\, da = \int_{A_s} \varrho\alpha \frac{\partial \mathbf{u}}{\partial t}\, da + \int_{A_f} \varrho \mathbf{v}_f^p\, da\,. \tag{2.2.2}$$

The term on the left hand side expresses the mass on the fluid side of the interface, $\mathbf{v}$ denotes the fluid velocity in Ω_f. On the right hand side, the velocity is split into the velocity of the solid skeleton $\frac{\partial \mathbf{u}}{\partial t}$ and the absolute velocity $\mathbf{v}_f^p$ of the fluid within the porous medium. $\mathbf{u}$ denotes the displacements of the solid, therefore, $\frac{\partial \mathbf{u}}{\partial t}$ represents the velocity of the moving solid. It is multiplied by the Biot-Willis constant α, which accounts for the compressibility of the grains. Integrating equation (2.2.2) and dividing it by the density ϱ, we obtain

$$\mathbf{v} = \alpha \frac{A_s}{A}\frac{\partial \mathbf{u}}{\partial t} + \frac{A_f}{A}\mathbf{v}_f^p\,.$$

Including the definition for the porosity (2.1.1) and the solid volume fraction (2.1.2), the equation above writes as

$$\mathbf{v} = \alpha(1-\phi)\frac{\partial \mathbf{u}}{\partial t} + \phi \mathbf{v}_f^p\,.$$

With the Dupuit-Forchheimer assumption $\mathbf{q} = \phi \mathbf{v}_f^p$, we get the mass conservation equation for the three-dimensional case

$$\mathbf{v} = \alpha(1-\phi)\frac{\partial \mathbf{u}}{\partial t} + \mathbf{q}\,. \tag{2.2.3}$$

Continuity of tractions

The second condition we require to be fulfilled across the interface is the continuity of tractions. For the formulation of this condition, we start with the equilibrium of forces along the interface.

We are dealing with area forces, which can be expressed by integration of the traction vectors over the corresponding area

$$\mathbf{F} = \int_A \mathbf{t}\, da = \int_A \sigma \cdot \mathbf{n}\, da\,.$$

So, for our interface area we obtain

$$\int_A \sigma_f \cdot \mathbf{n}\, da = \int_{A_s} \sigma_s \cdot \mathbf{n}\, da + \int_{A_f} \sigma_f^p \cdot \mathbf{n}\, da\,.$$

Integrating this equation, using the definitions for the porosity (2.1.1) and the solid volume fraction (2.1.2) and the definitions for the stress tensors (1.1.4) and (1.2.2), we get

$$\begin{aligned}\eta\left(\nabla\mathbf{v} + (\nabla\mathbf{v})^T\right)\cdot\mathbf{n} - p_f\mathbf{n} = (1-\phi)&\left[\mu\left(\nabla\mathbf{u} + (\nabla\mathbf{u})^T\right)\cdot\mathbf{n} + \lambda(\nabla\cdot\mathbf{u})\,\mathbf{n}\right]\\ +\phi&\left[\eta\left(\nabla\mathbf{v}_f^p + (\nabla\mathbf{v}_f^p)^T\right)\cdot\mathbf{n} - p_p\mathbf{n}\right]\,.\end{aligned} \tag{2.2.4}$$

Pressure jump condition

Considering the model geometry on a microscopic level, the interface can be seen as a plate with a lot of holes. From classical fluid dynamics we know that there occurs a pressure difference when the cross-section of the fluid flow is changed. At this place, we have to distinguish between the inflow interface Γ_{in} and the outflow interface Γ_{out}. At Γ_{in}, the ”holes” in the interface plane act like a sudden constriction of the channel. Reducing the consideration to a channel of width A with only one hole of width A_f, Γ_{in} can be seen as a fluid flow channel with a discontinuous change of cross-section, as depicted in figure 2.4. At this constriction, the streamlines narrow shortly to a width $A_f^* < A_f$. Following [38], the pressure p_p^* behind the constriction can be expressed as

$$p_p^* = p_f + \frac{\varrho}{2}v_x^2\left(1 - \frac{A^2}{A_f^2}\frac{1}{C_{\text{c}}^2}\right)\,, \tag{2.2.5}$$

where $C_{\text{c}} = \frac{A_f^*}{A_f}$ is the so-called contraction number, which specifies the ratio between the constricted flow width A_f^* behind the constriction and the original width of the constriction A_f. In equation (2.2.5), only the normal component v_x of the fluid velocity enters.

To generalise this pressure jump equation to our inflow interface, we consider this area to consist

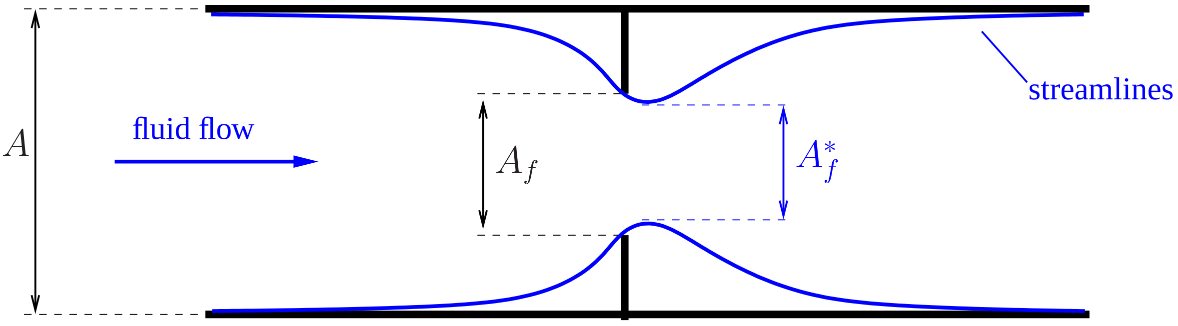

Figure 2.4: Streaming through a channel with a discontinuous change of cross-section.

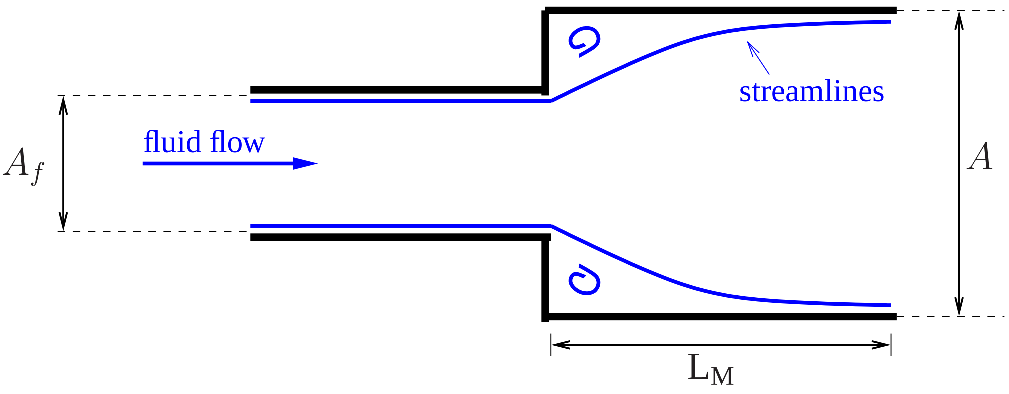

Figure 2.5: Streaming through a channel with a discontinuous expansion.

of a lot of little channels with constrictions, such that this law (2.2.5) is applicable to each of the holes in the interface. Let A_f be the sum of the area of all holes. Then, we can apply the porosity definition $\phi = \frac{A_f}{A}$ and obtain

$$p_p = p_f + \frac{\varrho}{2} v_x^2 \left(1 - \frac{1}{\phi^2 C_\mathrm{c}^2}\right) . \tag{2.2.6}$$

Note that there is no real pressure jump across the interface. The magnitude of the pressure value p_f in the fluid is split into the pressure value p_p and the term $\frac{\varrho}{2} v_x^2 \left(1 - \frac{1}{\phi^2 C_\mathrm{c}^2}\right)$. We call it ”pressure jump”, because the values p_f and p_p do not coincide.
Reducing the outflow interface to one pore, it can be considered to be a fluid flow channel with a discontinuous expansion, as depicted in figure 2.5. In the part in front of the expansion, we have pressure p_p. Behind the expansion, after a length $\mathrm{L_M} \approx 10 A_f$, we have again a stable flow profile. The loss of energy can be estimated by conservation laws. Following [38], we obtain

$$p_f = p_p + C_\mathrm{e} \frac{\varrho}{2} {v_{fx}^p}^2 \left(1 - \left(\frac{A_f}{A}\right)^2\right) ,$$

where C_e is the so-called efficiency number of the step diffusor. C_e depends on the ratio of A and A_f. For example, for $\frac{A}{A_f} = 0.5$, $C_\mathrm{e} \approx 0.65$.
Using A_f for the area of all the holes in Γ_out, and introducing $\phi = \frac{A_f}{A}$, one gets for the three-dimensional case

$$p_f = p_p + C_\mathrm{e} \frac{\varrho}{2} {v_{fx}^p}^2 \left(1 - \phi^2\right) . \tag{2.2.7}$$

2.2.2 The transmission conditions in one dimension

Now we derive the transmission conditions for the one-dimensional case. For this purpose, we define the one-dimensional mean value

$$w := \langle \mathbf{w} \rangle = \frac{1}{A} \int_A \mathbf{w} \, dx . \tag{2.2.8}$$

Conservation of mass

Equating the mass which ”enters” the interface from one side with the mass which ”leaves” it on the other side, gives

$$\int_A \varrho \mathbf{v}\, dx = \int_{A_s} \varrho\alpha \frac{\partial \mathbf{u}}{\partial t}\, dx + \int_{A_f} \varrho \mathbf{v}_f^p\, dx\,.$$

Dividing this equation by the density ϱ and using the mean value notation (2.2.8), we obtain

$$\langle \mathbf{v} \rangle = \alpha \frac{A_s}{A} \frac{\langle \mathbf{u} \rangle}{\partial t} + \frac{A_f}{A} \langle \mathbf{v}_f^p \rangle\,.$$

For a one-dimensional model on a microscopic level, one cannot define the porosity. But here, we obtain one-dimensional parameter values by taking the mean-value of the three-dimensional components and consider the problem then from a macroscopical point of view. Therefore, we use the earlier introduced definition for the porosity (2.1.1) and the solid volume fraction (2.1.2). With the Dupuit-Forchheimer assumption $\mathbf{q} = \phi \mathbf{v}_f^p$ we then obtain the mass conservation equation for the one-dimensional case

$$v = (1-\phi)\alpha \frac{\partial u}{\partial t} + q\,. \tag{2.2.9}$$

Continuity of tractions

The continuity of tractions equation in one dimension is also derived from the equilibrium of forces

$$\int_A \sigma_f \cdot \mathbf{n}\, dx = \int_{A_s} \sigma_s \cdot \mathbf{n}\, dx + \int_{A_f} \sigma_f^p \cdot \mathbf{n}\, dx\,.$$

Integrating this equation, using the definitions for the porosity (2.1.1) and the solid volume fraction (2.1.2) and the definitions for the stress tensors in one dimension, we get

$$2\eta \frac{\partial v}{\partial x} - p_f = (1-\phi)(2\mu + \lambda)\frac{\partial u}{\partial x} + 2\eta\phi \frac{\partial v_f^p}{\partial x} - \phi p_p\,. \tag{2.2.10}$$

Pressure jump condition

The pressure jump conditions (2.2.6) and (2.2.7) simply need to be transferred to the one-dimensional case, by using the appropriate notation. For Γ_{in} we get

$$p_p = p_f + \frac{\varrho}{2} v^2 \left(1 - \frac{1}{\phi^2 C_{\text{c}}^2}\right)\,, \tag{2.2.11}$$

and for Γ_{out}

$$p_f = p_p + C_{\text{e}} \frac{\varrho}{2} v_f^{p\,2} \left(1 - \phi^2\right)\,. \tag{2.2.12}$$

2.3 The continuous coupled formulation in three dimensions

At the end of this chapter, we want to state the entire continuous coupled formulation of the Biot-Stokes system in three dimensions.
We consider our model problem (section 2.1). Thus, we have a domain $\Omega \subset \mathbb{R}^3$, which consists

of two disjoint fluid domains Ω_{f1} and Ω_{f2}, such that $\Omega_f = \Omega_{f1} \cup \Omega_{f2}$, and a porous part Ω_p, such that $\Omega = \Omega_f \cup \Omega_p$ and $\Omega_f \cap \Omega_p = \emptyset$. The boundary of the fluid domain is denoted by $\partial\Omega_f$ and consists of four disjoint parts $\partial\Omega_f = \partial\Omega_{f,\text{in}} \cup \partial\Omega_{f,\text{out}} \cup \partial\Omega_{f,\text{fixed}} \cup \Gamma$, where $\partial\Omega_{f,\text{in}}$ denotes the inflow boundary, $\partial\Omega_{f,\text{out}}$ the outflow boundary and $\partial\Omega_{f,\text{fixed}}$ the part of $\partial\Omega_f$, which is fixed, i.e. the channel walls. Γ denotes the interface between Ω_p and Ω_f. For the boundary of the porous domain, it is similar. It is denoted by $\partial\Omega_p$, where $\partial\Omega_p = \partial\Omega_{p,\text{in}} \cup \partial\Omega_{p,\text{out}} \cup \partial\Omega_{p,\text{fixed}}$. $\partial\Omega_{p,\text{in}}$ is the inflow boundary of the porous medium, $\partial\Omega_{p,\text{out}}$ the outflow boundary and $\partial\Omega_{p,\text{fixed}}$ denotes the part of the porous medium which is fixed to the channel walls.
Γ denotes the interface between Ω_f and Ω_p: $\Gamma = \partial\Omega_f \cap \partial\Omega_p$. In our model domain we distinguish between the inflow interface $\Gamma_{\text{in}} = \partial\Omega_{f1,\text{out}} \cap \partial\Omega_{p,\text{in}}$ and the outflow interface $\Gamma_{\text{out}} = \partial\Omega_{f2,\text{in}} \cap \partial\Omega_{p,\text{out}}$. Thus, $\Gamma = \Gamma_{\text{in}} \cup \Gamma_{\text{out}}$ with $\Gamma_{\text{in}} \cap \Gamma_{\text{out}} = \emptyset$. Note that $\Gamma_{\text{in}} = \partial\Omega_{p,\text{in}}$ and $\Gamma_{\text{out}} = \partial\Omega_{p,\text{out}}$.

In this domain, the continuous coupled Biot-Stokes system looks as follows:
In Ω_f, the Stokes equations are valid

$$\left.\begin{aligned} \varrho\frac{\partial \mathbf{v}}{\partial t} - \eta\Delta\mathbf{v} + \nabla p_f = \mathbf{f}_f \\ \nabla\cdot\mathbf{v} = 0 \end{aligned}\right. \qquad \text{in}\,\Omega_f\,. \tag{2.3.1a}$$

In Ω_p, we solve the Biot poroelasticity equations

$$\left.\begin{aligned} -\nabla\cdot\sigma_p + \alpha\nabla p_p = \mathbf{0} \\ \frac{\partial}{\partial t}(\phi\beta p_p + \alpha\nabla\cdot\mathbf{u}) + \nabla\cdot\mathbf{q} = f_p \end{aligned}\right. \qquad \text{in}\,\Omega_p\,. \tag{2.3.1b}$$

Along the interface Γ, the mass conservation equation and the continuity of tractions equation have to be fulfilled

$$\mathbf{v} = (1-\phi)\alpha\frac{\partial\mathbf{u}}{\partial t} + \mathbf{q} \qquad \text{on}\,\Gamma\,, \tag{2.3.1c}$$

$$\sigma_f\cdot\mathbf{n} = (1-\phi)\,\sigma_s\cdot\mathbf{n} + \phi\,\sigma_f^p\cdot\mathbf{n} \qquad \text{on}\,\Gamma\,. \tag{2.3.1d}$$

Dependent on whether we consider the inflow interface Γ_{in} or the outflow interface Γ_{out}, the pressure jump condition looks slightly different

$$p_p = p_f + \frac{\varrho}{2}v_x^2\left(1 - \frac{1}{\phi^2 C_{\text{c}}^2}\right) \qquad \text{on}\,\Gamma_{\text{in}}\,, \tag{2.3.1e}$$

$$p_f = p_p + C_{\text{e}}\frac{\varrho}{2}{v_{fx}^p}^2\left(1-\phi^2\right) \qquad \text{on}\,\Gamma_{\text{out}}\,. \tag{2.3.1f}$$

The remaining boundaries have to be provided with suitable boundary conditions. For the fluid domain these conditions are the following

$$\mathbf{v} = \mathbf{v}_0 \qquad \text{on}\,\partial\Omega_{f,\text{in}}\,, \tag{2.3.1g}$$

$$p_f = p_{f,0} \qquad \text{on}\,\partial\Omega_{f,\text{out}}\,, \tag{2.3.1h}$$

$$\mathbf{v} = \mathbf{0} \qquad \text{on}\,\partial\Omega_{f,\text{fixed}}\,, \tag{2.3.1i}$$

and for Ω_p, we have

$$\left.\begin{aligned}\mathbf{u} &= 0\\ \mathbf{q}\cdot\mathbf{n} &= 0\end{aligned}\right.\qquad \text{on } \partial\Omega_{p,\text{fixed}}\,. \tag{2.3.1j}$$

This is the three-dimensional continuous coupled Biot-Stokes system with corresponding interface and boundary conditions. The coupled formulation in one dimension, is given in the next chapter, section 3.2.

Chapter 3

The coupled formulation in one dimension

In this chapter we consider the coupled problem in one dimension, $\Omega \subset \mathbb{R}$. The one dimensional domain is denoted by $\Omega = \Omega_f \cup \Omega_p = [0, \Gamma] \cup [\Gamma, \mathcal{L}]$, where Ω_f is the fluid domain and Ω_p the domain of the porous medium. $\partial\Omega_f \cap \partial\Omega_p = \Gamma$ denotes the interface. Since we are in 1d, $\Gamma \in \mathbb{R}$ and $\mathcal{L} \in \mathbb{R}$. Here we consider a domain that has only one fluid part and one porous part. So, we only investigate the coupled formulation at the inflow interface. For the outflow interface it works similarly.

In this chapter we first state the Biot equations and the Stokes equations in one dimension. Then, the continuous coupled formulation is presented. Afterwards we consider the extreme cases (fluid-fluid and fluid-solid coupling). The chapter is concluded with a numerical example.

3.1 Stokes and Biot equations in one dimension

In one dimension the Stokes equations look as follows:

$$\left.\begin{aligned} \varrho\frac{\partial v}{\partial t} - \eta\frac{\partial^2 v}{\partial x^2} + \frac{\partial p_f}{\partial x} &= f_f \\ \frac{\partial v}{\partial x} &= 0 \end{aligned}\right. \qquad x \in \Omega_f\,,$$

and the Biot equations can be written as

$$\left.\begin{aligned} -\frac{\partial}{\partial x}((2\mu+\lambda)\frac{\partial u}{\partial x}) + \frac{\partial p_p}{\partial x} &= 0 \\ \frac{\partial}{\partial t}(\phi\beta p_p + \frac{\partial u}{\partial x}) + \frac{\partial q}{\partial x} &= f_p \end{aligned}\right. \qquad x \in \Omega_p\,.$$

Providing these two systems of equations in Ω with boundary conditions at the inflow ($x = 0$) and the outflow ($x = \mathcal{L}$), we set

$$v = v_0 \quad \text{at} \quad x = 0\,, \tag{3.1.1a}$$

$$u = 0 \quad \text{at} \quad x = \mathcal{L}\,, \tag{3.1.1b}$$

$$p_p = p_0 \quad \text{at} \quad x = \mathcal{L}\,. \tag{3.1.1c}$$

At the inflow we have a Dirichlet velocity boundary condition (3.1.1a), which is suitable for the Stokes equations. The outflow conditions are chosen according to Biot equations. There, we need two conditions with clear physical meaning: Equations (3.1.1b) and (3.1.1c) qualify an undeformed outflow with a prescribed pressure p_0.

Considerations about the transmission conditions yield the following: Having prescribed a Dirichlet velocity condition at the inflow $x = 0$, we need a Dirichlet pressure condition for the Stokes equations at the outflow of the fluid domain, i.e. at $x = \Gamma$. For the Biot equations we prescribe a stress condition $(\lambda + 2\mu)\frac{\partial u}{\partial x}$ and a Dirichlet pressure condition at the inflow of Ω_p, i.e. at $x = \Gamma$. These considerations enter the formulation of the transmission conditions. We will return to it later in this chapter.

3.2 The continuous coupled formulation

Summarising, the coupled formulation in the domain $\Omega = \Omega_f \cup \Omega_p = [0, \Gamma] \cup [\Gamma, \mathcal{L}]$ is the following:

$$\left.\begin{aligned} v &= v_0 \end{aligned}\right\} \text{ for } x = 0 \tag{3.2.1a}$$

$$\left.\begin{aligned} \varrho\frac{\partial v}{\partial t} - \eta\frac{\partial^2 v}{\partial x^2} + \frac{\partial p_f}{\partial x} &= f_f \\ \frac{\partial v}{\partial x} &= 0 \end{aligned}\right\} \text{ for } x \in (0, \Gamma) \tag{3.2.1b}$$

$$\left.\begin{aligned} (1-\phi)\alpha\frac{\partial u}{\partial t} + \phi v_f^p &= v \\ (1-\phi)(2\mu+\lambda)\frac{\partial u}{\partial x} + 2\eta\phi\frac{\partial v_f^p}{\partial x} - \phi p_p &= 2\eta\frac{\partial v}{\partial x} - p_f \\ p_f + \frac{\varrho}{2}v^2\left(1 - \frac{1}{\phi^2 C_c^2}\right) &= p_p \end{aligned}\right\} \text{ for } x = \Gamma \tag{3.2.1c}$$

$$\left.\begin{aligned} -\frac{\partial}{\partial x}\left((2\mu+\lambda)\frac{\partial u}{\partial x}\right) + \frac{\partial p_p}{\partial x} &= 0 \\ \frac{\partial}{\partial t}\left(\phi\beta p_p + \frac{\partial u}{\partial x}\right) + \frac{\partial q}{\partial x} &= f_p \end{aligned}\right\} \text{ for } x \in (\Gamma, \mathcal{L}) \tag{3.2.1d}$$

$$\left.\begin{aligned} u &= 0 \\ p_p &= p_0 \end{aligned}\right\} \text{ for } x = \mathcal{L}\,. \tag{3.2.1e}$$

3.3 Consideration of extreme cases

When we couple a fluid with a porous medium, there are two extreme cases that can appear. The first one is the fluid-fluid limit, i.e. when the porosity tends to 1 and the porous medium vanishes. The second case is the fluid-solid limit, when the porous medium corresponds to a solid body with porosity $\phi = 0$.

In the fluid-fluid case $\phi = 1$. Thus, the transmission conditions (3.2.1c) become:

$$\begin{aligned} v &= v_f^p = q && (3.3.1a) \\ 2\eta \frac{\partial v}{\partial x} - p_f &= 2\eta \frac{\partial v_f^p}{\partial x} - p_p && (3.3.1b) \\ p_p &= p_f \, . && (3.3.1c) \end{aligned}$$

That means, we have continuity of the velocity (3.3.1a), continuity of tractions (3.3.1b) and continuity of pressure (3.3.1c). In case of incompressible fluid, the space derivative of v and v_f^p, respectively, in (3.3.1b) vanish and we also get continuity of pressure from the second transmission condition. Thus, the system degenerates, we can omit the second or the last equation for this case. According to [14] or [27], the first two conditions are sufficient for the coupling of two fluids.

In the fluid-solid case $\phi = 0$. Then, the first and second transmission conditions become:

$$\begin{aligned} v &= \alpha \frac{\partial u}{\partial t} && (3.3.2a) \\ 2\eta \frac{\partial v}{\partial x} - p_f &= (2\mu + \lambda) \frac{\partial u}{\partial x} \, . && (3.3.2b) \end{aligned}$$

Equation (3.3.2a) describes the continuity of the velocities, i.e. the mass conservation, and (3.3.2b) the continuity of tractions. Plugging in $\phi = 0$ into the third transmission condition (3.2.1c), the term $\frac{1}{\phi^2 C_\mathrm{c}^2}$ goes to infinity and hence, p_f also goes to infinity. In this case, according to e.g. [34], equations (3.3.2a) and (3.3.2b) suffice for the fluid-solid coupling.

3.4 Numerical example

As a numerical example consider the coupling of an incompressible fluid with a rigid solid material. Thus, it corresponds to the case of the fluid-solid coupling described above. Since our code does not provide the possibility to choose $\phi = 1$, we approximate the permeability by $\phi = 0.99$. As boundary conditions we choose $v = v_0 = 10^{-3}\ \frac{\mathrm{m}}{\mathrm{s}}$ for the inflow and $p_p = 0\ \frac{\mathrm{N}}{\mathrm{m}^2}$ and $u = 0$ m at the outflow. For the fluid and the remaining porous medium, we choose the following parameters: permeability $k = 10^{-10}\ \mathrm{m}^2$, dynamic viscosity $\eta = 10^{-5}\ \frac{\mathrm{kg}}{\mathrm{m\,s}}$ and the Lamé coefficients $\mu = 4.19 \cdot 10^9\ \frac{\mathrm{N}}{\mathrm{m}^2}$ and $\lambda = 1.62 \cdot 10^9\ \frac{\mathrm{N}}{\mathrm{m}^2}$. Let the geometry be $[0, \Gamma] \cup [\Gamma, \mathcal{L}] = [0, 1] \cup [1, 2]$. From the solution of the Stokes equations we know that v is constant within Ω_f, so, $v = 10^{-3}\ \frac{\mathrm{m}}{\mathrm{s}}$. By using Darcy's law (1.3.2) and the Dupuit-Forchheimer equation (1.3.3)

$$v = q = \phi v_f^p = -\frac{k}{\eta} \frac{p_0 - p_p}{\mathcal{L} - \Gamma}$$

it follows $p_p = 10^2\ \frac{\mathrm{N}}{\mathrm{m}^2}$.

p_p is the fluid pressure from the porous side of the interface. From the third transmission condition we know that the pressure on the macroscopic level has a jump across the interface. So, using $\phi = 0.99$, $C_\mathrm{c} = 0.95$ and $\varrho = 10^3\ \frac{\mathrm{kg}}{\mathrm{m}^3}$, we can compute p_f at the interface from equation (2.2.11):

$$p_f = (10^2 + 2.97 \cdot 10^{-4})\ \frac{\mathrm{N}}{\mathrm{m}^2} \, .$$

Since the velocity is constant in Ω_f, it follows that $\frac{\partial v}{\partial x} = 0$. Assuming that $\frac{\partial v_f^p}{\partial x}$ is also equal to 0 due to incompressibility of the fluid, we obtain by equation (2.2.10)

$$-p_f = (-10^2 - 2.97 \cdot 10^{-4})\,\frac{\mathrm{N}}{\mathrm{m}^2} = (10^8 \frac{\partial u}{\partial x} - 0.99\,\cdot\,10^2)\,\frac{\mathrm{N}}{\mathrm{m}^2} \;\Rightarrow\; \frac{\partial u}{\partial x} = O(10^{-8})\,.$$

The discrete system of equations for the three transmission conditions is the following:

$$\begin{aligned} \phi v_f^p + (1-\phi)\frac{\alpha}{\Delta t} u &= v + (1-\phi)\frac{\alpha}{\Delta t}\breve{u} \\ -(1-\phi)\frac{2\mu+\lambda}{\Delta x} u - \frac{2\eta\phi}{\Delta x} v_f^p - \phi p_p &= 2\eta \frac{v - v_{i-1}}{\Delta x} - p_f \\ &\quad -(1-\phi)\frac{2\mu+\lambda}{\Delta x} u_{i+1} - \frac{2\eta\phi}{\Delta x} v_{f,i+1}^p \\ p_p &= p_f + \frac{\varrho}{2} v^2 (1 - \frac{1}{\phi^2 C_{\mathrm{c}}^2})\,. \end{aligned} \tag{3.4.1}$$

Note that we used $q = \phi\, v_f^p$ in the first equation of the system.
For the solution of the system of equations (3.4.1) an iterative solution procedure is used (see description in section 6.2). Variables in (3.4.1) which have no index i, are variables at the interface. The index $i+1$ denotes variables which lie in the porous domain, $i-1$ those, which lie in the fluid domain. These values are assumed to be known from previous iterations. Δx denote the step size in x-direction. Δt denotes the time step. We take backward differences in time, variables from a previous time step are denoted with a superscript $\breve{\ }$.
Since we consider a rigid porous medium, $\breve{u}$ and u_{i+1} are set to be 0. The time step is $\Delta t = 0.1$ s. The velocity is constant, so, $v_{i-1} = 10^{-3}\,\frac{\mathrm{m}}{\mathrm{s}}$ and $v_{f,i+1}^p = 10^{-3}\,\frac{\mathrm{m}}{\mathrm{s}}$. The pressure drops linearly throughout the porous medium. So, for a step size $\Delta x = 0.25$m, we have $p_{p,i+1} = (10^2 - 10^2 \cdot 0.25)\,\frac{\mathrm{N}}{\mathrm{m}^2} = 75\,\frac{\mathrm{N}}{\mathrm{m}^2}$.
Using these values, we get the following system of equations:

$$\begin{pmatrix} 0.99 & 0.1 & 0 \\ -7.9 \cdot 10^{-5} & -4 \cdot 10^8 & -0.99 \\ 0 & 0 & 1 \end{pmatrix} \begin{pmatrix} v_f^p \\ u \\ p_p \end{pmatrix} = \begin{pmatrix} 10^{-3}\,\frac{\mathrm{m}}{\mathrm{s}} \\ (-10^2 - 2.97 \cdot 10^{-4})\,\frac{\mathrm{N}}{\mathrm{m}^2} \\ (10^2 + 2.317 \cdot 10^{-4})\,\frac{\mathrm{N}}{\mathrm{m}^2} \end{pmatrix}.$$

The matrix is diagonally dominant. Solved by Gaussian elimination, the solution is $v_f^p = 1.0101 \cdot 10^{-3}\,\frac{\mathrm{m}}{\mathrm{s}}$, $u = 2.5 \cdot 10^{-9}$ m, $p_p = (100 + 2.373 \cdot 10^{-4})\,\frac{\mathrm{N}}{\mathrm{m}^2}$. These are approximately the values we obtained by our theoretical studies above. Thus, for the 1d case, the transmission conditions (3.2.1c) deliver the expected results.

Chapter 4

The discrete coupled Biot-Stokes system on matching node-based grids

In this chapter we derive the discrete coupled system for the Stokes equations and the Biot poroelasticity equations on node-based matching grids in three dimensions, i.e. we work on the model domain which was described in section 2.1.

First, we use a finite volume (FV) approach to discretise the Stokes equations, the Biot poroelasticity equations and the transmission conditions on node-based grids. A three-dimensional node-based grid with appropriate notations is displayed in figure 4.1. We introduce an operator notation for the Stokes equations, the Biot equations and the transmission conditions. Finally, the entire discrete coupled system is obtained.

In the porous medium Ω_p the grid has $N_{px} \times N_{py} \times N_{pz}$ grid cells and thus, $(N_{px}+1) \times (N_{py}+1) \times (N_{pz}+1)$ grid nodes. The grid size is denoted by $h_{px} \times h_{py} \times h_{pz}$.

The grid in the fluid region consists of $N_{fx} \times N_{fy} \times N_{fz}$ grid blocks. Since we consider a node-based grid, the number of nodes in the fluid region is $(N_{fx}+1) \times (N_{fy}+1) \times (N_{fz}+1)$. The grid width is $h_{fx} \times h_{fy} \times h_{fz}$.

The area of the interface Γ is given by $N_{py}h_{py} \times N_{pz}h_{pz}$ or $N_{fy}h_{fy} \times N_{fz}h_{fz}$, respectively.

In this chapter we only deal with matching grids. That implies $N_{py} = N_{fy}$, $N_{pz} = N_{fz}$ and $h_{py} = h_{fy}$, $h_{pz} = h_{fz}$. Therefore, we introduce a common notation for the number of grid cells and the grid size in y-direction and z-direction:

$$\begin{aligned} N_y &:= N_{py} = N_{fy}\,, & h_y &:= h_{py} = h_{fy}\,, \\ N_z &:= N_{pz} = N_{fz}\,, & h_z &:= h_{pz} = h_{fz}\,. \end{aligned}$$

The time step is h_t in both regions. We discretise the system in a fully implicit way and thus, we use backward differences for time derivatives. To indicate that a variable belongs to the previous time iteration we use the symbol $\breve{\ }$.

A node-based grid has the following types of grid points:

$$\begin{aligned} \omega_{nb} = \omega_{nb,h_x,h_y,h_z} = \{&(x_i, y_j, z_k) = ((i-1)h_x, (j-1)h_y, (k-1)h_z), \\ &i = 1, \ldots, N_{px}+1,\ j = 1, \ldots, N_{py}+1,\ k = 1, \ldots, N_{pz}+1\}\,. \end{aligned}$$

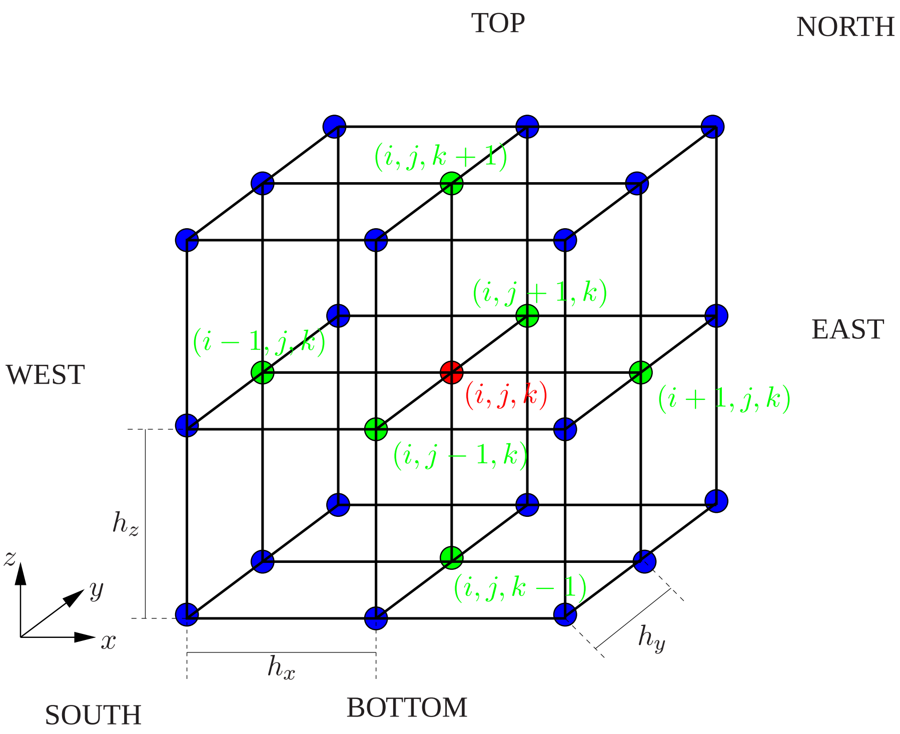

Figure 4.1: Three-dimensional node-based grid.

For the time discretisation we use a grid with step size h_t:

$$\omega^t = \{t_\tau : t_\tau = \tau h_t, \tau = 1, \ldots, t_{\text{end}}\} \ .$$

Based on these grids we introduce the following discrete grid functions for displacements and pressure:

$$\begin{array}{rclcll} u_{x(i,j,k)} & := & u^\tau_{x(i,j,k)} & = & u_x(x_i, y_j, z_k, t_\tau) & \text{on} \quad \omega_{nb} \times \omega^t \\ u_{y(i,j,k)} & := & u^\tau_{y(i,j,k)} & = & u_y(x_i, y_j, z_k, t_\tau) & \text{on} \quad \omega_{nb} \times \omega^t \\ u_{z(i,j,k)} & := & u^\tau_{z(i,j,k)} & = & u_z(x_i, y_j, z_k, t_\tau) & \text{on} \quad \omega_{nb} \times \omega^t \\ p_{p(i,j,k)} & := & p^\tau_{p(i,j,k)} & = & p_p(x_i, y_j, z_k, t_\tau) & \text{on} \quad \omega_{nb} \times \omega^t \, . \end{array} \tag{4.0.1}$$

For the sake of simplicity we have chosen the same notation for the discrete and the continuous functions. The discrete functions have a subscript specifying the index. We discretise the Biot poroelasticity model by using the FV method. The forward and backward derivatives at a point (x_i, y_j, z_k, t_τ) are defined to be:

$$\begin{array}{rcl} \Delta_x \, p_{p(i,j,k)} & = & \frac{p_{p(i+1,j,k)} - p_{p(i,j,k)}}{h_x} \, , \\ \Delta_{\overline{x}} \, p_{p(i,j,k)} & = & \frac{p_{p(i,j,k)} - p_{p(i-1,j,k)}}{h_x} \, , \\ \Delta_{xy} \, p_{p(i,j,k)} & = & \Delta_x \, \Delta_y \, p_{p(i,j,k)} = \frac{p_{p(i+1,j+1,k)} - p_{p(i+1,j,k)} - p_{p(i,j+1,k)} + p_{p(i,j,k)}}{h_x h_y} \, , \\ \Delta_{\overline{x}z} \, p_{p(i,j,k)} & = & \Delta_{\overline{x}} \, \Delta_z \, p_{p(i,j,k)} = \frac{p_{p(i,j,k+1)} - p_{p(i,j,k)} - p_{p(i-1,j,k+1)} + p_{p(i-1,j,k)}}{h_x h_z} \, . \end{array} \tag{4.0.2}$$

For time derivatives we use this notation:

$$\Delta_{\overline{t}} \, p_{p(i,j,k)} := \Delta_{\overline{t}} \, p^\tau_{p(i,j,k)} = \frac{p^\tau_{p(i,j,k)} - \check{p}_{p(i,j,k)}}{h_t} \, . \tag{4.0.3}$$

When the superscript τ is omitted, the corresponding variable is taken at the current time t_τ.

4.1 Discretisation of the Biot poroelasticity system on a node-based grid

In this section we derive a FV discretisation for the three-dimensional Biot poroelasticity system (1.3.16). Component-wise, the Biot system can be written as

$$
\begin{aligned}
&-\left((\lambda+2\mu)u_{x,x}+\lambda(u_{y,y}+u_{z,z})\right)_{,x}-\left(\mu(u_{x,y}+u_{y,x})\right)_{,y}-\left(\mu(u_{x,z}+u_{z,x})\right)_{,z}+\alpha p_{p,x}\\
&\qquad\qquad\qquad\qquad\qquad\qquad\qquad\qquad\qquad\qquad\qquad\qquad\qquad\qquad\qquad=0\\
&-\left(\mu(u_{y,x}+u_{x,y})\right)_{,x}-\left((\lambda+2\mu)u_{y,y}\;+\;\lambda(u_{z,z}+u_{x,x})\right)_{,y}-\left(\mu(u_{y,z}+u_{z,y})\right)_{,z}+\alpha p_{p,y}\\
&\qquad\qquad\qquad\qquad\qquad\qquad\qquad\qquad\qquad\qquad\qquad\qquad\qquad\qquad\qquad=0\\
&-\left(\mu(u_{z,x}+u_{x,z})\right)_{,x}-\left(\mu(u_{z,y}+u_{y,z})\right)_{,y}-\left((\lambda+2\mu)u_{z,z}+\lambda(u_{x,x}+u_{y,y})\right)_{,z}+\alpha p_{p,z}\\
&\qquad\qquad\qquad\qquad\qquad\qquad\qquad\qquad\qquad\qquad\qquad\qquad\qquad\qquad\qquad=0\\
&\left(\phi\beta p_p+\alpha u_{x,x}+\alpha u_{y,y}+\alpha u_{z,z}\right)_{,t}-\left(\frac{k}{\eta}p_{p,x}\right)_{,x}-\left(\frac{k}{\eta}p_{p,y}\right)_{,y}-\left(\frac{k}{\eta}p_{p,z}\right)_{,z}=f_p\,.
\end{aligned}
$$

where the subscripts $\cdot_{,x}$, $\cdot_{,y}$, $\cdot_{,z}$ and $\cdot_{,t}$ denote the derivatives with respect to x, y, z and t, respectively. Note that the pressure and displacement values are space-averaged values. For the sake of simplicity we have omitted the overbars.

Using the notation for the space and time derivatives, introduced in (4.0.2) and (4.0.3), the discrete Biot poroelasticity equations can be written as:

$$
\begin{aligned}
&-(\lambda+2\mu)\,\Delta_{\overline{x}x}\,u_{x(i,j,k)}-\lambda\,\Delta_{\overline{y}x}\,u_{y(i,j,k)}-\lambda\,\Delta_{\overline{z}x}\,u_{z(i,j,k)}-\mu\,\Delta_{\overline{y}y}\,u_{x(i,j,k)}\\
&\quad-\mu\,\Delta_{\overline{x}y}\,u_{y(i,j,k)}-\mu\,\Delta_{\overline{z}z}\,u_{x(i,j,k)}-\mu\,\Delta_{\overline{x}z}\,u_{z(i,j,k)}+\alpha\,\Delta_{\overline{x}}\,p_{p(i,j,k)}=0
\end{aligned}
\tag{4.1.1a}
$$

$$
\begin{aligned}
&-\mu\,\Delta_{\overline{x}x}\,u_{y(i,j,k)}-\mu\,\Delta_{\overline{x}y}\,u_{x(i,j,k)}-(\lambda+2\mu)\,\Delta_{\overline{y}y}\,u_{y(i,j,k)}-\lambda\,\Delta_{\overline{y}z}\,u_{z(i,j,k)}\\
&\quad-\lambda\,\Delta_{\overline{y}x}\,u_{x(i,j,k)}-\mu\,\Delta_{\overline{z}z}\,u_{y(i,j,k)}-\mu\,\Delta_{\overline{z}y}\,u_{z(i,j,k)}+\alpha\,\Delta_{\overline{y}}\,p_{p(i,j,k)}=0
\end{aligned}
\tag{4.1.1b}
$$

$$
\begin{aligned}
&-\mu\,\Delta_{\overline{x}x}\,u_{z(i,j,k)}-\mu\,\Delta_{\overline{x}z}\,u_{x(i,j,k)}-\mu\,\Delta_{\overline{y}y}\,u_{z(i,j,k)}-\mu\,\Delta_{\overline{y}z}\,u_{y(i,j,k)}\\
&\quad-(\lambda+2\mu)\,\Delta_{\overline{z}z}\,u_{z(i,j,k)}-\lambda\,\Delta_{\overline{z}x}\,u_{x(i,j,k)}-\lambda\,\Delta_{\overline{z}y}\,u_{y(i,j,k)}+\alpha\,\Delta_{\overline{z}}\,p_{p(i,j,k)}=0
\end{aligned}
\tag{4.1.1c}
$$

$$
\begin{aligned}
&\phi\beta\,\Delta_{\overline{t}}\,p_{p(i,j,k)}+\alpha\,\Delta_{x\overline{t}}\,u_{x(i,j,k)}+\alpha\,\Delta_{y\overline{t}}\,u_{y(i,j,k)}+\alpha\,\Delta_{z\overline{t}}\,u_{z(i,j,k)}\\
&\quad-\frac{k}{\eta}\,\Delta_{\overline{x}x}\,p_{p(i,j,k)}-\frac{k}{\eta}\,\Delta_{\overline{y}y}\,p_{p(i,j,k)}-\frac{k}{\eta}\,\Delta_{\overline{z}z}\,p_{p(i,j,k)}=f_p\,.
\end{aligned}
\tag{4.1.1d}
$$

4.2 Discretisation of the Stokes equations on a node-based grid

In the fluid region $\Omega_f \subset \Omega$ we solve the Stokes equations (1.1.2). Component-wise, they are

$$\begin{aligned}
\varrho v_{x,t} - \eta \left(v_{x,xx} + v_{x,yy} + v_{x,zz} \right) + p_{f,x} &= f_{fx} \\
\varrho v_{y,t} - \eta \left(v_{y,xx} + v_{y,yy} + v_{y,zz} \right) + p_{f,y} &= f_{fy} \\
\varrho v_{z,t} - \eta \left(v_{z,xx} + v_{z,yy} + v_{z,zz} \right) + p_{f,z} &= f_{fz} \\
v_{x,x} + v_{y,y} + v_{z,z} &= 0\,.
\end{aligned}$$

This is also discretised by the FV method. According to [47] we use forward differences for the discretisation of the gradient and backward differences for the divergence. This is done to avoid a checkerboard pressure field. We use the difference operators introduced above ((4.0.2) and (4.0.3)). Moreover, we use the same notation for the discrete and the continuous variables. Thus, the discrete Stokes equations read as

$$\varrho\, \Delta_{\overline{t}}\, v_{x(i,j,k)} - \eta\, \Delta_{\overline{x}x}\, v_{x(i,j,k)} - \eta\, \Delta_{\overline{y}y}\, v_{x(i,j,k)} - \eta\, \Delta_{\overline{z}z}\, v_{x(i,j,k)} + \Delta_x\, p_{f(i,j,k)} = f_{fx} \tag{4.2.1a}$$

$$\varrho\, \Delta_{\overline{t}}\, v_{y(i,j,k)} - \eta\, \Delta_{\overline{x}x}\, v_{y(i,j,k)} - \eta\, \Delta_{\overline{y}y}\, v_{y(i,j,k)} - \eta\, \Delta_{\overline{z}z}\, v_{y(i,j,k)} + \Delta_y\, p_{f(i,j,k)} = f_{fy} \tag{4.2.1b}$$

$$\varrho\, \Delta_{\overline{t}}\, v_{z(i,j,k)} - \eta\, \Delta_{\overline{x}x}\, v_{z(i,j,k)} - \eta\, \Delta_{\overline{y}y}\, v_{z(i,j,k)} - \eta\, \Delta_{\overline{z}z}\, v_{z(i,j,k)} + \Delta_z\, p_{f(i,j,k)} = f_{fz} \tag{4.2.1c}$$

$$\Delta_{\overline{x}}\, v_{x(i,j,k)} + \Delta_{\overline{y}}\, v_{y(i,j,k)} + \Delta_{\overline{z}}\, v_{z(i,j,k)} = 0\,. \tag{4.2.1d}$$

4.3 Discretisation of the transmission conditions

For the discretisation of the transmission conditions we use the FV method on a three-dimensional node-based grid as displayed in figure 4.1. The primary variables in the porous medium are the displacements $\mathbf{u} = (u_x, u_y, u_z)^T$ of the porous skeleton, and the fluid pressure p_p. By using the Dupuit-Forchheimer assumption $\mathbf{q} = \phi \mathbf{v}_f^p$, Darcy's law and the fact that the elastic stress σ_s in the porous medium can be expressed through the displacements (see equation (1.2.2)), the flux $\mathbf{q}$ and the stress tensor σ_s can be eliminated from the transmission conditions.
In the fluid regions, the primary variables are the fluid velocity $\mathbf{v} = (v_x, v_y, v_z)^T$ and the pressure p_f. By definition, the stress σ_f can be expressed by the fluid velocities and the pressure (see equation (1.1.4)). Here, we neglect the viscous term for the fluid inside the porous medium. Thus, the transmission conditions can be written as:

Conservation of mass

$$\mathbf{v} = (1-\phi)\alpha \frac{\partial \mathbf{u}}{\partial t} - \frac{k}{\eta} \nabla p_p\,.$$

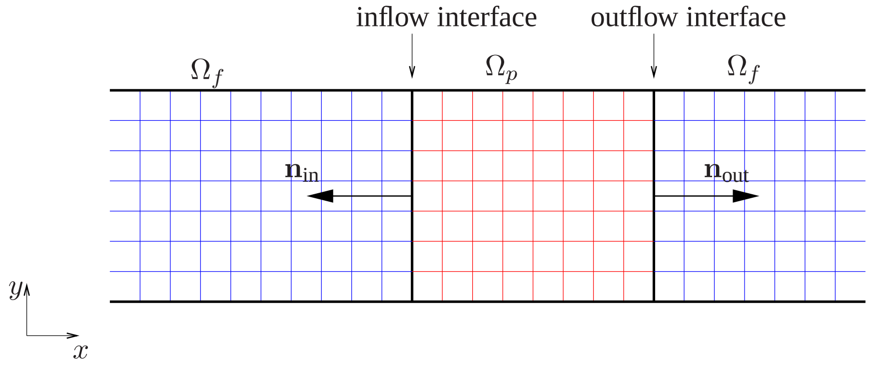

Figure 4.2: 2d sketch of the filter channel with matching grids

Conservation of momentum

$$\begin{aligned}\left(\eta\left(\nabla\mathbf{v}+(\nabla\mathbf{v})^T\right)-p_f\mathbf{I}\right)\cdot\mathbf{n} &= (1-\phi)\left(\mu\left(\nabla\mathbf{u}+(\nabla\mathbf{u})^T\right)+\lambda\nabla\cdot\mathbf{u}\mathbf{I}\right)\cdot\mathbf{n}\\ &\quad -\phi\left(p_p\mathbf{I}\right)\cdot\mathbf{n}\,.\end{aligned}$$

Pressure jump condition - inflow

$$p_f+\frac{\varrho}{2}v_x^2\left(1-\frac{1}{\phi^2C_{\text{c}}^2}\right)=p_p\,.$$

Pressure jump condition - outflow

$$p_f=p_p+C_{\text{e}}\frac{\varrho}{2}{v_{fx}^p}^2\left(1-\phi^2\right)\,.$$

Using backward differences for the time derivatives, one-sided differences for the spatial derivatives in normal direction and central differences for the spatial derivatives in tangential directions, the transmission conditions can be discretised easily.

Considering normal fluid flow means that the interfaces are parallel to the y-z-plane, i.e. normal to the x-axis. We define the unit normal vector $\mathbf{n}$ to point from the porous medium outwards to the fluid region. Thus, dependent on whether we consider the inflow interface Γ_{in} or the outflow interface Γ_{out}, the normal vector is either

$$\mathbf{n}_{\text{in}}=\begin{pmatrix}-1\\0\\0\end{pmatrix}\quad\text{or}\quad\mathbf{n}_{\text{out}}=\begin{pmatrix}1\\0\\0\end{pmatrix}.$$

Moreover, we have to use different spatial discretisation schemes for the normal derivatives at the inflow and outflow, respectively. For the porous medium we use forward discretisation for derivatives with respect to x at the inflow, whereas at the outflow we use backward differences. For the derivatives in the fluid equations it is the opposite, i.e. backward differences at the inflow interface and forward differences at the outflow interface. Figure 4.2 shows a two-dimensional sketch of our discretised model geometry with the normals at inflow and outflow interface.

For the inflow interface, we need only four transmission conditions, because the outflow boundary condition for Ω_f is a Dirichlet pressure condition. Since we want to show how all transmission conditions look like, we restrict ourselves in the following to the outflow interface. The discretisation for the inflow interface works similarly.

The discrete transmission conditions at Γ_{out} are as follows:

Conservation of mass

$$
\begin{aligned}
v_{x(i,j,k)} &= (1-\phi)\alpha\frac{1}{h_t}(u_{x(i,j,k)} - \check{u}_{x(i,j,k)}) - \frac{k}{\eta}\frac{1}{h_{px}}(p_{p(i,j,k)} - p_{p(i-1,j,k)}) && \text{(4.3.2a)}\\
v_{y(i,j,k)} &= (1-\phi)\alpha\frac{1}{h_t}(u_{y(i,j,k)} - \check{u}_{y(i,j,k)}) - \frac{k}{\eta}\frac{1}{2h_y}(p_{p(i,j+1,k)} - p_{p(i,j-1,k)}) && \text{(4.3.2b)}\\
v_{z(i,j,k)} &= (1-\phi)\alpha\frac{1}{h_t}(u_{z(i,j,k)} - \check{u}_{z(i,j,k)}) - \frac{k}{\eta}\frac{1}{2h_z}(p_{p(i,j,k+1)} - p_{p(i,j,k-1)}) && \text{(4.3.2c)}
\end{aligned}
$$

Conservation of momentum

$$
\begin{aligned}
2\eta\frac{1}{h_{fx}}(v_{x(i+1,j,k)} - v_{x(i,j,k)}) - p_{f(i,j,k)} = (1-\phi)\bigg[(2\mu+\lambda)\frac{1}{h_{px}}(u_{x(i,j,k)} - u_{x(i-1,j,k)})\\
+\lambda\left(\frac{1}{2h_y}(u_{y(i,j+1,k)} - u_{y(i,j-1,k)}) + \frac{1}{2h_z}(u_{z(i,j,k+1)} - u_{z(i,j,k-1)})\right)\bigg] - \phi p_{p(i,j,k)}
\end{aligned} \qquad \text{(4.3.2d)}
$$

$$
\begin{aligned}
\eta\left(\frac{1}{h_{fx}}(v_{y(i+1,j,k)} - v_{y(i,j,k)}) + \frac{1}{2h_y}(v_{x(i,j+1,k)} - v_{x(i,j-1,k)})\right) =\\
(1-\phi)\mu\left(\frac{1}{h_{px}}(u_{y(i,j,k)} - u_{y(i-1,j,k)}) + \frac{1}{2h_y}(u_{x(i,j+1,k)} - u_{x(i,j-1,k)})\right)
\end{aligned} \qquad \text{(4.3.2e)}
$$

$$
\begin{aligned}
\eta\left(\frac{1}{h_{fx}}(v_{z(i+1,j,k)} - v_{z(i,j,k)}) + \frac{1}{2h_z}(v_{x(i,j,k+1)} - v_{x(i,j,k-1)})\right) =\\
(1-\phi)\mu\left(\frac{1}{h_{px}}(u_{z(i,j,k)} - u_{z(i-1,j,k)}) + \frac{1}{2h_z}(u_{x(i,j,k+1)} - u_{x(i,j,k-1)})\right)
\end{aligned} \qquad \text{(4.3.2f)}
$$

Pressure jump condition - inflow

$$
p_{f(i,j,k)} + \frac{\varrho}{2}v_{x(i,j,k)}\check{v}_{x(i,j,k)}\left(1 - \frac{1}{\phi^2 C_{\text{c}}^2}\right) = p_{p(i,j,k)} \qquad \text{(4.3.2g)}
$$

Pressure jump condition - outflow

$$
\begin{aligned}
p_{f(i,j,k)} &= p_{p(i,j,k)} + C_{\text{e}}\frac{\varrho}{2}v^p_{fx(i,j,k)}\check{v}^p_{fx(i,j,k)}\left(1-\phi^2\right)\\
&= p_{p(i,j,k)} + C_{\text{e}}\frac{\varrho}{2}\left(\frac{1}{\phi}\frac{k}{\eta}\right)^2\frac{1}{h_{px}^2}(p_{p(i,j,k)} - p_{p(i-1,j,k)})(\check{p}_{p(i,j,k)} - \check{p}_{p(i-1,j,k)})\left(1-\phi^2\right) .
\end{aligned} \qquad \text{(4.3.2h)}
$$

4.4 The discrete coupled Biot-Stokes system

In this section we derive the discrete coupled Biot-Stokes system for matching node-based grids. The solution variables for the Biot-Stokes system are the primary variables of the particular systems of equations, i.e. displacements $\mathbf{u}$ and pressure p_p for the porous region Ω_p and velocities $\mathbf{v}$

and pressure p_f for the fluid domain Ω_f. The models are supplemented with relevant boundary conditions. Thus, we can split the solution variables into the values inside the domains Ω_p and Ω_f, those on the outer boundaries $\partial\Omega_p\backslash\Gamma$ and $\partial\Omega_f\backslash\Gamma$ and the values on the interface Γ_p and Γ_f, respectively. Note that $\Gamma_p = \Gamma = \Gamma_f$, but for the formulation of the coupled system of equations we have to distinguish between the nodes "from the porous side" of the interface and those "from the fluid side".

We denote the internal values of the porous domain by $\mathring{\mathbf{x}}_B = (\mathring{\mathbf{u}}, \mathring{p}_p)^T$, where the subscript B stands for Biot. The outer boundary values are indicated by a hat: $\hat{\mathbf{x}}_B = (\hat{\mathbf{u}}, \hat{p}_p)^T$. The interface values are marked by a tilde: $\tilde{\mathbf{x}}_B = (\tilde{\mathbf{u}}, \tilde{p}_p)^T$. The same notation holds for the fluid domain: internal values are denoted by $\mathring{\mathbf{x}}_S = (\mathring{\mathbf{v}}, \mathring{p}_f)^T$, outer boundary values are denoted by $\hat{\mathbf{x}}_S = (\hat{\mathbf{v}}, \hat{p}_f)^T$ and interface values are denoted by $\tilde{\mathbf{x}}_S = (\tilde{\mathbf{v}}, \tilde{p}_f)^T$. Here the subscript S stands for Stokes.

According to the splitting up of the vectors of unknowns $\mathbf{x}_B$ and $\mathbf{x}_S$, we introduce the following number of grid nodes for the separate parts of the domains Ω_p and Ω_f:

Number of nodes in Ω_p:
in $\Omega_p\backslash\partial\Omega_p$: $\mathring{N}_p := (N_{px}-1)\,(N_y-1)\,(N_z-1)$
on $\partial\Omega_p\backslash\Gamma$: $\hat{N}_p := (N_y+1)(N_z+1) + 2(N_{px}-1)(N_z+1) + 2(N_{px}-1)(N_y-1)$
on Γ_p: $\tilde{N}_p := (N_y+1)(N_z+1)$

Number of nodes in Ω_f:
in $\Omega_f\backslash\partial\Omega_f$: $\mathring{N}_f := (N_{fx}-1)\,(N_y-1)\,(N_z-1)$
on $\partial\Omega_f\backslash\Gamma$: $\hat{N}_f := (N_y+1)(N_z+1) + 2(N_{fx}-1)(N_z+1) + 2(N_{fx}-1)(N_y-1)$
on Γ_f: $\tilde{N}_f := (N_y+1)(N_z+1)$

In the case of matching grids, it holds $\tilde{N} := \tilde{N}_p = \tilde{N}_f$.

Collecting the discretised Biot equations (4.1.1a) - (4.1.1d), the discretised Stokes equations (4.2.1a) - (4.2.1d) and the discretised transmission conditions (4.3.2a) - (4.3.2h), we obtain a system of equations of the following structure:

$$\left(\begin{array}{ccc|ccc} \mathring{B} & \mathring{B}_{\partial\Omega_p\backslash\Gamma} & \mathring{B}_{\Gamma_p} & \mathbf{0} & \mathbf{0} & \mathbf{0} \\ \hat{B}_{\Omega_p\backslash\partial\Omega_p} & \hat{B} & \mathbf{0} & \mathbf{0} & \mathbf{0} & \mathbf{0} \\ T^B_{\Omega_p\backslash\partial\Omega_p} & T^B_{\partial\Omega_p\backslash\Gamma} & T^B_{\Gamma_p} & T^B_{\Omega_f\backslash\partial\Omega_f} & T^B_{\partial\Omega_f\backslash\Gamma} & T^B_{\Gamma_f} \\ \hline \mathbf{0} & \mathbf{0} & \mathbf{0} & \mathring{S} & \mathring{S}_{\partial\Omega_p\backslash\Gamma} & \mathring{S}_{\Gamma_f} \\ \mathbf{0} & \mathbf{0} & \mathbf{0} & \mathbf{0} & \hat{S} & \mathbf{0} \\ T^S_{\Omega_p\backslash\partial\Omega_p} & T^S_{\partial\Omega_p\backslash\Gamma} & T^S_{\Gamma_p} & \mathbf{0} & \mathbf{0} & T^S_{\Gamma_f} \end{array}\right) \begin{pmatrix} \mathring{\mathbf{x}}_B \\ \hat{\mathbf{x}}_B \\ \tilde{\mathbf{x}}_B \\ \mathring{\mathbf{x}}_S \\ \hat{\mathbf{x}}_S \\ \tilde{\mathbf{x}}_S \end{pmatrix} = \begin{pmatrix} \mathring{\mathbf{r}}_B \\ \hat{\mathbf{r}}_B \\ \mathbf{0} \\ \mathring{\mathbf{r}}_S \\ \hat{\mathbf{r}}_S \\ \mathbf{0} \end{pmatrix} . \qquad (4.4.1)$$

This system of equations contains all information for the entire domain Ω including the boundaries and the interface. The first two lines of the matrix correspond to the Biot equations (4.1.1a) - (4.1.1d). Due to the splitting of the unknowns ($\mathbf{x}_B = (\mathring{\mathbf{x}}_B, \hat{\mathbf{x}}_B, \tilde{\mathbf{x}}_B)^T$), we obtained the submatrices given above. These operators are defined as follows:

$$\mathring{B} : \mathbb{R}^{4\mathring{N}_p} \to \mathbb{R}^{4\mathring{N}_p}\,, \qquad \mathring{B}_{\partial\Omega_p\backslash\Gamma} : \mathbb{R}^{4\mathring{N}_p} \to \mathbb{R}^{4\hat{N}_p}\,, \quad \mathring{B}_{\Gamma_p} : \mathbb{R}^{4\mathring{N}_p} \to \mathbb{R}^{4\tilde{N}_p}\,,$$

$$\hat{B}_{\Omega_p\backslash\partial\Omega_p} : \mathbb{R}^{4\hat{N}_p} \to \mathbb{R}^{4\mathring{N}_p}\,, \quad \hat{B} : \mathbb{R}^{4\hat{N}_p} \to \mathbb{R}^{4\hat{N}_p}\,.$$

The third line of system (4.4.1) contains the continuity of tractions and the pressure jump transmission conditions (4.3.2d) - (4.3.2f) and (4.3.2h). The operators are defined in the following way:

$$\begin{aligned} &T^B_{\Omega_p\backslash\partial\Omega_p} : \mathbb{R}^{4\tilde{N}_p} \to \mathbb{R}^{4\mathring{N}_p}\,, \quad T^B_{\partial\Omega_p\backslash\Gamma} : \mathbb{R}^{4\tilde{N}_p} \to \mathbb{R}^{4\hat{N}_p}\,, \quad T^B_{\Gamma_p} : \mathbb{R}^{4\tilde{N}_p} \to \mathbb{R}^{4\tilde{N}_p}\,, \\ &T^B_{\Omega_f\backslash\partial\Omega_f} : \mathbb{R}^{4\tilde{N}_p} \to \mathbb{R}^{4\mathring{N}_f}\,, \quad T^B_{\partial\Omega_f\backslash\Gamma} : \mathbb{R}^{4\tilde{N}_p} \to \mathbb{R}^{4\hat{N}_f}\,, \quad T^B_{\Gamma_f} : \mathbb{R}^{4\tilde{N}_p} \to \mathbb{R}^{3\tilde{N}_f}\,. \end{aligned} \tag{4.4.2}$$

Line four and five contain the Stokes equations (4.2.1a) - (4.2.1d) with the operators

$$\begin{aligned} &\mathring{S} : \mathbb{R}^{4\mathring{N}_f} \to \mathbb{R}^{4\mathring{N}_f}\,, \quad \mathring{S}_{\partial\Omega_p\backslash\Gamma} : \mathbb{R}^{4\mathring{N}_f} \to \mathbb{R}^{4\hat{N}_f}\,, \quad \mathring{S}_{\Gamma_f} : \mathbb{R}^{4\mathring{N}_f} \to \mathbb{R}^{3\tilde{N}_f}\,, \\ &\hat{S} : \mathbb{R}^{4\hat{N}_f} \to \mathbb{R}^{4\hat{N}_f}\,, \end{aligned}$$

and the last line corresponds to the mass conservation equations (4.3.2a) - (4.3.2c) with operators defined in the following way:

$$\begin{aligned} &T^S_{\Omega_p\backslash\partial\Omega_p} : \mathbb{R}^{3\tilde{N}_f} \to \mathbb{R}^{4\mathring{N}_p}\,, \quad T^S_{\partial\Omega_p\backslash\Gamma} : \mathbb{R}^{3\tilde{N}_f} \to \mathbb{R}^{4\hat{N}_p}\,, \quad T^S_{\Gamma_p} : \mathbb{R}^{3\tilde{N}_f} \to \mathbb{R}^{4\tilde{N}_p}\,, \\ &T^S_{\Gamma_f} : \mathbb{R}^{3\tilde{N}_f} \to \mathbb{R}^{3\tilde{N}_f}\,. \end{aligned} \tag{4.4.3}$$

System (4.4.1) is organised in such a way that the second quadrant contains the Biot equations with sufficient boundary conditions. The Stokes equations with sufficient boundary conditions are contained in the fourth quadrant. The first and third quadrant represent the coupling of both systems. Sufficient boundary conditions means that the system is well-posed. Note that the $\mathbf{0}$'s in this system are not all of the same size. They are in general rectangular matrices. Their size can be concluded from the surrounding operators. The vector on the right hand side has also been split into internal and outer boundary values.

The matrices resulting from the discretisation of the Biot poroelasticity equations

The Biot model consists of four equations and has four unknowns (u_x, u_y, u_z, p_p). Thus, the size of the matrix $\mathring{B}$ is $4\mathring{N}_p \times 4\mathring{N}_p$. Define operators

$$\mathring{B}_{IJ} : \mathbb{R}^{\mathring{N}_p} \to \mathbb{R}^{\mathring{N}_p},\ I = 1, 2, 3, 4,\ J = u_x, u_y, u_z, p_p\,.$$

The first index of $\mathring{B}$ indicates which equation of the Biot model the operator belongs to and the second index shows which variables it acts on. Thus, $\mathring{B}$ can be written as:

$$\mathring{B} = \begin{pmatrix} \mathring{B}_{1u_x} & \mathring{B}_{1u_y} & \mathring{B}_{1u_z} & \mathring{B}_{1p_p} \\ \mathring{B}_{2u_x} & \mathring{B}_{2u_y} & \mathring{B}_{2u_z} & \mathring{B}_{2p_p} \\ \mathring{B}_{3u_x} & \mathring{B}_{3u_y} & \mathring{B}_{3u_z} & \mathring{B}_{3p_p} \\ \mathring{B}_{4u_x} & \mathring{B}_{4u_y} & \mathring{B}_{4u_z} & \mathring{B}_{4p_p} \end{pmatrix}.$$

As an example we show the structure of $\mathring{B}_{1u_x}$. It contains the coefficients of the first discretised Biot equation (4.1.1a) that act on the displacements in x-direction $\mathring{u}_x$ of all internal nodes. It has the following structure:

$$\mathring{B}_{1u_x} = \begin{pmatrix} \mathring{B}^{\text{d}}_{1u_x} & \mathring{B}^{\text{dj+}}_{1u_x} & \mathbf{0} & \mathring{B}^{\text{dk+}}_{1u_x} & \mathbf{0} \\ \mathring{B}^{\text{dj-}}_{1u_x} & \ddots & \ddots & \ddots & \ddots \\ \mathbf{0} & \ddots & \ddots & \ddots & \ddots \\ \mathring{B}^{\text{dk-}}_{1u_x} & \ddots & \ddots & \ddots & \ddots \\ \mathbf{0} & \ddots & \ddots & \ddots & \ddots \end{pmatrix}. \tag{4.4.4}$$

All submatrices are of the size $(N_{px}-1)(N_{px}-1)$. From the discretisation of the first Biot equation (4.1.1a) we get the elements of the submatrices above. For clearness of the representation of the submatrices, we introduce some variables:

$$\chi_{\mu\xi\zeta} := \frac{\mu}{h_{p\xi}h_{p\zeta}}\,, \quad \gamma_{\xi\zeta} := \frac{\lambda+2\mu}{h_{p\xi}h_{p\zeta}}\,, \quad \beta_{\xi} := 2\gamma_{\xi\xi} + 2\chi_{\mu\zeta\zeta} + 2\chi_{\mu\upsilon\upsilon}\,, \quad \xi \neq \zeta \neq \upsilon \tag{4.4.5}$$

with $\xi, \zeta, \upsilon = x, y, z$.

The diagonal blocks $\mathring{B}^{\text{d}}_{1u_x}$ of the matrix $\mathring{B}_{1u_x}$ (4.4.4) have three-band diagonal structure:

$$\mathring{B}^{\text{d}}_{1u_x} = \begin{pmatrix} \beta_x & -\gamma_{xx} & & \mathbf{0} \\ -\gamma_{xx} & \ddots & \ddots & \\ & \ddots & \ddots & \ddots \\ \mathbf{0} & & \ddots & \ddots \end{pmatrix}.$$

The off-diagonal matrices $\mathring{B}^{\text{dj+}}_{1u_x}$, $\mathring{B}^{\text{dj-}}_{1u_x}$, $\mathring{B}^{\text{dk+}}_{1u_x}$ and $\mathring{B}^{\text{dk-}}_{1u_x}$ of the matrix $\mathring{B}_{1u_x}$ are all diagonal matrices:

$$\mathring{B}^{\text{dj+}}_{1u_x} = \mathring{B}^{\text{dj-}}_{1u_x} = -\chi_{\mu yy}\mathbf{I}_{N_{px}-1}\,, \qquad \mathring{B}^{\text{dk+}}_{1u_x} = \mathring{B}^{\text{dk-}}_{1u_x} = -\chi_{\mu zz}\mathbf{I}_{N_{px}-1}\,,$$

where $\mathbf{I}_{N_{px}-1}$ is the unit matrix of size $(N_{px}-1)\times(N_{px}-1)$.

This notation shows the structure of the matrices for internal nodes. Internal grid nodes which lie next to the outer boundary of Ω_p are connected to it. These values enter the matrix $\mathring{B}_{\partial\Omega_p\backslash\Gamma}$:

$$\mathring{B}_{\partial\Omega_p\backslash\Gamma} := \begin{pmatrix} \mathring{B}_{\partial\Omega_p\backslash\Gamma,1u_x} & \mathring{B}_{\partial\Omega_p\backslash\Gamma,1u_y} & \mathring{B}_{\partial\Omega_p\backslash\Gamma,1u_z} & \mathring{B}_{\partial\Omega_p\backslash\Gamma,1p_p} \\ \mathring{B}_{\partial\Omega_p\backslash\Gamma,2u_x} & \mathring{B}_{\partial\Omega_p\backslash\Gamma,2u_y} & \mathring{B}_{\partial\Omega_p\backslash\Gamma,2u_z} & \mathring{B}_{\partial\Omega_p\backslash\Gamma,2p_p} \\ \mathring{B}_{\partial\Omega_p\backslash\Gamma,3u_x} & \mathring{B}_{\partial\Omega_p\backslash\Gamma,3u_y} & \mathring{B}_{\partial\Omega_p\backslash\Gamma,3u_z} & \mathring{B}_{\partial\Omega_p\backslash\Gamma,3p_p} \\ \mathbf{0} & \mathring{B}_{\partial\Omega_p\backslash\Gamma,4u_y} & \mathring{B}_{\partial\Omega_p\backslash\Gamma,4u_z} & \mathring{B}_{\partial\Omega_p\backslash\Gamma,4p_p} \end{pmatrix}.$$

There is no entry in the lower left corner, because we only have a forward derivative of u_x with respect to x in the fourth discrete Biot equation. Remember that in our example the outer boundaries lie at the top, bottom, north, south and west wall of Ω_p. Thus, the term $\Delta_{x\bar{t}}\, u_{x(i,j,k)}$ causes an entry into the matrix $\mathring{B}_{\Gamma_p}$, but not into the matrix $\mathring{B}_{\partial\Omega_p\backslash\Gamma}$, since the interface is located at the east wall of Ω_p. With the same considerations for all unknowns and equations, one obtains the structure of $\mathring{B}_{\Gamma_p}$:

$$\mathring{B}_{\Gamma_p} := \begin{pmatrix} \tilde{B}_{\Gamma_p,1u_x} & \tilde{B}_{\Gamma_p,1u_y} & \tilde{B}_{\Gamma_p,1u_z} & \mathbf{0} \\ \tilde{B}_{\Gamma_p,2u_x} & \tilde{B}_{\Gamma_p,2u_y} & \mathbf{0} & \mathbf{0} \\ \tilde{B}_{\Gamma_p,3u_x} & \mathbf{0} & \tilde{B}_{\Gamma_p,3u_z} & \mathbf{0} \\ \tilde{B}_{\Gamma_p,4u_x} & \mathbf{0} & \mathbf{0} & \tilde{B}_{\Gamma_p,4p_p} \end{pmatrix}.$$

With similar considerations one obtains the structure of the matrices $\hat{B}_{\Omega_p\backslash\partial\Omega_p}$ and $\mathring{B}$. They are both fully occupied because at each wall we have a Neumann and a Dirichlet boundary condition. We refrain from writing down the structure of further submatrices, because we want to concentrate on the matrices of the transmission conditions.

The matrices resulting from the discretisation of the Stokes equations

The structure of the matrices arising from the discretisation of the Stokes equations can be derived similarly as the ones for the Biot equations. $\mathring{S}$ acts on the internal values of the four variables (v_x, v_y, v_z, p_f) and maps them onto the interior of Ω_f. Thus,

$$\mathring{S} = \begin{pmatrix} \mathring{S}_{1v_x} & \mathbf{0} & \mathbf{0} & \mathring{S}_{1p_f} \\ \mathbf{0} & \mathring{S}_{2v_y} & \mathbf{0} & \mathring{S}_{2p_f} \\ \mathbf{0} & \mathbf{0} & \mathring{S}_{3v_z} & \mathring{S}_{3p_f} \\ \mathring{S}_{4v_x} & \mathring{S}_{4v_y} & \mathring{S}_{4v_z} & \mathbf{0} \end{pmatrix} \quad \in \mathbb{R}^{4\mathring{N}_f \times 4\mathring{N}_f} ,$$

where all the submatrices are of size $\mathring{N}_f \times \mathring{N}_f$. Note that the matrices on the diagonal all look alike. We present the structure of $\mathring{S}_{2v_y}$ as an example:

$$\mathring{S}_{2v_y} = \begin{pmatrix} \mathring{S}^{\text{d}}_{2v_y} & \mathring{S}^{\text{dj+}}_{2v_y} & \mathbf{0} & \mathring{S}^{\text{dk+}}_{2v_y} & \mathbf{0} \\ \mathring{S}^{\text{dj-}}_{2v_y} & \ddots & \ddots & \ddots & \ddots \\ \mathbf{0} & \ddots & \ddots & \ddots & \ddots \\ \mathring{S}^{\text{dk-}}_{2v_y} & \ddots & \ddots & \ddots & \ddots \\ \mathbf{0} & \ddots & \ddots & \ddots & \ddots \end{pmatrix} . \tag{4.4.6}$$

All submatrices are of the size $(N_{fx} - 1) \times (N_{fx} - 1)$. For the representation of the submatrices of $\mathring{S}_{2v_y}$ we use similar variables as introduced above (4.4.5) and also define some additional ones:

$$\chi_{\eta\xi\zeta} := \frac{\eta}{h_{f\xi} h_{f\zeta}} , \quad \vartheta := \frac{\varrho}{h_t} + 2\chi_{\eta xx} + 2\chi_{\eta yy} + 2\chi_{\eta zz} , \quad \xi, \zeta = x, y, z .$$

Then, the diagonal blocks $\mathring{S}^{d}_{2v_y}$ of $\mathring{S}_{2v_y}$ are

$$\mathring{S}^{d}_{2v_y} = \begin{pmatrix} \vartheta & -\chi_{\eta xx} & & \mathbf{0} \\ -\chi_{\eta xx} & \ddots & \ddots & \\ & \ddots & \ddots & \ddots \\ \mathbf{0} & & \ddots & \ddots \end{pmatrix} .$$

The off-diagonal matrices of $\mathring{S}_{2v_y}$ are all diagonal matrices:

$$\mathring{S}^{\text{dj+}}_{2v_y} = \mathring{S}^{\text{dj-}}_{2v_y} = -\chi_{\eta yy} \mathbf{I}_{(N_{fx}-1)} , \qquad \mathring{S}^{\text{dk+}}_{2v_y} = \mathring{S}^{\text{dk-}}_{2v_y} = -\chi_{\eta zz} \mathbf{I}_{(N_{fx}-1)} ,$$

where $\mathbf{I}_{(N_{fx}-1)}$ is the unit matrix of size $(N_{fx} - 1) \times (N_{fx} - 1)$. These matrices show the discretisation scheme for internal nodes. For nodes near the outer boundaries we get entries into the matrix $\mathring{S}_{\partial\Omega_p \setminus \Gamma}$ so that

$$\mathring{S}_{\partial\Omega_p \setminus \Gamma} = \begin{pmatrix} \mathring{S}_{\partial\Omega_p \setminus \Gamma, 1v_x} & \mathbf{0} & \mathbf{0} & \mathring{S}_{\partial\Omega_p \setminus \Gamma, 1p_f} \\ \mathbf{0} & \mathring{S}_{\partial\Omega_p \setminus \Gamma, 2v_y} & \mathbf{0} & \mathring{S}_{\partial\Omega_p \setminus \Gamma, 2p_f} \\ \mathbf{0} & \mathbf{0} & \mathring{S}_{\partial\Omega_p \setminus \Gamma, 3v_z} & \mathring{S}_{\partial\Omega_p \setminus \Gamma, 3p_f} \\ \mathring{S}_{\partial\Omega_p \setminus \Gamma, 4v_x} & \mathring{S}_{\partial\Omega_p \setminus \Gamma, 4v_y} & \mathring{S}_{\partial\Omega_p \setminus \Gamma, 4v_z} & \mathbf{0} \end{pmatrix} \quad \in \mathbb{R}^{4\mathring{N}_f \times 4\hat{N}_f} .$$

The structure of $\mathring{S}_{\Gamma_f}$, and $\hat{S}$ can be obtained by similar considerations.

The matrices resulting from the discretisation of the transmission conditions

In the last two sections we considered the operators resulting from the discretisation of the Biot and Stokes equations. Now we turn to the operators which stem from the discrete transmission conditions (4.3.2a) - (4.3.2h). As already mentioned above, the mass conservation equations are represented as

$$T^S_{\Omega_p\backslash\partial\Omega_p}\begin{pmatrix}\mathring{\mathbf{u}}\\ \mathring{p}_p\end{pmatrix}+T^S_{\partial\Omega_p\backslash\Gamma}\begin{pmatrix}\hat{\mathbf{u}}\\ \hat{p}_p\end{pmatrix}+T^S_{\Gamma_p}\begin{pmatrix}\tilde{\mathbf{u}}\\ \tilde{p}_p\end{pmatrix}+T^S_{\Gamma_f}\begin{pmatrix}\tilde{\mathbf{v}}\\ \tilde{p}_f\end{pmatrix}=\mathbf{0} \tag{4.4.7}$$

in system (4.4.1). Therefore, the number of rows of these matrices is $3\tilde{N}_f$, because we have three equations for the conservation of mass. The number of columns depends on the domain the values are mapped onto. See the definition of these operators (4.4.3). The continuity of tractions equations and the pressure jump condition are written as

$$\begin{aligned}T^B_{\Omega_p\backslash\partial\Omega_p}\begin{pmatrix}\mathring{\mathbf{u}}\\ \mathring{p}_p\end{pmatrix}+T^B_{\partial\Omega_p\backslash\Gamma}\begin{pmatrix}\hat{\mathbf{u}}\\ \hat{p}_p\end{pmatrix}+T^B_{\Gamma_p}\begin{pmatrix}\tilde{\mathbf{u}}\\ \tilde{p}_p\end{pmatrix}&\\ +T^B_{\Omega_f\backslash\partial\Omega_f}\begin{pmatrix}\mathring{\mathbf{v}}\\ \mathring{p}_f\end{pmatrix}+T^B_{\partial\Omega_f\backslash\Gamma}\begin{pmatrix}\hat{\mathbf{v}}\\ \hat{p}_f\end{pmatrix}+T^B_{\Gamma_f}\begin{pmatrix}\tilde{\mathbf{v}}\\ \tilde{p}_f\end{pmatrix}&=\mathbf{0}\,.\end{aligned} \tag{4.4.8}$$

These matrices all have $4\tilde{N}_p$ rows. For the number of columns see (4.4.2). As it is far too much to discuss all these operators, we restrict to the ones in (4.4.8). We will analyse their structure and show further details for all submatrices which are related to the unknowns in the fourth transmission condition (4.3.2d), which corresponds to the first line in these matrices.

First we study the operators in (4.4.8) in more detail. $T^B_{\Omega_p\backslash\partial\Omega_p}$ maps values from the interface nodes to the internal nodes of Ω_p. Thus, it has only entries for the variables u_x, u_y, u_z and p_p which have derivatives with respect to x. Thus,

$$T^B_{\Omega_p\backslash\partial\Omega_p}=\begin{pmatrix}T^B_{\Omega_p\backslash\partial\Omega_p,1u_x} & \mathbf{0} & \mathbf{0} & \mathbf{0}\\ \mathbf{0} & T^B_{\Omega_p\backslash\partial\Omega_p,2u_y} & \mathbf{0} & \mathbf{0}\\ \mathbf{0} & \mathbf{0} & T^B_{\Omega_p\backslash\partial\Omega_p,3u_z} & \mathbf{0}\\ \mathbf{0} & \mathbf{0} & \mathbf{0} & T^B_{\Omega_p\backslash\partial\Omega_p,4p_p}\end{pmatrix}\in\mathbb{R}^{4\tilde{N}_p\times 4\mathring{N}_p}\,. \tag{4.4.9}$$

If the nodes lie on the outer boundaries of the interface, the derivatives with respect to x result in entries in $T^B_{\partial\Omega_p\backslash\Gamma}$, which maps values from the interface nodes to the outer boundary of Ω_p:

$$T^B_{\partial\Omega_p\backslash\Gamma}=\begin{pmatrix}T^B_{\partial\Omega_p\backslash\Gamma,1u_x} & \mathbf{0} & \mathbf{0} & \mathbf{0}\\ \mathbf{0} & T^B_{\partial\Omega_p\backslash\Gamma,2u_y} & \mathbf{0} & \mathbf{0}\\ \mathbf{0} & \mathbf{0} & T^B_{\partial\Omega_p\backslash\Gamma,3u_z} & \mathbf{0}\\ \mathbf{0} & \mathbf{0} & \mathbf{0} & T^B_{\partial\Omega_p\backslash\Gamma,4p_p}\end{pmatrix}\in\mathbb{R}^{4\tilde{N}_p\times 4\hat{N}_p}\,. \tag{4.4.10}$$

It has the same structure as $T^B_{\Omega_p\backslash\partial\Omega_p}$.

The matrix $T^B_{\Gamma_p}$ contains all values which are mapped from the ”porous side” of the interface to the interface Γ_p itself. So, all values u_x, u_y, u_z and p_p that have index i in equation (4.3.2d):

$$T^B_{\Gamma_p} = \begin{pmatrix} T^B_{\Gamma_p,1u_x} & T^B_{\Gamma_p,1u_y} & T^B_{\Gamma_p,1u_z} & T^B_{\Gamma_p,1p_p} \\ T^B_{\Gamma_p,2u_x} & T^B_{\Gamma_p,2u_y} & \mathbf{0} & \mathbf{0} \\ T^B_{\Gamma_p,3u_x} & \mathbf{0} & T^B_{\Gamma_p,3u_z} & \mathbf{0} \\ \mathbf{0} & \mathbf{0} & \mathbf{0} & T^B_{\Gamma_p,4p_p} \end{pmatrix} \in \mathbb{R}^{4\tilde{N}_p \times 4\tilde{N}_p} . \tag{4.4.11}$$

Since the transmission conditions connect the values of the porous domain and the values of the fluid domain, we also have entries in $T^B_{\Omega_f\setminus\partial\Omega_f}$, $T^B_{\partial\Omega_f\setminus\Gamma}$ and $T^B_{\Gamma_f}$. $T^B_{\Omega_f\setminus\partial\Omega_f}$ maps values from Γ_p to the interior of Ω_f. So, we have entries where derivatives with respect to x are present for the variables v_x, v_y, v_z and p_f:

$$T^B_{\Omega_f\setminus\partial\Omega_f} = \begin{pmatrix} T^B_{\Omega_f\setminus\partial\Omega_f,1v_x} & \mathbf{0} & \mathbf{0} & \mathbf{0} \\ \mathbf{0} & T^B_{\Omega_f\setminus\partial\Omega_f,2v_y} & \mathbf{0} & \mathbf{0} \\ \mathbf{0} & \mathbf{0} & T^B_{\Omega_f\setminus\partial\Omega_f,3v_z} & \mathbf{0} \\ \mathbf{0} & \mathbf{0} & \mathbf{0} & \mathbf{0} \end{pmatrix} \in \mathbb{R}^{4\tilde{N}_p \times 4\mathring{N}_f} , \tag{4.4.12}$$

Values lying on the outer boundary of the interface, are mapped onto the outer boundary of Ω_f:

$$T^B_{\partial\Omega_f\setminus\Gamma} = \begin{pmatrix} T^B_{\partial\Omega_f\setminus\Gamma,1v_x} & \mathbf{0} & \mathbf{0} & \mathbf{0} \\ \mathbf{0} & T^B_{\partial\Omega_f\setminus\Gamma,2v_y} & \mathbf{0} & \mathbf{0} \\ \mathbf{0} & \mathbf{0} & T^B_{\partial\Omega_f\setminus\Gamma,3v_z} & \mathbf{0} \\ \mathbf{0} & \mathbf{0} & \mathbf{0} & \mathbf{0} \end{pmatrix} \in \mathbb{R}^{4\tilde{N}_p \times 4\hat{N}_f} , \tag{4.4.13}$$

Finally, equation (4.3.2d) also contains values which lie on the ”fluid side” of the interface. These values are contained in

$$T^B_{\Gamma_f} = \begin{pmatrix} T^B_{\Gamma_f,1v_x} & \mathbf{0} & \mathbf{0} & T^B_{\Gamma_f,1p_f} \\ T^B_{\Gamma_f,2v_x} & T^B_{\Gamma_f,2v_y} & \mathbf{0} & \mathbf{0} \\ T^B_{\Gamma_f,3v_x} & \mathbf{0} & T^B_{\Gamma_f,3v_z} & \mathbf{0} \\ \mathbf{0} & \mathbf{0} & \mathbf{0} & T^B_{\Gamma_f,4p_f} \end{pmatrix} \in \mathbb{R}^{4\tilde{N}_p \times 3\tilde{N}_f} . \tag{4.4.14}$$

Now we consider the first line in the above matrices (4.4.9) - (4.4.14) in more detail. The entry $T^B_{\Omega_p\setminus\partial\Omega_p,1u_x}$ in the first row of $T^B_{\Omega_p\setminus\partial\Omega_p}$ (4.4.9) results from the term $(1-\phi)(2\mu+\lambda)\frac{1}{h_{px}}(u_{x(i,j,k)} - u_{x(i-1,j,k)}))$ of equation (4.3.2d) and looks as follows:

$$T^B_{\Omega_p\setminus\partial\Omega_p,1u_x} = \begin{pmatrix} \mathbf{0} & \cdots & \cdots & \cdots & \mathbf{0} \\ T^{B*}_{\Omega_p\setminus\partial\Omega_p,1u_x} & \ddots & & & \vdots \\ \mathbf{0} & \ddots & \ddots & & \vdots \\ \vdots & \ddots & \ddots & \ddots & \vdots \\ \vdots & & \ddots & \ddots & \mathbf{0} \\ \vdots & & & \ddots & T^{B*}_{\Omega_p\setminus\partial\Omega_p,1u_x} \\ \mathbf{0} & \cdots & \cdots & \cdots & \mathbf{0} \end{pmatrix} \in \mathbb{R}^{\tilde{N}_p \times \mathring{N}_p}$$

with

$$T^{B*}_{\Omega_p\setminus\partial\Omega_p,1u_x} = \begin{pmatrix} T^{B,1}_{\Omega_p\setminus\partial\Omega_p,1u_x} & \dots & T^{B,N_y-1}_{\Omega_p\setminus\partial\Omega_p,1u_x} \end{pmatrix} \in \mathbb{R}^{(N_y+1)\times(N_y-1)(N_{px}-1)}\,,$$

where

$$T^{B,K}_{\Omega_p\setminus\partial\Omega_p,1u_x} = -(1-\phi)\frac{2\mu+\lambda}{h_{px}} \begin{pmatrix} 0 & \dots & \dots & 0 \\ \vdots & & & \vdots \\ 0 & \dots & \dots & 0 \\ 0 & \dots & 0 & 1 \\ 0 & \dots & \dots & 0 \\ \vdots & & & \vdots \\ 0 & \dots & \dots & 0 \end{pmatrix} \in \mathbb{R}^{(N_y+1)\times(N_{px}-1)}\,, K = 1,\dots,N_y-1\,.$$

The entry '1' is always located in the last column and in row $K+1$, $K = 1,\dots,N_y-1$.

The matrix $T^B_{\partial\Omega_p\setminus\Gamma,1u_x}$ in the first row of $T^B_{\partial\Omega_p\setminus\Gamma}$ (4.4.10) has the following structure:

$$T^B_{\partial\Omega_p\setminus\Gamma,1u_x} = \begin{pmatrix} T^{B*}_{\partial\Omega_p\setminus\Gamma,1u_x} & & & & \mathbf{0} \\ & T^{B**}_{\partial\Omega_p\setminus\Gamma,1u_x} & & & \\ & & \ddots & & \\ & & & T^{B**}_{\partial\Omega_p\setminus\Gamma,1u_x} & \\ \mathbf{0} & & & & T^{B*}_{\partial\Omega_p\setminus\Gamma,1u_x} \end{pmatrix} \tag{4.4.15}$$

with

$$T^{B*}_{\partial\Omega_p\setminus\Gamma,1u_x} = \begin{pmatrix} T^{B*,1}_{\partial\Omega_p\setminus\Gamma,1u_x} & \dots & T^{B*,N_y+1}_{\partial\Omega_p\setminus\Gamma,1u_x} \end{pmatrix} \in \mathbb{R}^{(N_y+1)\times N_{px}(N_y+1)}\,,$$

where

$$T^{B*,K}_{\partial\Omega_p\setminus\Gamma,1u_x} = -(1-\phi)\frac{2\mu+\lambda}{h_{px}} \begin{pmatrix} 0 & \dots & \dots & 0 \\ \vdots & & & \vdots \\ 0 & \dots & \dots & 0 \\ 0 & \dots & 0 & 1 \\ 0 & \dots & \dots & 0 \\ \vdots & & & \vdots \\ 0 & \dots & \dots & 0 \end{pmatrix} \in \mathbb{R}^{(N_y+1)\times N_{px}}\,, K = 1,\dots,N_y+1\,. \tag{4.4.16}$$

The entry '1' is always located in the last column and in row K, $K = 1,\dots,N_y+1$. $T^{B**}_{\partial\Omega_p\setminus\Gamma,1u_x}$ is defined as

$$T^{B**}_{\partial\Omega_p\setminus\Gamma,1u_x} = (T^{B*,1}_{\partial\Omega_p\setminus\Gamma,1u_x}\ \underbrace{0\ \dots\ 0}_{N_y-1}\ T^{B*,N_y+1}_{\partial\Omega_p\setminus\Gamma,1u_x}) \in \mathbb{R}^{(N_y+1)\times(2N_{px}+(N_y-1))}\,.$$

The matrix $T^B_{\Gamma_p}$ (4.4.11) contains coefficients for all unknowns u_x, u_y, u_z and p_p that have an index i in equation (4.3.2d). Thus,

$$T^B_{\Gamma_p,1u_x} = (1-\phi)\frac{2\mu+\lambda}{h_{px}}\,\mathbf{I}_{\tilde{N}_p}\,.$$

The terms $(1-\phi)\lambda\,\Delta_y\,u_y$ and $(1-\phi)\lambda\,\Delta_z\,u_z$ are discretised by central differences in equation (4.3.2d). Thus,

$$T^{B}_{\Gamma_p,1u_y} = \begin{pmatrix} T^{B*}_{\Gamma_p,1u_y} & & \mathbf{0} \\ & \ddots & \\ \mathbf{0} & & T^{B*}_{\Gamma_p,1u_y} \end{pmatrix} \in \mathbb{R}^{\tilde{N}_p \times \tilde{N}_p}$$

with

$$T^{B*}_{\Gamma_p,1u_y} = \frac{1}{2}(1-\phi)\frac{\lambda}{h_y} \begin{pmatrix} -2 & 1 & & & \mathbf{0} \\ -1 & 0 & 1 & & \\ & \ddots & \ddots & \ddots & \\ & & -1 & 0 & 1 \\ \mathbf{0} & & & -1 & 2 \end{pmatrix} \in \mathbb{R}^{(N_y+1)\times(N_y+1)} .$$

$T^{B}_{\Gamma_p,1u_z}$ is defined as

$$T^{B}_{\Gamma_p,1u_z} = (1-\phi)\frac{\lambda}{2h_z} \begin{pmatrix} -2\mathbf{I}_{N_y+1} & \mathbf{I}_{N_y+1} & & & 0 \\ -\mathbf{I}_{N_y+1} & \mathbf{0} & \mathbf{I}_{N_y+1} & & \\ & \ddots & \ddots & \ddots & \\ & & -\mathbf{I}_{N_y+1} & \mathbf{0} & \mathbf{I}_{N_y+1} \\ 0 & & & -\mathbf{I}_{N_y+1} & 2\mathbf{I}_{N_y+1} \end{pmatrix} \in \mathbb{R}^{\tilde{N}_p \times \tilde{N}_p} .$$

The term $-\phi p_p$ in the continuity of tractions equation (4.3.2d) is represented by $T^{B}_{\Gamma_p,1p_p} = -\phi\mathbf{I}_{\tilde{N}_p}$.

Now we turn to the parts of the transmission conditions which couple the Biot equations and the Stokes equations in system (4.4.1). For the first continuity of tractions equation, these are the matrices $T^{B}_{\Omega_f\setminus\partial\Omega_f,1v_x}$, $T^{B}_{\partial\Omega_f\setminus\Gamma,1v_x}$, $T^{B}_{\Gamma_f,1v_x}$ and $T^{B}_{\Gamma_f,1p_f}$ in equations (4.4.12) - (4.4.14). $T^{B}_{\Omega_f\setminus\partial\Omega_f,1v_x}$ maps values from Γ_p into the interior of Ω_f. So, it contains coefficients for the x-derivative of the variable v_x:

$$T^{B}_{\Omega_f\setminus\partial\Omega_f,1v_x} = \begin{pmatrix} \mathbf{0} & \dots & \dots & \dots & \mathbf{0} \\ T^{B*}_{\Omega_f\setminus\partial\Omega_f,1v_x} & \ddots & & & \vdots \\ \mathbf{0} & \ddots & \ddots & & \vdots \\ \vdots & \ddots & \ddots & \ddots & \vdots \\ \vdots & & \ddots & \ddots & \mathbf{0} \\ \vdots & & & \ddots & T^{B*}_{\Omega_f\setminus\partial\Omega_f,1v_x} \\ \mathbf{0} & \dots & \dots & \dots & \mathbf{0} \end{pmatrix} \in \mathbb{R}^{\tilde{N}_p \times \mathring{N}_f}$$

with

$$T^{B*}_{\Omega_f\setminus\partial\Omega_f,1v_x} = \begin{pmatrix} T^{B,1}_{\Omega_f\setminus\partial\Omega_f,1v_x} & \dots & T^{B,N_y-1}_{\Omega_f\setminus\partial\Omega_f,1v_x} \end{pmatrix} \in \mathbb{R}^{(N_y+1)\times(N_y-1)(N_{fx}-1)} ,$$

where

$$T^{B,K}_{\Omega_f\backslash\partial\Omega_f,1v_x} = 2\frac{\eta}{h_{fx}}\begin{pmatrix} 0 & \dots & \dots & 0 \\ \vdots & & & \vdots \\ 0 & \dots & \dots & 0 \\ 1 & 0 & \dots & 0 \\ 0 & \dots & \dots & 0 \\ \vdots & & & \vdots \\ 0 & \dots & \dots & 0 \end{pmatrix} \in \mathbb{R}^{(N_y+1)\times(N_{fx}-1)}\,, K = 1,\dots,N_y-1\,.$$

This matrix looks similar to (4.4.16). But here, in $T^{B,K}_{\Omega_f\backslash\partial\Omega_f,1v_x}$ the entry ’1’ lies in the first column, but also in row $K+1,\ K=1,\dots,N_y-1$. This difference occurs, because the interface is located on the east wall of Ω_p, but on the west wall of Ω_f.

The same appears for the matrix $T^B_{\partial\Omega_f\backslash\Gamma,1v_x}$. Its structure is similar to the structure of $T^B_{\partial\Omega_p\backslash\Gamma,1u_x}$ (4.4.15):

$$T^B_{\partial\Omega_f\backslash\Gamma,1v_x} = \begin{pmatrix} T^{B*}_{\partial\Omega_f\backslash\Gamma,1v_x} & & & & \mathbf{0} \\ & T^{B**}_{\partial\Omega_f\backslash\Gamma,1v_x} & & & \\ & & \ddots & & \\ & & & T^{B**}_{\partial\Omega_f\backslash\Gamma,1v_x} & \\ \mathbf{0} & & & & T^{B*}_{\partial\Omega_f\backslash\Gamma,1v_x} \end{pmatrix}$$

with

$$T^{B*}_{\partial\Omega_f\backslash\Gamma,1v_x} = \left(T^{B,1}_{\partial\Omega_f\backslash\Gamma,1v_x} \cdots T^{B,N_y-1}_{\partial\Omega_f\backslash\Gamma,1v_x}\right) \in \mathbb{R}^{(N_y+1)\times N_{fx}(N_y+1)}\,,$$

where

$$T^{B,K}_{\partial\Omega_f\backslash\Gamma,1v_x} = 2\frac{\eta}{h_{fx}}\begin{pmatrix} 0 & \dots & \dots & 0 \\ \vdots & & & \vdots \\ 0 & \dots & \dots & 0 \\ 1 & 0 & \dots & 0 \\ 0 & \dots & \dots & 0 \\ \vdots & & & \vdots \\ 0 & \dots & \dots & 0 \end{pmatrix} \in \mathbb{R}^{(N_y+1)\times N_{fx}}\,, K = 1,\dots,N_y+1\,.$$

The entry ’1’ is always located in the first column and in row $K,\ K=1,\dots,N_y+1$. $T^{B**}_{\partial\Omega_f\backslash\Gamma,1v_x}$ is defined as

$$T^{B**}_{\partial\Omega_f\backslash\Gamma,1v_x} = (T^{B,1}_{\partial\Omega_f\backslash\Gamma,1v_x}\ \underbrace{0\dots0}_{N_y-1}\ T^{B,N_y-1}_{\partial\Omega_f\backslash\Gamma,1v_x}) \in \mathbb{R}^{(N_y+1)\times(2N_{fx}+(N_y-1))}\,.$$

Values which are mapped from the ”porous side” of the interface to the ”fluid side” of the interface are contained in matrix $T^B_{\Gamma_f}$ (4.4.14). For the first equation of the continuity of tractions, the entries are simply diagonal matrices of dimension $\tilde{N}$:

$$T^B_{\Gamma_f,1v_x} = 2\frac{\eta}{h_{fx}}\mathbf{I}_{\tilde{N}} \quad T^B_{\Gamma_f,1p_f} = -\mathbf{I}_{\tilde{N}}\,.$$

Chapter 5

The discrete coupled Biot-Stokes system on non-matching grids

In the previous chapter we explained the discretisation of the Biot-Stokes system of equations on matching node-based grids. In this chapter we expand that approach and consider the Biot-Stokes system on non-matching meshes. With regard to the software we use for the solution of this problem (see section 6.3), we consider a cell-centred grid in the fluid region and a staggered grid in the porous domain.

First, we introduce the notation for grid points of a staggered grid. Then, the Biot model is discretised by means of the finite volume (FV) method. Next, we discretise the Stokes equations on a cell-centred grid. For the discretisation of the transmission conditions we have to introduce an additional grid on the interface, in order to have some determined points, where the information between the fluid region and the porous region is exchanged. The coupling between this additional grid and the grid in the porous medium and in the fluid region, respectively, is done via a matching function. In our case, we choose bilinear interpolation.

As in the chapter before we introduce an operator notation for the Stokes equations, the Biot system and the transmission conditions and present it in detail for several equations. Due to the different grids and the additionally introduced matching functions, the discretisation is more difficult than in chapter 4. At the end of this chapter a simple example is given.

In order to distinguish between the values on the three different grids, we use the following index notation throughout this chapter: $(\mathtt{i},\mathtt{j},\mathtt{k})$ denotes values on the cell-centred grid (i.e. in Ω_f), (i,j,k) denotes values on the staggered grid (i.e. in Ω_p) and $(\mathcal{I},\mathcal{J},\mathcal{K})$ denotes values on the interface grid (i.e. on Γ).

5.1 Discretisation of the Biot poroelasticity system on a staggered grid

In order to overcome stability difficulties, the poroelasticity solver we use (”Poro3D”, for a description see 6.3), is based on a staggered grid. Stability difficulties often arise when the Biot model is discretised on a collocated grid. Therefore, the use of staggered grids was proposed in

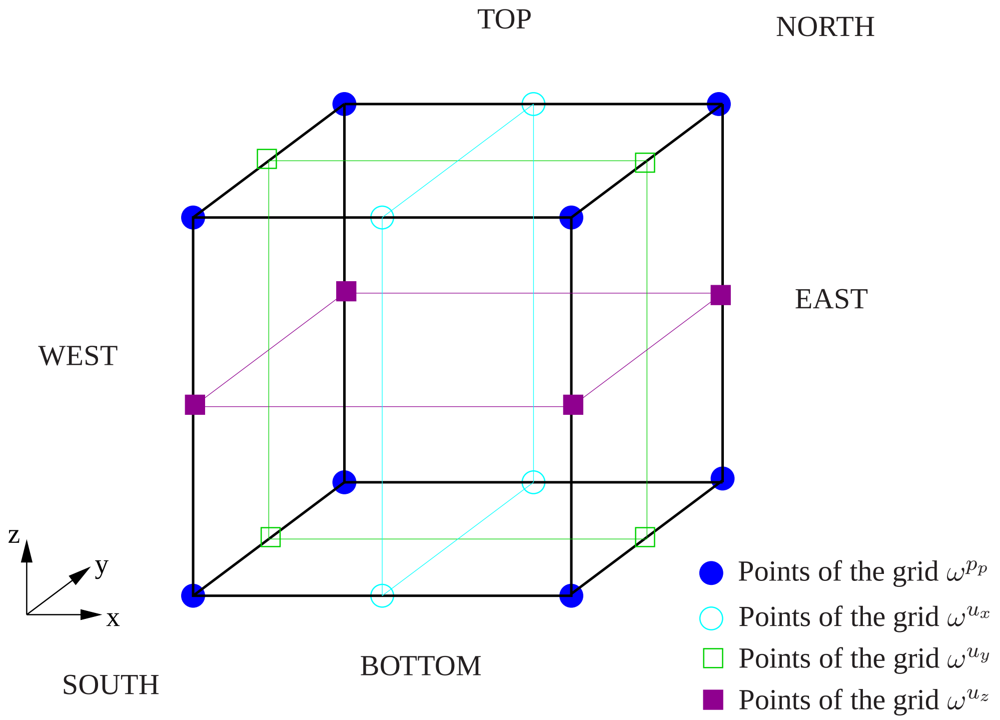

Figure 5.1: Grid cell of a three-dimensional staggered grid.

[65]. In [46], the Biot model on staggered grid is investigated for multilayered domains. As shown in [46], there are the following four types of grid points on the staggered grid we use:

$$
\begin{aligned}
\omega^{u_x}_{sg} = \omega^{u_x}_{sg,h_{px},h_{py},h_{pz}} &= \{(x_{i+1/2}, y_j, z_k) = ((i-1/2)h_{px}, (j-1)h_{py}, (k-1)h_{pz}),\\
&\quad\ i = 1, ..., N_{px},\ j = 1, ..., N_{py}+1,\ k = 1, ..., N_{pz}+1\},\\
\omega^{u_y}_{sg} = \omega^{u_y}_{sg,h_{px},h_{py},h_{pz}} &= \{(x_i, y_{j+1/2}, z_k) = ((i-1)h_{px}, (j-1/2)h_{py}, (k-1)h_{pz}),\\
&\quad\ i = 1, ..., N_{px}+1,\ j = 1, ..., N_{py},\ k = 1, ..., N_{pz}+1\},\\
\omega^{u_z}_{sg} = \omega^{u_z}_{sg,h_{px},h_{py},h_{pz}} &= \{(x_i, y_j, z_{k+1/2}) = ((i-1)h_{px}, (j-1)h_{py}, (k-1/2)h_{pz}),\\
&\quad\ i = 1, ..., N_{px}+1,\ j = 1, ..., N_{py}+1,\ k = 1, ..., N_{pz}\},\\
\omega^{p_p}_{sg} = \omega^{p_p}_{sg,h_{px},h_{py},h_{pz}} &= \{(x_i, y_j, z_k) = ((i-1)h_{px}, (j-1)h_{py}, (k-1)h_{pz}),\\
&\quad\ i = 1, ..., N_{px}+1,\ j = 1, ..., N_{py}+1,\ k = 1, ..., N_{pz}+1\}.
\end{aligned}
$$

This implies that the pressure points p_p are located at the corners of the grid cells. The displacements are situated on the respective edges. A three-dimensional grid cell with the corresponding location of the grid points is depicted in figure 5.1.

For the time discretisation we use the following grid with step size h_t:

$$\omega^t = \{t_\tau : t_\tau = \tau h_t, \tau = 1, ..., t_{\text{end}}\}\ . \tag{5.1.1}$$

Based on these grids, the following grid functions for the pressure and the displacements are introduced:

$$\begin{array}{rclcll} u_{x(i+1/2,j,k)} & := & u^{\tau}_{x(i+1/2,j,k)} & = & u_x(x_{i+1/2}, y_j, z_k, t_\tau) & \text{on} \quad \omega^{u_x}_{sg} \times \omega^t \\ u_{y(i,j+1/2,k)} & := & u^{\tau}_{y(i,j+1/2,k)} & = & u_y(x_i, y_{j+1/2}, z_k, t_\tau) & \text{on} \quad \omega^{u_y}_{sg} \times \omega^t \\ u_{z(i,j,k+1/2)} & := & u^{\tau}_{z(i,j,k+1/2)} & = & u_z(x_i, y_j, z_{k+1/2}, t_\tau) & \text{on} \quad \omega^{u_z}_{sg} \times \omega^t \\ p_{p(i,j,k)} & := & p^{\tau}_{p(i,j,k)} & = & p_p(x_i, y_j, z_k, t_\tau) & \text{on} \quad \omega^{p_p}_{sg} \times \omega^t \,. \end{array} \tag{5.1.2}$$

The components of the discrete stress tensor are located at the following grid points:

$$\begin{array}{rcll} \sigma_{p,xx} & := & \sigma^{\tau}_{p,xx(i,j,k)} & = \sigma_{p,xx}(x_i, y_j, z_k, t_\tau) \\ \sigma_{p,yy} & := & \sigma^{\tau}_{p,yy(i,j,k)} & = \sigma_{p,yy}(x_i, y_j, z_k, t_\tau) \\ \sigma_{p,zz} & := & \sigma^{\tau}_{p,zz(i,j,k)} & = \sigma_{p,zz}(x_i, y_j, z_k, t_\tau) \\ \sigma_{p,xy} & := & \sigma^{\tau}_{p,xy(i+1/2,j+1/2,k)} & = \sigma_{p,xy}(x_{i+1/2}, y_{j+1/2}, z_k, t_\tau) \\ \sigma_{p,xz} & := & \sigma^{\tau}_{p,xz(i+1/2,j,k+1/2)} & = \sigma_{p,xz}(x_{i+1/2}, y_j, z_{k+1/2}, t_\tau) \\ \sigma_{p,yz} & := & \sigma^{\tau}_{p,yz(i,j+1/2,k+1/2)} & = \sigma_{p,yz}(x_i, y_{j+1/2}, z_{k+1/2}, t_\tau) \,. \end{array} \tag{5.1.3}$$

For an ease of notation, we introduce difference operators for forward and backward finite differences on a uniform mesh:

$$\begin{array}{rcl} \Delta_x \, p_{p(i,j,k)} & := & \frac{p_{p(i+1,j,k)} - p_{p(i,j,k)}}{h_{px}} \,, \\ \Delta_{\overline{x}} \, p_{p(i,j,k)} & := & \frac{p_{p(i,j,k)} - p_{p(i-1,j,k)}}{h_{px}} \,, \\ \Delta_x \, u_{x(i,j,k)} & := & \frac{u_{x(i+3/2,j,k)} - u_{x(i+1/2,j,k)}}{h_{px}} \,, \\ \Delta_{\overline{x}} \, u_{x(i,j,k)} & := & \frac{u_{x(i+1/2,j,k)} - u_{x(i-1/2,j,k)}}{h_{px}} \,, \\ \Delta_{xy} \, u_{x(i,j,k)} & := & \frac{u_{x(i+3/2,j+1,k)} - u_{x(i+3/2,j,k)} - u_{x(i+1/2,j+1,k)} + u_{x(i+1/2,j,k)}}{h_{px} h_{py}} \,. \end{array}$$

Here, we have omitted the superscript τ. That means that we consider the variables at the current time t_τ. The other finite differences are defined analogously.
For the time discretisation we introduce the backward finite differences

$$\Delta_{\overline{t}} \, p_{p(i,j,k)} := \frac{p^{\tau}_{p(i,j,k)} - \check{p}_{p(i,j,k)}}{h_t}$$

and

$$\Delta_{\overline{t}} \, p^{\Theta}_p := \Theta p^{\tau}_p + (1 - \Theta) \check{p}_p \,. \tag{5.1.4}$$

$\check{p}_{p(i,j,k)}$ is a synonym for $p^{\tau-1}_{p(i,j,k)}$. Equation (5.1.4) is the formula for a weighted discretisation in time. With $\Theta = 1/2$ it corresponds to the Crank-Nicolson discretisation, with $\Theta = 1$ to the fully implicit discretisation.

Following the description in [46] and applying it to a single-layer porous medium, the discretised Biot equations on a staggered grid have this form:

$$\begin{aligned} -(\lambda + 2\mu) \, \Delta_{\overline{x}x} \, u_{x(i+1/2,j,k)} - \lambda \, \Delta_{\overline{y}x} \, u_{y(i,j+1/2,k)} - \lambda \, \Delta_{\overline{z}x} \, u_{z(i,j,k+1/2)} \\ - \mu \, \Delta_{\overline{y}y} \, u_{x(i+1/2,j,k)} - \mu \, \Delta_{\overline{x}y} \, u_{y(i+1,j-1/2,k)} - \mu \, \Delta_{\overline{z}z} \, u_{x(i+1/2,j,k)} \\ - \mu \, \Delta_{\overline{x}z} \, u_{z(i,j,k-1/2)} + \alpha \, \Delta_{\overline{x}} \, p_{p(i,j,k)} = 0 \,, \end{aligned} \tag{5.1.5a}$$

$$\begin{aligned} &-(\lambda+2\mu)\,\Delta_{\overline{y}y}\,u_{y(i,j+1/2,k)} - \lambda\,\Delta_{\overline{x}y}\,u_{x(i+1/2,j,k)} - \lambda\,\Delta_{\overline{z}y}\,u_{z(i,j,k+1/2)} \\ &\quad - \mu\,\Delta_{\overline{x}x}\,u_{y(i,j+1/2,k)} - \mu\,\Delta_{\overline{y}x}\,u_{x(i-1/2,j+1,k)} - \mu\,\Delta_{\overline{z}z}\,u_{y(i,j+1/2,k)} \\ &\quad - \mu\,\Delta_{\overline{y}z}\,u_{z(i,j+1,k-1/2)} + \alpha\,\Delta_{\overline{y}}\,p_{p(i,j,k)} = 0\,, \end{aligned} \tag{5.1.5b}$$

$$\begin{aligned} &-(\lambda+2\mu)\,\Delta_{\overline{z}z}\,u_{z(i,j,k+1/2)} - \lambda\,\Delta_{\overline{x}z}\,u_{x(i+1/2,j,k)} - \lambda\,\Delta_{\overline{y}z}\,u_{y(i,j+1/2,k)} \\ &\quad - \mu\,\Delta_{\overline{x}x}\,u_{z(i,j,k+1/2)} - \mu\,\Delta_{\overline{z}x}\,u_{x(i-1/2,j,k+1)} - \mu\,\Delta_{\overline{y}y}\,u_{z(i,j,k+1/2)} \\ &\quad - \mu\,\Delta_{\overline{z}y}\,u_{y(i,j-1/2,k+1)} + \alpha\,\Delta_{\overline{z}}\,p_{p(i,j,k)} = 0\,, \end{aligned} \tag{5.1.5c}$$

$$\begin{aligned} &\phi\beta\,\Delta_{\bar{t}}\,p_{p(i,j,k)} + \alpha\,\Delta_{x\bar{t}}\,u_{x(i-1/2,j,k)} + \alpha\,\Delta_{y\bar{t}}\,u_{y(i,j-1/2,k)} + \alpha\,\Delta_{z\bar{t}}\,u_{z(i,j,k-1/2)} \\ &\qquad - \frac{k}{\eta}\,\Delta_{\overline{x}x}\,p^{\Theta}_{p(i,j,k)} - \frac{k}{\eta}\,\Delta_{\overline{y}y}\,p^{\Theta}_{p(i,j,k)} - \frac{k}{\eta}\,\Delta_{\overline{z}z}\,p^{\Theta}_{p(i,j,k)} = f_{p,i,j,k}\,. \end{aligned} \tag{5.1.5d}$$

5.2 Discretisation of the Stokes equations on a cell-centred grid

For the Stokes equations we use a cell-centered grid with $N_{fx} \times N_{fy} \times N_{fz}$ grid points. Such a grid has the following type of points:

$$\begin{aligned} \omega_{cc} = \omega_{cc,h_{fx},h_{fy},h_{fz}} = &\{(x_{\mathtt{i}}, y_{\mathtt{j}}, z_{\mathtt{k}}) = ((\mathtt{i}-\frac{1}{2})h_x, (\mathtt{j}-\frac{1}{2})h_y, (\mathtt{k}-\frac{1}{2})h_z), \\ &\mathtt{i}=1,...,N_{fx},\ \mathtt{j}=1,...,N_{fy},\ \mathtt{k}=1,...,N_{fz}\}\,. \end{aligned}$$

The time discretisation is the same as we use for the staggered grid (5.1.1).

Using notation (4.0.1) for the discrete functions on $\omega_{cc} \times \omega^t$ and notation (4.0.2) and (4.0.3) for the space and time derivatives, respectively, the discrete version of the Stokes equations looks like in the case for the node-based grid (4.2.1a) - (4.2.1d).

5.3 Discretisation of the transmission conditions on non-matching grids

In the case of non-matching meshes, additional functions have to be introduced for the matching of the transmission conditions along the interfaces. Thus, we assure that we operate on the same grid points. An extract of the geometry we consider in this chapter is depicted in figure 5.2. The red lines indicate the interface between the cell-centred grid (fluid region Ω_f) on the left hand side and the staggered grid (porous medium Ω_p) on the right hand side. The location of the grid points of the cell-centred grid is denoted by crosses in figure 5.2. Here, all solution variables (v_x, v_y, v_z, p_f) are collocated in one point. For the porous medium we use a staggered grid. The respective location of the solution variables is also depicted in figure 5.2, and in figure 5.1. Note that we consider the outflow interface in this chapter, whereas figures 5.2 and 5.3 show the inflow interface.

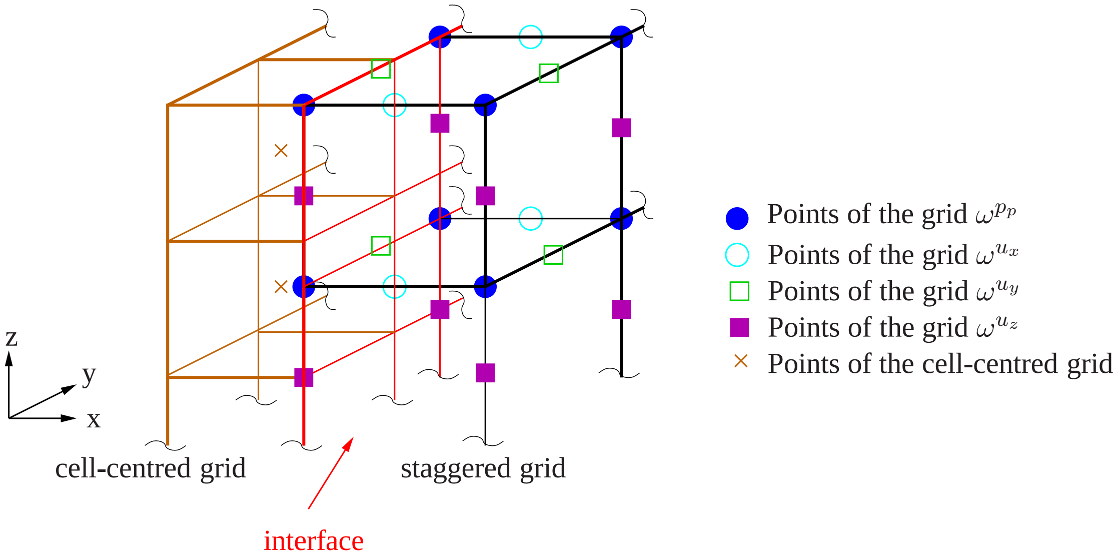

Figure 5.2: 3d sketch of non-matching grids: The interface (red) is the common boundary of the cell-centred grid on the left hand side and the staggered grid on the right hand side. Note that this figure displays the inflow interface Γ_{in}, in the text we derive the equations for the outflow interface.

The transmission conditions we use are the ones stated in chapter 4.3, but we have to discretise them on the respective grids and introduce matching functions.

In the cell-centred grid, all variables (v_x,v_y,v_z,p_f) are collocated in the centre of a grid cell. Therefore, the number of nodes is the same for all variables. But all grid nodes are internal nodes ($\mathring{v}_x$,$\mathring{v}_y$,$\mathring{v}_z$,$\mathring{p}_f$). So, for the application of boundary conditions, we need additional boundary nodes, that lie on the respective faces of the grid cells. These boundary nodes are further split into the outer boundary nodes ($\hat{v}_x$,$\hat{v}_y$,$\hat{v}_z$,$\hat{p}_f$) and the nodes which lie on the interface ($\tilde{v}_x$,$\tilde{v}_y$,$\tilde{v}_z$,$\tilde{p}_f$). To establish clarity, repeat the notation for the number of grid nodes:

$$\begin{array}{lrcl}
\text{Nr. of internal nodes:} & \mathring{N}_f & = & N_{fx}N_{fy}N_{fz} \\
\text{Nr. of outer boundary nodes:} & \hat{N}_f & = & N_{fy}N_{fz} + 2(N_{fx}N_{fy} + N_{fx}N_{fz}) \\
\text{Nr. of interface nodes:} & \tilde{N}_f & = & N_{fy}N_{fz}
\end{array}$$

In the staggered grid, the number of nodes is different for each variable, as can be seen in figure 5.1. Therefore, introduce new variables for the corresponding numbers:

Total number of nodes (without additional boundary nodes):

$$\begin{array}{llll}
p_p\text{:} & (N_{px}+1) & (N_{py}+1) & (N_{pz}+1) \\
u_x\text{:} & N_{px} & (N_{py}+1) & (N_{pz}+1) \\
u_y\text{:} & (N_{px}+1) & N_{py} & (N_{pz}+1) \\
u_z\text{:} & (N_{px}+1) & (N_{py}+1) & N_{pz}
\end{array}$$

Also the number of internal and boundary nodes differs for the various variables, due to the shift of the displacement nodes in the respective direction. This shift implicates that there are no nodes on some boundaries, e.g. there are no nodes for u_x on the east and west boundary of Ω_p. Therefore, we introduce additional grid nodes at the respective boundaries:

Total number of nodes (with additional boundary nodes):

$$\begin{array}{llcccc}
p_p\text{:} & N_{p,p_p} & := & (N_{px}+1) & (N_{py}+1) & (N_{pz}+1) \\
u_x\text{:} & N_{p,u_x} & := & (N_{px}+2) & (N_{py}+1) & (N_{pz}+1) \\
u_y\text{:} & N_{p,u_y} & := & (N_{px}+1) & (N_{py}+2) & (N_{pz}+1) \\
u_z\text{:} & N_{p,u_z} & := & (N_{px}+1) & (N_{py}+1) & (N_{pz}+2)
\end{array}$$

Number of internal nodes:

$$\begin{array}{llcccc}
p_p\text{:} & \overset{\circ}{N}_{p,p_p} & := & (N_{px}-1) & (N_{py}-1) & (N_{pz}-1) \\
u_x\text{:} & \overset{\circ}{N}_{p,u_x} & := & N_{px} & (N_{py}-1) & (N_{pz}-1) \\
u_y\text{:} & \overset{\circ}{N}_{p,u_y} & := & (N_{px}-1) & N_{py} & (N_{pz}-1) \\
u_z\text{:} & \overset{\circ}{N}_{p,u_z} & := & (N_{px}-1) & (N_{py}-1) & N_{pz}
\end{array}$$

Number of outer boundary nodes:

$$\begin{array}{llcl}
p_p\text{:} & \hat{N}_{p,p_p} & := & (N_{py}+1)(N_{pz}+1)+2(N_{px}-1)(N_{py}+1)+2(N_{px}-1)(N_{pz}-1) \\
u_x\text{:} & \hat{N}_{p,u_x} & := & (N_{py}+1)(N_{pz}+1)+2N_{px}(N_{py}+1)+2N_{py}(N_{pz}+1) \\
u_y\text{:} & \hat{N}_{p,u_y} & := & N_{py}(N_{pz}+1)+2(N_{px}+1)(N_{py}+2)+2(N_{px}-1)(N_{pz}-1) \\
u_z\text{:} & \hat{N}_{p,u_z} & := & (N_{py}+1)N_{pz}+2(N_{px}+1)(N_{py}+1)+2(N_{px}-1)N_{pz}
\end{array}$$

Number of interface nodes:

$$\begin{array}{llcl}
p_p\text{:} & \tilde{N}_{p,p_p} & := & (N_{py}+1)(N_{pz}+1) \\
u_x\text{:} & \tilde{N}_{p,u_x} & := & (N_{py}+1)(N_{pz}+1) \\
u_y\text{:} & \tilde{N}_{p,u_y} & := & N_{py}(N_{pz}+1) \\
u_z\text{:} & \tilde{N}_{p,u_z} & := & (N_{py}+1)N_{pz}
\end{array}$$

Matching of grid nodes along the interface

For the matching of the cell-centred and the staggered grid, we introduce points on the interface, which are denoted in the following by subscripts $(\mathcal{I},\mathcal{J},\mathcal{K})$. For our purpose, we choose these points to be a projection of the cell-centred grid nodes onto the interface. Thus, there are $N_\Gamma := N_y \times N_z = N_{fy} \times N_{fz}$ nodes on the interface with distances $h_y = h_{fy}$ and $h_z = h_{fz}$. Figure 5.3 shows a 2d sketch of the non-matching grids and the additionally introduced interface nodes, which are displayed as red ellipses. This special choice of interface nodes implies that we have to do the matching only from one side, namely from the staggered grid side. Values from the cell-centred grid can simply be mapped onto the interface.

To match the points of the staggered grid to the interface nodes, we choose a matching function that uses weighted values at four nodes of the staggered grid. We choose four nodes that surround the interface node $(\mathcal{I},\mathcal{J},\mathcal{K})$ with respect to the y- and z-coordinate. The indices of these four nodes depend on the variable we consider. For the pressure p_p they are (i,j,k), $(i,j+1,k)$, $(i,j,k+1)$ and $(i,j+1,k+1)$. For the displacements in x-direction they are $(i-1/2,j,k)$, $(i-1/2,j+1,k)$, $(i-1/2,j,k+1)$ and $(i-1/2,j+1,k+1)$ (at the outflow of the porous medium), as can be seen in figure 5.4.

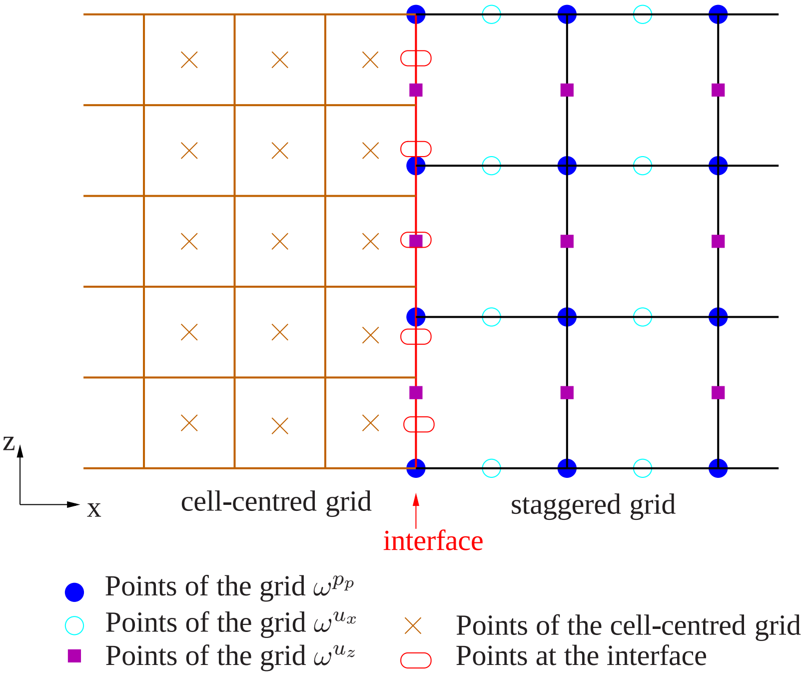

Figure 5.3: 2d sketch of non-matching grids. The interface is the common boundary of the cell-centred grid on the left hand side and the staggered grid on the right hand side. Nodes on the interface are introduced for the matching of the two different grids. Note that this figure displays the inflow interface Γ_{in}, in the text we derive the transmission conditions for the outflow interface.

How the indices of these four surrounding nodes are determined is demonstrated for the pressure p_p. In a cell-centred grid with grid width h_y and h_z we know that

$$\begin{aligned} &y_{(\mathcal{I},\mathcal{J},\mathcal{K})} = \left(\mathcal{J} - \frac{1}{2}\right) h_y \quad \text{and} \quad z_{(\mathcal{I},\mathcal{J},\mathcal{K})} = \left(\mathcal{K} - \frac{1}{2}\right) h_z \,, \\ &\mathcal{I} = \mathcal{I}_\Gamma, \quad \mathcal{J} = 1, \dots, N_y, \quad \mathcal{K} = 1, \dots, N_z \,, \end{aligned} \tag{5.3.1}$$

where $\mathcal{I}_\Gamma$ is the $\mathcal{I}$-index of the interface.
For the pressure values in the staggered grid we have

$$\begin{aligned} &y_{(i,j,k)} = (j-1)\, h_{py} \quad \text{and} \quad z_{(i,j,k)} = (k-1)\, h_{pz} \,, \\ &i = 1, \dots, N_{px}+1, \quad j = 1, \dots, N_{py}+1, \quad k = 1, \dots, N_{pz}+1 \,. \end{aligned} \tag{5.3.2}$$

For our interpolation we require

$$\begin{aligned} &y_{(i,j,k)} \leq y_{(\mathcal{I},\mathcal{J},\mathcal{K})} < y_{(i,j+1,k)} \quad \text{and} \quad z_{(i,j,k)} \leq z_{(\mathcal{I},\mathcal{J},\mathcal{K})} < z_{(i,j,k+1)} \,, \\ &j = 1, \dots, N_{py}+1, \quad \mathcal{J} = 1, \dots, N_y, \quad k = 1, \dots, N_{pz}+1, \quad \mathcal{K} = 1, \dots, N_z \,. \end{aligned}$$

Then, equations (5.3.1) and (5.3.2) imply

$$\begin{aligned} &(j-1)\, h_{py} \leq \left(\mathcal{J} - \frac{1}{2}\right) h_y < j h_{py} \quad \text{and} \quad (k-1)\, h_{pz} \leq \mathcal{K} h_z < k h_{pz} \,, \\ &j = 1, \dots, N_{py}+1, \quad \mathcal{J} = 1, \dots, N_y, \quad k = 1, \dots, N_{pz}+1, \quad \mathcal{K} = 1, \dots, N_z \,. \end{aligned} \tag{5.3.3}$$

Reformulation of the inequality above (5.3.3) gives

$$
\begin{aligned}
& j \leq \left(\mathcal{J} - \frac{1}{2}\right) \frac{h_y}{h_{py}} + 1 < j + 1 \quad \text{or} \quad j = \left\lfloor \left(\mathcal{J} - \frac{1}{2}\right) \frac{h_y}{h_{py}} + 1 \right\rfloor , \\
& j = 1, ..., N_{py} + 1, \quad \mathcal{J} = 1, ..., N_y ,
\end{aligned}
\tag{5.3.4}
$$

and

$$
\begin{aligned}
& k \leq \left(\mathcal{K} - \frac{1}{2}\right) \frac{h_z}{h_{pz}} + 1 < k + 1 \quad \text{or} \quad k = \left\lfloor \left(\mathcal{K} - \frac{1}{2}\right) \frac{h_z}{h_{pz}} + 1 \right\rfloor , \\
& k = 1, ..., N_{pz}, \quad \mathcal{K} = 1, ..., N_z + 1 .
\end{aligned}
\tag{5.3.5}
$$

By these two formulae, (5.3.4) and (5.3.5), the indices of the four surrounding points on the staggered grid can be determined. Note that the inequalities given above are only valid for the pressure p_p and the x-displacements u_x, because those two variables have the same y- and z-coordinates. For the displacements in y- and z-direction, the formulae can be derived analogously.

Now we interpolate the values to get a corresponding value at the interface node $(\mathcal{I}, \mathcal{J}, \mathcal{K})$. For the pressure p_p we introduce weights φ_1 , φ_2 , φ_3 and $\varphi_4 \in \mathbb{R}$. Then, the value of p_p at the interface node $(\mathcal{I}, \mathcal{J}, \mathcal{K})$ can be expressed as:

$$
p_{p(\mathcal{I},\mathcal{J},\mathcal{K})} = \varphi_1 \, p_{p(i,j,k)} + \varphi_2 \, p_{p(i,j+1,k)} + \varphi_3 \, p_{p(i,j,k+1)} + \varphi_4 \, p_{p(i,j+1,k+1)} \, . \tag{5.3.6a}
$$

Bilinear interpolation can be used as matching function. Then, the coefficients in (5.3.6a) are

$$
\begin{aligned}
\varphi_1 &= \frac{1}{h_{py} h_{pz}} \left(y_{(i,j,k+1)} - y_{(\mathcal{I},\mathcal{J},\mathcal{K})} \right) \left(z_{(i,j+1,k)} - z_{(\mathcal{I},\mathcal{J},\mathcal{K})} \right) , \\
\varphi_2 &= \frac{1}{h_{py} h_{pz}} \left(y_{(i,j,k+1)} - y_{(\mathcal{I},\mathcal{J},\mathcal{K})} \right) \left(z_{(\mathcal{I},\mathcal{J},\mathcal{K})} - z_{(i,j,k)} \right) , \\
\varphi_3 &= \frac{1}{h_{py} h_{pz}} \left(y_{(\mathcal{I},\mathcal{J},\mathcal{K})} - y_{(i,j,k)} \right) \left(z_{(i,j+1,k+1)} - z_{(\mathcal{I},\mathcal{J},\mathcal{K})} \right) , \\
\varphi_4 &= \frac{1}{h_{py} h_{pz}} \left(y_{(\mathcal{I},\mathcal{J},\mathcal{K})} - y_{(i,j,k)} \right) \left(z_{(\mathcal{I},\mathcal{J},\mathcal{K})} - z_{(i,j,k+1)} \right) .
\end{aligned}
$$

For the displacements u_x, u_y, u_z we also introduce weights $\psi_{\xi,\zeta} \in \mathbb{R}$ with $\xi = x, y, z$ and $\zeta = 1, 2, 3, 4$ to obtain:

$$
\begin{aligned}
u_{x(\mathcal{I},\mathcal{J},\mathcal{K})} &= \psi_{x1} \, u_{x(i-1/2,j,k)} + \psi_{x2} \, u_{x(i-1/2,j+1,k)} + \psi_{x3} \, u_{x(i-1/2,j,k+1)} \\
&\qquad + \psi_{x4} \, u_{x(i-1/2,j+1,k+1)} , \qquad (5.3.6\text{b}) \\
u_{y(\mathcal{I},\mathcal{J},\mathcal{K})} &= \psi_{y1} \, u_{y(i,j+1/2,k)} + \psi_{y2} \, u_{y(i,j+3/2,k)} + \psi_{y3} \, u_{y(i,j+1/2,k+1)} \\
&\qquad + \psi_{y4} \, u_{y(i,j+3/2,k+1)} , \qquad (5.3.6\text{c}) \\
u_{z(\mathcal{I},\mathcal{J},\mathcal{K})} &= \psi_{z1} \, u_{z(i,j,k+1/2)} + \psi_{z2} \, u_{z(i,j+1,k+1/2)} + \psi_{z3} \, u_{z(i,j,k+3/2)} \\
&\qquad + \psi_{z4} \, u_{z(i,j+1,k+3/2)} . \qquad (5.3.6\text{d})
\end{aligned}
$$

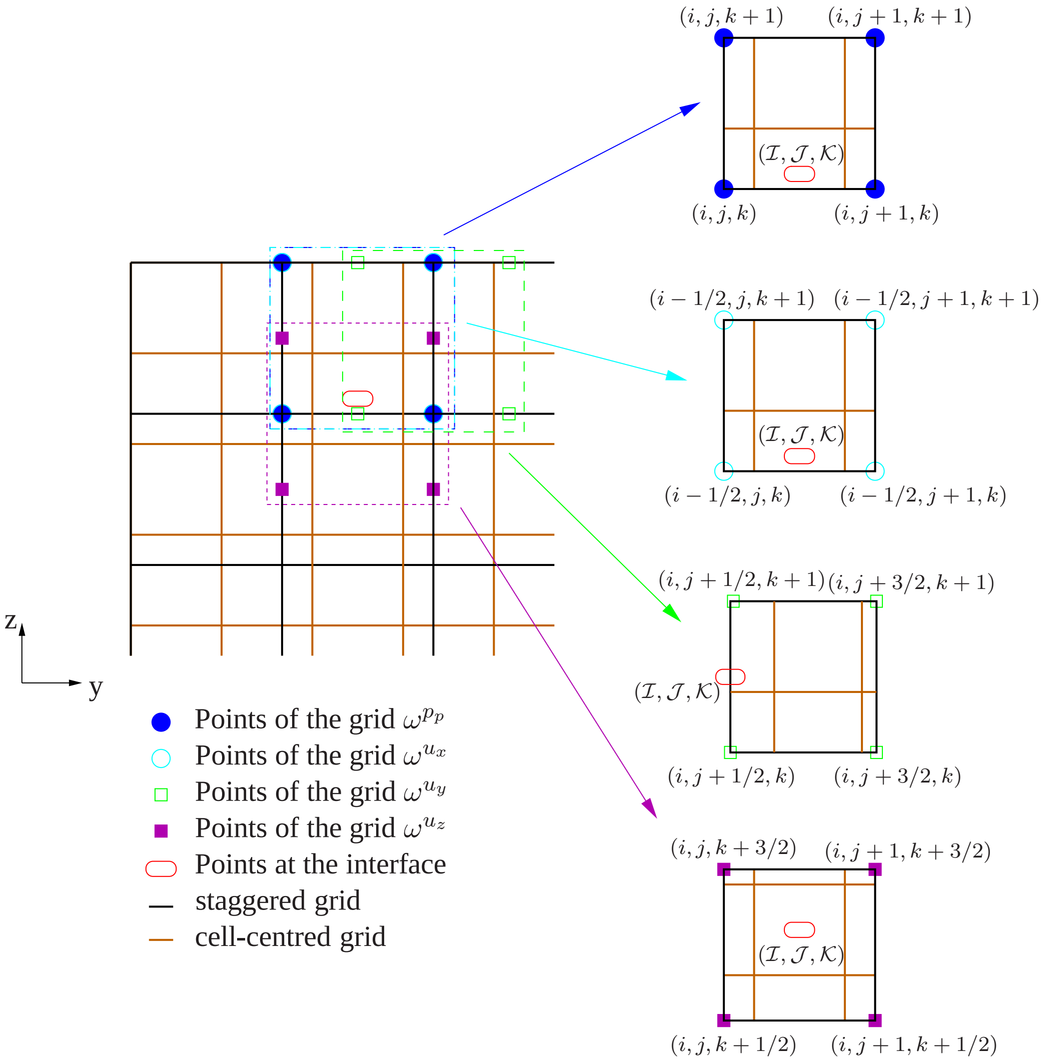

Figure 5.4: 2d sketch of the interface of non-matching grids. Depending on the staggered grid variable we want to match to the interface, we have to choose different grid points to get the new value.

Using bilinear interpolation, the coefficients for u_x in equation (5.3.6b) are:

$$\begin{aligned}
\psi_{x1} &= \frac{1}{h_{py}h_{pz}}\left(y_{(i-1/2,j,k+1)} - y_{(\mathcal{I},\mathcal{J},\mathcal{K})}\right)\left(z_{(i-1/2,j+1,k)} - z_{(\mathcal{I},\mathcal{J},\mathcal{K})}\right) \,, \\
\psi_{x2} &= \frac{1}{h_{py}h_{pz}}\left(y_{(i-1/2,j,k+1)} - y_{(\mathcal{I},\mathcal{J},\mathcal{K})}\right)\left(z_{(\mathcal{I},\mathcal{J},\mathcal{K})} - z_{(i-1/2,j,k)}\right) \,, \\
\psi_{x3} &= \frac{1}{h_{py}h_{pz}}\left(y_{(\mathcal{I},\mathcal{J},\mathcal{K})} - y_{(i-1/2,j,k)}\right)\left(z_{(i-1/2,j+1,k+1)} - z_{(\mathcal{I},\mathcal{J},\mathcal{K})}\right) \,, \\
\psi_{x4} &= \frac{1}{h_{py}h_{pz}}\left(y_{(\mathcal{I},\mathcal{J},\mathcal{K})} - y_{(i-1/2,j,k)}\right)\left(z_{(\mathcal{I},\mathcal{J},\mathcal{K})} - z_{(i-1/2,j,k+1)}\right) \,.
\end{aligned}$$

Note that in the case of a uniform mesh, the coefficients for the pressure p_p and the x-displacements u_x are equal, because y- and z-coordinates coincide. The coefficients for u_y and u_z are derived analogously.

The discrete transmission conditions for non-matching grids

The transmission conditions for non-matching grids stay basically the same as for matching grids (4.3.2a)-(4.3.2h), except that we have to account for the additional grid on the interface. Let $\mathcal{I} = \mathcal{I}_\Gamma$ be the $\mathcal{I}$-index of the interface. For derivatives with respect to x, we use $\mathcal{I}_\Gamma - 1$ and $\mathcal{I}_\Gamma + 1$, respectively, and assume that the fictive grid width in x-direction is h_x. These interface indices will be replaced later on by the respective values from the fluid grid and the porous grid. With respect to that, we obtain the transmission conditions in the following form:

Conservation of mass

$$v_{x(\mathcal{I},\mathcal{J},\mathcal{K})} = (1-\phi)\alpha\frac{1}{h_t}\left(u_{x(\mathcal{I},\mathcal{J},\mathcal{K})} - \check{u}_{x(\mathcal{I},\mathcal{J},\mathcal{K})}\right) - \frac{k}{\eta}\frac{1}{h_x}\left(p_{p(\mathcal{I},\mathcal{J},\mathcal{K})} - p_{p(\mathcal{I}-1,\mathcal{J},\mathcal{K})}\right) \tag{5.3.7a}$$

$$v_{y(\mathcal{I},\mathcal{J},\mathcal{K})} = (1-\phi)\alpha\frac{1}{h_t}\left(u_{y(\mathcal{I},\mathcal{J},\mathcal{K})} - \check{u}_{y(\mathcal{I},\mathcal{J},\mathcal{K})}\right) - \frac{k}{\eta}\frac{1}{2h_y}\left(p_{p(\mathcal{I},\mathcal{J}+1,\mathcal{K})} - p_{p(\mathcal{I},\mathcal{J}-1,\mathcal{K})}\right) \tag{5.3.7b}$$

$$v_{z(\mathcal{I},\mathcal{J},\mathcal{K})} = (1-\phi)\alpha\frac{1}{h_t}\left(u_{z(\mathcal{I},\mathcal{J},\mathcal{K})} - \check{u}_{z(\mathcal{I},\mathcal{J},\mathcal{K})}\right) - \frac{k}{\eta}\frac{1}{2h_z}\left(p_{p(\mathcal{I},\mathcal{J},\mathcal{K}+1)} - p_{p(\mathcal{I},\mathcal{J},\mathcal{K}-1)}\right) \tag{5.3.7c}$$

Conservation of momentum

$$\begin{aligned}
&2\eta\frac{1}{h_x}(v_{x(\mathcal{I}+1,\mathcal{J},\mathcal{K})} - v_{x(\mathcal{I},\mathcal{J},\mathcal{K})}) - p_{f(\mathcal{I},\mathcal{J},\mathcal{K})} = \\
&\quad (1-\phi)\left[(2\mu+\lambda)\frac{1}{h_x}(u_{x(\mathcal{I},\mathcal{J},\mathcal{K})} - u_{x(\mathcal{I}-1,\mathcal{J},\mathcal{K})}) + \lambda\left(\frac{1}{2h_y}(u_{y(\mathcal{I},\mathcal{J}+1,\mathcal{K})} - u_{y(\mathcal{I},\mathcal{J}-1,\mathcal{K})})\right.\right. \\
&\quad \left.\left. + \frac{1}{2h_z}(u_{z(\mathcal{I},\mathcal{J},\mathcal{K}+1)} - u_{z(\mathcal{I},\mathcal{J},\mathcal{K}-1)})\right)\right] - \phi p_{p(\mathcal{I},\mathcal{J},\mathcal{K})}
\end{aligned} \tag{5.3.7d}$$

$$\begin{aligned}
\eta\left(\frac{1}{h_x}(v_{y(\mathcal{I}+1,\mathcal{J},\mathcal{K})} - v_{y(\mathcal{I},\mathcal{J},\mathcal{K})}) + \frac{1}{2h_y}(v_{x(\mathcal{I},\mathcal{J}+1,\mathcal{K})} - v_{x(\mathcal{I},\mathcal{J}-1,\mathcal{K})})\right) = \\
(1-\phi)\mu\left(\frac{1}{h_x}(u_{y(\mathcal{I},\mathcal{J},\mathcal{K})} - u_{y(\mathcal{I}-1,\mathcal{J},\mathcal{K})}) + \frac{1}{2h_y}(u_{x(\mathcal{I},\mathcal{J}+1,\mathcal{K})} - u_{x(\mathcal{I},\mathcal{J}-1,\mathcal{K})})\right)
\end{aligned} \tag{5.3.7e}$$

$$\begin{aligned}
\eta\left(\frac{1}{h_x}(v_{z(\mathcal{I}+1,\mathcal{J},\mathcal{K})} - v_{z(\mathcal{I},\mathcal{J},\mathcal{K})}) + \frac{1}{2h_z}(v_{x(\mathcal{I},\mathcal{J},\mathcal{K}+1)} - v_{x(\mathcal{I},\mathcal{J},\mathcal{K}-1)})\right) = \\
(1-\phi)\mu\left(\frac{1}{h_x}(u_{z(\mathcal{I},\mathcal{J},\mathcal{K})} - u_{z(\mathcal{I}-1,\mathcal{J},\mathcal{K})}) + \frac{1}{2h_z}(u_{x(\mathcal{I},\mathcal{J},\mathcal{K}+1)} - u_{x(\mathcal{I},\mathcal{J},\mathcal{K}-1)})\right)
\end{aligned} \tag{5.3.7f}$$

Pressure jump condition - inflow

$$p_{f(\mathcal{I},\mathcal{J},\mathcal{K})} + \frac{\varrho}{2}\, v_{x(\mathcal{I},\mathcal{J},\mathcal{K})}\, \check{v}_{x(\mathcal{I},\mathcal{J},\mathcal{K})}\left(1 - \frac{1}{\phi^2 C_{\mathrm{c}}^2}\right) = p_{p(\mathcal{I},\mathcal{J},\mathcal{K})} \tag{5.3.7g}$$

Pressure jump condition - outflow

$$\begin{aligned}
p_{f(\mathcal{I},\mathcal{J},\mathcal{K})} &= p_{p(\mathcal{I},\mathcal{J},\mathcal{K})} + C_{\mathrm{e}}\,\frac{\varrho}{2}\, v^p_{fx(\mathcal{I},\mathcal{J},\mathcal{K})}\, \check{v}^p_{fx(\mathcal{I},\mathcal{J},\mathcal{K})}(1-\phi^2) \\
&= p_{p(\mathcal{I},\mathcal{J},\mathcal{K})} + C_{\mathrm{e}}\,\frac{\varrho}{2}\left(\frac{1}{\phi}\frac{k}{\eta}\right)^2 \frac{1}{h_{px}^2}(p_{p(\mathcal{I},\mathcal{J},\mathcal{K})} - p_{p(\mathcal{I}-1,\mathcal{J},\mathcal{K})}) \\
&\qquad (\check{p}_{p(\mathcal{I},\mathcal{J},\mathcal{K})} - \check{p}_{p(\mathcal{I}-1,\mathcal{J},\mathcal{K})})\left(1-\phi^2\right) .
\end{aligned} \tag{5.3.7h}$$

Replacing the fluid flow variables on the interface by fluid flow variables from Ω_f and inserting the matching functions (5.3.6a) and (5.3.6b) into the transmission conditions (5.3.7a) - (5.3.7h), one obtains the transmission conditions for non-matching grids. Here, we only present the fourth transmission condition (5.3.7d):

$$\begin{aligned}
&2\eta\frac{1}{0.5\,h_{fy}}\left(v_{x(\mathtt{i+1,j,k})}-v_{x(\mathtt{i,j,k})}\right)-p_{f(\mathtt{i,j,k})}= \\
&\quad(1-\phi)\Bigg[(2\mu+\lambda)\frac{1}{0.5\,h_{px}}\Big\{\psi_{x1}\left(u_{x(i,j,k)}-u_{x(i-1/2,j,k)}\right) \\
&\quad\quad+\psi_{x2}\left(u_{x(i,j+1,k)}-u_{x(i-1/2,j+1,k)}\right)+\psi_{x3}\left(u_{x(i,j,k+1)}-u_{x(i-1/2,j,k+1)}\right) \\
&\quad\quad+\psi_{x4}\left(u_{x(i,j+1,k+1)}-u_{x(i-1/2,j+1,k+1)}\right)\Big\} \\
&\quad\quad+\lambda\frac{1}{2h_{py}}\Big\{\psi_{y1}\left(u_{y(i,j+3/2,k)}-u_{y(i,j-1/2,k)}\right)+\psi_{y2}\left(u_{y(i,j+5/2,k)}-u_{y(i,j+1/2,k)}\right) \\
&\quad\quad+\psi_{y3}\left(u_{y(i,j+3/2,k+1)}-u_{y(i,j-1/2,k+1)}\right)+\psi_{y4}\left(u_{y(i,j+5/2,k+1)}-u_{y(i,j+1/2,k+1)}\right)\Big\} \\
&\quad\quad+\lambda\frac{1}{2h_{pz}}\Big\{\psi_{z1}\left(u_{z(i,j,k+3/2)}-u_{z(i,j,k-1/2)}\right)+\psi_{z2}\left(u_{z(i,j+1,k+3/2)}-u_{z(i,j+1,k-1/2)}\right) \\
&\quad\quad+\psi_{z3}\left(u_{z(i,j,k+5/2)}-u_{z(i,j,k+1/2)}\right)+\psi_{z4}\left(u_{z(i,j+1,k+5/2)}-u_{z(i,j+1,k+1/2)}\right)\Big\}\Bigg] \\
&\quad\quad-\phi\left\{\varphi_1\,p_{p(i,j,k)}+\varphi_2\,p_{p(i,j+1,k)}+\varphi_3\,p_{p(i,j,k+1)}+\varphi_4\,p_{p(i,j+1,k+1)}\right\}
\end{aligned} \tag{5.3.8}$$

For all other transmission conditions it works similarly.

5.4 The discrete coupled Biot-Stokes system

In this section we derive the entire discrete coupled Biot-Stokes system for non-matching grids. The notation for the operators is maintained from the previous chapter, but note that the sizes are different now. We introduce these operators at the corresponding locations.
Collecting the discrete Biot equations, the discrete Stokes equations and the discrete transmission conditions, we obtain a system of the following structure:

$$\left(\begin{array}{ccc|ccc}
\mathring{B} & \mathring{B}_{\partial\Omega_p\setminus\Gamma} & \mathring{B}_{\Gamma_p} & \mathbf{0} & \mathbf{0} & \mathbf{0} \\
\hat{B}_{\Omega_p\setminus\partial\Omega_p} & \hat{B} & \mathbf{0} & \mathbf{0} & \mathbf{0} & \mathbf{0} \\
T^B_{\Omega_p\setminus\partial\Omega_p} & T^B_{\partial\Omega_p\setminus\Gamma} & T^B_{\Gamma_p} & T^B_{\Omega_f\setminus\partial\Omega_f} & T^B_{\partial\Omega_f\setminus\Gamma} & T^B_{\Gamma_f} \\
\hline
\mathbf{0} & \mathbf{0} & \mathbf{0} & \mathring{S} & \mathring{S}_{\partial\Omega_p\setminus\Gamma} & \mathring{S}_{\Gamma_f} \\
\mathbf{0} & \mathbf{0} & \mathbf{0} & \mathbf{0} & \hat{S} & \mathbf{0} \\
T^S_{\Omega_p\setminus\partial\Omega_p} & T^S_{\partial\Omega_p\setminus\Gamma} & T^S_{\Gamma_p} & \mathbf{0} & \mathbf{0} & T^S_{\Gamma_f}
\end{array}\right)
\begin{pmatrix} \mathring{\mathbf{x}}_B \\ \hat{\mathbf{x}}_B \\ \tilde{\mathbf{x}}_B \\ \mathring{\mathbf{x}}_S \\ \hat{\mathbf{x}}_S \\ \tilde{\mathbf{x}}_S \end{pmatrix}
=
\begin{pmatrix} \mathring{\mathbf{r}}_B \\ \hat{\mathbf{r}}_B \\ \mathbf{0} \\ \mathring{\mathbf{r}}_S \\ \hat{\mathbf{r}}_S \\ \mathbf{0} \end{pmatrix}. \tag{5.4.1}$$

This system looks similar to the one for the matching grids (4.4.1), but the size and structure of the submatrices differ due to the properties of the non-matching grids. To make the description easier, define the following numbers:

$$\begin{aligned}
\mathring{N}_{p,\text{tot}} &:= \mathring{N}_{p,u_x}+\mathring{N}_{p,u_y}+\mathring{N}_{p,u_z}+\mathring{N}_{p,p_p} \\
\hat{N}_{p,\text{tot}} &:= \hat{N}_{p,u_x}+\hat{N}_{p,u_y}+\hat{N}_{p,u_z}+\hat{N}_{p,p_p} \\
\tilde{N}_{p,\text{tot}} &:= \tilde{N}_{p,u_x}+\tilde{N}_{p,u_y}+\tilde{N}_{p,u_z}+\tilde{N}_{p,p_p}
\end{aligned}$$

Then, the operators read as follows:

$$\begin{aligned}
&\mathring{B} : \mathbb{R}^{\mathring{N}_{p,\text{tot}}} \longrightarrow \mathbb{R}^{\mathring{N}_{p,\text{tot}}} , \qquad \mathring{B}_{\partial\Omega_p\setminus\Gamma} : \mathbb{R}^{\mathring{N}_{p,\text{tot}}} \longrightarrow \mathbb{R}^{\hat{N}_{p,\text{tot}}} , \quad \mathring{B}_{\Gamma_p} : \mathbb{R}^{\mathring{N}_{p,\text{tot}}} \longrightarrow \mathbb{R}^{\tilde{N}_{p,\text{tot}}} , \\
&\hat{B}_{\Omega_p\setminus\partial\Omega_p} : \mathbb{R}^{\hat{N}_{p,\text{tot}}} \longrightarrow \mathbb{R}^{\mathring{N}_{p,\text{tot}}} , \quad \hat{B} : \mathbb{R}^{\hat{N}_{p,\text{tot}}} \longrightarrow \mathbb{R}^{\hat{N}_{p,\text{tot}}} .
\end{aligned}$$

The third line of system (5.4.1) contains the continuity of tractions and the pressure jump transmission conditions (5.3.7d) - (5.3.7f) and (5.3.7h). The operators are defined in the following way:

$$\begin{aligned}
&T^B_{\Omega_p\setminus\partial\Omega_p} : \mathbb{R}^{4N_\Gamma} \longrightarrow \mathbb{R}^{\mathring{N}_{p,\text{tot}}} , \quad T^B_{\partial\Omega_p\setminus\Gamma} : \mathbb{R}^{4N_\Gamma} \longrightarrow \mathbb{R}^{\hat{N}_{p,\text{tot}}} , \quad T^B_{\Gamma_p} : \mathbb{R}^{4N_\Gamma} \longrightarrow \mathbb{R}^{\tilde{N}_{p,\text{tot}}} , \\
&T^B_{\Omega_f\setminus\partial\Omega_f} : \mathbb{R}^{4N_\Gamma} \longrightarrow \mathbb{R}^{4\mathring{N}_f} , \quad T^B_{\partial\Omega_f\setminus\Gamma} : \mathbb{R}^{4N_\Gamma} \longrightarrow \mathbb{R}^{4\hat{N}_f} , \quad T^B_{\Gamma_f} : \mathbb{R}^{4N_\Gamma} \longrightarrow \mathbb{R}^{3\tilde{N}_f} .
\end{aligned} \tag{5.4.2}$$

Line four and five contain the Stokes equations with the operators

$$\begin{aligned}
&\mathring{S} : \mathbb{R}^{4\mathring{N}_f} \longrightarrow \mathbb{R}^{4\mathring{N}_f} , \quad \mathring{S}_{\partial\Omega_p\setminus\Gamma} : \mathbb{R}^{4\mathring{N}_f} \longrightarrow \mathbb{R}^{4\hat{N}_f} , \quad \mathring{S}_{\Gamma_f} : \mathbb{R}^{4\mathring{N}_f} \longrightarrow \mathbb{R}^{3\tilde{N}_f} , \\
&\hat{S} : \mathbb{R}^{4\hat{N}_f} \longrightarrow \mathbb{R}^{4\hat{N}_f} ,
\end{aligned}$$

and the last line corresponds to the mass conservation equations (5.3.7a) - (5.3.7c) with operators defined in the following way:

$$\begin{aligned}
&T^S_{\Omega_p\setminus\partial\Omega_p} : \mathbb{R}^{3N_\Gamma} \longrightarrow \mathbb{R}^{\mathring{N}_{p,\text{tot}}} , \quad T^S_{\partial\Omega_p\setminus\Gamma} : \mathbb{R}^{3N_\Gamma} \longrightarrow \mathbb{R}^{\hat{N}_{p,\text{tot}}} , \quad T^S_{\Gamma_p} : \mathbb{R}^{3N_\Gamma} \longrightarrow \mathbb{R}^{\tilde{N}_{p,\text{tot}}} , \\
&T^S_{\Gamma_f} : \mathbb{R}^{3N_\Gamma} \longrightarrow \mathbb{R}^{3\tilde{N}_f} .
\end{aligned} \tag{5.4.3}$$

Recall that N_Γ is the number of additionally introduced interface nodes.

The structure of the matrices in system (5.4.1) is equal to the structure in the previous chapter (4.4.9) - (4.4.14), but the submatrices are different. In the following we investigate some of them in more detail. In order to avoid confusion by introducing more indices and/or superscripts, we maintain the notation of the previous chapter for the operators. Note that the sizes and structures might be different. They will be explained at the corresponding places.

The matrices resulting from the discretisation of the Biot poroelasticity equations

For the Biot equations on a staggered grid we introduce the following operators for the variables inside the porous domain Ω_p:

$$\mathring{B}_{IJ} : \mathbb{R}^{\mathring{N}_{p,J}} \longrightarrow \mathbb{R}^{\mathring{N}_{p,J}} , \; I = 1,2,3,4, \; J = u_x, u_y, u_z, p_p .$$

The spaces on which these operators act are all different, because the number of nodes is different for each variable u_x, u_y, u_z and p_p. Recall the definitions on page 56.

This is similar for all matrices that define the discrete system of Biot equations. In the previous chapter we investigated the structure of some submatrices. The structure of the matrices for the staggered grid can be derived by similar considerations. Therefore, we refrain from writing down more details on the discrete Biot poroelasticity equations. Note that in the staggered grid, there are no boundary nodes for the displacements at certain boundary walls. Therefore additional boundary nodes have been introduced. This has to be taken into account when the equations are discretised.

The matrices resulting from the discretisation of the Stokes equations

For the discretisation of the Stokes equations on a cell-centred grid we use the discretisation of the previous chapter. But note that the boundary nodes are additionally introduced and thus, they have a distance of $\frac{1}{2}h_{fx}$, $\frac{1}{2}h_{fy}$ or $\frac{1}{2}h_{fz}$, respectively, to the next internal node. The discretisation matrices are similar to the ones in chapter (4.1) on page 44 et seqq., but please note that the size of the matrices has to be adapted.

The matrices resulting from the discretisation of the transmission conditions

In this section we investigate the operator notation for the transmission conditions. Since the transmission conditions have to account for the non-matching grids, the operators are distinct from the ones for the matching grids (4.4.7) and (4.4.8). We introduced them in (5.4.2) and (5.4.3). The matrices $T^B_{\Omega_p\backslash\partial\Omega_p}$, $T^B_{\partial\Omega_p\backslash\Gamma}$, $T^B_{\Gamma_p}$, $T^B_{\Omega_f\backslash\partial\Omega_f}$, $T^B_{\partial\Omega_f\backslash\Gamma}$ and $T^B_{\Gamma_f}$ have the same structure as given in (4.4.9) - (4.4.14). In the following we describe some of the submatrices in more detail, namely the matrices related to the unknown u_x in the first equations of the continuity of tractions equations (5.3.8).

First, we consider the operator $T^B_{\Omega_p\backslash\partial\Omega_p,1u_x}$ in (4.4.9). It is defined as follows

$$T^B_{\Omega_p\backslash\partial\Omega_p} : \mathbb{R}^{\mathring{N}_{p,u_x}} \longrightarrow \mathbb{R}^{\mathring{N}_{p,u_x}} .$$

It contains all coefficients that are related to the derivative with respect to x in equation (5.3.8). From equations (5.3.4) and (5.3.5) we know, that the indices of the porous domain variables (i,j,k) depend on the indices of the fluid domain $(\mathtt{i},\mathtt{j},\mathtt{k})$ (in our case $\mathtt{j} = \mathcal{J}$ and $\mathtt{k} = \mathcal{K}$). That is, the position of the entries of the matrix $T^B_{\Omega_p\backslash\partial\Omega_p,1u_x}$ depends on these formulae. Thus,

$$T^B_{\Omega_p\backslash\partial\Omega_p,1u_x} = (1-\phi)\frac{2\mu+\lambda}{0.5\ h_{px}} \begin{pmatrix} T^{B,(1,k)}_{\Omega_p\backslash\partial\Omega_p,1u_x} & & 0 \\ & \ddots & \\ 0 & & T^{B,(N_{fz},k)}_{\Omega_p\backslash\partial\Omega_p,1u_x} \end{pmatrix} \in \mathbb{R}^{N_\Gamma \times \mathring{N}_{p,u_x}} .$$

$\mathring{T}_{B,4u_x}$ has N_Γ rows: N_{fz} submatrices with N_{fy} rows each. The number of columns corresponds to the number of internal nodes $\mathring{N}_{p,u_x}$: $N_{fz}-1$ submatrices with $N_{fx}(N_{fy}-1)$ columns each. The submatrices are defined as follows:

$$T^{B,(\mathtt{k},k)}_{\Omega_p\backslash\partial\Omega_p,1u_x} = \begin{cases} T^{B*}_{\Omega_p\backslash\partial\Omega_p,1u_x}(\psi_{x3}\,,\psi_{x4}\,) & \text{if } k=1 \\ T^{B*}_{\Omega_p\backslash\partial\Omega_p,1u_x}(\psi_{x1}\,,\psi_{x2}\,) & \text{if } k=N_{pz} \\ T^{B*}_{\Omega_p\backslash\partial\Omega_p,1u_x}(\psi_{x1}\,,\psi_{x2}\,)T^{B*}_{\Omega_p\backslash\partial\Omega_p,1u_x}(\psi_{x3}\,,\psi_{x4}\,) & \text{otherwise}\,, \end{cases}$$

$$\mathtt{k} = 1,...,N_{fz}\,, \quad k = \left\lfloor \frac{1}{2}\frac{h_{fz}}{h_{pz}}+1 \right\rfloor,...,\left\lfloor \left(N_{fz}-\frac{1}{2}\right)\frac{h_{fz}}{h_{pz}}+1 \right\rfloor ,$$

where

$$T^{B*}_{\Omega_p\backslash\partial\Omega_p,1u_x}(\psi'_x,\psi''_x) = \begin{pmatrix} \mathring{\Psi}^{(1,j)}_x & & 0 \\ & \ddots & \\ 0 & & \mathring{\Psi}^{(N_{fy},j)}_x \end{pmatrix} \in \mathbb{R}^{N_{fy}\times N_{px}(N_{py}-1)} ,$$

$$j = \left\lfloor \frac{1}{2}\frac{h_{fy}}{h_{py}}+1 \right\rfloor,...,\left\lfloor \left(N_{fy}-\frac{1}{2}\right)\frac{h_{fy}}{h_{py}}+1 \right\rfloor .$$

Each of these submatrices $\mathring{\Psi}_x^{(\mathtt{j},j)}$ has N_{fy} rows and $N_{px}(N_{py}-1)$ columns and is of the following structure:

$$\mathring{\Psi}_x^{(\mathtt{j},j)}(\psi_x', \psi_x'') = \begin{cases} \underbrace{(0\ \dots\ 0\ -\psi_x'')}_{N_{px}} & \text{if } j = 1 \\ \underbrace{(0\ \dots\ 0\ -\psi_x')}_{N_{px}} & \text{if } j = N_{py} \\ \underbrace{(0\ \dots\ 0\ -\psi_x')}_{N_{px}}\ \underbrace{(0\ \dots\ 0\ -\psi_x'')}_{N_{px}} & \text{otherwise}\,. \end{cases}$$

Note that $(\psi_x', \psi_x'') = (\psi_{x1}, \psi_{x2})$ or $(\psi_x', \psi_x'') = (\psi_{x3}, \psi_{x4})$, respectively. Some of the values are mapped from the interface to the outer boundary of Ω_p. These coefficients are contained in the matrix $T^B_{\partial\Omega_p\setminus\Gamma,1u_x}$:

$$T^B_{\partial\Omega_p\setminus\Gamma,1u_x} = (1-\phi)\frac{2\mu+\lambda}{0.5\ h_{px}} \begin{pmatrix} T^{B,(1,k)}_{\partial\Omega_p\setminus\Gamma,1u_x} & & \mathbf{0} \\ & \ddots & \\ & & \ddots \\ \mathbf{0} & & T^{B,(N_{fz},k)}_{\partial\Omega_p\setminus\Gamma,1u_x} \end{pmatrix} \in \mathbb{R}^{N_\Gamma \times \tilde{N}_{p,u_x}}\,.$$

$T^B_{\partial\Omega_p\setminus\Gamma,1u_x}$ has N_Γ rows: It consists of N_{fz} submatrices with N_{fy} rows each. The number of columns corresponds to $\tilde{N}_{p,u_x}$. The position of these submatrices $T^{B,(\mathtt{k},k)}_{\partial\Omega_p\setminus\Gamma,1u_x}$ is given by the superscript $(\mathtt{k},k)$, where $\mathtt{k} = 1,\dots,N_{fz}$ and $k = \left\lfloor \frac{1}{2}\frac{h_{fy}}{h_{py}} + 1 \right\rfloor, \dots, \left\lfloor \left(N_{fz} - \frac{1}{2}\right)\frac{h_{fy}}{h_{py}} + 1 \right\rfloor$, according to equation (5.3.5). That means that the location of the submatrices $T^{B,(\mathtt{k},k)}_{\partial\Omega_p\setminus\Gamma,1u_x}$ depends on the ratio of the grid widths. The structure of the submatrices is the following:

$$T^{B(\mathtt{k},k)}_{\partial\Omega_p\setminus\Gamma,1u_x} = \begin{cases} T^{B*}_{\partial\Omega_p\setminus\Gamma,1u_x}(\psi_{x1}, \psi_{x2})\, T^{B**}_{\partial\Omega_p\setminus\Gamma,1u_x}(\psi_{x3}, \psi_{x4}) & \text{if } k = 1 \\ T^{B**}_{\partial\Omega_p\setminus\Gamma,1u_x}(\psi_{x1}, \psi_{x2})\, T^{B*}_{\partial\Omega_p\setminus\Gamma,1u_x}(\psi_{x3}, \psi_{x4}) & \text{if } k = N_{pz} \\ T^{B**}_{\partial\Omega_p\setminus\Gamma,1u_x}(\psi_{x1}, \psi_{x2})\, T^{B**}_{\partial\Omega_p\setminus\Gamma,1u_x}(\psi_{x3}, \psi_{x4}) & \text{otherwise}\,, \end{cases}$$

where

$$T^{B*}_{\partial\Omega_p\setminus\Gamma,1u_x}(\psi_x', \psi_x'') = \begin{pmatrix} \hat{\Psi}^{*(1,j)} & & \mathbf{0} \\ & \ddots & \\ \mathbf{0} & & \hat{\Psi}^{*(N_{fy},j)} \end{pmatrix} \in \mathbb{R}^{N_{fy}\times(N_{px}+2)N_{py}}\,.$$

The exact position of these entries $\hat{\Psi}^{(\mathtt{j},j)}_{x,bt}$ is determined by the indices $(\mathtt{j},j)$, $\mathtt{j} = 1,\dots,N_{fy}$, $j = \left\lfloor \frac{1}{2}\frac{h_{fy}}{h_{py}} + 1 \right\rfloor, \dots, \left\lfloor \left(N_{fy} - \frac{1}{2}\right)\frac{h_{fy}}{h_{py}} + 1 \right\rfloor$. $\hat{\Psi}^{*(\mathtt{j},j)}$ is located in the $\mathtt{j}$th row, starting in column $(j-1)N_{py}+1$. The entries $\hat{\Psi}^{*(\mathtt{j},j)}$ are defined as:

$$\hat{\Psi}^{*(\mathtt{j},j)} = (\underbrace{0\ \dots\ 0\ -\psi_x'\ 0}_{N_{px}+2}\ \underbrace{0\ \dots\ 0\ -\psi_x''\ 0}_{N_{px}+2})\,.$$

The submatrices $T^{B**}_{\partial\Omega_p\setminus\Gamma,1u_x}$ have the following structure:

$$T^{B**}_{\partial\Omega_p\setminus\Gamma,1u_x}(\psi_x', \psi_x'') = \begin{pmatrix} \hat{\Psi}^{**(1,j)} & & \mathbf{0} \\ & \ddots & \\ \mathbf{0} & & \hat{\Psi}^{**(N_{fy},j)} \end{pmatrix} \in \mathbb{R}^{N_{fy}\times 2(N_{px}+2)+(N_{py}-2)}$$

with

$$\hat{\Psi}^{**(\mathtt{j},j)} = (\underbrace{0\ \ldots\ 0\ -\psi'_x\, 0}_{N_{px}+2}\underbrace{0\ \ldots\ 0}_{N_{py}-2}\underbrace{0\ \ldots\ 0\ -\psi''_x}_{N_{px}+2})\,.$$

In both cases, the tuple of coefficients (ψ'_x, ψ''_x) stands for

$$(\psi'_x, \psi''_x) = (\psi_{x1}\,, \psi_{x2}\,) \text{ or } (\psi'_x, \psi''_x) = (\psi_{x3}\,, \psi_{x4}\,)\,.$$

Finally we need to give the operator which maps the values from the interface onto the interface of Ω_p:

$$T^{B}_{\partial\Omega_p\backslash\Gamma,1u_x} = (1-\phi)\frac{2\mu+\lambda}{0.5\ h_{px}}\begin{pmatrix} T^{B,(1,k)}_{\partial\Omega_p\backslash\Gamma,1u_x} & & & 0 \\ & \ddots & & \\ & & \ddots & \\ 0 & & & T^{B,(N_{fz},k)}_{\partial\Omega_p\backslash\Gamma,1u_x} \end{pmatrix} \in \mathbb{R}^{N_\Gamma \times \tilde{N}_{p,u_x}}\,.$$

$T_{\partial\Omega_p\backslash\Gamma,1u_x}$ has N_Γ rows: It consists of N_{fz} submatrices with N_{fy} rows each. The number of columns corresponds to $\tilde{N}_{p,u_x}$, which is the number of interface nodes of u_x. The position of the submatrices $T^{B,(\mathtt{k},k)}_{\partial\Omega_p\backslash\Gamma,1u_x}$ is given by the superscript $(\mathtt{k}, k)$, where $\mathtt{k} = 1, ..., N_{fz}$ and $k = \left\lfloor \frac{1}{2}\frac{h_{fy}}{h_{py}} + 1 \right\rfloor, ..., \left\lfloor \left(N_{fz} - \frac{1}{2}\right)\frac{h_{fy}}{h_{py}} + 1 \right\rfloor$, according to equation (5.3.5). That means that the location of the submatrices $T^{B,(\mathtt{k},k)}_{\partial\Omega_p\backslash\Gamma,1u_x}$ depends on the ratio of the grid widths.
The structure of the submatrices is the following:

$$T^{B,(\mathtt{k},k)}_{\partial\Omega_p\backslash\Gamma,1u_x} = T^{B*}_{\partial\Omega_p\backslash\Gamma,1u_x}(\psi_{x1}\,, \psi_{x2}\,)\, T^{B*}_{\partial\Omega_p\backslash\Gamma,1u_x}(\psi_{x3}\,, \psi_{x4}\,)$$

where

$$T^{B*}_{\partial\Omega_p\backslash\Gamma,1u_x}(\psi'_x, \psi''_x) = (\psi'_x, \psi''_x)\ \in \mathbb{R}^{1\times 2}\,.$$

The tuple of coefficients (ψ'_x, ψ''_x) stands for

$$(\psi'_x, \psi''_x) = (\psi_{x1}\,, \psi_{x2}\,) \text{ or } (\psi'_x, \psi''_x) = (\psi_{x3}\,, \psi_{x4}\,)\,.$$

All other matrices can be derived in a similar way. Operators acting on the variables of Ω_f are simpler to derive. There, we do not need to take into account the matching functions.

Example

For better understandability, we illustrate the theory explained above for a concrete example. Take a cell-centred grid for the fluid region Ω_f with $N_{fx} \times N_{fy} \times N_{fz} = 3 \times 7 \times 7$ grid cells. Thus, the number of interface nodes is $N_\Gamma = 49$. For the porous domain Ω_p we use a staggered grid with $N_{px} \times N_{py} \times N_{pz} = 3 \times 4 \times 4$ grid cells. We investigate the matrix notation of the first of the continuity of tractions equations (5.3.8). Here, the interface is assumed to be parallel to the y-z-plane. The fluid domain is located on the right hand side of the interface, the porous domain on its left hand side. Thus, the i-coordinate of the interface nodes is $N_{fx} = 1$, whereas the i-coordinate of the interface nodes of the staggered grid is $i = 3$.

First, we have to find the indices of the four surrounding nodes on the staggered grid for each interface node $(\mathtt{i},\mathtt{j},\mathtt{k})$. They are determined by formulae (5.3.4) and (5.3.5):

$$j = \left\lfloor \left(\mathtt{j} - \frac{1}{2}\right) \frac{h_{fy}}{h_{py}} + 1 \right\rfloor = \left\lfloor \left(\mathtt{j} - \frac{1}{2}\right) \frac{N_{py}}{N_{fy}} + 1 \right\rfloor = \left\lfloor \left(\mathtt{j} - \frac{1}{2}\right) \frac{4}{7} + 1 \right\rfloor ,$$

$$k = \left\lfloor \left(\mathtt{k} - \frac{1}{2}\right) \frac{h_{fz}}{h_{pz}} + 1 \right\rfloor = \left\lfloor \left(\mathtt{k} - \frac{1}{2}\right) \frac{N_{pz}}{N_{fz}} + 1 \right\rfloor = \left\lfloor \left(\mathtt{k} - \frac{1}{2}\right) \frac{4}{7} + 1 \right\rfloor .$$

Hence, we obtain:

$$\begin{array}{c||c|c|c|c|c|c|c} \mathtt{j} & 1 & 2 & 3 & 4 & 5 & 6 & 7 \\ \hline j & 1 & 1 & 2 & 3 & 3 & 4 & 4 \end{array}, \quad \begin{array}{c||c|c|c|c|c|c|c} \mathtt{k} & 1 & 2 & 3 & 4 & 5 & 6 & 7 \\ \hline k & 1 & 1 & 2 & 3 & 3 & 4 & 4 \end{array}. \tag{5.4.4}$$

Using the explanations above, we get for the matrix $T^{B}_{\Omega_p\setminus\partial\Omega_p,1u_x}$:

$$T^{B}_{\Omega_p\setminus\partial\Omega_p,1u_x} = (1-\phi)\frac{2\mu+\lambda}{0.5\;h_{px}} \begin{pmatrix} T^{B*,3,4}_{\Omega_p\setminus\partial\Omega_p,1u_x} & & \mathbf{0} \\ T^{B*,3,4}_{\Omega_p\setminus\partial\Omega_p,1u_x} & & \\ T^{B*,1,2}_{\Omega_p\setminus\partial\Omega_p,1u_x} & T^{B*,3,4}_{\Omega_p\setminus\partial\Omega_p,1u_x} & \\ & T^{B*,1,2}_{\Omega_p\setminus\partial\Omega_p,1u_x} & T^{B*,3,4}_{\Omega_p\setminus\partial\Omega_p,1u_x} \\ & T^{B*,1,2}_{\Omega_p\setminus\partial\Omega_p,1u_x} & T^{B*,3,4}_{\Omega_p\setminus\partial\Omega_p,1u_x} \\ & & T^{B*,1,2}_{\Omega_p\setminus\partial\Omega_p,1u_x} \\ \mathbf{0} & & T^{B*}_{\Omega_p\setminus\partial\Omega_p,1u_x} \end{pmatrix}$$

$$\in \mathbb{R}^{N_\Gamma \times \mathring{N}_{p,u_x}} = \mathbb{R}^{49\times 27} ,$$

where $T^{B*,1,2}_{\Omega_p\setminus\partial\Omega_p,1u_x} := T^{B*}_{\Omega_p\setminus\partial\Omega_p,1u_x}(\psi_{x1}\,,\psi_{x2}\,)$ and $T^{B*,3,4}_{\Omega_p\setminus\partial\Omega_p,1u_x} := T^{B*}_{\Omega_p\setminus\partial\Omega_p,1u_x}(\psi_{x3}\,,\psi_{x4}\,)$ with

$$T^{B*}_{\Omega_p\setminus\partial\Omega_p,1u_x}(\psi'_x,\psi''_x) = (-1)\cdot \left(\begin{array}{ccccccccc} 0 & 0 & \psi''_x & & & & & & \mathbf{0} \\ 0 & 0 & \psi''_x & & & & & & \\ 0 & 0 & \psi'_x & 0 & 0 & \psi''_x & & & \\ & & & 0 & 0 & \psi'_x & 0 & 0 & \psi''_x \\ & & & 0 & 0 & \psi'_x & 0 & 0 & \psi''_x \\ & & & & & & 0 & 0 & \psi'_x \\ \mathbf{0} & & & & & & 0 & 0 & \psi'_x \end{array}\right)$$

$$\in \mathbb{R}^{N_{fy}\times N_{px}(N_{py}-1)} = \mathbb{R}^{7\times 9} ,$$

where $(\psi'_x,\psi''_x) = (\psi_{x1}\,,\psi_{x2}\,)$ or $(\psi'_x,\psi''_x) = (\psi_{x3}\,,\psi_{x4}\,)$, respectively. The matrix $T^{B**}_{\Omega_p\setminus\partial\Omega_p,1u_x}$ has the same structure as $T^{B*}_{\Omega_p\setminus\partial\Omega_p,1u_x}$. Only the entries are different: use ψ_{x3} instead of ψ_{x1} and ψ_{x4} instead of ψ_{x2}.

Values which are mapped from the interface onto the outer boundary of Ω_p are contained in matrix

$T^{B}_{\partial\Omega_p\setminus\Gamma,1u_x}$. This matrix has the following structure:

$$T^{B}_{\partial\Omega_p\setminus\Gamma,1u_x} = (1-\phi)\frac{2\mu+\lambda}{0.5\,h_{px}} \begin{pmatrix} T^{B*,1,2}_{\partial\Omega_p\setminus\Gamma,1u_x} & T^{B**,3,4}_{\partial\Omega_p\setminus\Gamma,1u_x} & \mathbf{0} & \mathbf{0} & \mathbf{0} \\ T^{B*,1,2}_{\partial\Omega_p\setminus\Gamma,1u_x} & T^{B**,3,4}_{\partial\Omega_p\setminus\Gamma,1u_x} & \mathbf{0} & \mathbf{0} & \mathbf{0} \\ \mathbf{0} & T^{B**,1,2}_{\partial\Omega_p\setminus\Gamma,1u_x} & T^{B**,3,4}_{\partial\Omega_p\setminus\Gamma,1u_x} & \mathbf{0} & \mathbf{0} \\ \mathbf{0} & \mathbf{0} & T^{B**,1,2}_{\partial\Omega_p\setminus\Gamma,1u_x} & T^{B**,3,4}_{\partial\Omega_p\setminus\Gamma,1u_x} & \mathbf{0} \\ \mathbf{0} & \mathbf{0} & T^{B**,1,2}_{\partial\Omega_p\setminus\Gamma,1u_x} & T^{B**,3,4}_{\partial\Omega_p\setminus\Gamma,1u_x} & \mathbf{0} \\ \mathbf{0} & \mathbf{0} & \mathbf{0} & T^{B**,1,2}_{\partial\Omega_p\setminus\Gamma,1u_x} & T^{B*,3,4}_{\partial\Omega_p\setminus\Gamma,1u_x} \\ \mathbf{0} & \mathbf{0} & \mathbf{0} & T^{B**,1,2}_{\partial\Omega_p\setminus\Gamma,1u_x} & T^{B*,3,4}_{\partial\Omega_p\setminus\Gamma,1u_x} \end{pmatrix}$$

$$\in \mathbb{R}^{N_\Gamma \times \tilde{N}_{p,u_x}} = \mathbb{R}^{49\times 89}\,,$$

where

$$\begin{aligned} T^{B*,1,2}_{\partial\Omega_p\setminus\Gamma,1u_x} &= T^{B*}_{\partial\Omega_p\setminus\Gamma,1u_x}(\psi_{x1}\,,\psi_{x2}\,)\,, \quad & T^{B*,3,4}_{\partial\Omega_p\setminus\Gamma,1u_x} &= T^{B*}_{\partial\Omega_p\setminus\Gamma,1u_x}(\psi_{x3}\,,\psi_{x4}\,)\,, \\ T^{B**,1,2}_{\partial\Omega_p\setminus\Gamma,1u_x} &= T^{B**}_{\partial\Omega_p\setminus\Gamma,1u_x}(\psi_{x1}\,,\psi_{x2}\,)\,, \quad & T^{B**,3,4}_{\partial\Omega_p\setminus\Gamma,1u_x} &= T^{B**}_{\partial\Omega_p\setminus\Gamma,1u_x}(\psi_{x3}\,,\psi_{x4}\,)\,. \end{aligned}$$

These matrices read as

$$T^{B*}_{\partial\Omega_p\setminus\Gamma,1u_x}(\psi'_x,\psi''_x) = (-1)\cdot$$

$$\left(\begin{array}{ccccc|ccccc|ccccc|ccccc|ccccc} 0&0&0&\psi'_x&0&0&0&0&\psi''_x&0&&&&&&&&&&&&&&&\mathbf{0} \\ 0&0&0&\psi'_x&0&0&0&0&\psi''_x&0&&&&&&&&&&&&&&& \\ &&&&&0&0&0&\psi'_x&0&0&0&0&\psi''_x&0&&&&&&&&&& \\ &&&&&&&&&&0&0&0&\psi'_x&0&0&0&0&\psi''_x&0&&&&& \\ &&&&&&&&&&0&0&0&\psi'_x&0&0&0&0&\psi''_x&0&&&&& \\ &&&&&&&&&&&&&&&0&0&0&\psi'_x&0&0&0&0&\psi''_x&0 \\ \mathbf{0}&&&&&&&&&&&&&&&0&0&0&\psi'_x&0&0&0&0&\psi''_x&0 \end{array}\right)$$

$$\in \mathbb{R}^{N_{fy}\times(N_{px}+2)N_{py}} = \mathbb{R}^{7\times 25}$$

and

$$T^{B**}_{\partial\Omega_p\setminus\Gamma,1u_x}(\psi'_x,\psi''_x) = (-1)\cdot \left(\begin{array}{ccccc|c|c|c|ccccc} 0&0&0&\psi'_x&0&0&0&0&&&&&\mathbf{0} \\ 0&0&0&\psi'_x&0&0&0&0&&&&& \\ &&&&&0&0&0&&&&& \\ &&&&&0&0&0&&&&& \\ &&&&&0&0&0&&&&& \\ &&&&&0&0&0&0&0&0&\psi''_x&0 \\ \mathbf{0}&&&&&0&0&0&0&0&0&\psi''_x&0 \end{array}\right)$$

$$\in \mathbb{R}^{N_{fy}\times 2(N_{px}+2)+(N_{py}-2)} = \mathbb{R}^{7\times 13}\,.$$

In both cases, the tuple of coefficients (ψ'_x,ψ''_x) stands for

$$(\psi'_x,\psi''_x) = (\psi_{x1}\,,\psi_{x2}\,) \text{ or } (\psi'_x,\psi''_x) = (\psi_{x3}\,,\psi_{x4}\,)\,.$$

The transmission condition under consideration (5.3.8) also produces entries in $T^{B}_{\Gamma_p}$, which maps values from the additionally introduces interface to the interface of Ω_p:

$$T^{B}_{\Gamma_p,1u_x} = (1-\phi)\frac{2\mu+\lambda}{0.5\;h_{px}} \begin{pmatrix} T^{B*,1,2}_{\Gamma_p,1u_x} & T^{B*,3,4}_{\Gamma_p,1u_x} & & & \mathbf{0} \\ T^{B*,1,2}_{\Gamma_p,1u_x} & T^{B*,3,4}_{\Gamma_p,1u_x} & & & \\ & T^{B*,1,2}_{\Gamma_p,1u_x} & T^{B*,3,4}_{\Gamma_p,1u_x} & & \\ & & T^{B*,1,2}_{\Gamma_p,1u_x} & T^{B*,3,4}_{\Gamma_p,1u_x} & \\ & & T^{B*,1,2}_{\Gamma_p,1u_x} & T^{B*,3,4}_{\Gamma_p,1u_x} & \\ & & & T^{B*,1,2}_{\Gamma_p,1u_x} & T^{B*,3,4}_{\Gamma_p,1u_x} \\ \mathbf{0} & & & T^{B*,1,2}_{\Gamma_p,1u_x} & T^{B*,3,4}_{\Gamma_p,1u_x} \end{pmatrix}$$

$$\in \mathbb{R}^{N_\Gamma \times \tilde{N}_{p,u_x}} = \mathbb{R}^{49\times 25}\,,$$

where the submatrices $T^{B*,1,2}_{\Gamma_p,1u_x} := T^{B*}_{\Gamma_p,1u_x}(\psi_{x1}\,,\psi_{x2}\,)$ and $T^{B*,3,4}_{\Gamma_p,1u_x} := T^{B*}_{\Gamma_p,1u_x}(\psi_{x3}\,,\psi_{x4}\,)$ are defined as follows:

$$T^{B*}_{\Gamma_p,1u_x}(\psi'_x,\psi''_x) = \begin{pmatrix} \psi'_x & \psi''_x & 0 & 0 & 0 \\ \psi'_x & \psi''_x & 0 & 0 & 0 \\ 0 & \psi'_x & \psi''_x & 0 & 0 \\ 0 & 0 & \psi'_x & \psi''_x & 0 \\ 0 & 0 & \psi'_x & \psi''_x & 0 \\ 0 & 0 & 0 & \psi'_x & \psi''_x \\ 0 & 0 & 0 & \psi'_x & \psi''_x \end{pmatrix} \in \mathbb{R}^{N_{fx}\times(N_{py}+1)} = \mathbb{R}^{7\times 5}\,.$$

All other matrices can be derived analogously.

Chapter 6

Numerical solution for the discrete coupled Biot-Stokes system on non-matching grids

In this chapter we explain the iterative algorithm used for the solution of the Biot-Stokes system of equations on non-matching grids. A domain decomposition method is used. Therefore, we give a short introduction to domain decomposition methods. Then, we explain the separate solvers that are used for the solution of the Biot-Stokes system and finally we present some results.

6.1 Domain decomposition methods

Domain decomposition (DD) methods are powerful tools for complex geometries, multiphysics problems and large systems of equations, as they often arise from the discretisation of partial differential equations (PDEs). The basic idea is to divide the problem domain into subdomains on which the boundary value problems can be solved independently, connected by proper transmission conditions across the interfaces. The DD approach makes it possible to use different numerical strategies in the separate subdomains: different types of elements, different solvers or different orders of approximation can be used. Also the meshing procedure is simplified, because individual meshes can be applied to separate subdomains.

In different areas, the expression ”domain decomposition” has different meanings. In parallel computing, it implies the distribution of data to different processors. In asymptotic analysis, it means the separation of physical phenomena, which are described by different equations. And in preconditioning methods, DD means the subdivision of the solution of a large linear system into smaller ones. Note that these three definitions may occur together in a single problem.

DD methods are usually divided into two classes: methods using overlapping domains, the so-called ”Schwarz methods”, and methods using nonoverlapping domains, the so-called ”substructuring methods”. When these methods use an iterative approach, they are called ”iterative substructuring methods” or ”Schur complement methods”. In the following, we do not dwell on the Schwarz methods, since our model problem deals only with nonoverlapping domains. We refer the interested reader, for example, to [62]. Applications can be found for example in [37] and [39].

Direct substructuring methods have been used in structural analysis already in the early 1950s. As the increasing number of unknowns in the resulting systems of equations could not be handled with the available computer resources, DD was used as a systematic way to organise large structural analysis. The finite element method emerged from one of these methods.

Let us shortly explain the idea of direct substructuring methods. Let $M\mathbf{x} = f$ be a linear system of equations, obtained from the discretisation of PDEs. Then, the entire domain is split into subdomains. Matrix M is consequently also split into parts: parts associated with the interior of the domain and parts associated with the interface. From these submatrices, the Schur complements are calculated independently for each subdomain. Then, a reduced Schur complement problem is solved. If this is solved directly, we call the method substructuring method.

In iterative substructuring methods, the reduced Schur complement problem is solved iteratively. Depending on the choice of the preconditioner for the Schur complement, we obtain different algorithms. For example, choosing $S^{(1)^{-1}}$ (the inverse of the Schur complement in subdomain 1) as preconditioner for the Schur complement, one ends up with the Neumann-Dirichlet Algorithm. That is, because the resulting linear system corresponds to solving the discrete problem in subdomain 1 with a Neumann boundary condition on the interior interface and solving the discrete problem in subdomain 2 with a Dirichlet boundary condition. Using $S^{(1)^{-1}} + S^{(2)^{-1}}$ as preconditioner leads to the Neumann-Neumann method. For details, please see [62].

6.2 The iterative solution algorithm

We solve the Biot-Stokes system in an iterative way. Assume that the boundary conditions are given and that there exists an initial guess at iteration $n = 0$ for the solution of the coupled system. In our case, this initial guess is computed by the solution of the Navier-Stokes-Brinkman system. Define $\mathring{\mathbf{x}}_B := (\mathring{\mathbf{u}}, \mathring{p}_p)^T$, $\hat{\mathbf{x}}_B := (\hat{\mathbf{u}}, \hat{p}_p)^T$, $\tilde{\mathbf{x}}_B := (\tilde{\mathbf{u}}, \tilde{p}_p)^T$, $\mathring{\mathbf{x}}_S := (\mathring{\mathbf{v}}, \mathring{p}_f)^T$, $\hat{\mathbf{x}}_S := (\hat{\mathbf{v}}, \hat{p}_f)^T$ and $\tilde{\mathbf{x}}_S := (\tilde{\mathbf{v}}, \tilde{p}_f)^T$ to be the vectors of unknowns in the interior, on the outer boundaries and on the interface of the porous and the fluid domain, respectively. Recall that the boundary of Ω_p is $\partial\Omega_p = \partial\Omega_{p,\text{fixed}} \cup \Gamma_{\text{in}} \cup \Gamma_{\text{out}} = \partial\Omega_{p,\text{fixed}} \cup \Gamma$, where all parts are disjoint. For the fluid domain, the boundary consists of the following disjoint parts: $\partial\Omega_f = \partial\Omega_{f,\text{fixed}} \cup \partial\Omega_{f,\text{in}} \cup \partial\Omega_{f,\text{out}} \cup \Gamma$ (see figure 2.1 on page 20). Using the operator notation from chapters 4 and 5, we obtain the following iterative procedure. In the porous domain we solve

$$\begin{pmatrix} \mathring{B} \\ \hat{B}_{\Omega_p \backslash \partial\Omega_p} \end{pmatrix} \mathring{\mathbf{x}}_B^n = \begin{pmatrix} \mathring{\mathbf{r}}_B^0 \\ \hat{\mathbf{r}}_B^0 \end{pmatrix} - \begin{pmatrix} \mathring{B}_{\partial\Omega_p \backslash \Gamma} \\ \hat{B} \end{pmatrix} \hat{\mathbf{x}}_B^0 - \begin{pmatrix} \mathring{B}_{\Gamma_p} \\ \mathbf{0} \end{pmatrix} \tilde{\mathbf{x}}_B^{n-1} \quad \text{in } \Omega_p \tag{6.2.1a}$$

with

$$T^B_{\Gamma_p} \tilde{\mathbf{x}}_B^n = -T^B_{\Omega_p \backslash \partial\Omega_p} \mathring{\mathbf{x}}_B^{n-1} - T^B_{\partial\Omega_p \backslash \Gamma} \hat{\mathbf{x}}_B^{n-1} - T^B_{\Omega_f \backslash \partial\Omega_f} \mathring{\mathbf{x}}_S^{n-1} - T^B_{\partial\Omega_f \backslash \Gamma} \hat{\mathbf{x}}_S^{n-1} - T^B_{\Gamma_f} \tilde{\mathbf{x}}_S^{n-1} \quad \text{on } \Gamma\,. \tag{6.2.1b}$$

Then, we solve in the fluid domain

$$\begin{pmatrix} \mathring{S} \\ \mathbf{0} \end{pmatrix} \mathring{\mathbf{x}}_S^n = \begin{pmatrix} \mathring{\mathbf{r}}_S^0 \\ \hat{\mathbf{r}}_S^0 \end{pmatrix} - \begin{pmatrix} \mathring{S}_{\partial\Omega_p \backslash \Gamma} \\ \hat{S} \end{pmatrix} \hat{\mathbf{x}}_S^0 - \begin{pmatrix} \mathring{S}_{\Gamma_f} \\ \mathbf{0} \end{pmatrix} \tilde{\mathbf{x}}_S^{n-1} \quad \text{in } \Omega_f \tag{6.2.1c}$$

with

$$T^S_{\Gamma_f}\tilde{\mathbf{x}}^n_S = -T^S_{\Omega_p\backslash\partial\Omega_p}\mathring{\mathbf{x}}^n_B - T^S_{\partial\Omega_p\backslash\Gamma}\mathring{\mathbf{x}}^n_B - T^S_{\Gamma_p}\tilde{\mathbf{x}}^n_B \quad \text{on}\,\Gamma\,. \tag{6.2.1d}$$

$n \in \mathbb{N}$, $n \geq 1$ denotes the number of the overall iteration loop. This procedure (solution of equations (6.2.1a) - (6.2.1d)) is repeated until a certain stopping criterion is fulfilled.
Equation (6.2.1a) corresponds to the Biot equations. We solve this equation for $\mathring{\mathbf{x}}_B$ in the current n-iteration loop. The right hand side contains the boundary conditions on $\partial\Omega_{p,\text{fixed}}$. They do not change during the iteration, we always have no flux ($\mathbf{q} \cdot \mathbf{n} = 0$) and no displacement ($\mathbf{u} = \mathbf{0}$) condition there. Thus, the superscript of the right hand side terms is 0. The solution of the transmission conditions (6.2.1b) delivers the boundary conditions at the interface. Recall, $\partial\Omega_{p,\text{in}} = \Gamma_{\text{in}}$ and $\partial\Omega_{p,\text{out}} = \Gamma_{\text{out}}$. We solve equation (6.2.1b) for $\tilde{\mathbf{x}}^n_B$ in the current n-iteration loop. The first and second terms on the right hand side contain values from the interior and the outer boundaries of Ω_p. They are taken from the previous n-iteration loop. The same holds for the third till fifth term. These terms contain internal, outer boundary and interface values of Ω_f, which were obtained in the solution of the Stokes equations, or, if $n = 1$, by the initial guess, respectively.
Equation (6.2.1c) are the Stokes equations, including boundary conditions on $\partial\Omega_{f,\text{in}}$, $\partial\Omega_{f,\text{out}}$ and $\partial\Omega_{f,\text{fixed}}$. These are also values which do not change during the computation. On $\partial\Omega_{f,\text{fixed}}$ we always have no-slip boundary conditions ($\mathbf{v} = 0$) and the inflow and outflow conditions (inflow: $\mathbf{v} = \mathbf{v}_0$, outflow: $p_f = p_{f,0}$) are established by the solution of the Navier-Stokes-Brinkman system. The boundary conditions at $\Gamma_{\text{in}} = \partial\Omega_{f1,\text{out}}$ and $\Gamma_{\text{out}} = \partial\Omega_{f2,\text{in}}$ are obtained by solution of equation (6.2.1d). The terms on the right hand side contain values of Ω_p, which were computed in the current n-iteration loop. Therefore, the terms on the right hand side have superscript n.

In figure 6.1 we have depicted the entire iterative solution algorithm. Let us comment on the separate parts and steps of the algorithm. Our iterative procedure consists of four nested iteration loops: the time-iteration loop, the n-iteration loop and the n_p- and n_f-iteration loops. The outermost iteration loop is the time-iteration loop. This is especially important for unsteady problems. The next loop to the interior is the n-iteration loop. Within one of these loops we solve the Biot equations and the Stokes equations. The two innermost loops are for the Biot equations and the Stokes equations itself. They are also solved in iterative procedures. The stopping criteria of all these iteration loops will be described in the next paragraph.
We start our iteration procedure at initial time $t = t_s$, $n = 1$, $n_p = 0$, $n_f = 0$. In the beginning we solve the Navier-Stokes-Brinkman system to obtain an initial guess for the boundary conditions and initial conditions in the fluid and porous domain. These initial guesses are stored in the vectors $\mathbf{x}_B = (\mathbf{u}^0, p^0_p)^T$ and $\mathbf{x}_S = (\mathbf{v}^0, p^0_f)^T$ and they are values at $n = 0$. Then, we start the time-iteration loop and the n-iteration loop. First, we solve the Biot poroelasticity model (6.2.1a) and thus, also start the n_p-iteration loop. This iteration loop is terminated when a certain stopping criterion is fulfilled. There are various possibilities for this stopping criterion. It will be discussed later. If the stopping criterion is fulfilled, the transmission conditions (6.2.1b) are solved in order to obtain the current boundary conditions for the Stokes equations along the interface. Afterwards, we start the n_f-iteration loop, where the Stokes equations (6.2.1c) are solved. We leave this loop as soon as the stopping criterion is fulfilled. Then, we check if all the transmission conditions are fulfilled. Within the n-iteration loop we use ”old” values when solving the transmission conditions to obtain boundary values for the Stokes equations. So, we have to check whether they are fulfilled

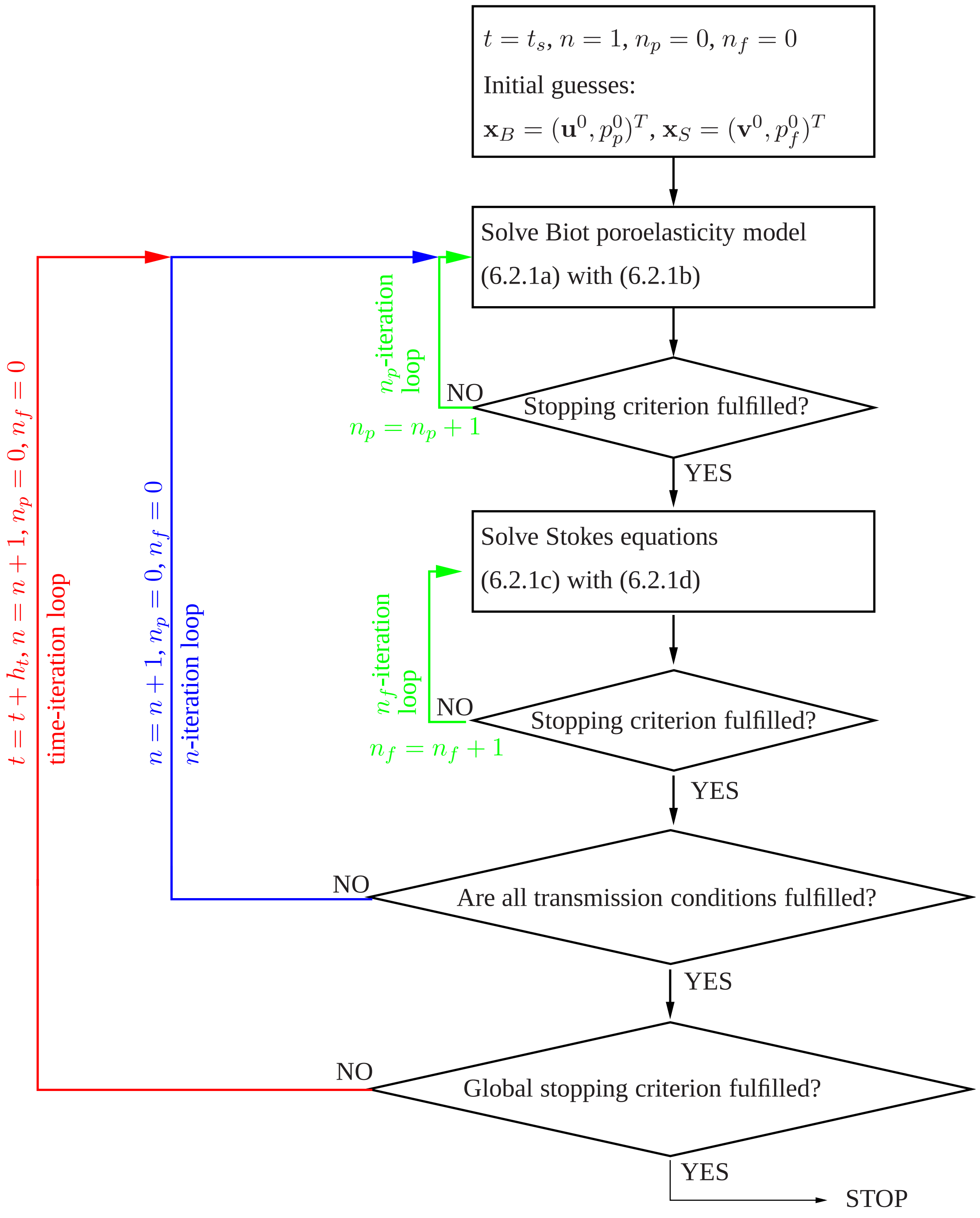

Figure 6.1: General diagram of the iterative algorithm for the solution of the Biot-Stokes system of equations.

with the current values, i.e. whether the norm of the residual is smaller than a certain tolerance ϵ:

$$|| \begin{pmatrix} T^B_{\Omega_p\backslash\partial\Omega_p} \\ T^S_{\Omega_p\backslash\partial\Omega_p} \end{pmatrix} \mathring{\mathbf{x}}^n_B + \begin{pmatrix} T^B_{\partial\Omega_p\backslash\Gamma} \\ T^S_{\partial\Omega_p\backslash\Gamma} \end{pmatrix} \hat{\mathbf{x}}^n_B + \begin{pmatrix} T^B_{\Gamma_p} \\ T^S_{\Gamma_p} \end{pmatrix} \tilde{\mathbf{x}}^n_B + \begin{pmatrix} T^B_{\Omega_f\backslash\partial\Omega_f} \\ \mathbf{0} \end{pmatrix} \mathring{\mathbf{x}}^n_S + \begin{pmatrix} T^B_{\partial\Omega_f\backslash\Gamma} \\ \mathbf{0} \end{pmatrix} \hat{\mathbf{x}}^n_S + \begin{pmatrix} T^B_{\Gamma_f} \\ T^S_{\Gamma_f} \end{pmatrix} \tilde{\mathbf{x}}^n_S || \le \epsilon\,. \tag{6.2.2}$$

If this is not the case, the n-iteration counter is increased by 1, n_p and n_f are set to 0 and then, a new n-iteration loop is started. This is done until condition (6.2.2) is fulfilled. Then, we check the global stopping criterion. If this is not fulfilled, the time step is increased by h_t, n is increased by 1, n_p and n_f are set to 0 and a new time-iteration loop is started. If the global stopping criterion is fulfilled, the iterative algorithm is stopped.

Stopping criteria

For the stopping criteria in the above iteration procedure there are various choices. One possibility is to solve the subdomain problems exactly in every n-iteration loop. That means, we solve the Biot and the Stokes equations accurately. Hence, the stopping criteria for the n_p-iteration loop is

$$|| \begin{pmatrix} \mathring{B} \\ \hat{B}_{\Omega_p \setminus \partial\Omega_p} \end{pmatrix} \mathring{\mathbf{x}}_B^n + \begin{pmatrix} \mathring{B}_{\partial\Omega_p \setminus \Gamma} \\ \hat{B} \end{pmatrix} \hat{\mathbf{x}}_B^0 + \begin{pmatrix} \mathring{B}_{\Gamma_p} \\ \mathbf{0} \end{pmatrix} \tilde{\mathbf{x}}_B^{n-1} - \begin{pmatrix} \mathring{\mathbf{r}}_B^0 \\ \hat{\mathbf{r}}_B^0 \end{pmatrix} || \leq \epsilon_B \tag{6.2.3}$$

and for the n_f-iteration it is

$$|| \begin{pmatrix} \mathring{S} \\ \mathbf{0} \end{pmatrix} \mathring{\mathbf{x}}_S^n + \begin{pmatrix} \mathring{S}_{\partial\Omega_p \setminus \Gamma} \\ \hat{S} \end{pmatrix} \hat{\mathbf{x}}_S^0 + \begin{pmatrix} \mathring{S}_{\Gamma_f} \\ \mathbf{0} \end{pmatrix} \tilde{\mathbf{x}}_S^{n-1} - \begin{pmatrix} \mathring{\mathbf{r}}_S^0 \\ \hat{\mathbf{r}}_S^0 \end{pmatrix} || \leq \epsilon_S \, , \tag{6.2.4}$$

where ϵ_B and ϵ_S are certain tolerance values.
Another possibility is to solve the subdomain problems inexactly, i.e. to run only a certain number of n_p- and n_f-iterations. Then the stopping criterion is to reach a maximum number of iterations:

$$n_p \leq n_{p,\text{max}} \tag{6.2.5}$$

and

$$n_f \leq n_{f,\text{max}} \, . \tag{6.2.6}$$

At the end of the n-iteration loop we always check criterion (6.2.2).
The global stopping criterion depends on the problem that is solved. For steady state problems, one has to check if the steady state is reached. This can be done by checking the displacements or the pressure, or any other quantity in the porous domain. In steady state problems, there is no dependence on the time. Therefore, the stopping criterion is also time independent. So, we check if

$$||\mathbf{u}^n - \mathbf{u}^{n-1}|| \leq \epsilon_n \, .$$

From our observations, this condition is fulfilled when (6.2.2) is fulfilled. For unsteady problems, this is not the case. Then, one can check for example if the transmission conditions are fulfilled.
There exist many choices for stopping criteria in such kind of coupling procedures. It goes behind the scope of a PhD thesis to investigate all of them. In our numerical examples, we tested both, stopping criteria (6.2.3) and (6.2.4) as well as (6.2.5) and (6.2.6). In the first case, we obtained an overall convergence. The results will be presented in sections 6.4 - 6.6. Solving the subdomain problems inaccurately, we did not obtain an overall convergence. Condition (6.2.2) was not fulfilled.

Parameters - choice and computation

For our test examples, we use water as fluid with density $\varrho = 1000 \, \frac{\text{kg}}{\text{m}^3}$, dynamic viscosity $\eta = 10^{-3}$ Pa s (values for 20 degrees Celsius and an air pressure of 1 bar), Reynolds number Re = 10^{-4}. We consider laminar incompressible flow. Thus, the compressibility $\beta = 0 \, \frac{\text{m}^2}{\text{N}}$ and we choose the flow rate to be $7.2 \cdot 10^{-4} \, \frac{\text{l}}{\text{min}}$.

For the porous medium, we need to specify the porosity ϕ and the permeability k. The solid material is characterised by Young's modulus E and corresponding Poisson's ratio ν_s. The effective parameters can then be computed by formulae (1.3.13), (1.3.14) and (1.3.15).

The choices we have taken in the numerical examples are mentioned at the corresponding places.

Coupling of different meshes and solvers

As mentioned earlier, we have to account for the different grids and units that are used by the various software packages we use. The coupling between the cell-centred fluid solver grid and the staggered grid in the porous medium has been explained extensively in chapter 5. What has not been described there is the transfer of the pressure values at the interface from the solution of the Navier-Stokes-Brinkman system to the staggered grid. The Navier-Stokes-Brinkman system is solved in the entire domain Ω. So, the pressure values are computed everywhere. In both fluid subdomains, the pressure is almost constant, whereas it decreases linearly throughout the porous medium. Thus, using the values from either side of the interface would not deliver proper values. Therefore, we do harmonic averaging to calculate the pressure values at the interface. Let c_f and c_p be coefficients in the fluid grid cell and in the porous grid cell, respectively. Then, the pressure p_Γ at the interface is obtained by

$$p_\Gamma = \frac{c_f \, p_p + c_p \, p_f}{c_f + c_p} \, .$$

Afterwards, bilinear interpolation is applied to compute the pressure values at the corresponding nodes of the staggered grid.

The Navier-Stokes-Brinkman system and the Stokes equations are both solved in physical units. The poroelasticity solver is written in dimensionless form. The scaling of variables and parameters seems to be a simple task, but very often it is a source of error. Therefore, we mention here the formulae how to nondimensionalise the quantities. Let $\mathrm{L_r}$ be the characteristic length of the porous medium and let η_r, k_r, μ_r, λ_r be some reference values. Then, the dimensionless variables are (cf. [46])

$$\begin{aligned}
&x := \frac{x}{\mathrm{L_r}}\,, \quad y := \frac{y}{\mathrm{L_r}}\,, \quad z := \frac{z}{\mathrm{L_r}}\,, \quad u_x := \frac{u_x}{\mathrm{L_r}}\,, \quad u_y := \frac{u_y}{\mathrm{L_r}}\,, \quad u_z := \frac{u_z}{\mathrm{L_r}}\,,\\
&p_p := \frac{p_p}{2\mu_\mathrm{r} + \lambda_\mathrm{r}}\,, \quad \mu := \frac{\mu}{2\mu_\mathrm{r} + \lambda_\mathrm{r}}\,, \quad \lambda := \frac{\lambda}{2\mu_\mathrm{r} + \lambda_\mathrm{r}}\,, \quad k := \frac{k}{k_\mathrm{r}}\,, \quad \eta := \frac{\eta}{\eta_\mathrm{r}}\,,\\
&v^p_{fx} := \frac{\mathrm{L_r}\eta_\mathrm{r}}{(2\mu_\mathrm{r} + \lambda_\mathrm{r})k_\mathrm{r}}\, v^p_{fx}\,, \quad v^p_{fy} := \frac{\mathrm{L_r}\eta_\mathrm{r}}{(2\mu_\mathrm{r} + \lambda_\mathrm{r})k_\mathrm{r}}\, v^p_{fy}\,, \quad v^p_{fz} := \frac{\mathrm{L_r}\eta_\mathrm{r}}{(2\mu_\mathrm{r} + \lambda_\mathrm{r})k_\mathrm{r}}\, v^p_{fz}\,,\\
&t := \frac{(2\mu_\mathrm{r} + \lambda_\mathrm{r})k_\mathrm{r}}{\mathrm{L_r^2}\eta_\mathrm{r}}\, t\,, \quad f_p := \frac{\mathrm{L_r^2}\eta_\mathrm{r}}{(2\mu_\mathrm{r} + \lambda_\mathrm{r})k_\mathrm{r}}\, f_p\,.
\end{aligned}$$

For the sake of simplicity, we use the same notation for dimensional and dimensionless values.

6.3 The software for the solution of the separate problems in the subdomains

For the iterative solution of the Biot-Stokes system of equations, we use three different software packages, which all were developed at the Fraunhofer ITWM (Poro3D only partially).

For the solution of the Navier-Stokes-Brinkman system (see section 1.3.3 and [32], [40]) we use SuFiS®[1], a software developed at the Fraunhofer ITWM. SuFiS® stands for ”suction filter simulation” and is based on the finite volume (FV) method on a cell-centred Cartesian grid. To solve the Navier-Stokes-Brinkman system, a SIMPLE-type projection method is applied. The idea behind is operator splitting. The equations are solved consecutively to decouple the computation of the pressure from the computation of the velocities. Starting with an initial guess for the pressure, the momentum equations are solved to obtain an intermediate velocity field. Since this usually does not fulfil mass conservation, a pressure (or pressure-correction) equation of Poisson type is solved in every time step. In the final step the velocity is corrected to fulfil the momentum equations. The intermediate velocity field is nonsolenoidal (not divergence-free). The pressure correction step can be viewed as the projection of the velocity field into solenoidal space. Therefore this type of methods are called projection methods. More details can be found in [18], [20] or [27]. For more details on the software SuFiS® and applications in oil filtration simulation, please see [32], [33] and [68].

The Stokes equations in the fluid domain is solved by CoRheoS, which stands for ”Complex Rheology Solver”. It was developed at the Fraunhofer ITWM for the solution of complex fluids, which comprise different kinds of fluids in technical, biological and medical applications, as well as suspensions. Current topics of research are granular flows and strongly non-Newtonian fluids, see [69] and [70]. Readers interested in viscoelastic fluids, we recommend [47]. We use CoRheoS for the solution of the Stokes equations. This is based on the FV Method on a cell-centred Cartesian grid, using the SIMPLE algorithm.

The Biot poroelasticity equations are discretised on a staggered grid and solved by a multigrid solver, see [21]. Multigrid methods are among the most efficient methods known today since the convergence rate is independent of the problem size. A system of n unknowns can be solved in $\mathcal{O}(n)$ time. The basic idea of multigrid is the use of a multilevel strategy. A sequence of related problems $P^{(i)}, P^{(i-1)}, ..., P^{(1)}$, $i \in \mathbb{N}$, is solved on increasingly coarse grids, where the solution to $P^{(i-1)}$ is a good approximation to the error in the solution of $P^{(i)}$. Starting with an approximate solution on the finest grid, the residual is computed and restricted to the next coarser grid. Then, the coarser problem is solved recursively. From the coarsest grid we map the solution back to the fine grid, subtract the correction computed on the coarse grid from the fine grid solution and improve the solution on the finest grid. For a more detailed description, please see [15]. The Biot poroelasticity equations are solved by Poro3D. This solver is based on the method described above. It solves the poroelasticity equations in a coupled way. Poro3D has been developed by a team from Zaragoza, Spain and the Fraunhofer SCAI, Germany. A. Naumovich of the Fraunhofer

---

[1] SuFiS® registered trademark of SPX Corporation / IBS FILTRAN

ITWM extended the solver for multilayer material (see [46]).

6.4 Steady state examples

In this section we present two steady state examples. We analyse the effect of changes in the elastic properties, the porosity and permeability of the porous medium on stresses, pressure and displacements inside the porous medium for two different geometries.

6.4.1 Example 1: Filter of dimension $2 \times 3 \times 3$ mm^3

As first example we consider a fluid flow channel of dimension $14 \times 3 \times 3$ mm^3 with a porous medium of dimension $2 \times 3 \times 3$ mm^3 inside, as displayed in figure 0.1 on page 3. The fluid channel parts before and behind the porous medium are both 6 mm long.

First, we study the relation between the stiffness of the porous medium and the stresses which are caused by the fluid flow through it. Figure 6.2(a) shows the relation between the E-modulus of the solid material the porous medium consists of and the maximum stress component $\sigma_{p,xx}$. Note that the E-modulus on the x-axis is the E-modulus of the solid material and not the effective E-modulus of the porous medium. The effective E-modulus can be computed using formula (1.3.13).
As can be seen in figure 6.2(a), the maximum stress component $\sigma_{p,xx}$ decreases when the E-modulus increases. This is clear, since an increasing E-modulus signifies that the material is stiffer and thus it better resists the fluid flow. This implies that we obtain smaller displacements for stiffer materials. The maximum stress values are located in the points $(0.25/1.5/1.5)$ and $(1.75/1.5/1.5)$ (this is for a grid with $8 \times 12 \times 12$ grid cells), i.e. in the middle of the layers next to inflow and outflow interface. The relation between the E-modulus and the maximum displacement in flow direction is shown in figure 6.2(b). The maximum displacement in flow direction appears in the middle of the porous medium (points $(0.875/1.5/1.5)$ and $(1.125/1.5/1.5)$ in a grid with $8 \times 12 \times 12$ grid cells).
Figures 6.3(a) and 6.3(b) show profiles of the stress component $\sigma_{p,xx}$ for two different materials with E-modulus E $= 6$ GPa and E $= 200$ GPa. The cross-section is parallel to the flow direction, located exactly in the middle of the porous medium. As one can see, the stresses in the softer material are much higher than in the stiffer one. Figures 6.4(a) and 6.4(b) underline that result. Here, one can see stress profiles in a layer next to the inflow which is perpendicular to the flow direction. The highest stresses occur in the middle of this plane, because here we have the largest displacements. Towards the boundaries, the stresses first decrease and then increase again (in absolute value). Along the boundaries where the porous medium is fixed (and there, especially in the corners), we have also high stress values. They occur because the fixing of the porous medium counteracts the deformation.
The pressure profiles for these two materials are displayed in figures 6.5(a) and 6.5(b). The pressure decreases more or less linearly and is approximately the same for both materials.
The number of iterations needed for the various computations can be learned from table 6.1. This table shows the total number of iterations, as well as the separate number of iterations needed for

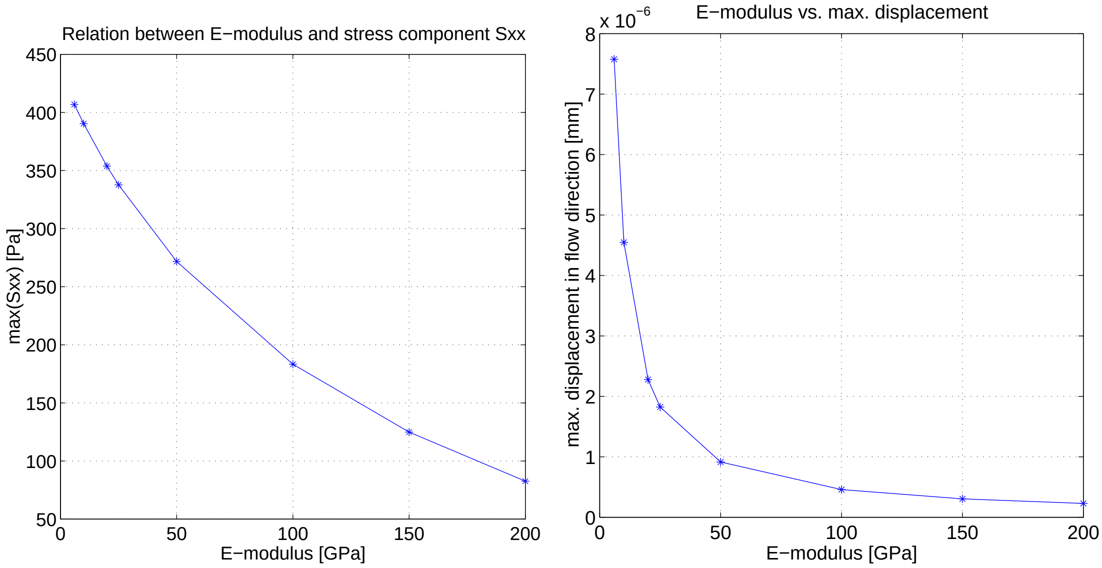

(a) (b)

Figure 6.2: Example 1: Relation between the E-modulus [GPa] and the maximum stress component $\sigma_{p,xx}$ [Pa] (a) and the maximum displacement in flow direction [mm] (b) for a porous medium with Poisson's ratio $\nu_s = 0.14$, porosity $\phi = 65\%$ and permeability $k = 10^{-6}$ mm^2.

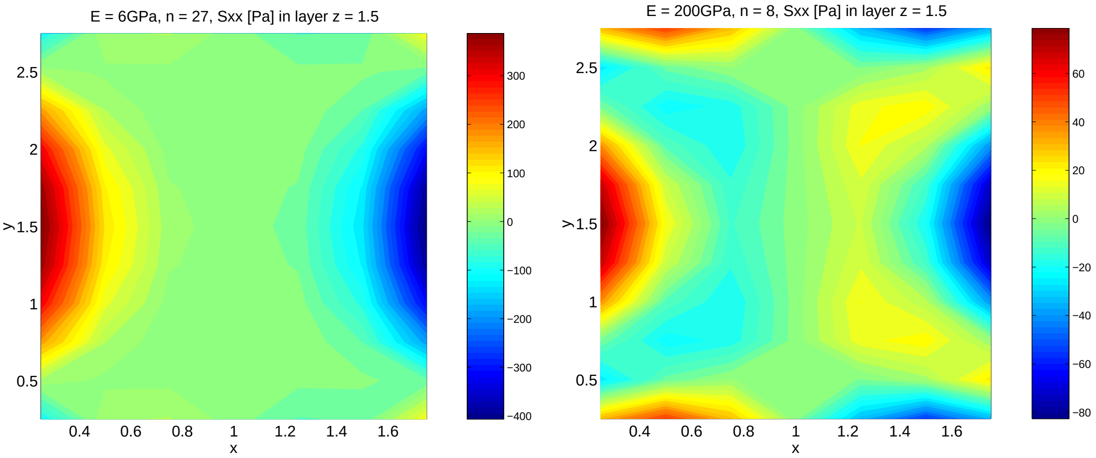

(a) (b)

Figure 6.3: Example 1: Stress profile in cross-section $z = 1.5$ for the porous medium with E-modulus E $=$ 6 GPa (a) and E-modulus E $=$ 200 GPa (b). Both materials have Poisson's ratio $\nu_s = 0.14$, porosity $\phi = 65\%$ and permeability $k = 10^{-6}$ mm^2. Note that the plots show only the stresses in the interior of Ω_p, the boundary values are not contained.

the solution of the Biot poroelasticity system and the Stokes equations in both fluid domains Ω_{f1} and Ω_{f2}. All computations are done with a time step $\Delta h_t = 0.005$ s.

Next we study the effect of a varying permeability. From a set of test computations we found out that the stress decreases when the permeability increases (see figure 6.6(a)). For a low permeabil-

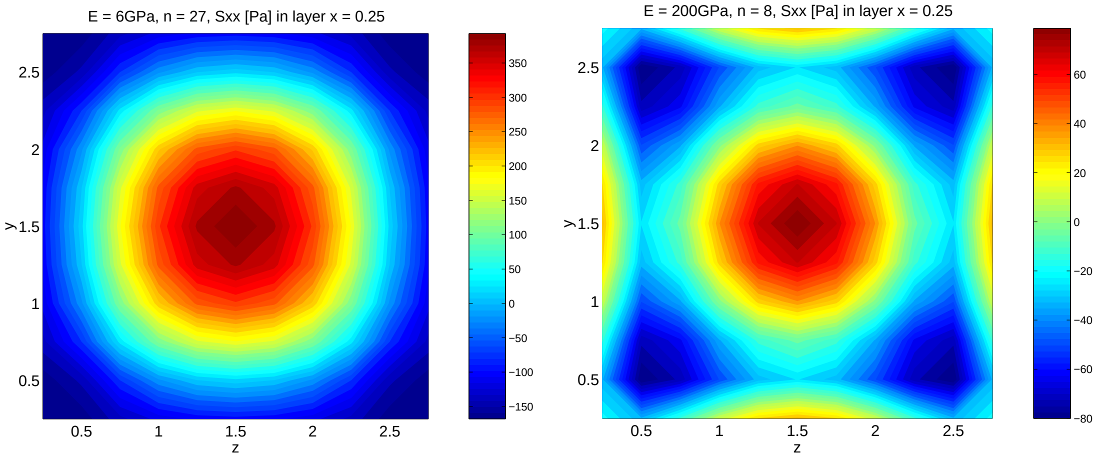

(a)

(b)

Figure 6.4: Example 1: Stress profile in cross-section $x = 0.25$ for the porous medium with E-modulus E $=$ 6 GPa (a) and E-modulus E $=$ 200 GPa (b). Both materials have Poisson's ratio $\nu_s = 0.14$, porosity $\phi = 65\%$ and permeability $k = 10^{-6}$ mm^2. Note that the plots show only the stresses in the interior of Ω_p, the boundary values are not contained.

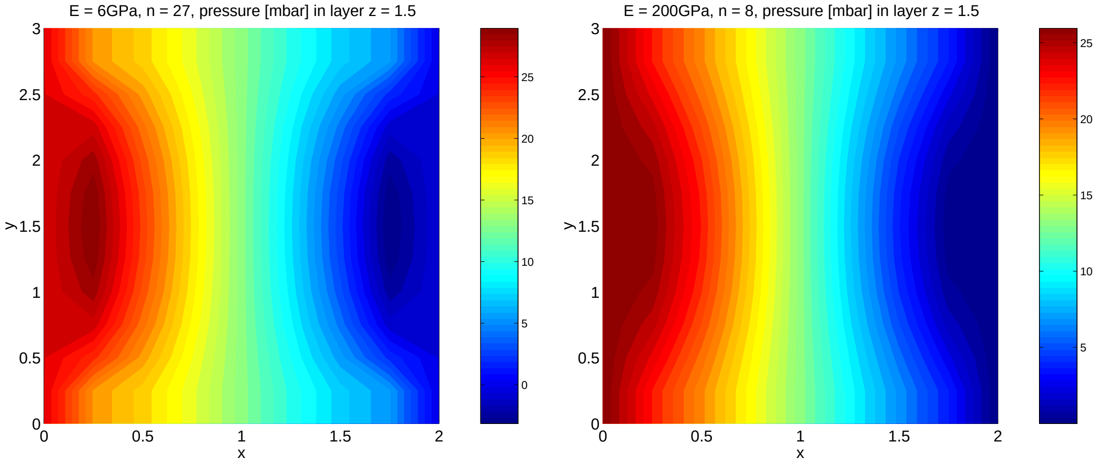

(a)

(b)

Figure 6.5: Example 1: Pressure profile in cross-section $z = 1.5$ for the porous medium with E-modulus E $=$ 6 GPa (a) and the porous medium with E-modulus E $=$ 200 GPa (b).

ity, the porous medium has a higher resistance to the fluid flow. Increasing permeability implies less resistance to the fluid flow and therefore, the stresses decrease. Decreasing stresses lead to decreasing displacements (see figure 6.6(b)).

Figures 6.7(a) and 6.7(b) show profiles of the stress component $\sigma_{p,xx}$ in a cross-section parallel to the fluid flow for a low permeability ($k = 10^{-8}$ mm^2) and a higher permeability ($k = 10^{-5}$ mm^2). For better comparability all these computations are done for a material with E-modulus 100 GPa and porosity $\phi = 65\%$. The highest stresses appear near the inflow and outflow interface of the porous medium in the middle of the y-z-plane and close to the fixed boundaries. This is for the

E [GPa]	nr of n-iteration-loops	nr iterations Biot (Ω_p)	nr iterations Stokes (Ω_{f1})	nr iterations Stokes (Ω_{f2})	total nr of iterations
200	9	963	76	81	1120
150	8	848	67	72	987
100	7	735	58	63	856
50	5	510	40	35	585
25	7	693	58	49	800
20	16	1552	139	112	1803
10	21	2583	184	147	2914
6	28	26432	247	196	26875

Table 6.1: Example 1: Number of iterations for varying E-modulus and porosity $\phi = 65\%$, permeability $k = 10^{-6}$ mm^2. This is for a grid with $8 \times 12 \times 12$ grid cells.

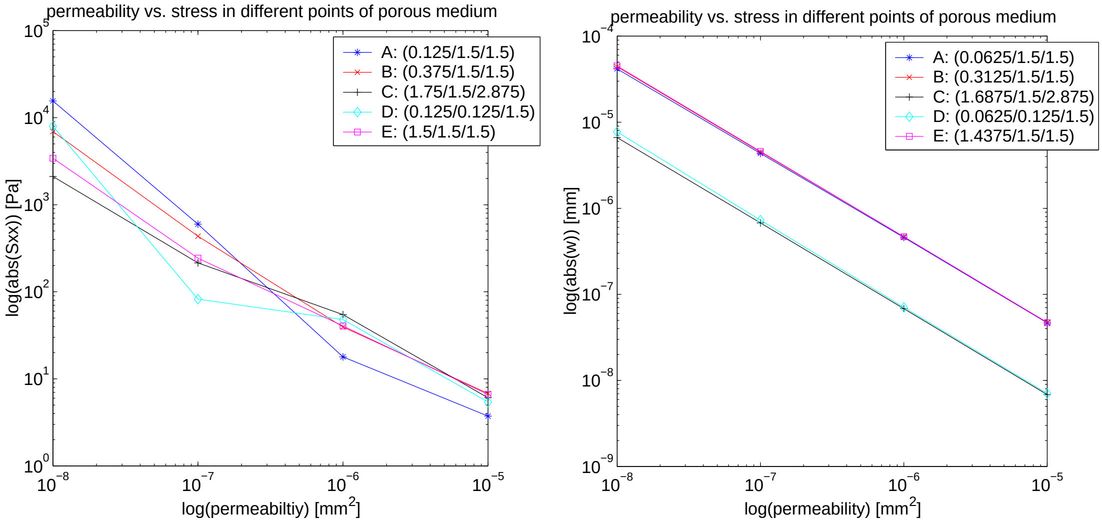

(a) (b)

Figure 6.6: Example 1: Relation between the permeability [mm^2] and the stress component $\sigma_{p,xx}$ [Pa] (a) and the displacement in flow direction [mm] (b) for different points in the porous medium. Note that x-axes and y-axes are both logarithmic. This is for grid with $16 \times 24 \times 24$ grid cells.

same reasons as mentioned above.
Table 6.2 shows the number of iterations needed for the computations, as well as the points where the maximum stress and the maximum displacement appear. Due to symmetry of the $y-z-$plane, the maximum values are located in the middle of this plane.

Now we analyse the effect of the porosity. For the test computations we are using a material with E-modulus E $= 100$ GPa, Poisson's ratio $\nu_s = 0.14$ and permeability $k = 10^{-6}$ mm^2. In figure 6.8(a) we plotted the development of the stress component $\sigma_{p,xx}$ for various points in the porous medium. Note that the absolute value of $\sigma_{p,xx}$ is shown, so, minima in the figure indicate a crossover from positive to negative values or vice versa. We only attach importance to the absolute

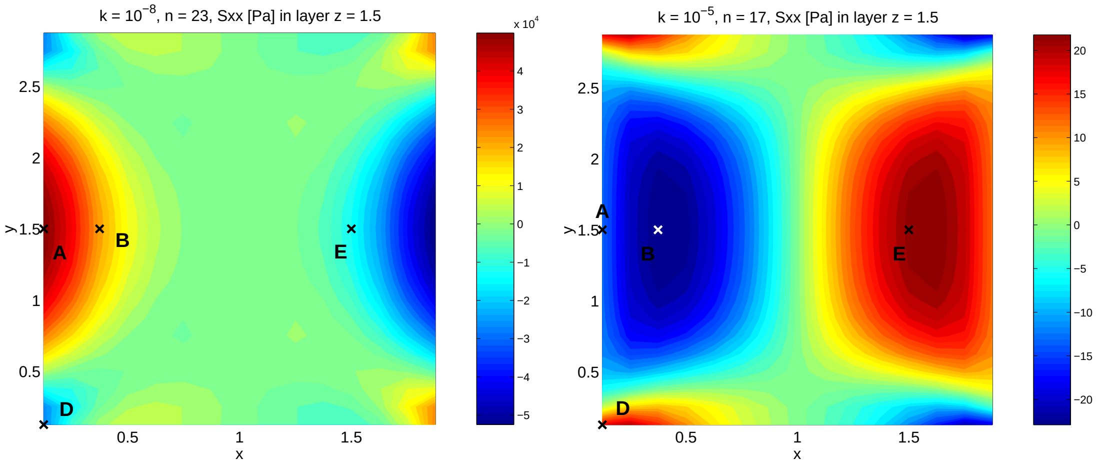

(a) (b)

Figure 6.7: Example 1: Stress profile in cross-section $z = 1.5$ for the porous medium with permeability $k = 10^{-8}$ mm^2 (a) and permeability $k = 10^{-5}$ mm^2 (b). Both materials have E-modulus E $= 100$ GPa, Poisson's ratio $\nu_s = 0.14$ and porosity $\phi = 65\%$. Note that the plots show only the stresses in the interior of Ω_p, the boundary values are not contained. The crosses indicate the points for which $\sigma_{p,xx}$ and u_x are plotted in figures 6.6(a) and 6.6(b).

k[mm^2]	nr of n-iteration-loops	nr iter. Biot (Ω_p)	nr iter. Stokes (Ω_{f1})	nr iter. Stokes (Ω_{f2})	total nr of iterations	grid node (max($\sigma_{p,xx}$))	grid node (max(u_x))
10^{-8}	–	–	–	–	–	–	–
	24	9600	260	144	10004	$(0.125/1.5/1.5)$	$(1.1875/1.5/1.5)$
10^{-7}	5	525	53	45	623	$(0.25/1.5/1.5)$	$(1.125/1.5/1.5)$
	3	1302	27	24	1353	$(0.25/1.5/1.5)$	$(1.0625/1.5/1.5)$
10^{-6}	4	444	31	36	511	$(1.5/1.5/1.5)$	$(1.625/1.5/1.5)$
	4	1816	43	44	1903	$(1.75/1.5/2.875)$	$(1.5625/1.5/1.5)$
10^{-5}	33	3729	292	297	4318	$(0.5/1.5/1.5)$	$(1.625/1.5/1.5)$
	18	8335	190	216	8741	$(0.1375/1.5/1.5)$	$(1.6875/1.5/1.5)$

Table 6.2: Example 1: Number of iterations and location of maximum stress component $\sigma_{p,xx}$ and maximum x-displacement for varying permeability. The first line in each row is for a grid with $8 \times 12 \times 12$ grid cells, the second line for a grid with $16 \times 24 \times 24$ grid cells.

value of $\sigma_{p,xx}$, because that is the decisive factor when caring about the break of a filter. Figure 6.8(b) shows the displacements u_x in flow direction for approximately the same points as for $\sigma_{p,xx}$ in figure 6.8(a). We have only "approximately" the same points due to the staggered grid. The grid nodes for u_x are shifted half a grid cell in x-direction compared to $\sigma_{p,xx}$, see definitions (5.1.2) and (5.1.3). As one would expect, the displacements increase for increasing porosity, since a filter with higher porosity offers less resistance to the fluid flow. The location of max($\sigma_{p,xx}$) and max(u_x) can be learned from table 6.3. There, also the number of iterations are recorded. The first line of a row in the table gives the data for a grid with $8 \times 12 \times 12$ grid cells, the second line for a grid

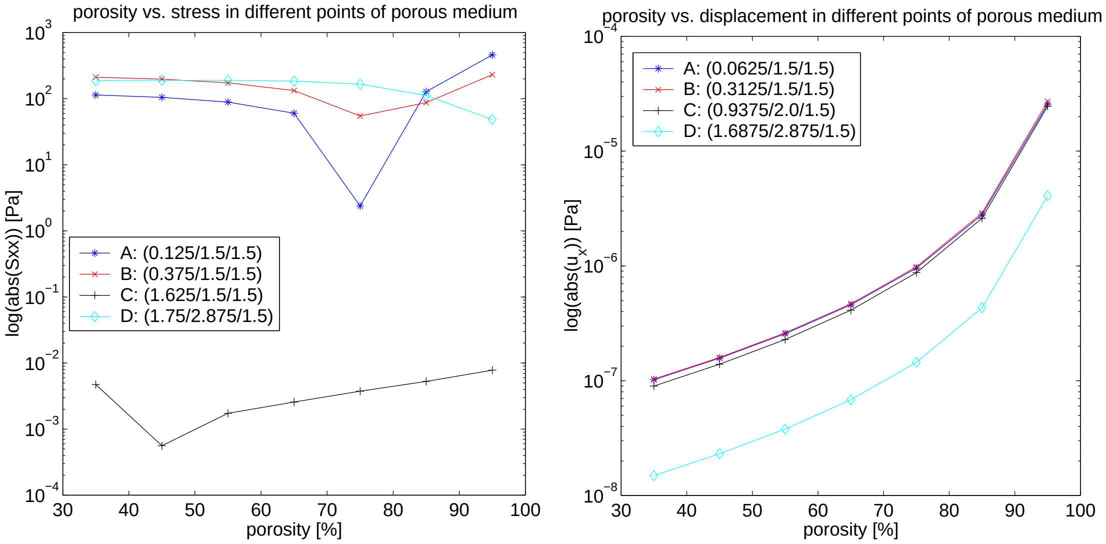

(a) (b)

Figure 6.8: Example 1: Relation between the porosity [%] and the stress component $\sigma_{p,xx}$ [Pa] (a) and the displacement in flow direction [mm] (b) for different points in the porous medium. Note that the y-axes are logarithmic. This is for grid with $16 \times 24 \times 24$ grid cells.

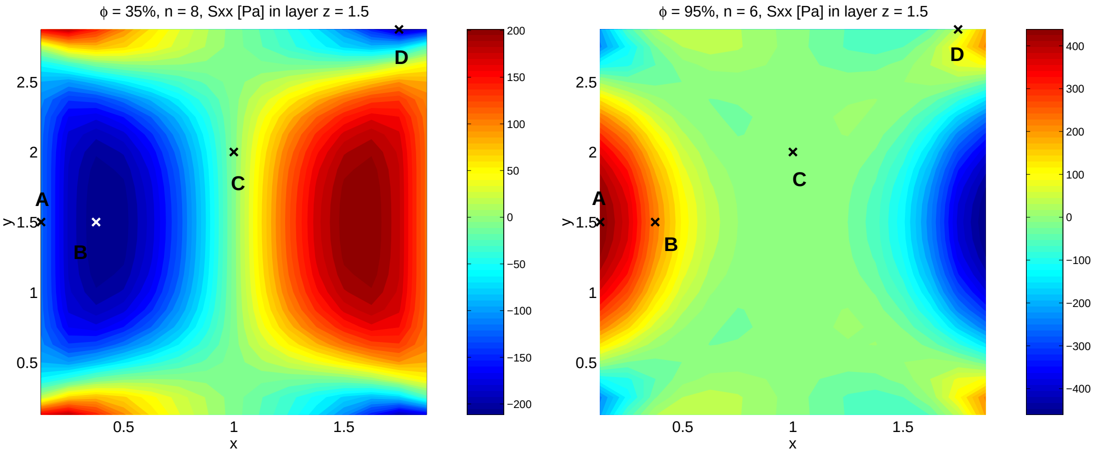

(a) (b)

Figure 6.9: Example 1: Stress profile in cross-section $z = 1.5$ for the porous medium with porosity $\phi = 35\%$ (a) and porosity $\phi = 95\%$ (b). Both materials have an E-modulus E $= 100$ GPa and permeability $k = 10^{-6}$ mm^2. Note that the plots show only the stresses in the interior of Ω_p, the boundary values are not contained. The crosses indicate the points for which $\sigma_{p,xx}$ and u_x are plotted in figures 6.8(a) and 6.8(b).

with $16 \times 24 \times 24$ grid cells. Figures 6.9(a) and 6.9(b) give an impression of the stress profiles in a cross-section parallel to the fluid flow direction for two different porosities. The crosses indicate the points for which $\sigma_{p,xx}$ and u_x are plotted in figures 6.8(a) and 6.8(b).

$\phi[\%]$	nr of n-iteration-loops	nr iter. Biot (Ω_p)	nr iter. Stokes (Ω_{f1})	nr iter. Stokes (Ω_{f2})	total nr of iterations	grid node $(\max(\sigma_{p,xx}))$	grid node $(\max(u_x))$
35	11	1320	103	108	1531	$(0.5/1.5/1.5)$	$(0.375/1.5/1.5)$
	8	4068	91	99	4258	$(0.375/1.5/1.5)$	$(0.3125/1.5/1.5)$
45	65	7326	580	585	8491	$(0.5/1.5/1.5)$	$(0.375/1.5/1.5)$
	8	4086	109	99	4294	$(0.375/1.5/1.5)$	$(0.3125/1.5/1.5)$
55	74	8325	661	666	9652	$(0.5/1.5/1.5)$	$(1.625/1.5/1.5)$
	7	3640	80	88	3808	$(1.75/1.5/2.875)$	$(1.6875/1.5/1.5)$
65	3	444	31	36	511	$(1.5/1.5/1.5)$	$(1.625/1.5/1.5)$
	3	1816	43	44	1903	$(1.75/1.5/2.875)$	$(1.5625/1.5/1.5)$
75	3	440	31	36	507	$(1.75/2.25/2.25)$	$(1.375/1.5/1.5)$
	3	1804	36	40	1880	$(1.75/2.875/1.5)$	$(1.4375/1.5/1.5)$
85	3	432	31	36	499	$(0.25/1.5/1.5)$	$(1.125/1.5/1.5)$
	4	2220	47	45	2312	$(0.25/1.5/1.5)$	$(1.1875/1.5/1.5)$
95	3	392	31	28	451	$(0.25/1.5/1.5)$	$(1.125/1.5/1.5)$
	6	2926	70	49	3045	$(0.125/1.5/1.5)$	$(1.1875/1.5/1.5)$

Table 6.3: Example 1: Number of iterations and location of maximum stress component $\sigma_{p,xx}$ and maximum x-displacement for varying porosity. The first line in each row is for a grid with $8 \times 12 \times 12$ grid cells, the second line for a grid with $16 \times 24 \times 24$ grid cells.

6.4.2 Example 2: Filter of dimension $1 \times 5 \times 5$ mm^3

Our second example is a fluid flow channel of dimension $14 \times 5 \times 5$ mm^3 with a filter of 1 mm thickness. So, the ratio between the filter dimension in y-direction and z-direction and the thickness of the filter is larger than in example 1. This ratio has an effect on the properties of the porous medium.

Figure 6.10(a) shows the absolute values of the stress component $\sigma_{p,xx}$ for various points in the porous medium, depending on the E-modulus of the material the porous medium consists of. Note that the E-modulus given, is the E-modulus of the solid material and not the effective E-modulus of the porous medium. The effective E-modulus can be computed using formula (1.3.13). We plotted the absolute value of $\sigma_{p,xx}$, since this is the decisive value in determination of the risk of a filter break. As we have only plotted the absolute values, the minima of the curves denote a crossover from positive to negative values or vice versa. Why this happens has to be investigated further.
Figures 6.11(a) and 6.11(b) show stress profiles for the softest and the stiffest material we have simulated. The crosses indicate the points for which $\sigma_{p,xx}$ have been plotted in figure 6.10(a). The stresses in the softer porous medium are higher than in the stiffer one. For the material with E $=$ 200 GPa the highest stresses occur along the fixed boundaries. Stress profiles for a cross-section which is perpendicular to the fluid flow are shown in figures 6.12(a) and 6.12(b). Computational details can be found in table 6.4.

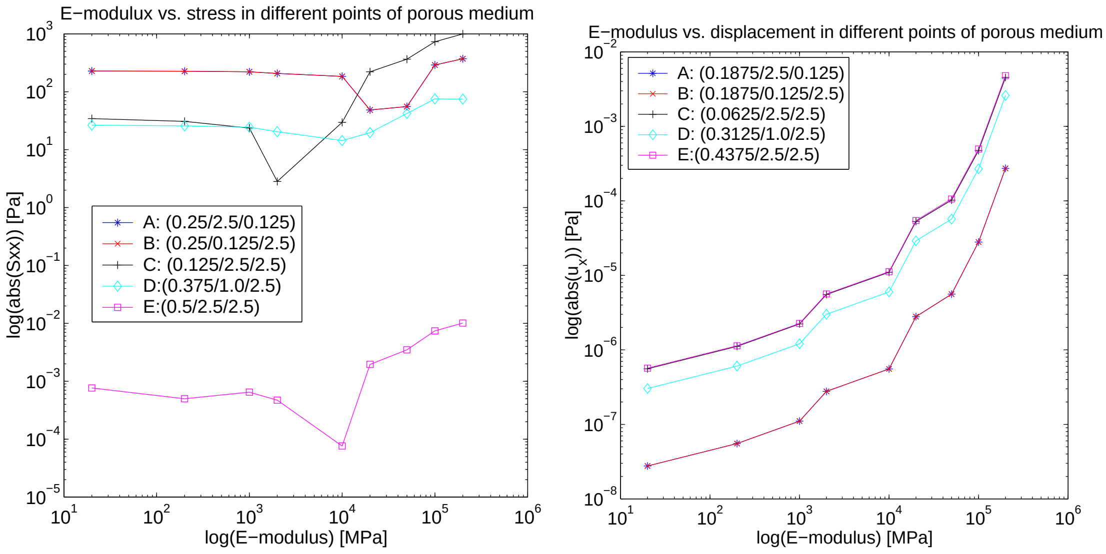

(a) (b)

Figure 6.10: Example 2: Relation between the E-modulus [GPa] and the stress component $\sigma_{p,xx}$ [Pa] (a) and the displacement in flow direction [mm] (b) for different points in a porous medium with porosity $\phi = 65\%$ and a permeability $k = 10^{-6}$ mm^2.

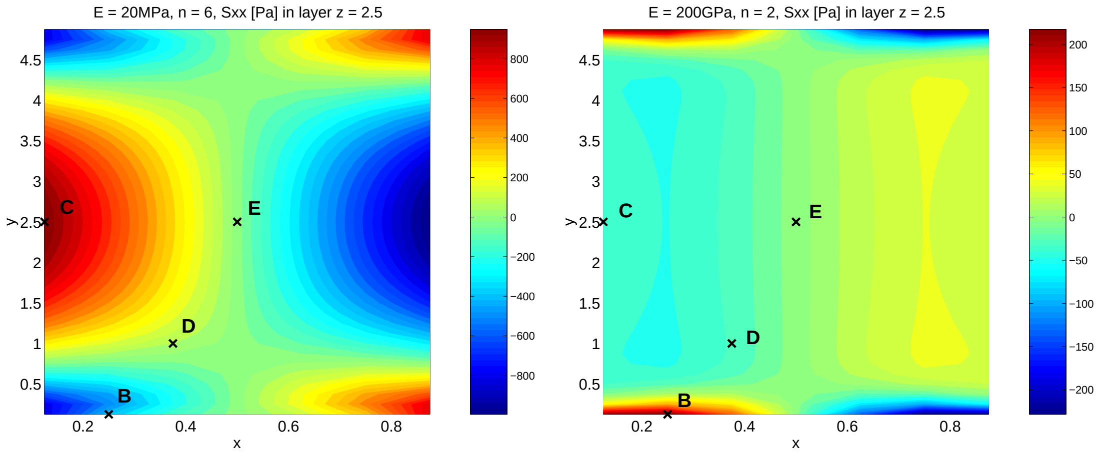

(a) (b)

Figure 6.11: Example 2: Stress profile in cross-section $z = 2.5$ for the porous medium with E-modulus $\mathrm{E} = 20$ MPa (a) and E-modulus $\mathrm{E} = 200$ GPa (b). Both materials have porosity $\phi = 65\%$ and permeability $k = 10^{-6}$ mm^2. Note that the plots show only the stresses in the interior of Ω_p, the boundary values are not contained.

Next, we study the effect of varying permeability. Figure 6.13(a) shows the relation between the permeability and the stress component $\sigma_{p,xx}$ for different points in the porous medium. $\sigma_{p,xx}$ decreases for increasing permeability. The higher the permeability, the smaller the resistance of the porous medium to the fluid flow and thus, the smaller the stresses. Lower stresses imply lower displacements, as can be seen in figure 6.13(b). There, u_x is plotted for approximately the same

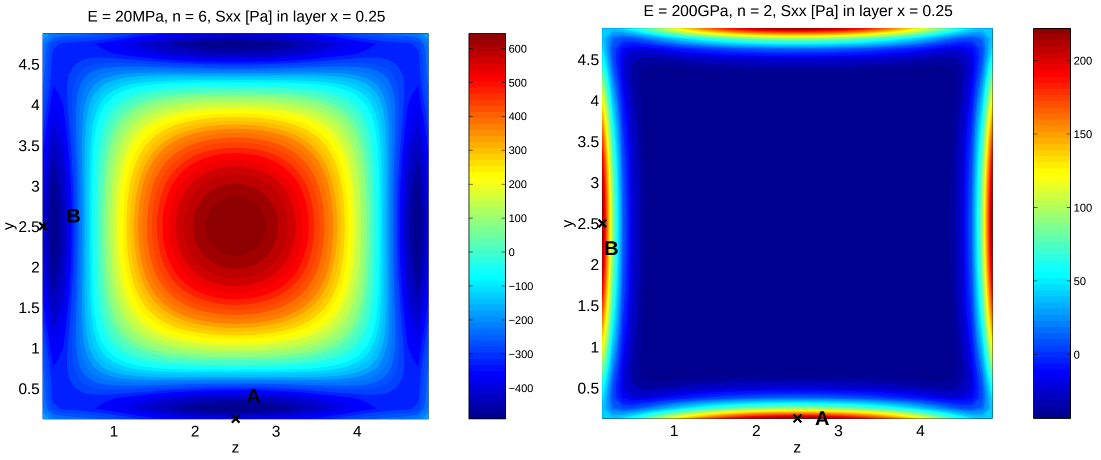

(a) (b)

Figure 6.12: Example 2: Stress profile in cross-section $x = 0.25$ for the porous medium with E-modulus E $=$ 20 MPa (a) and E-modulus E $=$ 200 GPa (b). Both materials have porosity $\phi = 65\%$ and permeability $k = 10^{-6}$ mm^2. Note that the plots show only the stresses in the interior of Ω_p, the boundary values are not contained.

E−modulus	nr of n-iteration-loops	nr iter. Biot (Ω_p)	nr iter. Stokes (Ω_{f1})	nr iter. Stokes (Ω_{f2})	total nr of iterations	grid node ($\max(\sigma_{p,xx})$)	grid node ($\max(u_x)$)
200 GPa	3	8853	27	36	8916	(0.25/2.5/0.125)	(0.4375/2.5/2.5)
100 GPa	4	11796	38	48	11882	(0.25/0.125/2.5)	(0.5625/2.5/2.5)
50 GPa	3	8835	27	36	8898	(0.25/2.5/0.125)	(0.4375/2.5/2.5)
20 GPa	3	8796	27	30	8853	(0.25/2.5/0.125)	(0.4375/2.5/2.5)
10 GPa	4	11648	38	36	11722	(0.25/0.125/2.5)	(0.5625/2.5/2.5)
2 GPa	4	11192	38	28	11258	(0.25/2.5/2.5)	(0.5625/2.5/2.5)
1 GPa	4	10845	38	20	10903	(0.25/2.5/2.5)	(0.5625/2.5/2.5)
200 MPa	4	9900	38	16	9954	(0.125/2.5/2.5)	(0.5625/2.5/2.5)
20 MPa	7	13993	72	28	14093	(0.125/2.5/2.5)	(0.5625/2.5/2.5)

Table 6.4: Example 2: Number of iterations for varying E-modulus and porosity $\phi = 65\%$ and permeability $k = 10^{-6}$ mm^2. This is for a grid with $8 \times 40 \times 40$ grid cells. For the computations we used time step $h_t = 0.5$ s.

points as $\sigma_{p,xx}$. "Approximately", because the grid nodes for u_x are shifted by $\frac{h_x}{2}$ in x-direction compared to the nodes for $\sigma_{p,xx}$, see definitions (5.1.2) and (5.1.3). Figure 6.14(a) and 6.14(b) show z-profiles of the porous medium for two different permeabilities. In the material with lower permeability (figure 6.14(a)), the stresses are two orders of magnitude larger than in the other material. This happens, because the material with the lower permeability offers more resistance to the fluid flow. The crosses indicate the points for which we have plotted $\sigma_{p,xx}$ and u_x in figures 6.13(a) and 6.13(b).

The location of the maximum stress component $\sigma_{p,xx}$ and the maximum displacement u_x are listed

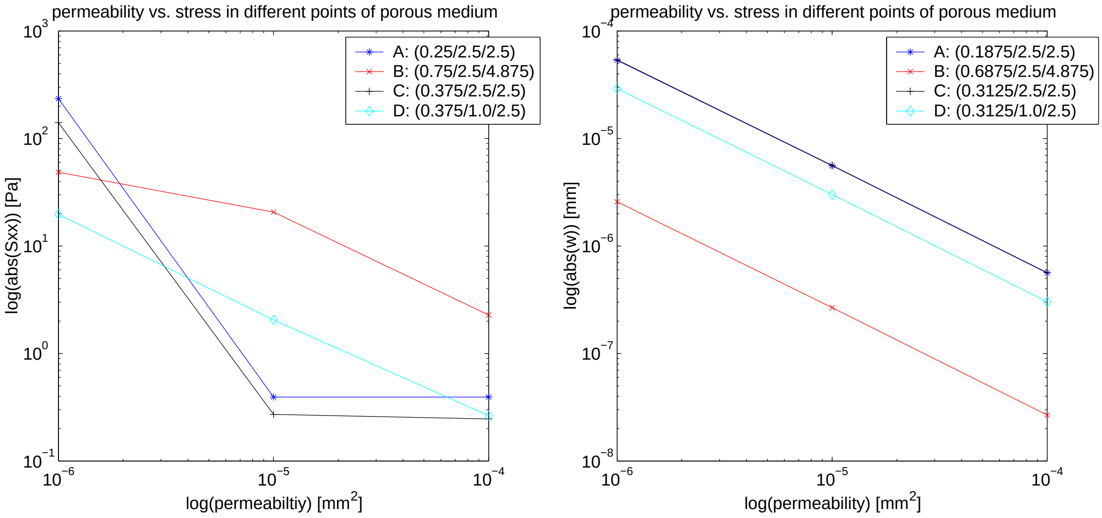

(a) (b)

Figure 6.13: Example 2: Relation between the permeability [mm^2] and the stress component $\sigma_{p,xx}$ [Pa] (a) and the displacement in flow direction [mm] (b) for different points in the porous medium (grid with $8 \times 40 \times 40$ grid cells). Note that x-axis and y-axis are both logarithmic.

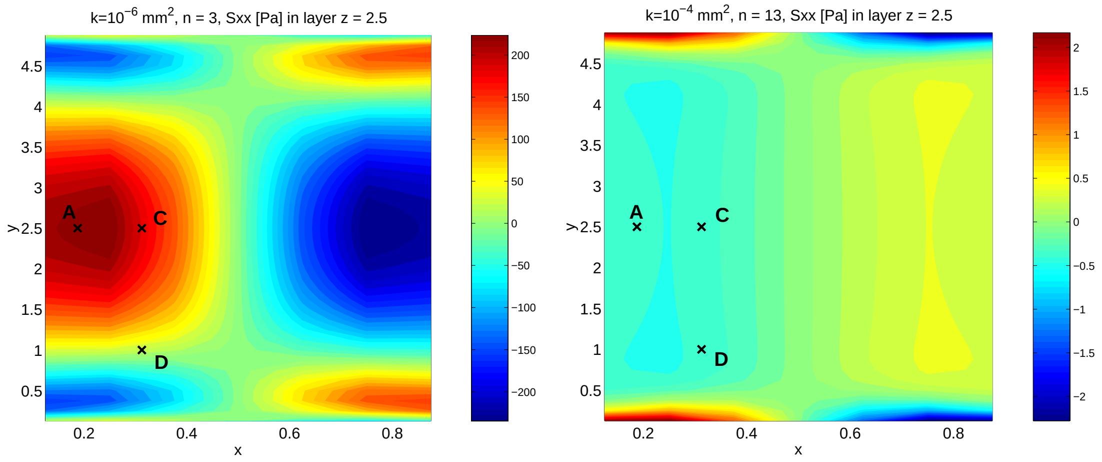

(a) (b)

Figure 6.14: Example 2: Stress profile in cross-section $z = 2.5$ for the porous medium with permeability $k = 10^{-6}$ mm^2 (a) and permeability $k = 10^{-4}$ mm^2 (b). Both materials have an E-modulus E $=$ 2 GPa and porosity $\phi = 65\%$. Note that the plots show only the stresses in the interior of Ω_p, the boundary values are not contained. The crosses indicate the points for which $\sigma_{p,xx}$ and u_x are plotted in figures 6.13(a) and 6.13(b).

in table 6.5. There, one can also find the number of iterations needed for the different computations. All computation were done with time step $h_t = 0.5$ s.

Finally, the effect of the variation of the porosity is studied. Figure 6.15(a) shows the relation between the porosity and the absolute value of the stress component $\sigma_{p,xx}$ in various points of

$k[\text{mm}^2]$	nr of n-iteration-loops	nr iter. Biot (Ω_p)	nr iter. Stokes (Ω_{f1})	nr iter. Stokes (Ω_{f2})	total nr of iterations	grid node ($\max(\sigma_{p,xx})$)	grid node ($\max(u_x)$)
10^{-6}	4	11192	38	28	11258	$(0.25/2.5/2.5)$	$(0.5625/2.5/2.5)$
10^{-5}	12	35172	132	120	35424	$(0.75/2.5/4.875)$	$(0.5625/2.5/2.5)$
10^{-4}	14	41249	157	168	41574	$(0.75/2.5/4.875)$	$(0.5625/2.5/2.5)$

Table 6.5: Example 2: Number of iterations and location of maximum stress component $\sigma_{p,xx}$ and maximum x-displacement for varying permeability. This is for a grid with $8 \times 40 \times 40$ grid cells.

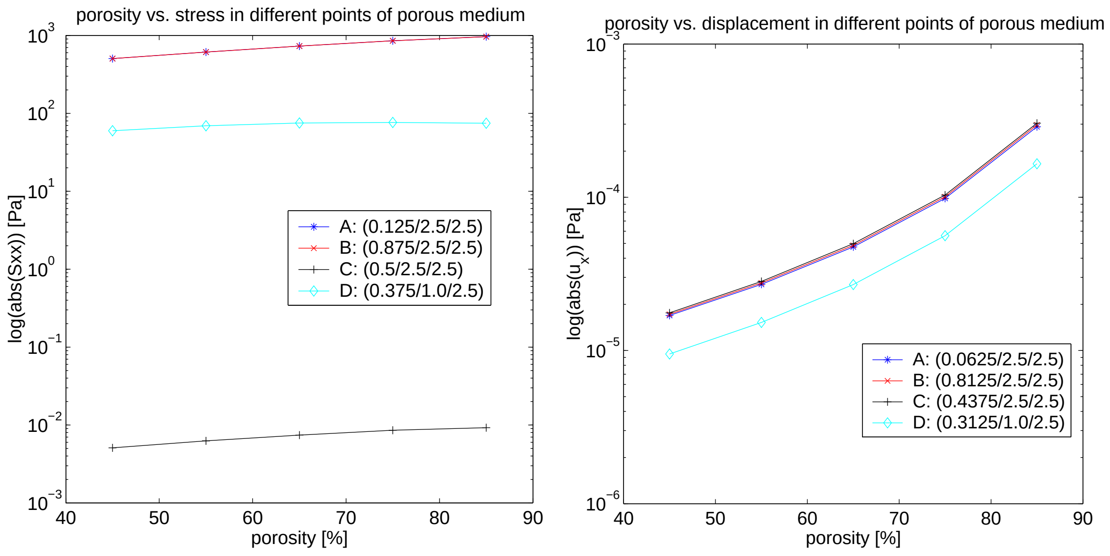

(a) (b)

Figure 6.15: Example 2: Relation between the porosity [%] and the stress component $\sigma_{p,xx}$ [Pa] (a) and the displacement in flow direction [mm] (b) for different points in the porous medium.

the porous medium. The stress in the chosen points increases when the porosity increases. This makes sense, since a porous medium with high porosity consists of less solid material than a porous medium with lower porosity. Increasing stresses cause increasing displacements, as can be seen in figure 6.15(b). The displacement curves for the points A, B and C lie on top of each other. All these points are located exactly in the middle of the y-z-plane. Thus, one can deduce that the displacements are uniform throughout the middle of the porous medium. The location of the points A, B, C and D are displayed by crosses in figures 6.16(a) and 6.16(b). There, the stress component in the cross-section $z = 2.5$ is depicted for two different porosities. These figures underline the result stated above: The stresses are higher in the porous medium with the higher porosity. All computations are done with time step $h_t = 0.05$ s. Computational data as well as the location of the maximum of $\sigma_{p,xx}$ and u_x can be learned from table 6.6.

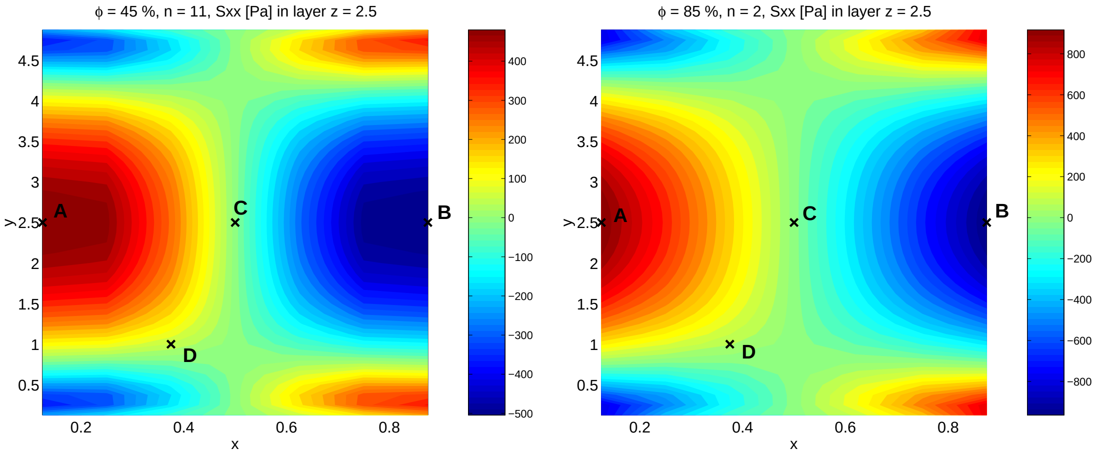

(a) (b)

Figure 6.16: Example 2: Stress profile in cross-section $z = 2.5$ for the porous medium with porosity $\phi = 45\%$ (a) and porosity $\phi = 85\%$ (b). Both materials have an E-modulus E $= 2$ GPa and permeability $k = 10^{-6}$ mm^2. Note that the plots show only the stresses in the interior of Ω_p, the boundary values are not contained.

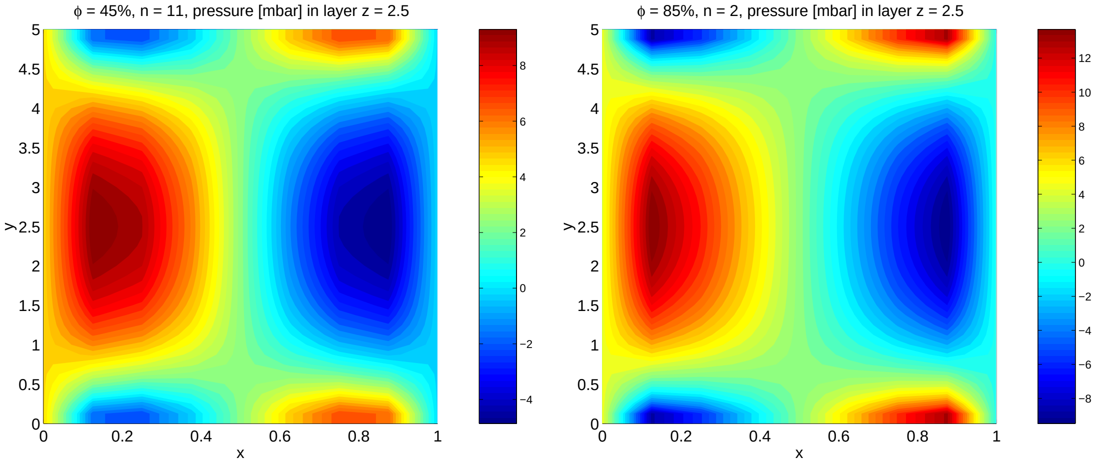

(a) (b)

Figure 6.17: Example 2: Pressure profile in cross-section $z = 2.5$ for the porous medium with porosity $\phi = 45\%$ (a) and the porous medium with porosity $\phi = 85\%$ (b). Both materials have an E-modulus E $= 2$ GPa and permeability $k = 10^{-6}$ mm^2.

ϕ[%]	nr of n-iteration-loops	nr iter. Biot (Ω_p)	nr iter. Stokes (Ω_{f1})	nr iter. Stokes (Ω_{f2})	total nr of iterations	grid node ($\max(\sigma_{p,xx})$)	grid node ($\max(u_x)$)
45	12	31297	132	60	31489	$(0.875/2.5/2.5)$	$(0.5625/2.5/2.5)$
55	4	10197	38	16	10251	$(0.125/2.5/2.5)$	$(0.5625/2.5/2.5)$
65	4	9900	38	16	9954	$(0.125/2.5/2.5)$	$(0.5625/2.5/2.5)$
75	4	9460	38	16	9514	$(0.125/2.5/2.5)$	$(0.5625/2.5/2.5)$
85	3	6415	27	12	6454	$(0.125/2.5/2.5)$	$(0.5625/2.5/2.5)$

Table 6.6: Example 2: Number of iterations and location of maximum stress component $\sigma_{p,xx}$ and maximum x-displacement for varying porosity. This is for a grid with $8 \times 40 \times 40$ grid cells.

6.5 Depth filtration examples

In filtration processes we distinguish between two different mechanisms: depth filtration and cake filtration. In this section we show two depth filtration examples, cake filtration examples are presented in section 6.6.

In depth filtration, the particles which have to be filtrated accumulate inside the porous medium due to inertia, sieving effects, adsorption, and so on. Not all particles are captured inside the porous medium. Of course, smaller particles can penetrate the filter medium. The accumulation of dirt inside the porous medium changes the properties of the filter: efficiency, pressure drop, permeability, porosity, mass flux, stresses and so on. This might lead to clogging or even to destruction of the filter. In the following we describe two depth filtration examples.

6.5.1 Filter of dimension $2 \times 3 \times 3$ mm^3

In this example, we consider a fluid channel with a porous medium of dimension $2 \times 3 \times 3$ mm^3. In the beginning of the depth filtration process, the porous medium has a porosity of 95% and a permeability of $k = 10^{-4}$ mm^2. The solid material has an E-modulus of 6 GPa and Poisson's ratio 0.14. In each iteration, the porosity is reduced by 3%. The permeability changes according to Kozeny-Carman equation (1.3.6). We assume that the dirt particles which are captured inside the porous medium do not change the elastic properties of the porous medium. Therefore, the elastic parameters like E-modulus, Poisson's ratio or the Lamé coefficients, respectively, are kept constant during the simulation. Since the permeability and the porosity change in each iteration loop, we cannot reach steady state. So, we stop the computation after some iterations.

The relation between the porosity and the permeability for this simulation is displayed in figure 6.18(a). The corresponding numbers are given in table 6.7. There, one can also find the position of the maximum stress component $\sigma_{p,xx}$. Its position changes during the depth filtration process. From the position of the maximum $\sigma_{p,xx}$ one can deduce the spot where the filter could break first. Table 6.7 also shows the number of iterations needed for the solution of the separate subproblems as well as for the entire solution in each iteration. The total number of iterations decreases

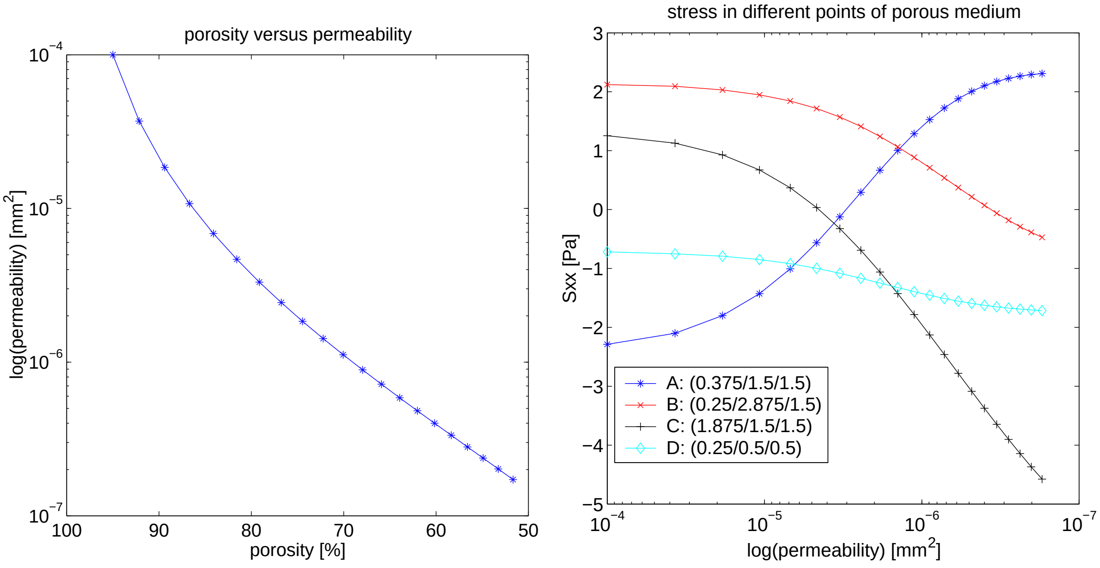

(a) (b)

Figure 6.18: Depth filtration (filter $2\times3\times3$ mm^3 - $16\times24\times24$ grid cells) - (a): Porosity is decreased by 3% in each iteration. The permeability changes according to Kozeny-Carman equation. (b): Stress component $\sigma_{p,xx}$ in different points of the porous medium. Note that the x-axes of both figures are directed from larger to smaller values.

during the filtration process. Figure 6.19(a) - 6.21(b) show stress profiles of the porous medium at iteration numbers $n = 0$, $n = 8$ and $n = 20$. For each of these iterations we depicted a x-cross-section and a z-cross-section. The cross-sections are chosen according to the appearance of the maximum stress component $\sigma_{p,xx}$. For $n = 0$ and $n = 20$, the x-cross-section shows that the maximum $\sigma_{p,xx}$ (absolute value) lies in the middle of the y-z-plane. Towards the boundaries, $\sigma_{p,xx}$ becomes smaller, changes its sign and increases again (in absolute values). This happens because the porous medium is fixed along the outer boundaries. From the z-cross-sections of $\sigma_{p,xx}$ at $n = 0$ and $n = 20$ one can see that the stresses are highest at the inflow and at the outflow of the porous medium. These results have to be studied further. At the moment, we can not explain the change of sign at $n = 8$.
Figure 6.18(b) shows the development of the stress component $\sigma_{p,xx}$ in several points of the porous medium, which were also indicated by crosses in figures 6.19(a) - 6.21(b). Note that the x-axis of this figure is directed from larger to smaller values. This corresponds to the course of the depth filtration process.

Figure 6.22(a) shows the integral over the pressure in the first layer behind the inflow. The pressure first increases and reaches its highest value for a permeability around $k = 8.9\cdot10^{-7}$ mm^2. Then, it slightly decreases. The same behaviour can be observed for the pressure drop (see figure 6.22(b)). Why this happens has also to be studied further. Note that the pressure drop plotted here is inside the porous medium (between first and last layer of the porous medium) and not between inflow and outflow interface. Figures 6.23(a) and 6.23(a) show pressure profiles for a cross-section $x = 0.125$ and a cross-section $z = 1.5$, respectively. The pressure is the highest in the middle of the y-z-

it. nr	porosity $\phi[\%]$	permeability $k[\text{mm}^2]$	grid node $(\max(\sigma_{p,xx}))$	nr of it. Biot (Ω_p)	nr of it. Stokes (Ω_{f1})	nr of it. Stokes (Ω_{f2})	total nr of iterations
0	95%	10^{-4}	$(0.5/1.5/1.5)$	115	7	9	131
			$(0.375/1.5/1.5)$	470	7	12	489
1	92.15%	$3.70 \cdot 10^{-5}$	$(0.5/1.5/1.5)$	114	7	9	130
			$(0.375/1.5/1.5)$	467	9	11	487
2	89.39%	$1.85 \cdot 10^{-5}$	$(0.5/1.5/1.5)$	113	9	9	131
			$(0.25/1.5/0.125)$	464	11	11	486
3	86.70%	$1.18 \cdot 10^{-5}$	$(0.5/1.5/1.5)$	113	9	9	131
			$(0.25/0.125/1.5)$	461	11	11	483
4	84.10%	$6.86 \cdot 10^{-6}$	$(0.5/1.25/1.25)$	112	9	9	130
			$(0.25/0.125/1.5)$	458	11	11	480
5	81.58%	$4.67 \cdot 10^{-6}$	$(0.25/0.75/0.75)$	111	9	7	127
			$(0.25/2.875/1.5)$	456	11	11	478
6	79.13%	$3.32 \cdot 10^{-6}$	$(0.25/0.75/0.75)$	110	9	7	126
			$(0.25/2.875/1.5)$	453	11	10	474
7	76.76%	$2.44 \cdot 10^{-6}$	$(0.25/0.5/0.5)$	109	9	6	124
			$(0.25/2.875/1.5)$	450	11	9	470
8	74.46%	$1.84 \cdot 10^{-6}$	$(1.75/1.5/1.5)$	109	7	6	124
			$(0.25/0.5/0.5)$	447	11	9	467
⋮	⋮	⋮	⋮	⋮	⋮	⋮	⋮
20	51.66%	$1.72 \cdot 10^{-7}$	$(1.75/1.5/1.5)$	98	9	5	112
			$(1.875/1.5/1.5)$	419	11	5	435

Table 6.7: Depth filtration (filter $2 \times 3 \times 3$ mm^3): The data in the first line of a row in the table is for a grid with $8 \times 12 \times 12$ grid cells, the second line is for a grid with $16 \times 24 \times 24$ grid cells.

plane. This is due to the fact that the fluid velocity is the highest in the middle of this plane and thus, the pressure at the infiltration is highest where the velocity is the highest. The pressure drops more or less linearly throughout the porous medium (figure 6.23(b)).

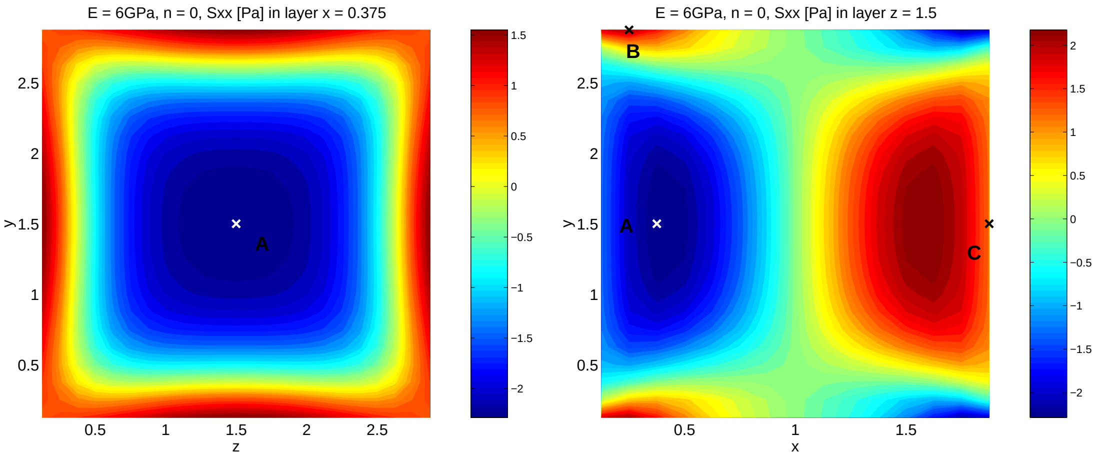

(a) (b)

Figure 6.19: Depth filtration (filter $2 \times 3 \times 3$ mm^3 - $16 \times 24 \times 24$ grid cells) - Stress profiles ($\sigma_{p,xx}$) in cross-section $x = 0.375$, iteration $n = 0$ (a) and in cross-section $z = 1.5$, iteration $n = 0$ (b). The crosses indicate points for which the development of $\sigma_{p,xx}$ throughout the clogging process is given in figure 6.18(b). Note that the stress boundary values are not contained in the plots.

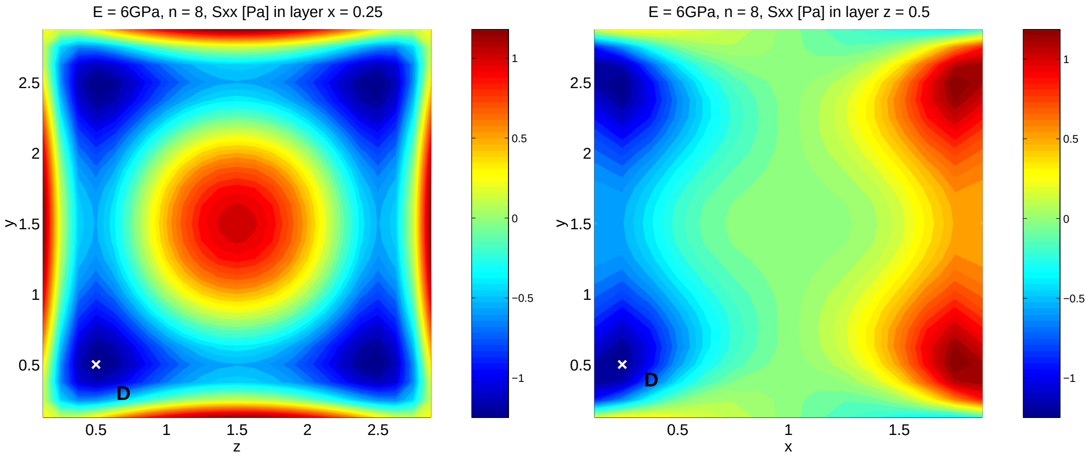

(a) (b)

Figure 6.20: Depth filtration (filter $2 \times 3 \times 3$ mm^3 - $16 \times 24 \times 24$ grid cells) - Stress profiles ($\sigma_{p,xx}$) in cross-section $x = 0.25$, iteration $n = 8$ (a) and in cross-section $z = 0.5$, iteration $n = 8$ (b). The cross indicates a point for which the development of $\sigma_{p,xx}$ throughout the clogging process is given in figure 6.18(b). Note that the stress boundary values are not contained in the plots.

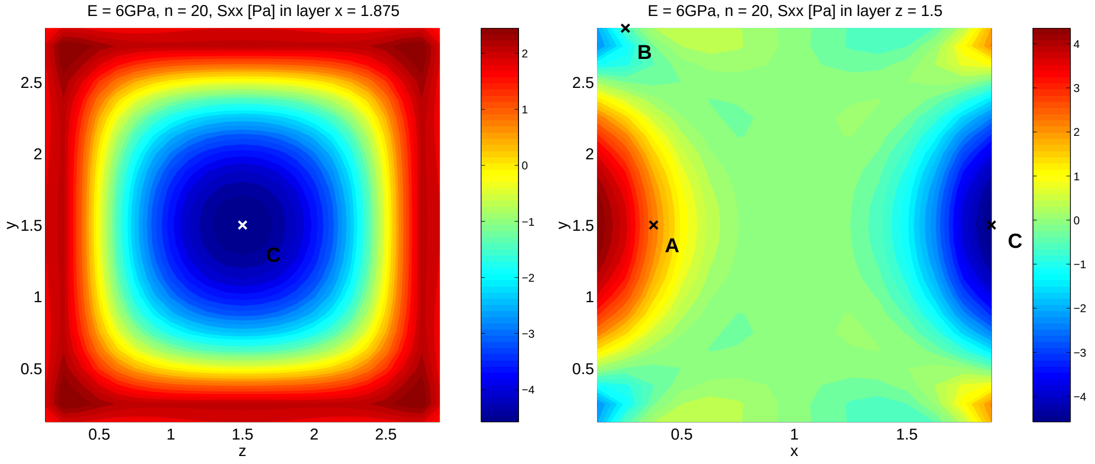

(a) (b)

Figure 6.21: Depth filtration (filter $2 \times 3 \times 3$ mm^3 - $16 \times 24 \times 24$ grid cells) - Stress profiles ($\sigma_{p,xx}$) in cross-section $x = 1.875$, iteration $n = 20$ (a) and in cross-section $z = 1.5$, iteration $n = 20$ (b). The crosses indicate points for which the development of $\sigma_{p,xx}$ throughout the clogging process is given in figure 6.18(b). Note that the stress boundary values are not contained in the plots.

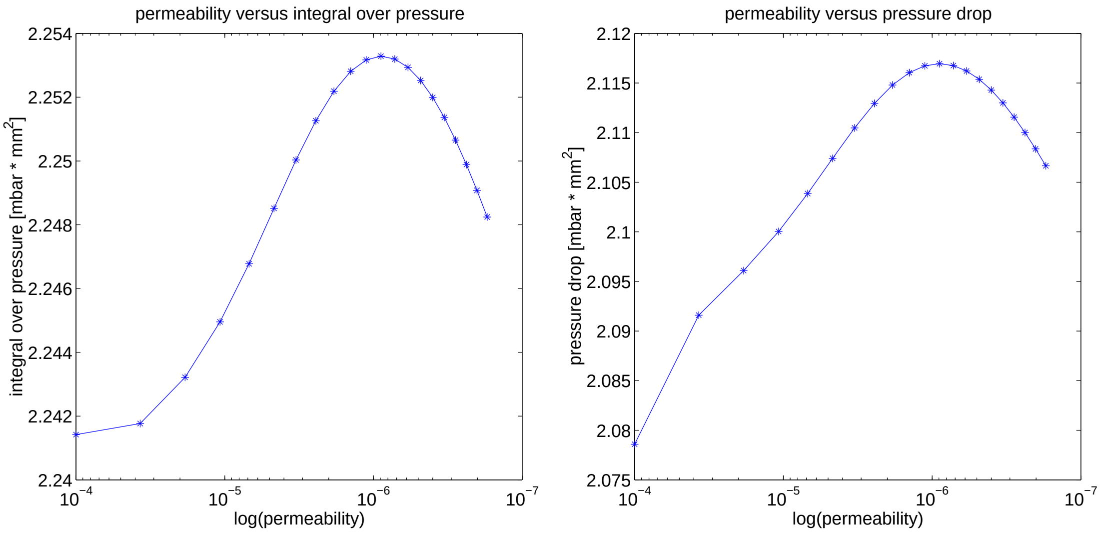

(a) (b)

Figure 6.22: Depth filtration (filter $2 \times 3 \times 3$ mm^3 - $16 \times 24 \times 24$ grid cells) - Relation between permeability and the integral of the pressure in the first layer behind the inflow (a) and the pressure drop across the porous medium (b). Note that the x-axes of both figures are directed from larger to smaller values.

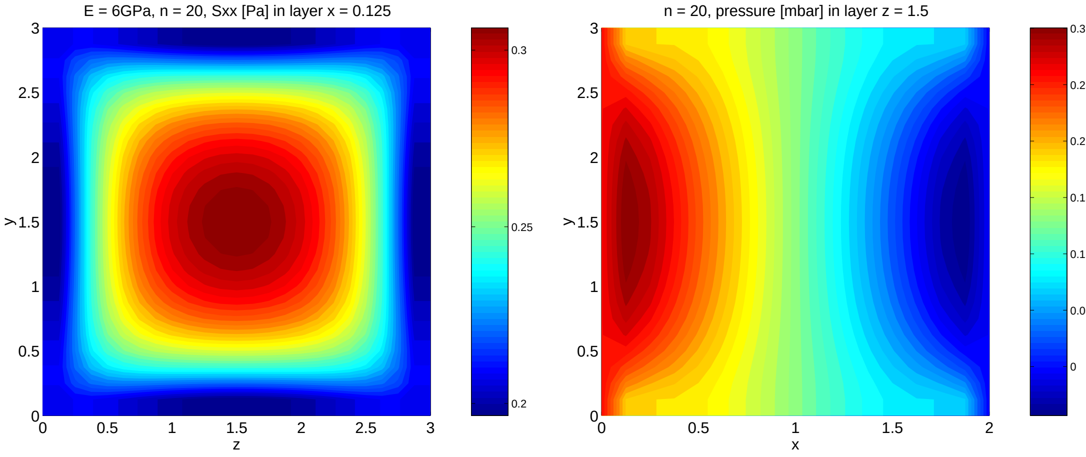

(a) (b)

Figure 6.23: Depth filtration (filter $2 \times 3 \times 3$ mm^3 - grid $16 \times 24 \times 24$ cells) - Pressure in cross-section $x = 0.125$ (layer behind inflow), iteration $n = 20$ (a) and in cross-section $z = 1.5$, iteration $n = 20$.

6.5.2 Filter $1 \times 5 \times 5$ mm^3

Our second example is a fluid channel with a filter medium of dimension $1 \times 5 \times 5$ mm^3. The ratio between thickness and width of this filter is smaller than in the example before. Moreover, the material is two orders of magnitude softer. The solid material in this example has an E-modulus of 20 MPa and Poisson's ratio 0.14. We start with a porosity of 85% and a permeability of $k = 10^{-4}$ mm^2. For higher porosities the displacements become too large such that they cannot be handled by linear elasticity anymore. In each iteration, the porosity is reduced by 3%. The permeability changes according to Kozeny-Carman equation (1.3.6). The relation between porosity and permeability is displayed in figure 6.24(a). Note that the x-axis is directed from large to small values. This corresponds to the course of the depth filtration process. The corresponding numbers can be found in table 6.8. There, one can also see the number of iterations needed for the solution of the subproblems as well as for the entire problem. The first line in each row of the table is related to a grid with $4 \times 20 \times 20$ grid cells and the second line to a grid with $8 \times 40 \times 40$ grid cells. The maximum stress component $\sigma_{p,xx}$ is located in the middle of the first layer behind the inflow of the porous medium. For the coarse grid ($4 \times 20 \times 20$ cells) this is point $(0.25/2.5/2.5)$ and for the fine grid ($8 \times 40 \times 40$ cells) this is point $(0.125/2.5/2.5)$. Figures 6.25(a) and 6.25(b) show the stress profiles in the corresponding x- and z-cross-section at iteration $n = 12$. The crosses in these figures indicate the points for which we plotted the development of stress component $\sigma_{p,xx}$, see figure 6.24(b). Point A is the point where the maximum $\sigma_{p,xx}$ occurs.

Figure 6.26(a) shows the development of the integral over the pressure at the inflow interface of the porous medium. The red line ('×'-sign) shows the integral over the pressure which is applied as boundary condition at the inflow, whereas the blue line ('*'-sign) shows the value in the first layer inside the porous medium. One can clearly see the pressure jump, given by equation (2.3.1e). In this equation $1 - \frac{1}{\phi^2 C_c^2} < 0$, because $\phi < 1$ and $C_\mathrm{c} = 0.8$. The integral over the pressure inflow boundary values slightly decreases, whereas the decrease of the interior values is larger. The

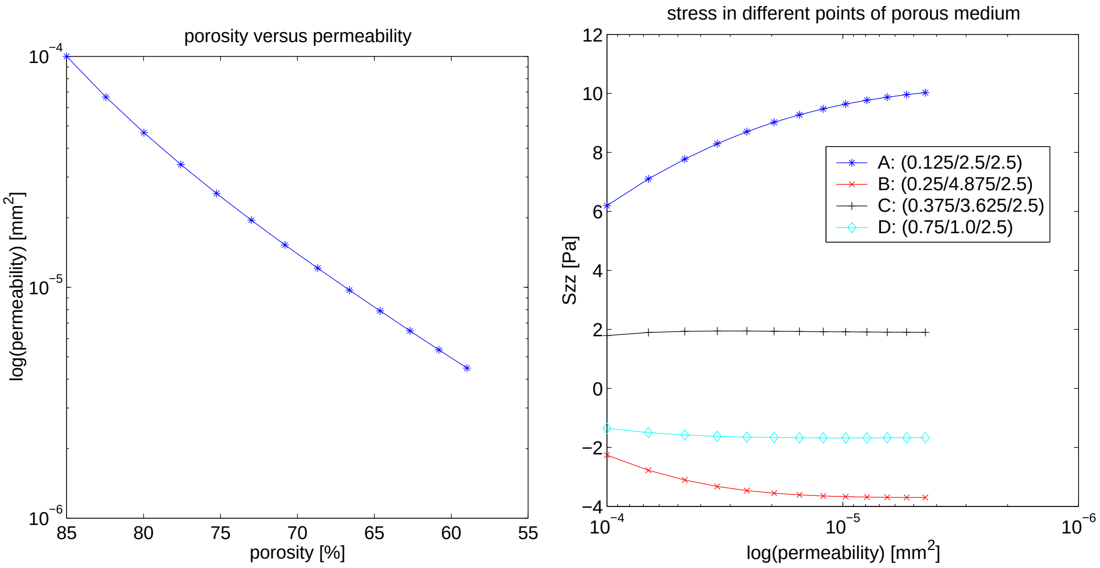

(a) (b)

Figure 6.24: Depth filtration (filter $1 \times 5 \times 5$ mm^3 - $8 \times 40 \times 40$ grid cells) - (a): Porosity is decreased by 3% in each iteration. The permeability changes according to Kozeny-Carman equation. (b): Stress component $\sigma_{p,xx}$ in different points in the porous medium.

reason for this is the decrease of the term $1 - \frac{1}{\phi^2 C_c^2}$ in the pressure jump equation (2.3.1e). Figure 6.26(b) depicts the pressure drop during the depth filtration process. The red line ('$\times$'-sign) shows the pressure drop between inflow and outflow boundary condition for the porous medium, whereas the blue line ('*'-sign) represents the pressure drop inside the porous medium (between first layer behind inflow and last layer before outflow). Here, one can also notice the pressure difference between the exterior and the interior of the porous medium. The pressure drop for the boundary values slightly increases during the filtration process, which is caused by the clogging of the filter. The pressure drop inside the porous medium decreases. The reason for that can again be found in the pressure jump equations (2.3.1e) and (2.3.1f). Due to the change of the porosity, the difference between p_f and p_p becomes larger during the filtration process. Two pressure cross-sections are shown in figures 6.27(a) and 6.27(b).

it. nr	porosity $\phi[\%]$	permeability $k[\text{mm}^2]$	nr of it. Biot (Ω_p)	nr of it. Stokes (Ω_{f1})	nr of it. Stokes (Ω_{f2})	total nr of iterations
0	85%	10^{-4}	603	7	7	617
			2567	7	4	2578
1	82.45%	$6.67 \cdot 10^{-5}$	593	8	6	607
			2469	9	4	2482
2	79.98%	$4.67 \cdot 10^{-5}$	687	10	6	603
			2424	11	4	2439
3	77.58%	$3.40 \cdot 10^{-5}$	586	11	5	602
			2378	11	4	2393
4	75.25%	$2.55 \cdot 10^{-5}$	588	11	5	604
			2331	11	4	2346
5	72.99%	$1.95 \cdot 10^{-5}$	593	11	5	609
			2281	12	4	2297
6	70.80%	$1.53 \cdot 10^{-5}$	598	11	5	614
			2230	12	4	2246
7	68.68%	$1.21 \cdot 10^{-5}$	603	11	5	619
			2177	12	4	2193
8	66.62%	$9.72 \cdot 10^{-6}$	609	11	5	625
			2124	12	4	2140
9	64.62%	$7.90 \cdot 10^{-6}$	613	11	6	630
			2073	12	4	2089
10	62.68%	$6.48 \cdot 10^{-6}$	618	11	6	635
			2028	12	4	2044
11	60.80%	$5.36 \cdot 10^{-6}$	622	11	6	639
			1992	12	4	2008
12	58.98%	$4.47 \cdot 10^{-6}$	625	11	6	642
			2013	12	4	2029

Table 6.8: Depth filtration (filter $1 \times 5 \times 5$ mm^3): The data in the first line of a row in the table is for a grid with $4 \times 20 \times 20$ grid cells, the second line is for a grid with $8 \times 40 \times 40$ grid cells.

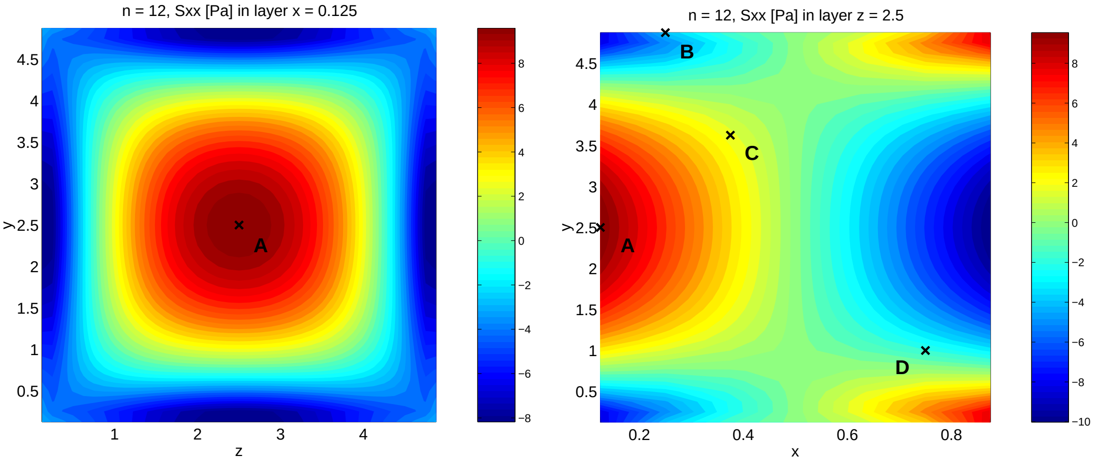

(a) (b)

Figure 6.25: Depth filtration (filter $1 \times 5 \times 5$ mm^3 - $8 \times 40 \times 40$ grid cells) - Stress profiles ($\sigma_{p,xx}$) in cross-section $x = 0.125$, iteration $n = 12$ (a) and in cross-section $z = 2.5$, iteration $n = 12$ (b). Note that the stress boundary values are not contained in the plots.

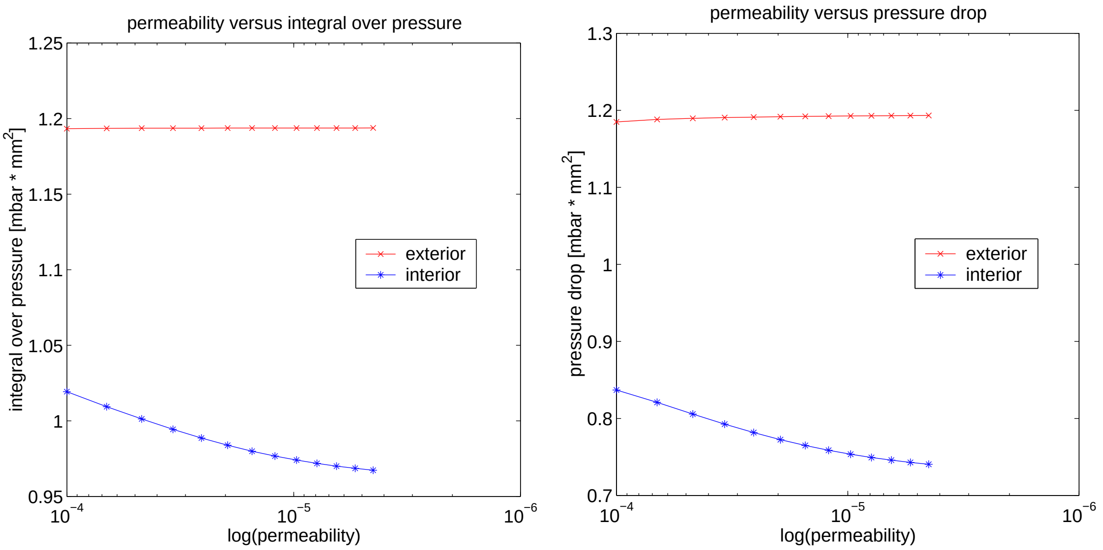

(a) (b)

Figure 6.26: Depth filtration (filter $1 \times 5 \times 5$ mm^3 - $8 \times 40 \times 40$ grid cells) - Relation between permeability and the integral of the pressure in the first layer behind the inflow ($x = 0.125$) (a) and the pressure drop across the porous medium (b).

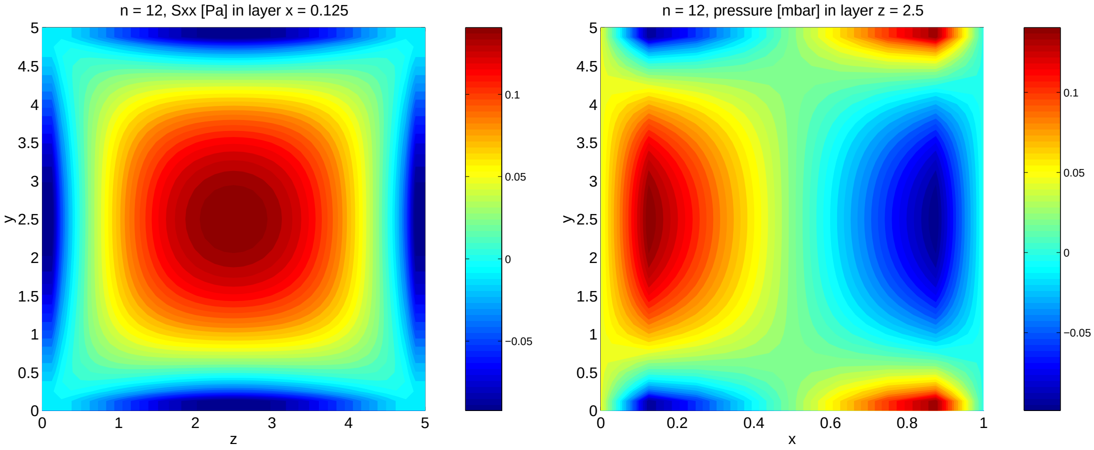

(a) (b)

Figure 6.27: Depth filtration (filter $1 \times 5 \times 5$ mm^3 - $8 \times 40 \times 40$ grid cells) - Pressure in cross-section $x = 0.125$ (layer behind inflow), iteration $n = 12$ (a) and pressure in cross-section $z = 2.5$, iteration $n = 12$ (b).

6.6 Cake filtration examples

In the process of cake filtration, the particles are captured on the surface of the filter medium, i.e. they do not penetrate the porous medium. They form a layer on the top of the filter and act like a ”second filter”. During the filtration process the cake layer grows and thus, like in depth filtration, the filter properties (permeability, efficiency, pressure drop, mass flux,...) change continuously. This might also lead to a clogging or even to a destruction of the filter. In this chapter we show results of a cake filtration simulation process.

To model the process of cake filtration we use Poro3D for a two-layer material. Detailed studies can be found in [46]. Considering two different layers means that the parameters like the Lamé coefficients λ and μ, the permeability k and the porosity ϕ can be discontinuous across the interface $x = \Gamma$. For a first approach, we assume them to be piecewise constant

$$\lambda(\mathbf{x}) = \begin{cases} \lambda_1 & \text{for } x < \Gamma \\ \lambda_2 & \text{for } x > \Gamma \end{cases}, \quad \mu(\mathbf{x}) = \begin{cases} \mu_1 & \text{for } x < \Gamma \\ \mu_2 & \text{for } x > \Gamma \end{cases},$$

$$k(\mathbf{x}) = \begin{cases} k_1 & \text{for } x < \Gamma \\ k_2 & \text{for } x > \Gamma \end{cases}, \quad \phi(\mathbf{x}) = \begin{cases} \phi_1 & \text{for } x < \Gamma \\ \phi_2 & \text{for } x > \Gamma \end{cases}.$$

To take into account the discontinuities of these coefficients, the Biot model (1.3.16) has to be supplemented by the following interface conditions (see [45] and [46]):

$$[\mathbf{u}]_\Gamma = 0,\ [p_p]_\Gamma = 0,\ \left[\frac{k}{\eta}\nabla p_p \cdot \mathbf{n}\right]_\Gamma = 0,\ [\sigma_p \cdot \mathbf{n}]_\Gamma = 0\,,$$

where the symbol $[.]_\Gamma$ denotes the jump across the interface Γ. By using this two-layer model, the diverse propagation of pressure and stresses in different materials can be investigated. In the following we use this version for modelling the process of cake filtration.

6.6.1 Filter of dimension $2 \times 3 \times 3$ mm^3 (thickness of cake 1 mm)

As first example, we consider a fluid flow channel with a porous medium of dimension $2 \times 3 \times 3$ mm^3, the filter cake is 1 mm thick. Thus, we simulate a fluid flow channel with a porous medium of dimension $3 \times 3 \times 3$ mm^3, where the interface between the two different porous layers is located at $x = 1$ mm.

For the filter medium we use the following material parameters: E-modulus E $= 200$ GPa, Poisson's ratio $\nu_s = 0.14$, porosity $\phi = 95$ % and permeability $k = 10^{-4}$ mm^2. We simulate two different types of cake. One with E-modulus E $= 6$ GPa and one with E-modulus E $= 200$ MPa. In both cases the filter cake has porosity $\phi = 65$ % and permeability $k = 10^{-6}$ mm^2. So, the filter cake is softer, but less permeable than the filter medium. The computations are done with a time step $h_t = 5 \cdot 10^{-2}$ s.

Figures 6.28(a) and 6.28(b) show the stress profiles in a cross-section in the middle of the porous media. The white line indicates the interface between the filter cake and the filter. The highest stress occurs around the interface between the two different porous layers. The filter cake is more compressed than the filter itself (see figures 6.29(a) and 6.29(b)), because the filter cake is softer. The filter acts like a resistance for the filter cake, which cannot deform freely. Therefore, we have the highest stress where the two media touch each other.

Figures 6.30(a) and 6.30(b) show the pressure profiles in the corresponding cross-section. The pressure in the filter cake is higher than in the filter. This is due to the fact that the filter cake has lower porosity and permeability.

It took 5 iteration loops with 620 iterations in total for the example with filter cake with E-modulus E $= 6$ GPa ($5 \cdot 109$ for the solution of the Biot poroelasticity equations and $13 + 14 + 3 \cdot 16$ for the solution of the Stokes equations).

The example with filter cake with E-modulus E $= 200$ MPa needed 6 iteration loops with 739 iteration in total to converge ($6 \cdot 108$ for the solution of the Biot poroelasticity equations and $13 + 14 + 4 \cdot 16$ for the solution of the Stokes equations).

6.6.2 Filter of dimension $1 \times 5 \times 5$ mm^3 (thickness of cake 1 mm)

In our second cake filtration example we investigate a fluid flow channel with a porous medium of dimension $1 \times 5 \times 5$ mm^3, the filter cake on top of the filter is 1 mm thick. Thus, the porous medium we simulate has dimension $2 \times 5 \times 5$ mm^3, the interface between the two porous layers is exactly in the middle, at $x = 1$.

The filter medium we use is the same as in the example above (E-modulus E $= 200$ GPa, Poisson's ratio $\nu_s = 0.14$, porosity $\phi = 95\%$ and permeability $k = 10^{-6}$ mm^2). The two different filter cakes we use here, have E-modulus E $= 200$ MPa and E $= 2$ MPa, respectively. The permeability is $k = 10^{-6}$ mm^2 and the porosity $\phi = 65\%$.

As in the example before, the highest stresses occur at the interface between the two porous media

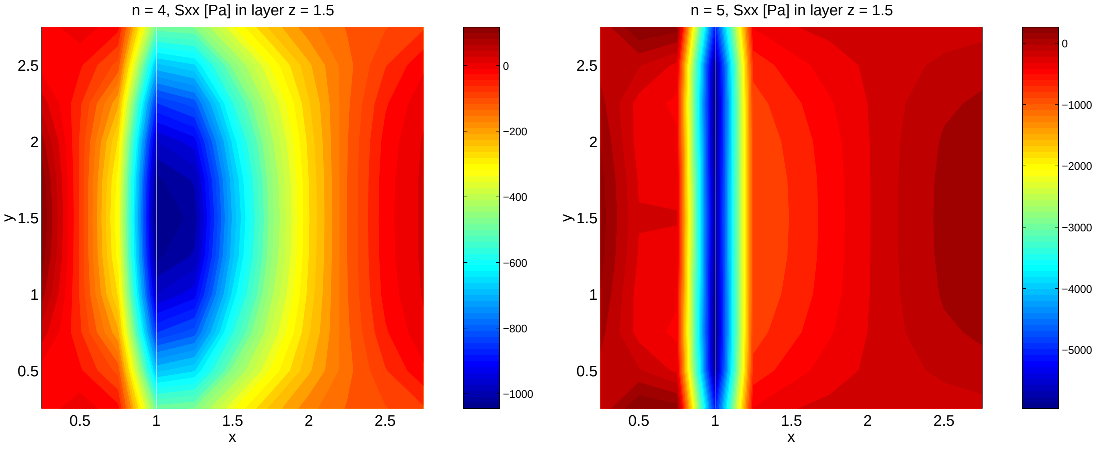

(a) (b)

Figure 6.28: Cake filtration (filter cake $1 \times 3 \times 3$ mm^3 + filter $2 \times 3 \times 3$ mm^3) - Stress component $\sigma_{p,xx}$ in cross-section $z = 1.5$ for a cake with E-modulus E $= 6$ GPa (a) and E-modulus E $= 200$ MPa (b). In both cases, the filter cake has porosity $\phi = 65$ % and permeability $k = 10^{-6}$ mm^2. The filter medium has E-modulus E $= 200$ GPa, porosity $\phi = 95$ % and permeability $k = 10^{-4}$ mm^2. Note that the stress boundary values are not contained in the plots.

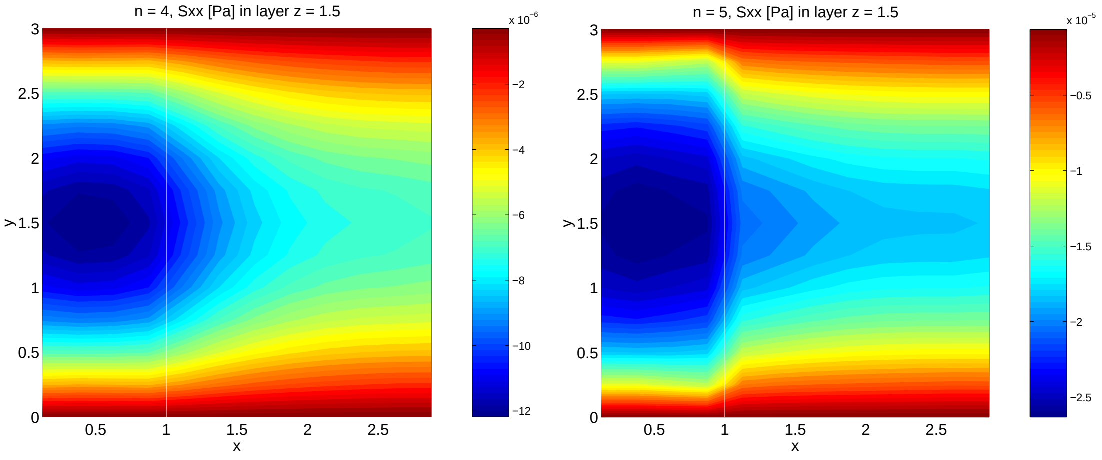

(a) (b)

Figure 6.29: Cake filtration (filter cake $1 \times 3 \times 3$ mm^3 + filter $2 \times 3 \times 3$ mm^3) - Displacements in flow direction in cross-section $z = 1.5$ for a cake with E-modulus E $= 6$ GPa (a) and E-modulus E $= 200$ MPa (b). In both cases, the filter cake has porosity $\phi = 65$ % and permeability $k = 10^{-6}$ mm^2. The filter medium has E-modulus E $= 200$ GPa, porosity $\phi = 95$ % and permeability $k = 10^{-4}$ mm^2.

(see figures 6.31(a) and 6.31(b)). The stresses in the porous medium with the softer filter cake are approximately two orders of magnitude larger than the stresses in the porous medium with the less soft filter cake. From this, one can deduce that it plays an important role which material the filter cake consists of with respect to the life time of the filter.

The displacement profiles of these two examples are displayed in figures 6.31(a) and 6.31(b). Of course, the displacements are larger in the softer filter cake. The displacements in the filter are

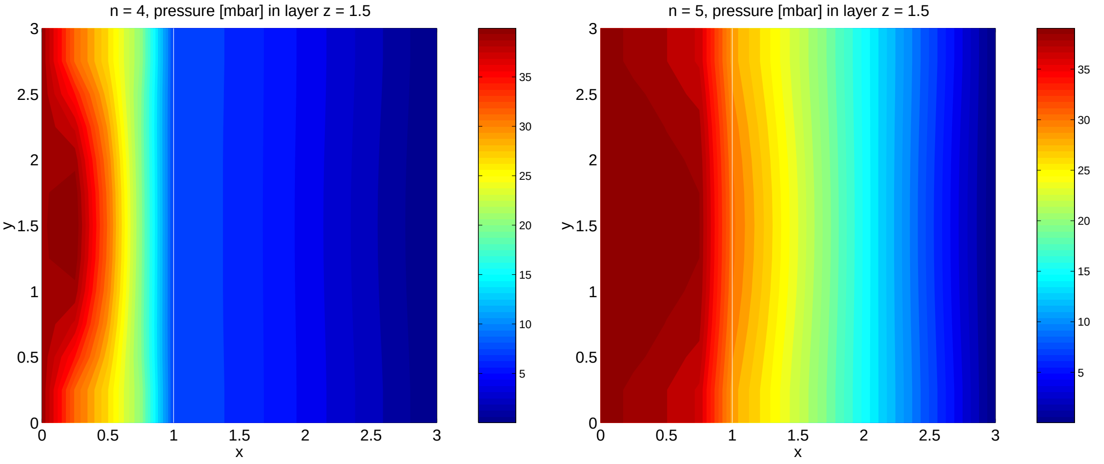

(a)

(b)

Figure 6.30: Cake filtration (filter cake $1 \times 3 \times 3$ mm^3 + filter $2 \times 3 \times 3$ mm^3) - Pressure in cross-section $z = 1.5$ for a cake with E-modulus E $= 6$ GPa (a) and E-modulus E $= 200$ MPa (b). In both cases, the filter cake has porosity $\phi = 65$ % and permeability $k = 10^{-6}$ mm^2. The filter medium has E-modulus E $= 200$ GPa, porosity $\phi = 95$ % and permeability $k = 10^{-4}$ mm^2.

approximately of the same size in both cases.

Figures 6.33(a) and 6.33(b) show pressure profiles in a cross-section in the middle of the porous medium.

The computations for these two examples are done with a time step $h_t = 0.5$ s.

For the example with the stiffer filter cake (E $= 200$ MPa), it took 2691 iterations to reach convergence ($5 \cdot 520$ for the solution of the Biot poroelasticity equations and $16 + 16 + 19 + 2 \cdot 20$ for the solution of the Stokes equations).

The example with the softer filter cake (E $= 2$ MPa) needed 3555 iterations to converge ($6 \cdot 574$ for the solution of the Biot poroelasticity equations and $16 + 16 + 19 + 3 \cdot 20$ for the solution of the Stokes equations).

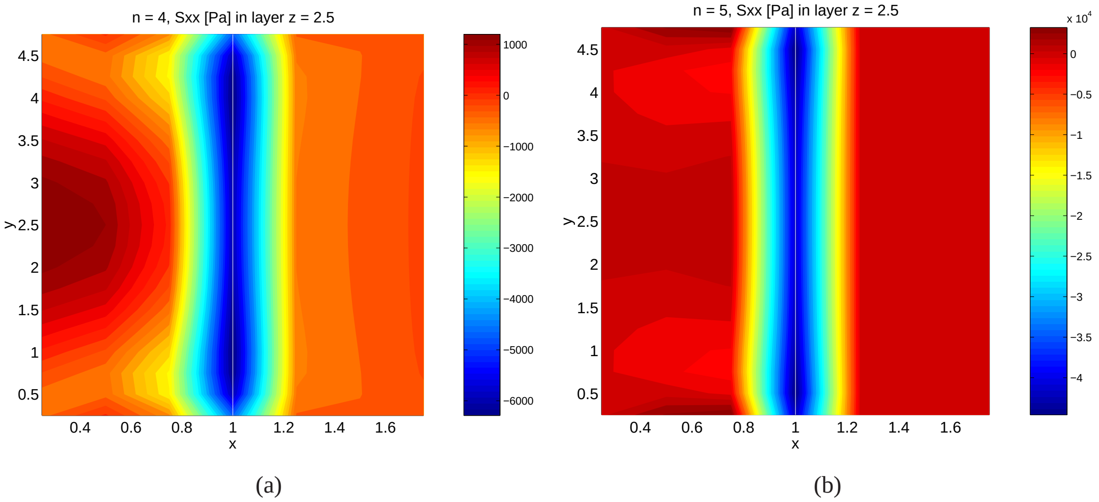

(a) (b)

Figure 6.31: Cake filtration (filter cake $1 \times 5 \times 5$ mm^3 + filter $1 \times 5 \times 5$ mm^3) - Stress component $\sigma_{p,xx}$ in cross-section $z = 1.5$ for a cake with E-modulus E $=$ 200 MPa (a) and E-modulus E $=$ 2 MPa (b). In both cases, the filter cake has porosity $\phi = 65\%$ and permeability $k = 10^{-6}$ mm^2. The filter medium has E-modulus E $=$ 200 GPa, porosity $\phi = 95\%$ and permeability $k = 10^{-4}$ mm^2. Note that the stress boundary values are not contained in the plots.

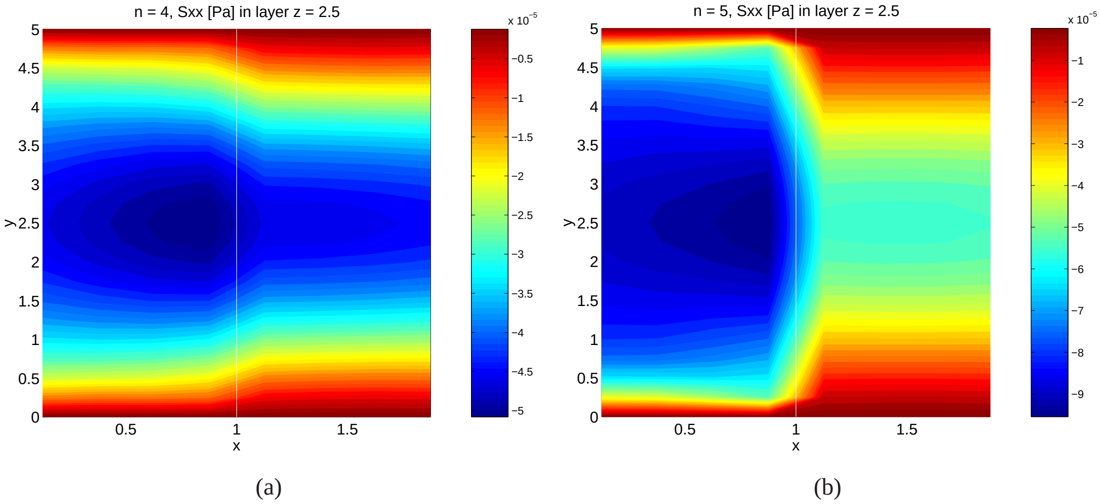

(a) (b)

Figure 6.32: Cake filtration (filter cake $1 \times 5 \times 5$ mm^3 + filter $1 \times 5 \times 5$ mm^3) - Displacements in flow direction in cross-section $z = 1.5$ for a cake with E-modulus E $= 200$ MPa (a) and E-modulus $E = 2$ MPa (b). In both cases, the filter cake has porosity $\phi = 65\%$ and permeability $k = 10^{-6}$ mm^2. The filter medium has E-modulus E $= 200$ GPa, porosity $\phi = 95\%$ and permeability $k = 10^{-4}$ mm^2.

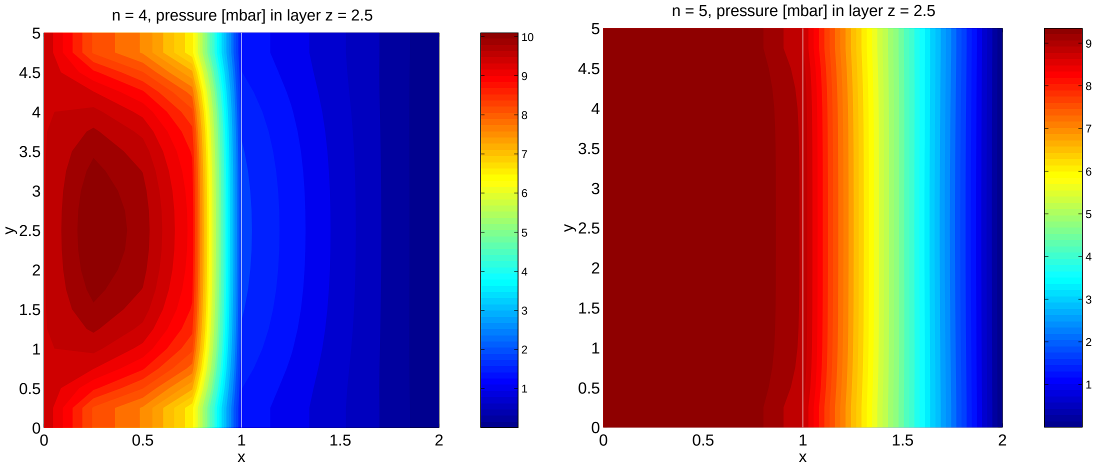

(a) (b)

Figure 6.33: Cake filtration (filter cake $1 \times 5 \times 5$ mm^3 + filter $1 \times 5 \times 5$ mm^3) - Pressure in cross-section $z = 1.5$ for a cake with E-modulus E $=$ 200 MPa (a) and E-modulus E $=$ 2 MPa (b). In both cases, the filter cake has porosity $\phi = 65\%$ and permeability $k = 10^{-6}$ mm^2. The filter medium has E-modulus E $=$ 200 GPa, porosity $\phi = 95\%$ and permeability $k = 10^{-4}$ mm^2.

Summary

In this thesis, the coupling of the Stokes equations and the Biot poroelasticity equations for fluid flow normal to porous media was investigated. For that purpose, the transmission conditions across the interfaces between the fluid regions and the porous domain were derived.

First, some basic laws governing the phenomena in pure fluid flow regions, solid materials and porous media were given and thus, a basis for the thesis was established (sections 1.1 - 1.3.6). We also motivated the use of the Biot poroelasticity equations instead of the linear elasticity equations in the porous domain (section 1.4) for the cases we considered.

Afterwards, we reviewed transmission conditions for the coupling of various physical phenomena, like fluid-fluid coupling, fluid-solid coupling, the coupling of fluid flow with rigid porous media and the coupling of fluid flow with poroelastic media for parallel flow (section 2.2). For the coupling of free flow with porous media, we have to distinguish whether the fluid flows tangentially or perpendicularly to the porous medium. This plays an essential role for the formulation of the transmission conditions. We derived the transmission conditions for the coupling of the Stokes equations and the Biot poroelasticity equations for fluid flow normal to the porous medium in one and three dimensions (sections 2.2.1 and 2.2.2). As far as we know, they have not been formulated before. With these conditions, we formulated the continuous fully coupled system of equations in one and three dimensions (sections 2.3 and 3.2). Some investigations of the one dimensional case were done in chapter 3.

Chapters 4 and 5 were devoted to the discretisation of the fully coupled Biot-Stokes system for matching and non-matching grids, respectively. In chapter 4 the entire system was discretised for matching node-based grids. Operators were introduced that map the internal and boundary variables to the respective domains via Stokes equations, Biot equations and the transmission conditions. The matrix representation of some of these operators was shown. In chapter 5 we did the same for non-matching grids. We used a cell-centred grid in the fluid region and a staggered grid in the porous domain. For non-matching grids, the discretisation is more difficult than in the matching case, since an additional grid on the interface has to be introduce. We also need corresponding matching functions to transfer the values properly from one domain to the other across the interface.

In chapter 6 we dwelled on the iterative solution procedure for the Biot-Stokes system on non-matching grids. First, we gave a short review of domain decomposition methods (section 6.1), which are often the methods of choice for such coupled problems. Then, we presented the iterative solution algorithm for our case, including details like stopping criteria, choice and computation of parameters, formulae for non-dimensionalisation and so on (section 6.2). The software in use was described in section 6.3. Finally, we presented numerical results for steady state examples, depth

filtration and cake filtration examples (sections 6.4 - 6.6).

Notation

In this list we summarise the meaning of variables and symbols used in the thesis. If not mentioned otherwise, this meaning is applied within the text.

a	fluid entry resistance of the porous medium ($a \geq 0$)
A	interface area
A_f	fluid part of the interface area A
A_f^*	area behind constriction (channel with discontinuous contraction of cross-section)
A_{fs}	interfacial area between fluid and solid phase in Ω_p
A_s	solid part of the interface area A
B	operator mapping values from Ω_p to Ω_p via Biot equations (exists only as $\mathring{B}$ and $\hat{B}$)
C_c	contraction number (channel with discontinuous contraction)
C_e	efficiency number of a step diffuser (channel with discontinuous expansion)
C_KC	coefficient in Kozeny-Carman equation
d_h	diameter of the capillary tubes through the porous medium
d	mean particle diameter
E	Young’s modulus (or E-modulus) of solid material
E_{ijkl}	elasticity tensor (of 4th order)
$\mathbf{f}_B$	right hand side of the Brinkman equation
f_f, $\mathbf{f}_f$	right hand side of Stokes equations (1d, 3d)
f_p	right hand side of Biot poroelasticity equations
$\mathbf{F}$	force
G	shear modulus of solid material
h_t	time step
h_x, h_y, h_z	grid width in x-, y- and z-direction
$\mathbf{I}$	unit matrix
k	permeability
$\mathbf{K}$	permeability tensor
K	bulk modulus of solid material

$\mathcal{L}$	length of $\Omega \subset \mathbb{R}$ in 1d example
$\mathcal{M}$	elastic modulus of a solid material with zero porosity
$\mathbf{n}$	normal vector
$\mathbb{N}$	set of natural numbers
N_f	number of nodes in Ω_f
N_p	number of nodes in Ω_p
N_{TC}	number of transmission conditions
N_x, N_y, N_z	number of grid cells in x-, y- and z-direction
N_Γ	number of interface nodes
$\mathcal{O}$	Landau symbol
p_f	fluid pressure in Ω_f (1d, 3d)
p_p	fluid pressure in Ω_p (1d, 3d)
p_p^*	pressure behind discontinuous constriction in flow channel
P	point in undeformed domain Ω
P’	point in deformed domain Ω'
q, $\mathbf{q}$	fluid flux in Ω_p (1d, 3d)
$\mathcal{Q}$	flow resistance tensor
$\mathbf{r}_B$, $\mathbf{r}_S$	right hand sides of the Biot equations and Stokes equations in the discrete case
$\mathbb{R}$	set of real numbers
s_k	Kozeny constant ($s_k = s\theta^2$)
S	operator mapping values from Ω_f to Ω_f via Stokes equations (exists only as $\mathring{S}$ and $\hat{S}$)
t	time
$\mathbf{t}$	traction vector
T_B, T_S	operators mapping values from Γ to boundary and interior of Ω_p and Ω_f, respectively, via transmission conditions (exist only as $\hat{T}_B$, $\mathring{T}_B$, $\hat{T}_S$ and $\mathring{T}_S$)
u, $\mathbf{u}$	displacements in Ω_p (1d, 3d)
v, $\mathbf{v}$	fluid velocity in Ω_f (1d, 3d)
v_f^p, $\mathbf{v}_f^p$	fluid velocity of the fluid within Ω_p (1d, 3d)
V_f^p	volume occupied by the fluid in Ω_p
V_p	volume of the domain occupied by the porous medium Ω_p
V_s	solid volume fraction in Ω_p
$\mathbf{x}$	position vector of P in deformed domain Ω' (section 1.2) or solution vector for Biot or Stokes equations (chapters 4 - 6)
$\mathbf{X}$	position vector of P in undeformed domain
x, y, z	coordinate directions

α	Biot-Willis constant
β	compressibility of the fluid
β_ξ	variable, introduced for the discretisation of the Biot-Stokes system
$\gamma_{\xi\zeta}$	variable, introduced for the discretisation of the Biot-Stokes system
γ	slip rate coefficient
Γ	interface between Ω_f and Ω_p
δ_ξ, δ'_ξ	variables, introduced for the discretisation of the Biot-Stokes system
δ_{ij}	Kronecker-Delta
ϵ	tolerance
ε	strain tensor
η	dynamic viscosity of the fluid
θ	tortuosity
$\kappa_{\mathcal{M}}$	coefficient in the derivation of the effective elastic moduli
λ	Lamé coefficient
μ	Lamé coefficient
ν_s	Poisson's ratio of solid material
ϱ	fluid density
σ	general notation for a stress tensor
σ_f	stress tensor for incompressible Newtonian fluids
σ_f^p	fluid stress tensor for the fluid inside Ω_p
σ_p	effective stress tensor of porous medium
σ_s	stress tensor of solid material (elastic stress)
$\overline{\sigma_{\text{tot}}}$	averaged total stress tensor of the porous medium
ς	material quantity
τ	time step counter
Υ	variable, introduced for discretisation of Biot-Stokes system
ϕ	porosity
φ	coefficient for bilinear interpolation of pressure values
$\chi_{\mu\xi\zeta}$, $\chi_{\lambda\xi\zeta}$, $\chi_{\mu\lambda\xi\zeta}$	variables used for the discretistion of the Biot-Stokes system
ψ	coefficient for bilinear interpolation of displacement values
Ψ	variable, introduced for discretisation of Biot-Stokes system
ω_{cc}	grid points of cell-centred grid
ω_{nb}	grid points of node-based grid
ω_{sg}	grid points of staggered grid
ω^t	grid points of the time discretisation grid

Ω	model domain
Ω_f	fluid domain
$\partial\Omega_f$	boundary of Ω_f
Ω_{f1}, Ω_{f2}	fluid subdomains
$\partial\Omega_{f1}$, $\partial\Omega_{f2}$	boundary of Ω_{f1} and Ω_{f2}
Ω_p	porous domain
$\partial\Omega_p$	boundary of Ω_p
Ω'	domain in deformed state

Subscripts

B	related to Biot equations
f	related to Ω_f
fixed	related to a fixed boundary
(i, j, k)	index notation for node-based and staggered grid
$(\mathtt{i}, \mathtt{j}, \mathtt{k})$	index notation for cell-centred grid
$(\mathcal{I}, \mathcal{J}, \mathcal{K})$	index notation for interface nodes on interface of non-matching meshes
in	related to an inflow boundary or inflow interface, respectively
out	related to an outflow boundary or outflow interface, respectively
p	related to Ω_p
p_p	related to pressure p_p
r	denotes reference values in non-dimensionalisation
s	related to the solid material
S	related to Stokes equations
u_x, u_y, u_z	related to displacement components u_x, u_y, u_z, respectively
x, y, z	coordinate direction x, y and z
$,x$, $,y$, $,z$	derivative with respect to x, y and z
0	denotes a boundary condition value
ξ, ζ, υ	index notation in the discretisation of the Biot-Stokes system

Superscripts

t	tangential component
T	transposed

Symbols

$\emptyset$	empty set
$\Delta_x\,,\ \Delta_y\,,\ \Delta_z$	forward space discretisation operators
$\Delta_{\bar{t}}$	backward time discretisation operator
$[]_{\vert\Gamma}$	jump across the interface Γ
$\langle . \rangle$	one-dimensional mean value
$\check{(.)}$	denotes value from a previous time step
$\overline{(.)}$	volume-averaged quantity over V_p
$\overline{(.)}^{fp}$	volume-averaged quantity over V_f^p
$\overline{(.)}^{s}$	volume-averaged quantity over V_s
$\hat{(.)}$	denotes boundary values
$\mathring{(.)}$	denotes internal values

Bibliography

[1] F. P. T. Baaijens, *A ficticious domain/mortar element method for fluid-structure interaction*, Int. J. Numer. Meth. Fluids, 35, pp. 743-761, 2001.

[2] S. I. Barry, G. N. Mercer, C. Zoppou, *Deformation and fluid flow due to a source in a poro-elastic layer*, Appl. Math. Modelling, 21, pp. 681-689, 1997.

[3] J. Bear, *Dynamics of Fluids in Porous Media*, Dover Publications, Inc., New York, 1988.

[4] J. Bear, Y. Bachmat, *Introduction to modeling of transport phenomena in porous media*, Kluwer Academic, Dordrecht, 1990.

[5] J. Bear, A. Verruijt, *Modeling Groundwater Flow and Pollution*, D. Reidel Publishing Company, Dordrecht, Holland, 1987.

[6] J. Betten, *Kontinuumsmechanik - Elastisches und inelastisches Verhalten isotroper und anisotroper Stoffe*, 2. Auflage, Springer-Verlag Berlin Heidelberg, 2001.

[7] G. S. Beavers, D. D. Joseph, *Boundary conditions at a naturally permeable wall*, Journal of Fluid Mechanics, Vol. 30, part 1, pp. 197-207, 1967.

[8] M. Biot, *General theory of three dimensional consolidation*, J. Appl. Phys., Vol. 12, pp. 155-169, 1941.

[9] P. von Böckh, *Fluidmechanik*, Einführendes Lehrbuch, 2. Auflage, Springer-Verlag Berlin Heidelberg, 2004.

[10] R. de Boer, *Theory of Porous Media - Highlights in the Historical Development and Current State*, Springer-Verlag Berlin Heidelberg, 2000.

[11] A. J. Chorin, J. E. Marsden, *A Mathematical Introduction to Fluid Mechanics*, Third Edition, Springer-Verlag New York, 1998.

[12] P. G. Ciarlet, *Mathematical Elasticity, Volume 1: Three Dimensional Elasticity*, North-Holland, Amsterdam, 1988.

[13] L. P. Dake, *Fundamentals of reservoir engineering*, Developments in Petroleum Science 8, Elsevier, Amsterdam - Oxford - New York, 1978.

[14] R. Dautray, J.-L. Lions, *Mathematical Analysis and numerical methods for sciences and technology*, 1990.

[15] J. W. Demmel, *Applied Numerical Linear Algebra*, SIAM Society for Industrial and Applied Mathematics, pp. 371 et seqq., Philadelphia, 1997.

[16] F. A. L. Dullien, *Porous Media - Fluid Transport and Pore Structure*, Academic Press, New York, 1979.

[17] A. Ern, J.-L. Guermond, *Theory and Practice of Finite Elements*, Applied Mathematical Sciences 159, Springer-Verlag New York, 2004.

[18] J. H. Ferziger, M. Perić, *Computational Methods for Fluid Dynamics, Second Edition*, Springer-Verlag Berlin Heidelberg 1999.

[19] C. A. J. Fletcher, *Computational Techniques for Fluid Dynamics, Volume I*, Fundamental and General Techniques, Springer Series in Computational Physics, Springer-Verlag Berlin Heidelberg, 1991.

[20] C. A. J. Fletcher, *Computational Techniques for Fluid Dynamics, Volume II*, Specific Techniques for Different Flow Categories, Second Edition, Springer Series in Computational Physics, Springer-Verlag Berlin Heidelberg, 1988.

[21] F. J. Gaspar, F. J. Lisbona, C. W. Osterlee, R. Wienands, *A systematic comparison of coupled and distributive smoothing in multigrid for the poroelasticity system*, Num. Lin. Algebra Appl. 11, pp. 93-113, 2004.

[22] F. J. Gaspar, F. J. Lisbona, P. N. Vabischevich, *A finite difference analysis of Biot's consolidation model*, Appl. Num. Math., pp. 487-506, 44, 2003.

[23] F. J. Gaspar, F. J. Lisbona, P. N. Vabischevich, *A numerical model for radial flow through porous and deformable shells*, CMAM, pp. 34-47, 1(4), 2004.

[24] C. Grandmont, Y. Maday, *Nonconforming Grids for the Simulation of Fluid-Structure Interaction*, Contemporary Mathematics, Vol. 218, 1998.

[25] D. Gross, W. Hauger, W. Schnell, J. Schröder, *Technische Mechanik, Band 2: Elastostatik*, Springer-Verlag Berlin Heidelberg, 2005.

[26] D. Gross, W. Hauger, W. Schnell, P. Wriggers, *Technische Mechanik, Band 4: Hydromechanik, Elemente der Höheren Mechanik, Numerische Methoden*, Springer-Verlag Berlin Heidelberg, 2007.

[27] R. W. Johnson, *The Handbook of Fluid Dynamics*, CRC Press LLC Boca Raton (USA), Springer-Verlag Heidelberg, 1998.

[28] Z. Hashin, *Elastic Moduli of Heterogeneous Materials*, J. Appl. Mech., 29 [1], pp. 43-50, 1962.

[29] Z. Hashin, S. Shtrikman, *A Variational Approach to the Theory of the Elastic Behavior of Multiphase Materials*, J. Mech. Phys. Solids, Vol. 11 [2], pp. 127-140, 1963.

[30] U. Hornung, *Homogenization and Porous Media*, Interdisciplinary Applied Mathematics, Springer-Verlag New York, 1997.

[31] P. A. Hsieh, *Poroelasticity Simulation of Ground-Water Flow and Subsurface Deformation*, U.S. Geological Survey Open-File Report, Subsidence Interest Group Conference, Las Vegas, Nevada, February 14-16, 97-47, pp. 5-9, 1995.

[32] O. Iliev, V. Laptev, *On Numerical Simulation of Flow Through Oil Filters*, Computing and Visualization in Science 6, pp. 139-146, 2004. Also published in: Berichte des Fraunhofer ITWM, Nr. 51, 2003.

[33] O. Iliev, V. Laptev, D. Vasileva, *Algorithms and software for computer simulation of flow through oil filters*, Proc. Int. Conf. Filtech Europa, Vol. 1, pp. 327-334, 2003.

[34] O. Iliev, A. Mikelić, P. Popov, *On upscaling certain flows in deformable porous media*, SIAM J. on Multiscale Modeling and Simulation 7, No. 1, pp. 93-123, 2008. Also published in: Berichte des Fraunhofer ITWM, Nr. 65, 2004.

[35] I. P. Jones, *Low Reynolds number flow past a porous spherical shell*, Proc. Camb. Phil. Soc., 73, pp. 231-238, 1973.

[36] M. Kaviany, *Principles of Heat Transfer in Porous Media*, Springer-Verlag New York, 1991.

[37] R. Kornhuber, J. Périaux, O. Widlund, R. Hoppe, O. Pironneau, J. Xu (Editors), *Domain Decomposition Methods in Science and Engineering*, Lecture Notes in Computational Science and Engineering, Vol. 40, Springer-Verlag Berlin Heidelberg, 2005.

[38] W. Kümmel, *Technische Strömungsmechanik, Theorie und Praxis*, 2. Auflage, Teubner, Wiesbaden, 2004.

[39] U. Langer, M. Discacciati, D. Keyes, O. Widlund, W. Zulehner (Editors), *Domain Decomposition Methods in Science and Engineering XVII*, Lecture Notes in Computational Science and Engineering, Vol. 60, Springer-Verlag Berlin Heidelberg, 2008.

[40] V. Laptev, *Numerical solution of coupled flow in plain and porous media*, Dissertation, University of Kaiserslautern, 2003.

[41] W. J. Layton, F. Schieweck, I. Yotov, *Coupling fluid flow with porous media flow*, SIAM J. Numer. Anal., Vol. 40, No. 6, pp. 2195-2218, 2003.

[42] R. W. Lewis, B. A. Schrefler, *The Finite Element Method in the Static and Dynamic Deformation and Consolidation of Porous Media*, John Wiley & Sons, Chichester, 1998.

[43] A. Mikelić, *Homogenization theory and applications to filtration through porous media*, Lecture Notes in Mathematics, Vol. 1734, Springer-Verlag Berlin, 2000.

[44] S. Muntz, *Simulation of fluid structure interaction in porous deformable media*, Diploma Thesis, Technical University of Kaiserslautern, 2004.

[45] A. Naumovich, F. J. Gaspar, *On a multigrid solver for the three-dimensional Biot poroelasticity system in multilayered domains*, Comput. Vis. Sci. 11, pp. 77-87, 2008. Also published in: Berichte des Fraunhofer ITWM, Nr. 85, 2006.

[46] A. Naumovich, *Efficient numerical methods for the Biot poroelasticity system in multilayered domains*, PhD Thesis, Technical University Kaiserslautern, 2007.

[47] D. Niedziela, *On numerical simulation of viscoelastic fluids*, PhD Thesis, Technical University Kaiserslautern, 2006.

[48] D. A. Nield, A. Bejan, *Convection in Porous media*, Springer-Verlag New York, 1992.

[49] J. A. Ochoa-Tapia, S. Whitaker, *Momentum transfer at the boundary between a porous medium and a homogeneous fluid. II. Comparison with experiment.*, Int. J. Heat Mass Transfer, Vol. 38, pp. 2635 - 2646, 2005.

[50] N. Ramakrishnan, V. S. Arunachalam, *Effective Elastic Moduli of Porous Solids*, J. Mater. Sci. 25 [9], pp. 3930-3937, 1990.

[51] N. Ramakrishnan, V. S. Arunachalam, *Effective Elastic Moduli of Porous Ceramic Materials*, J. Am. Ceram. Soc. 76 [11], pp. 2745-2752, 1993.

[52] H. Rumpf, A. R. Gupte, *Einflüsse und Korngrößenverteilung im Widerstandsgesetz der Porenströmung*, Chemie-Ing. Techn., 43, 1971, pp. 367-375.

[53] P. G. Saffman, *On the boundary condition at the surface of a porous medium*, Studies in Appl. Math., Vol. 50, pp. 93-101, 1971.

[54] A. A. Samarskii, *The Theory of Difference Schemes*, Pure and Applied Mathematics, A Series of Monographs, Textbooks and Lecture Notes, 2001.

[55] E. Sanchez-Palencia, *Non-homogeneous media and vibration theory*, Lecture Notes in Physics, Vol. 127, Springer-Verlag, 1980.

[56] R. E. Showalter, *Diffusion in poro-elastic media*, Jour. Math. Anal. Appl. 251, pp. 310-340, 2000.

[57] R. E. Showalter, *Diffusion in Deformable Media*. Published in J. Chadam, A. Cunningham, R. E. Ewing, P. Ortoleva, M. F. Wheeler (Editors), *Resource Recovery, Confinement, and Remediation of Environmental Hazards*, The IMA Volumes in Mathematics and its Applications, Vol. 131, pp. 115-130, Springer-Verlag New York, 2002.

[58] R. E. Showalter, *Diffusion in Deforming Porous Media*, Dynamics of Continuous, Discrete and Impulsive Systems, Series A: Mathematical Analysis 10, pp. 661-678, 2003.

[59] R. E. Showalter, *Poroelastic filtration coupled to Stokes flow*. Published in O. Imanuvilov, G. Leugering, R. Triggiani, and B.-Y. Zhang (Editors), *Control Theory of Partial Differential Equations*, Lecture Notes in Pure and Applied Mathematics, Vol. 242, pp. 229-241, Chapman & Hall, Boca Raton, 2005.

[60] R. E. Showalter, *Poro-Plastic Filtration Coupled to Stokes Flow*. Published in Y. Abousleiman, A.H.-D. Cheng, F.-J. Ulm, *Poromechanics III - Biot Centennial (1905-2005)*, Proceedings, 3rd Biot Conference on Poromechanics, A.A. Balkema, Leidon/London/New York/Philadelphia/Singapore, pp. 523-528, 2005.

[61] D. Singh, *On the Design and Analysis of Tubular Ceramic Filters*, report of Dhruv Singh, Undergraduate Student of Indian Institute of Technology, internship May-July 2005 at Fraunhofer ITWM, Kaiserslautern.

[62] B. Smith, P. Bjørstad, W. Gropp, *Domain Decomposition - Parallel Multilevel Methods for Elliptic Partial Differential Equations*, Cambridge University Press, Cambridge, 1996.

[63] J. H. Spurk, *Strömungslehre - Einführung in die Theorie der Strömungen*, Zweite überarbeitete und erweiterte Auflage, Springer-Verlag Berlin Heidelberg, 1989.

[64] H. F. Wang, *Theory of Linear Poroelasticity with Applications to Geomechanics and Hydrogeology*, Princeton Series in Geophysics, Princeton University Press, Princeton, 2000.

[65] R. Wienands, F. J. Gaspar, F. J. Lisbona, C. W. Oosterlee, *An efficient multigrid solver based on the distributive smoothing for poroelasticity equations*, Computing, pp. 99-119, Vol. 73(2), 2004.

[66] J. Winkler, H. Aurich, *Taschenbuch der Technischen Mechanik*, 8. Auflage, Fachbuchverlag Leipzig im Carl Hanser Verlag, München, 2006.

[67] P. Wriggers, *Nichtlineare Finite-Element-Methoden*, Springer-Verlag Berlin Heidelberg, 2001.

[68] http://www.itwm.fhg.de/de/sks__projects__sks_hydrodynamik__sufis/sufis/

[69] http://www.itwm.fhg.de/de/sks__projects__sks_komplexefluide/sksfluide/

[70] http://www.itwm.fhg.de/sks/flyer/sks_flyer_CoRheoS_DE.pdf

CURRICULUM VITAE

26.09.1979	Born in Ludwigshafen/Rhein, Germany
1986 – 1990	Albert-Schweitzer-Grundschule, Altrip (primary school)
1990 – 1999	Geschwister-Scholl-Gymnasium, Ludwigshafen/Rhein (secondary school)
10/1999 – 07/2004	Technical University of Kaiserslautern, Studies of Industrial Mathematics
08/2002 – 03/2003	Chalmers University of Technology, Gothenburg, Sweden, Semester abroad within the Erasmus programme of the European Union, Studies of Mathematics
07/2004	Diploma in Industrial Mathematics
09/2004 – 07/2008	PhD student at the Fraunhofer Institute for Industrial Mathematics (Fraunhofer Institut für Techno- und Wirtschaftsmathematik) and the Technical University of Kaiserslautern, Department of Mathematics, Kaiserslautern
09/2006 – 03/2007	Rock Deformation Research Ltd. and University of Leeds, Leeds, England, Research Fellow within the Marie Curie programme of the European Union

CURRICULUM VITAE

26.09.1979	Geboren in Ludwigshafen/Rhein
1986 – 1990	Albert-Schweitzer-Grundschule, Altrip
1990 – 1999	Geschwister-Scholl-Gymnasium, Ludwigshafen/Rhein
10/1999 – 07/2004	Technische Universität Kaiserslautern Studium der Technomathematik mit Nebenfach Maschinenbau
08/2002 – 03/2003	Chalmers Tekniska Högskola, Göteborg, Schweden Studium der Mathematik, Auslandssemester im Rahmen des Erasmus-Programms der Europäischen Union
07/2004	Diplom in Technomathematik
09/2004 – 07/2008	Doktorandin am Fraunhofer Institut für Techno- und Wirtschaftsmathematik und der Technischen Universität Kaiserslautern, Fachbereich Mathematik
09/2006 – 03/2007	University of Leeds und Rock Deformation Research Ltd., Leeds, England Forschungsstipendiatin im Rahmen des Marie-Curie-Programms der Europäischen Union